

Alma Mater Studiorum – Università di Bologna

DOTTORATO DI RICERCA IN
AUTOMOTIVE PER UNA MOBILITÀ
INTELLIGENTE

Ciclo 35

Settore Concorsuale: 09/B1 – TECNOLOGIE E SISTEMI DI LAVORAZIONE

Settore Scientifico Disciplinare: ING-IND/16 – TECNOLOGIE E SISTEMI DI LAVORAZIONE

NUMERICAL MODELING AND EXPERIMENTAL
VALIDATION OF THE RECRYSTALLIZATION
BEHAVIOUR IN THE EXTRUSION OF 6XXX
ALUMINUM ALLOYS

Presentata da: Marco Negozio

Coordinatore Dottorato

Nicolò Cavina

Supervisore

Lorenzo Donati

Co-supervisore

Alessandro Fortunato

Esame finale anno 2023

Abstract

The microstructure of 6XXX aluminum alloys deeply affects mechanical, crash, corrosion and aesthetic properties of extruded profiles. Unfortunately, grain structure evolution during manufacturing processes is a complex phenomenon because several process and material parameters such as alloy chemical composition, temperature, extrusion speed, tools geometries, quenching and thermal treatment parameters affect the grain evolution during the manufacturing process. The aim of the present PhD thesis was the analysis of the recrystallization kinetics during the hot extrusion of 6XXX aluminum alloys and the development of reliable recrystallization models to be used in FEM codes for the microstructure prediction at a die design stage. Experimental activities have been carried out in order to acquire data for the recrystallization models development, validation and also to investigate the effect of process parameters and die design on the microstructure of the final component. The experimental campaign reported in this thesis involved the extrusion of AA6063, AA6060 and AA6082 profiles with different process parameters in order to provide a reliable amount of data for the models validation. A particular focus was made to investigate the PCG defect evolution during the extrusion of medium-strength alloys such as AA6082. Several die designs and process conditions were analysed in order to understand the influence of each of them on the recrystallization behaviour of the investigated alloy. From the numerical point of view, innovative models for the microstructure prediction were developed and validated over the extrusion of industrial-scale profiles with complex geometries, showing a good matching in terms of the grain size and surface recrystallization prediction. The achieved results suggest the reliability of the developed models and their application in the industrial field for process and material properties optimization at a die-design stage.

Acknowledgements

The most important people that deserve more than one thanks are Prof. Lorenzo Donati and Prof. Luca Tomesani for their guidance, encouragement and scientific support. They not only gave me lessons in the research and science but also in many aspects of my professional life. During my PhD, I also had the amazing support of Prof. Barbara Reggiani, Dr. Riccardo Pelaccia and Mrs Sara Di Donato whom I would like to thank. Another special thanks with my entire heart goes to my parents and brother for supporting me on this PhD journey. Without them none of this would have been possible. Finally, I would like to thank my friends and girlfriend for believing in me, for caring about me and for helping me to keep my focus during the whole period.

TABLE OF CONTENTS

1. Introduction.....	6
1.1 Extrusion Process of Aluminum Alloys	6
1.1.1 Die Design	7
1.1.2 Extrusion Process Parameters	9
1.1.3 Thermodynamics	10
1.2 Grain Size Measurement Methods	11
1.3 The Influence of Microstructure on Material Properties	12
2. Recrystallization During the Extrusion of 6XXX Aluminum Alloys	28
2.1 Introduction	28
2.2 Recrystallization during the extrusion process of 6XXX aluminum alloys.	28
2.3 Dynamic and Static Recovery	31
2.4 Dynamic Recrystallization (DRX)	33
2.5 Stored Energy and Zener-Drag Pressure	37
2.6 Static Recrystallization (SRX).....	39
2.7 Peripheral Coarse Grain (PCG) and Abnormal Grain Growth (AGG).....	43
2.8 Modeling of the Recrystallization Mechanisms	46
2.8.1 Modeling of the Dynamic Recrystallization.....	46
2.8.2 Modeling of the Static Recrystallization	49
3. FEM Simulation of the Extrusion Process.....	63
3.1 FEM simulation of manufacturing processes	63
3.2 Approaches of FEM Codes.....	64
3.3 Qform UK® software.....	66
3.3.1 Numerical Modeling of the Extrusion Process using Qform Extrusion	66
3.3.2 Post-Process Analysis through the Use of Sub-Routines	74
3.4 Validation of the FEM code in the extrusion of aluminum alloys.....	78
4. Modeling of the Recrystallization Behaviour of AA6063 Aluminum Alloy Extruded Profiles.....	81
4.1 Experimental Investigation.....	81
4.2 Modeling of the AA6063 Recrystallization Behaviour	89
4.3 Numerical Simulation of the Extrusion Processes.....	92
4.4 Comparison Between Numerical and Experimental Results.....	96
5. Modeling of the Recrystallization Behaviour of AA6060 Aluminum Alloy Extruded Profiles.....	105
5.1 Experimental Investigation.....	105
5.2 Modeling of the AA6060 Recrystallization Behaviour	107
5.3 Numerical Simulation of the Extrusion Processes.....	107

5.4	Comparison Between Numerical and Experimental Results	109
6.	Modeling of the Recrystallization Behaviour of AA6082 Aluminum Alloy Extruded Profiles.....	116
6.1	Case 1	117
6.1.1	Experimental Investigation	117
6.1.2	Recrystallization Modeling in AA6082 Aluminum Alloy.....	119
6.1.3	Numerical Simulation of the Extrusion Process	121
6.1.4	Comparison Between Numerical and Experimental Results	122
6.1.5	Remarks	131
6.2	Case 2	132
6.2.1	Experimental Investigation.....	132
6.2.2	PCG Modeling in AA6082 Aluminum Alloy.....	143
6.2.3	Numerical Simulation of the Extrusion Processes.....	145
6.2.4	Comparison Between Numerical and Experimental Results.....	147
6.2.5	Remarks	153
7.	Summary, Conclusions and Future Work.....	156

1. Introduction

1.1 Extrusion Process of Aluminum Alloys

The extrusion of aluminum alloys is a manufacturing process that allows the production of profiles with constant cross-section and complex geometry [1-3]. During this process, a pre-heated billet is forced to flow through the die opening/s generating the shape of the extruded profile. A simple schematization of the direct extrusion process is reported in Fig. 1.1. In this figure, the main process components are shown: the cylindrical billet is placed inside a container and the pressure is applied by the ram which is regulated by a hydraulic press. The billet must have slightly lower diameter in order to be inserted into the container. In the first step of the ram stroke, there is the upset of the billet which corresponds to its first compression until it reaches the same diameter as the container. After this phase, the material starts to flow inside the die and through its exit section. The thinner section of the die gives the external final shape to the profile and it is called the “bearing zone”. This configuration is called “direct extrusion” and it is characterized by the same direction between ram and extruded profile motion.

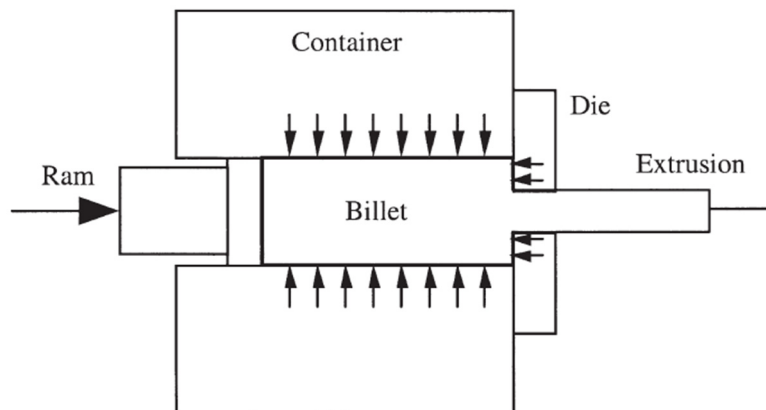


Figure 1.1: Schematization of the direct extrusion process [1].

There is also the possibility to perform the “indirect extrusion”, which is schematized in Fig. 1.2. Using this setting, the direction of the extruded profile is opposed to the ram direction thus causing a decrease in the friction between billet and container. This results in a decrease in the extrusion force and an increase in the process speed [1]. The main issue of the latter is the limit in the geometries achievable from the process since the die, as shown in Fig. 1.2, must move inside the container and perform the work made by the ram in the direct extrusion (Fig. 1.1).

However, the most common and important method used in the extrusion of lightweight alloys is the direct extrusion process. In Fig. 1.3, it is reported an example of the achievable complexity of the

extruded profile geometry in multi-hollow profiles, thin gauges, profiles with sophisticated appendices and wings etc.

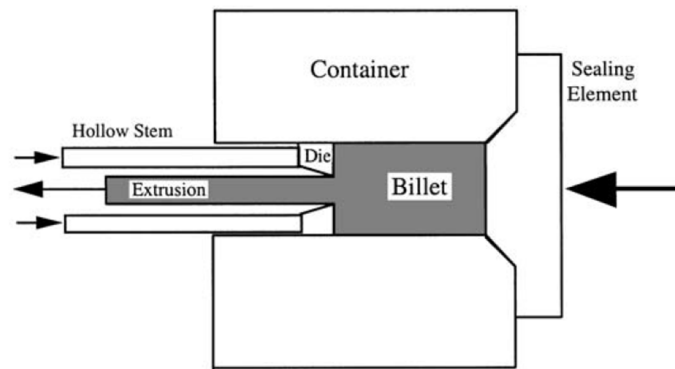


Figure 1.2: Schematization of the indirect extrusion process [1].



Fig. 1.3: Examples of profiles achievable with the hot extrusion process [3].

In order to control the hot extrusion process, several key-aspects must be taken into consideration. These aspects deal with the design of the tools, the extrusion main process parameters and the thermodynamics of the extrusion process.

1.1.1 Die Design

The most important part of the process tools equipment is the die, typically made by tool steels (AISI H-11 or H-13) or sintered carbides due to the high stresses and temperature reached during the manufacturing process. The design of the dies requires a particular experience as each die is characterized by a unique geometry for the production of a particular extruded profile. Therefore, the design requirements are often very stringent thus causing the high cost for the realization of the extrusion tool setup.

There are three different types of extrusion dies available [2, 3]: solid dies, semi-solid dies and hollow dies. Each one of them is used for the production of solid, semi-solid and hollow profiles,

respectively. They are made in order to provide high mechanical, temperature and wear resistances to increase the die life and, consequently, reduce the costs. Together with the die, supporting tools are present also made of hardened tool steel. These tools are known as backers, bolsters and sub-bolsters and support the die during the whole extrusion process (Fig. 1.4a).

In Fig. 1.4b and Fig. 1.4c, examples of a solid die and a hollow die are reported, respectively. The simplest type of solid die is the flat-face die: by using the latter, the billet material flows directly into the openings which have the exact same shape as the extruded profile. In order to have more control over the welding of subsequent billets during the continuous extrusion or over the spread of the aluminum in different areas of the die, pocket dies or feeder dies may be used which are characterized by intermediate cavities between the container and the bearing zone. In order to produce profiles with voids, hollow dies must be used as they present a component called “mandrel” for the realization of the internal shape of the voids in the profile (Fig. 1.4c). The semi-hollow die comes from the comparison between the area of the partially enclosed void and the square of the size of the gap called the “tongue ratio”. With respect to the tongue ratio, semi-hollow dies can present several settings (flat, pocket, etc.).

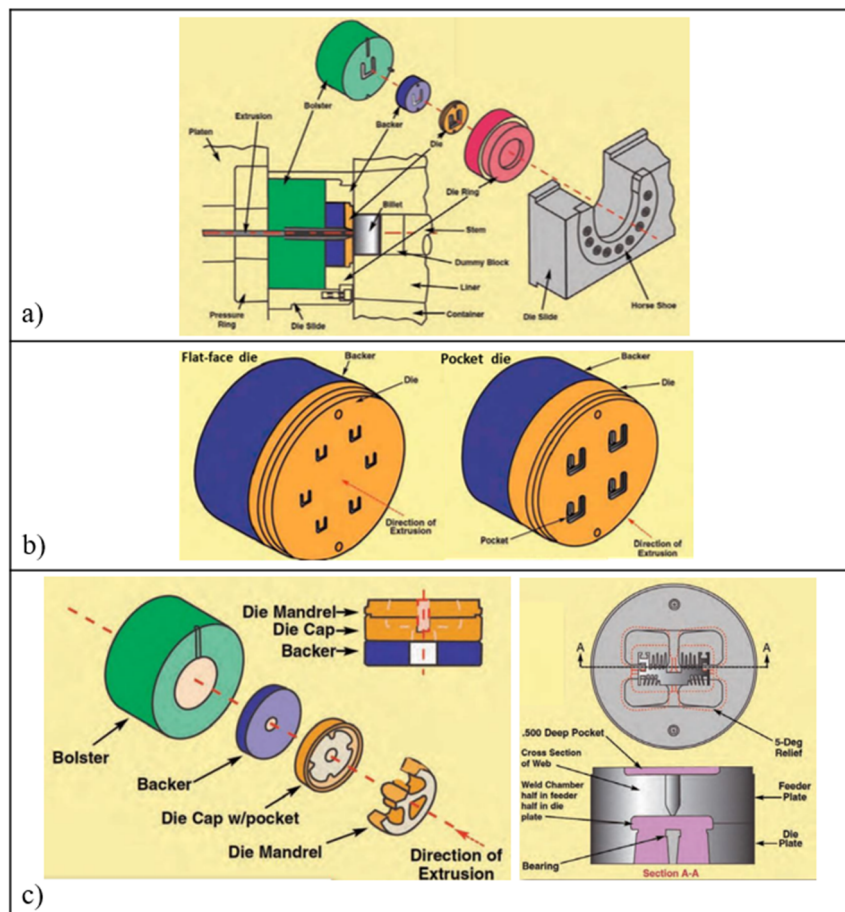


Figure 1.4: Schematization of a) die support tools, b) solid die, c) hollow die [3].

1.1.2 Extrusion Process Parameters

In Fig. 1.5, the typical extrusion load behaviour is reported for direct and indirect extrusion. The total extrusion force is affected by the plastic deformation of the material and the frictional forces which oppose to the movement of the billet material. In the first part of the ram stroke, the force increases until the extrusion chamber is filled (upsetting). In the case of direct extrusion, the force reaches a higher value as the initial frictional detachment between the surfaces of the billet and the internal walls of the tools must be overcome; on the contrary, this condition does not occur during indirect extrusion, so the extrusion force, in this configuration, is significantly lower and constant during the ram stroke with respect to direct extrusion case.

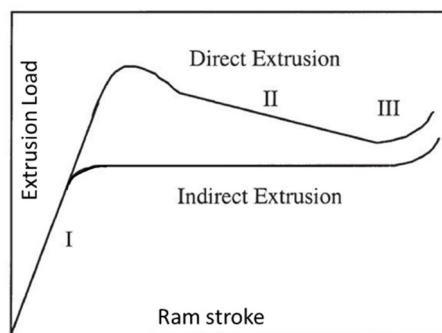


Fig. 1.5 Evolution of the extrusion load during the ram stroke [1].

The main extrusion process parameters are summarized as follows [1, 2]:

- extrusion ratio;
- working temperature;
- extrusion speed;
- flow stress.

The extrusion ratio ER is defined as:

$$ER = \frac{A_c}{n \cdot A_e} \quad (1.1)$$

where n is the number of symmetrical holes, A_c is the area of the container, and A_e is the area of the extruded profile. By analysing the extrusion ratio, information about the amount of mechanical work to reach the final shape of the profile will be acquired. Consequently, by increasing the extrusion ratio also the extrusion load will be increased. The normal ER range reached for soft alloys is 10-100 while, for hard alloys, 10-35.

The extrusion temperature is another important parameter because it affects the flow stress of the billet material. In order to decrease the total required extrusion load, high temperature must be achieved.

The extrusion speed is a key-parameter to control the productivity of the process. However, an increase in the speed, which is an increase in the strain rate, leads to an increase in the extrusion load. Even if also the working temperature increases with the ram speed, the influence of the strain rate is predominant in terms of extrusion load increase.

The material flow stress σ defines the extrusion load and is directly related to the chemical composition of the alloy and the process parameters (strain, strain rate and temperature).

$$\sigma = f(\varepsilon, \dot{\varepsilon}, T) \tag{1.2}$$

1.1.3 Thermodynamics

The control over the temperature during the hot extrusion of aluminum alloy is mandatory in order to achieve profiles with particular mechanical, corrosion and crash properties. Moreover, is a fundamental parameter because it may cause the formation of defects and limit the process productivity [4-6]. The main contributions to the thermal field are the heat generated by the plastic deformation of the billet material, the friction between aluminum and tool steel or dead metal zones, the convection between billet and air during the movement from the oven to the press, the conduction between billet and extrusion tools and by air/water (depending on the quenching system) at the die exit (Fig. 1.6). In Tab. 1.1, the typical range of temperature reached during the extrusion process is reported.

Table 1.2: Temperature ranges during hot extrusion processes.

Component	Billet preheat	Ram	Container	Die preheat	Exit profile
Temperature range	440-480°C	300-400°C	400-450°C	450-500°C	520-570°C

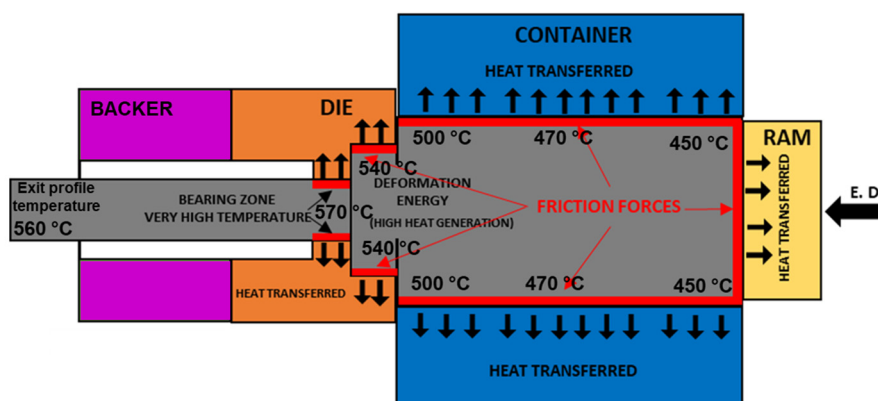


Figure 1.6: Schematization of the heat transfer history in hot extrusion process.

1.2 Grain Size Measurement Methods

The average grain size dimensions reported in this thesis were calculated according to the ASTM-E112 regulation [7], which contains a number of methods to determine the average diameter of equiaxed-shaped grains. It also contains information about measurements when grains have been elongated during the manufacturing process.

Three basic procedures are reported: the Comparison Procedure, the Planimetric Procedure and the Intercept Procedure (Fig. 1.7). The Comparison Procedure (Fig. 1.7a, as suggested by the name, involves the visual comparison of the investigated grain structure to a series of graded images of known grain size either in the form of a wall chart, clear plastic overlays or an eyepiece reticle. The user choose the standard image that looks more similar to the investigated microstructure. There are several types of comparison charts depending on what type of microstructure is investigated.

The Planimetric Procedure (Fig. 1.7b) involves the actual count of the number of grains within a particular known area. This number called N_A is used to determine the G value (ASTM grain size number, Fig. 1.8) which is a number that will then be entered in a standard table reported in the ASTM-E112 regulation to find the average grain diameter of the investigated microstructure. The accuracy of the method is a function of the number of grains counted.

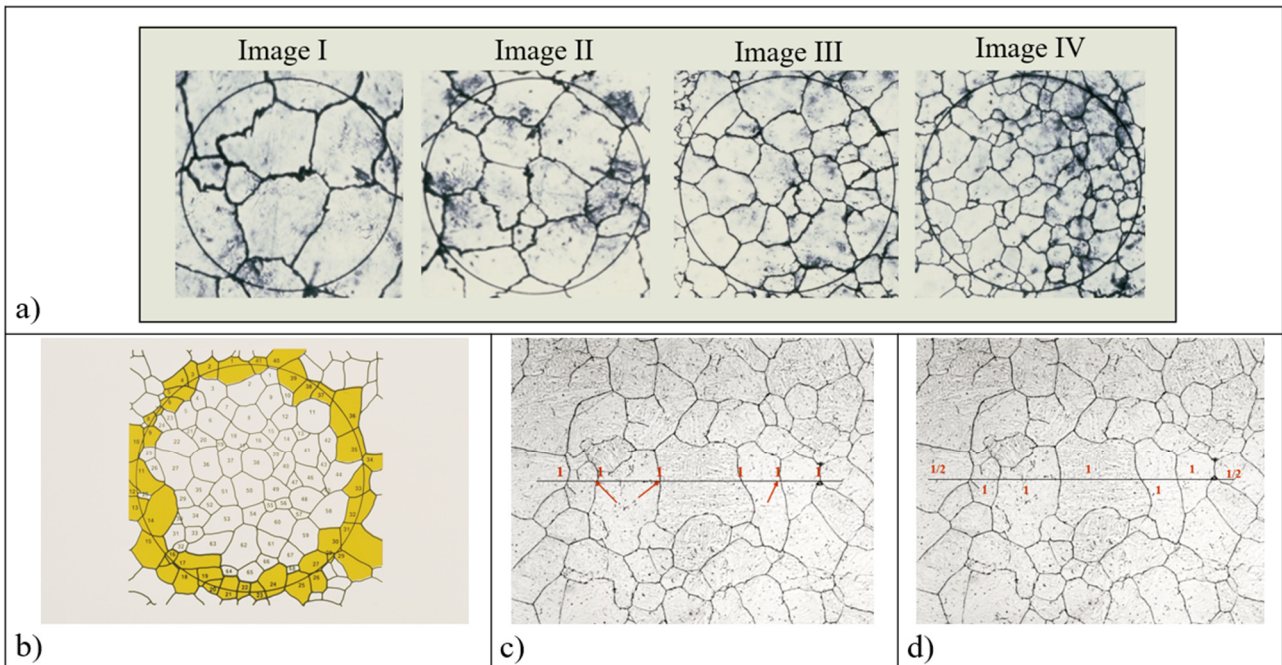


Figure 1.7: Examples of grain size measurement methods: a) Comparison, b) Planimetric, c,d) Intercept.

Grain Size No. G	\bar{N}_A Grains/Unit Area		\bar{A} Average Grain Area		\bar{d} Average Diameter		\bar{l} Mean Intercept		\bar{N}_L No./mm
	No./in. ² at 100X	No./mm ² at 1X	mm ²	μm ²	mm	μm	mm	μm	
00	0.25	3.88	0.2581	258064	0.5080	508.0	0.4525	452.5	2.21
0	0.50	7.75	0.1290	129032	0.3592	359.2	0.3200	320.0	3.12
0.5	0.71	10.96	0.0912	91239	0.3021	302.1	0.2691	269.1	3.72
1.0	1.00	15.50	0.0645	64516	0.2540	254.0	0.2263	226.3	4.42
1.5	1.41	21.92	0.0456	45620	0.2136	213.6	0.1903	190.3	5.26
2.0	2.00	31.00	0.0323	32258	0.1796	179.6	0.1600	160.0	6.25
2.5	2.83	43.84	0.0228	22810	0.1510	151.0	0.1345	134.5	7.43
3.0	4.00	62.00	0.0161	16129	0.1270	127.0	0.1131	113.1	8.84
3.5	5.66	87.68	0.0114	11405	0.1068	106.8	0.0951	95.1	10.51
4.0	8.00	124.00	0.00806	8065	0.0898	89.8	0.0800	80.0	12.50
4.5	11.31	175.36	0.00570	5703	0.0755	75.5	0.0673	67.3	14.87
5.0	16.00	248.00	0.00403	4032	0.0635	63.5	0.0566	56.6	17.68
5.5	22.63	350.73	0.00285	2851	0.0534	53.4	0.0476	47.6	21.02
6.0	32.00	496.00	0.00202	2016	0.0449	44.9	0.0400	40.0	25.00
6.5	45.25	701.45	0.00143	1426	0.0378	37.8	0.0336	33.6	29.73
7.0	64.00	992.00	0.00101	1008	0.0318	31.8	0.0283	28.3	35.36
7.5	90.51	1402.9	0.00071	713	0.0267	26.7	0.0238	23.8	42.04
8.0	128.00	1984.0	0.00050	504	0.0225	22.5	0.0200	20.0	50.00
8.5	181.02	2805.8	0.00036	356	0.0189	18.9	0.0168	16.8	59.46
9.0	256.00	3968.0	0.00025	252	0.0159	15.9	0.0141	14.1	70.71
9.5	362.04	5611.6	0.00018	178	0.0133	13.3	0.0119	11.9	84.09
10.0	512.00	7936.0	0.00013	126	0.0112	11.2	0.0100	10.0	100.0
10.5	724.08	11223.2	0.000089	89.1	0.0094	9.4	0.0084	8.4	118.9
11.0	1024.00	15872.0	0.000063	63.0	0.0079	7.9	0.0071	7.1	141.4
11.5	1448.15	22446.4	0.000045	44.6	0.0067	6.7	0.0060	5.9	168.2
12.0	2048.00	31744.1	0.000032	31.5	0.0056	5.6	0.0050	5.0	200.0
12.5	2896.31	44892.9	0.000022	22.3	0.0047	4.7	0.0042	4.2	237.8
13.0	4096.00	63488.1	0.000016	15.8	0.0040	4.0	0.0035	3.5	282.8
13.5	5792.62	89785.8	0.000011	11.1	0.0033	3.3	0.0030	3.0	336.4
14.0	8192.00	126976.3	0.000008	7.9	0.0028	2.8	0.0025	2.5	400.0

Figure 1.8: Grain Size Relationships Computed for Uniform, Randomly Oriented, Equiaxed Grains [7].

The Intercept Procedure (Fig. 1.7c,d) involves the count of the number of grains or grain boundaries intercepted by a test line in a known area to calculate the mean linear intercept length \bar{l} . \bar{l} is used to find the G value and then the average grain size as described above. As for the Planimetric Procedure, the accuracy of the method is a function of the number of intercepts or intersections counted.

The average grain size measurements reported in this thesis represent the mean value between the average grain size calculated according to the Planimetric Procedure and the Intercept Procedure.

It is important to understand that, by using these test methods, the measurement of average grain size is not an exact measurement. A grain structure is a number of three-dimensional grains of different sizes and shapes. The grain cross-section is a random plane through such a structure, would have a distribution of areas varying from a maximum value to zero, depending upon where the plane cuts each individual crystal. Clearly, no two plains of observation can be exactly the same and this is the reason why there is always a slight error in the average grain size measurement.

1.3 The Influence of Microstructure on Material Properties

The microstructure of aluminum alloys significantly affects mechanical, aesthetic, corrosion and crash properties [8-12]. Especially in the transportation field (i.e. aeronautical, automotive, railway, etc.), requirements in terms of grain structure need to be matched in order to ensure the quality of the

product. This condition imposes control over the evolution of the microstructure during the hot forming processes and the heat treatments of aluminum alloys. Unfortunately, the grain structure evolution is a complex phenomenon being affected by several process parameters such as the alloy chemical composition, temperatures, extrusion speed, tools geometries, quenching and thermal treatment settings. To date, the mechanisms occurring during recrystallization are not fully understood and, consequently, investigations are needed to evaluate the influence of the process parameters on the microstructure evolution for critical aluminum alloys.

The properties of the engineering materials are related to the atomic arrangement, the presence of crystal defects and the morphology and distribution of the constituting particles/phases. Moreover, grain size and texture deeply affect the mechanical strength, the corrosion resistance, the aesthetic properties and the crash performances of the extruded profile.

The grains are individual crystals within the polycrystalline material [13-16]. Depending on the basic crystal structure (face-centered cubic FCC, body-centered cubic BCC, hexagonal closed-packed HCP, and tetragonal), atoms are arranged. In this context, the presence of several imperfections in the atomic structure may occur thus influencing the properties of the material. These defects are distinguished into point defects (vacancies and interstitial atoms), line defects (dislocations), planar defects (stacking faults, twin boundaries) and volume defects (voids or cavities). In order to study the plastic deformation theory, dislocations are very important because their motion represents the response of the material to the applied shear stress. Consequently, hindering the motion of these linear defects is the primary strengthening mechanism of metallic materials. To obstruct this motion, dislocations must encounter obstacles that can be represented by precipitate particles. However, some distinctions are needed because the influence of precipitates on material properties changes with the volume fraction, size, distribution, type of precipitate and arrangement in the microstructure. In this sense, the production of fine, equiaxed and uniformly dispersed metastable precipitates provides the most adaptable strengthening solution for metallic materials such as aluminum alloy in addition to solid solution strengthening. Moreover, the production of extremely small (nanosized) particles called dispersoids may act as a strengthening mechanism.

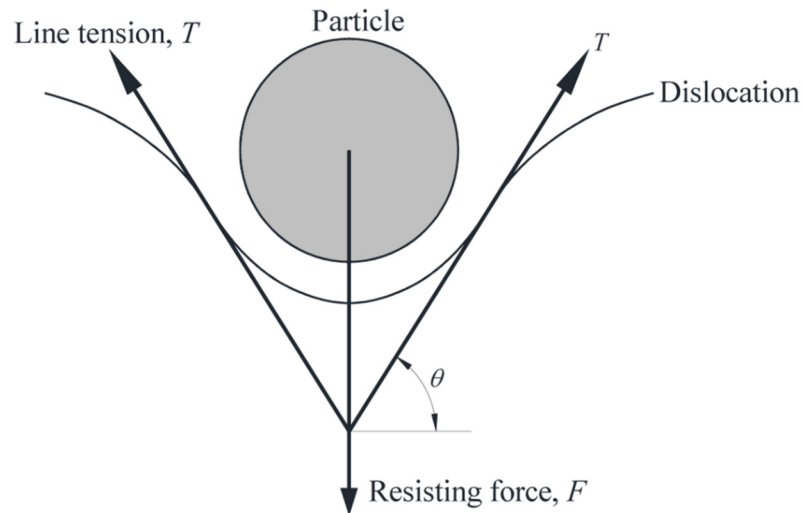


Figure 1.9: Balance of forces acting during particle resistance to dislocation movement [17].

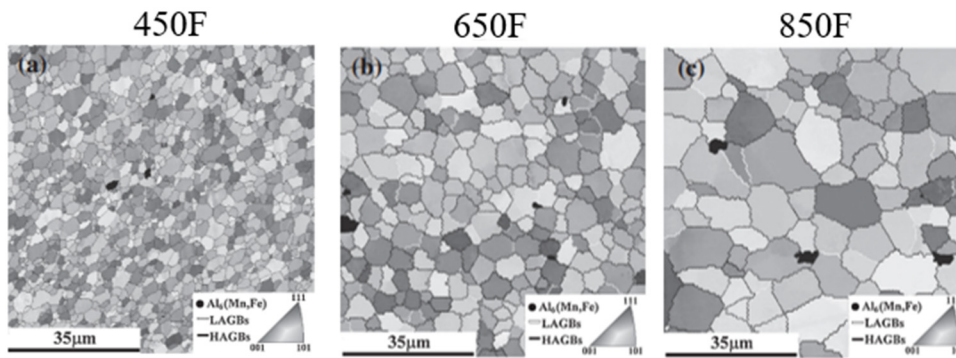
In general, as previously stated, the motion and the number of dislocations affect the mechanical strength of the investigated material. To retard this motion and increase the strength, several solutions can be adopted: on the one hand, internal stresses must be generated which will act in opposition to the movement of dislocations; on the other hand, particles must be produced by precipitation to act as obstacles to their motion. Similar to precipitation hardening, solid solution hardening may be used as an effective method to increase the mechanical properties because, when an alloying atom is dissolved into the matrix, it may act as an obstacle to the motion of dislocations. There is also the work hardening phenomenon which is based on the cold working theory of metallic materials. When there is the application of a deformation at low temperature, an increase in the number of dislocation is caused and, as a consequence, the mean distance between dislocations decreases. Since, on the average, the dislocation-dislocation interaction is repulsive, the resistance to the dislocation motion and, consequently, the strength of material increase.

It has been universally observed that the strength of the material is also dependent on the grain size. Hall-Petch equation [18, 19], correlates tensile yield stress and average grain size as reported in the following equation:

$$\sigma_y = \sigma_0 + k_y d^{-1/2} \quad (1.1)$$

where σ_y is the yield stress of the investigated material, d is the average grain size, σ_0 is the friction stress and k_y is the stress intensity coefficient associated with the stress required to extend the dislocation activity in to the adjacent unyielded grains. This equation shows that the final yield stress of the material is associated with the reciprocal value of the square root of the average grain size. The

strengthening resulted from the grain boundary capability of blocking the dislocation movement. This mechanism can be explained with two main reasons: on the one hand, since the grains are characterized by different crystallographic orientations, if a dislocation moves from one grain to another it must change direction and it is as difficult as the misorientation between to adjacent grains increase. On the other hand, boundaries represent barriers to dislocation motion. Consequently, if the grain is smaller, the total grain boundary area increases retarding the motion of dislocations and increasing the mechanical properties of the material. Several authors investigated the effect of the grain size on the mechanical properties. As an example, Lin A.Y. et al. [18], studied the effect of different microstructures in an Al-5Mg-0.5Mn alloy and the results are summarized in Fig. 1.10. As expected, smaller grain size (Fig. 1.10a) resulted in higher yield stress and ultimate tensile strength, while coarser grain size (Fig. 1.10c) in lower YS and UTS. The same trend was also observed by Liao Q. et al. [19] and the result of this work is reported in Fig. 1.11.



	YS	UTS	UE	TE
450F	198.6 MPa	339.3 MPa	24.4%	29.9%
650F	176.9 MPa	335.2 MPa	23.5%	28.5%
850F	163.0 MPa	319.0 MPa	26.4%	30.9%

YS: yield strength, UTS: ultimate strength,
UE: uniform elongation, TE: total elongation.

Figure 1.10: Influence of grain size on the tensile properties [18].

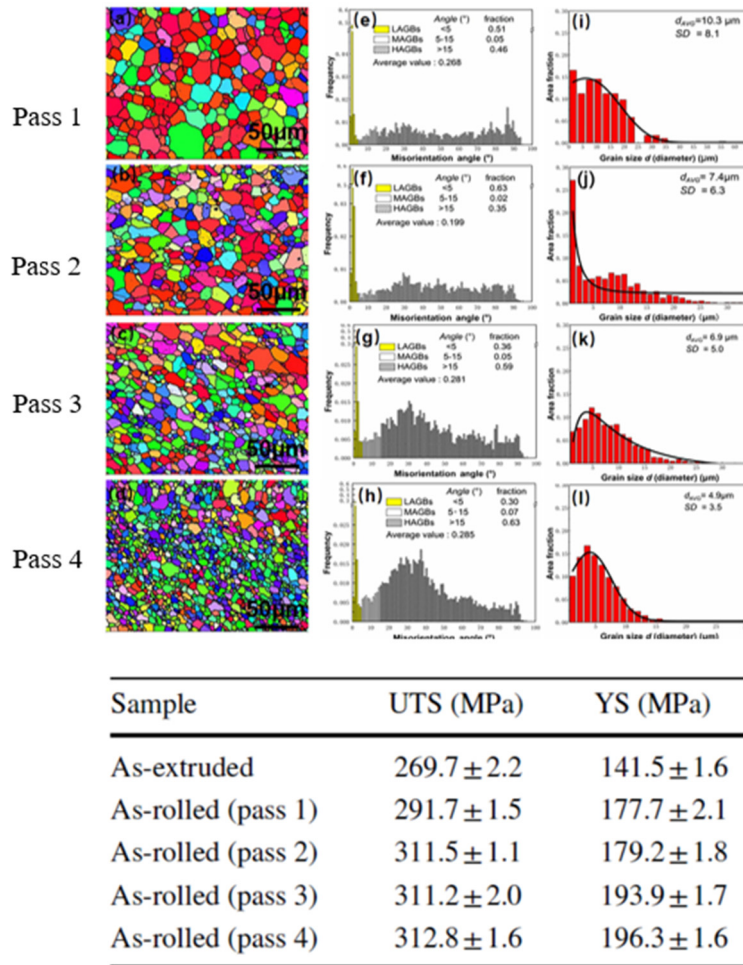


Figure 1.11: Microstructure characteristics and tensile properties of the alloy after the multi-rolling processes [19].

It has been also proven that the chemical composition and grain size of the investigated alloy have a huge effect on the corrosion resistance. Intergranular corrosion (IGC) is one of the main defects which may occur in Al-Mg-Si-Cu alloys because of the Cu addition, which results in the increase in the mechanical properties but also in a decrease in the corrosion resistance. In 2002, Minoda T. and Yoshida H. [20, 21] investigated this defect behaviour in an AA60601 aluminum alloy by performing several tests: the authors found that precipitate-free zones (PFZs) have an impact in the matter as they cause a decrease in the corrosion resistance. In 2015, Zander D. et al. [20] investigated the influence of grain shape on IGC: it results that elongated grains (Fig. 1.12) show an increase in the resistance to the penetration depth of the IGC if compared to grains without a predominant direction. In 2010, Bauger Ø. and Furu T. [21] investigated the effect of the grain size and chemical composition with accelerated corrosion testing (Fig. 1.13). Several profiles of different 6XXX and 7XXX aluminum alloys were tested and it results that a recrystallized surface layer with grains almost perpendicular to the surface seems to be subjected to intracrystalline corrosion down to the underlying structure with

stronger texture. It can be assumed that, if the surface recrystallized layer is characterized by grains with an average smaller dimension, there is more grain boundary area and the corrosion penetration will be decreased.

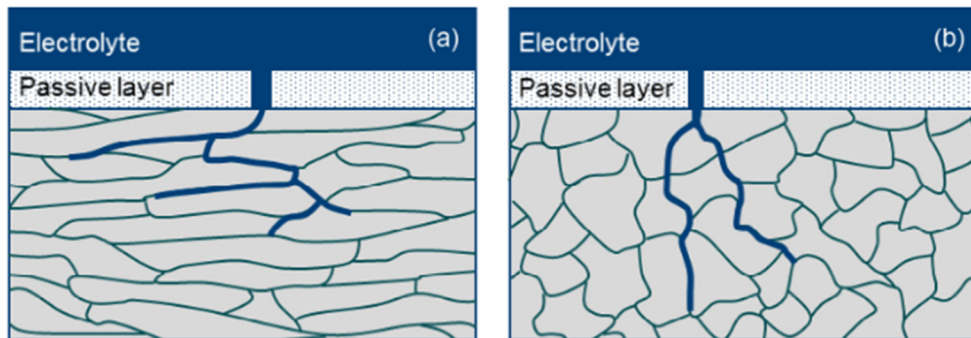


Figure 1.12: Influence of grain shape on the penetration morphology of IGC; strongly elongated grains (a) and grain shapes without predominant direction (b) [20].

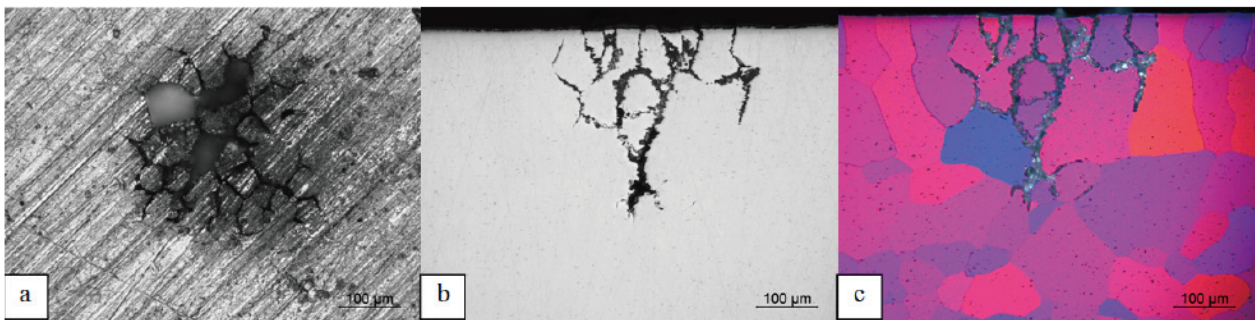


Figure 1.13: IGC and grain size [21].

The grain size has also an effect on the fatigue crack growth. Turnbull A. and De Los Rios E.R. [22] investigated this behaviour in an aluminum magnesium alloy: they tested and studied the growth of fatigue surface cracks in an Al-2.63Mg alloy at two levels of applied stress (280 MPa and 310 MPa) and three of grain size dimensions (22.3 μm , 36.6 μm , 108.3 μm). Single cracks were formed in the two samples with finer grains but failure in the sample with 108.3 μm occurred, caused by the coalescence of three sub-cracks. In conclusion, as the grain size is refined, the initial crack growth rate is successively reduced (Fig. 1.14) because the distance which the cracks extend, per load cycle, is a function of the crack tip plastic displacement. They also found out that, as the crack grows, the effect of the grain size on fatigue crack propagation became less significant. The growth of the longer cracks is independent of the surrounding microstructure and can be described by the continuum fracture mechanics analyses. Moreover, according to the work of Yue T.M. et al. [23], the microstructure with coarser grains, by imposing tortuous crack paths, exhibits higher crack resistance

but finer-grained material results in an increase in the fatigue strength due to the greater difficulty of fatigue crack initiation and early growth in small-grains microstructures (Fig. 1.15).

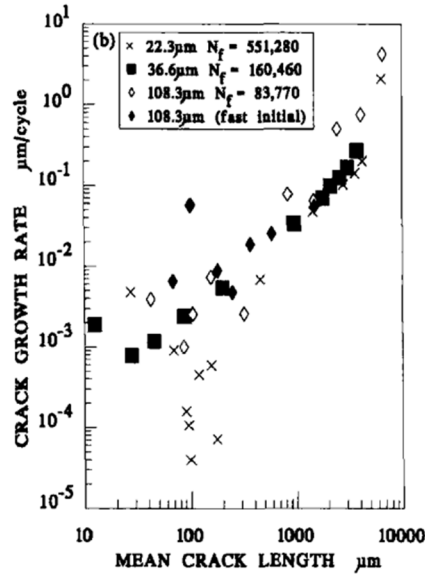


Figure 1.14: Effect of grain size on crack growth rate and mean crack length [22].

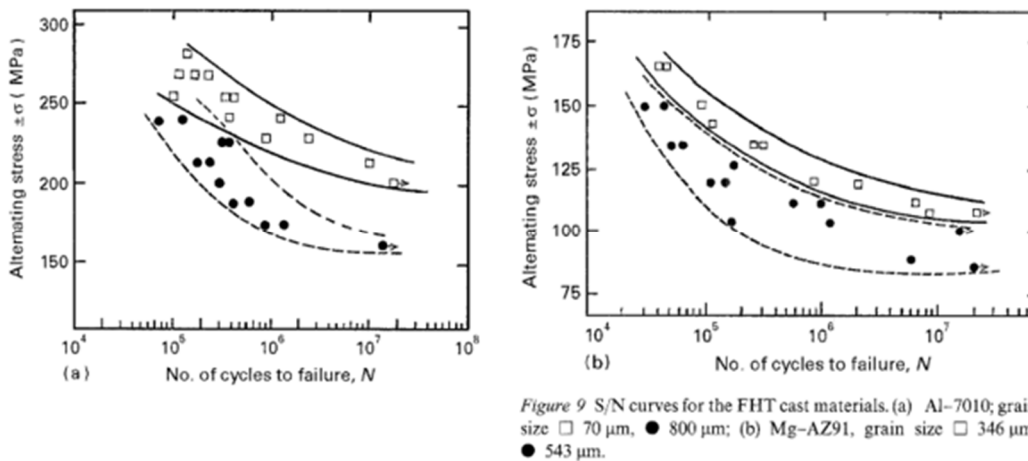


Figure 1.15: S/N curves for (a) Al-7010; (b) Mg-AZ91. Squares: smaller grain samples, black circles: coarser grain samples [23].

The study of the component microstructure is mandatory also because it deeply affects the crash performances of extruded profiles. In the last two decades, several research activities have been carried out in order to investigate how grain size and texture affect the crash properties because of the increasing interest in applying extruded 6XXX profiles in the automotive and transportation sector [24-27]. In order to understand the influence of the microstructure in the crash behaviour of aluminum alloy components, some basic concepts need to be introduced. In response to the need of reducing the weight of components in automotive production, the use of lightweight alloys such as 6XXX aluminum alloy becomes increasingly important. The design aims to minimize the weight of

components without affecting the functionality, safety and life in operation. The main parameter that needs to be introduced to characterize crash profiles is the specific energy absorption (SEA): this parameter describes the profile ability to absorb energy per unit of weight. The SEA is depending on the mean crash force MCF, which is the average force absorbed by the profile during a quasi-static compression test. This parameter allows the design of the structure because the MCF has a direct influence on the deceleration and the length reduction of the structure of a car in case of a collision. There are two limits that must not be exceeded in order to guarantee the driver survival during an event of crash: the survival limit and the design limit. In Fig. 1.16, a schematization of these limits is reported. In the x-axis, there is the reduction of the structure length during the crash while in the y-axis, the deceleration caused by the impact. If the design limit is passed, the reduction of the length of the car became too high and the components hit the driver, if the survival limit is passed, the deceleration becomes too high for the human body resistance given by biomechanical parameters. For these two reasons, the deceleration must be as indicated in the figure, in which an example of the deceleration produced by an optimized structure is reported. Moreover, if the MCF value goes to 0, the limit along the x-axis will be exceeded, if it goes to infinite values, the limit along the y-axis will be exceeded. In order to design the correct structure, it is important to analyse the quality of the folds resulting from the quasi-static compression of crash structures. In order to do this, the developed crush rating system is reported in Fig. 1.17. In order to control the MCF and to achieve the best results in terms of energy absorption behaviour, the grade of the crash component should be as close as possible to grade 1. If the component shows a behaviour like in grade 9 (complete fragmentation), it will result in a significant drop of the MCF.

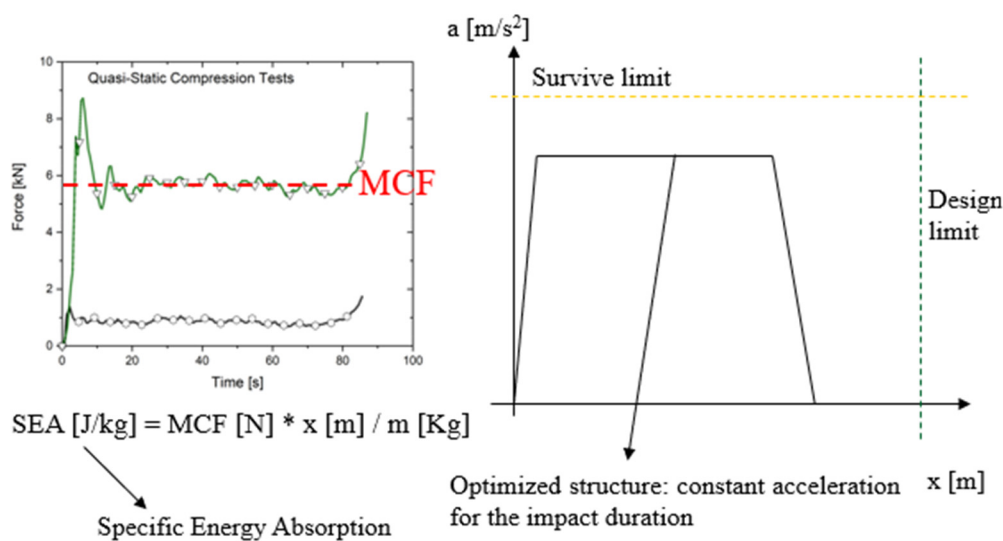


Figure 1.16: Schematization of the mean crash force MCF, survive limit and design limit in crash behaviour.

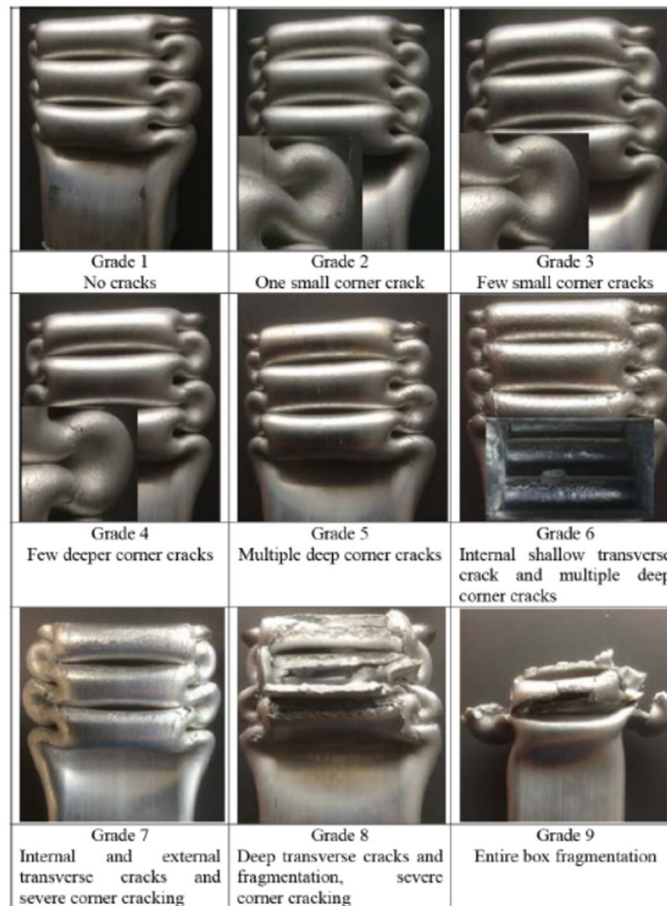


Figure 1.17: Crash rating system [24].

The microstructure of the crash components deeply affects the crash performances in terms of crash rating (Fig. 1.17). In this sense, the work of Parson N. et al. [24] resulted helpful to understand the characteristics of this influence. In this work, several 6XXX alloys were analysed and the data about microstructures, tensile strengths and crash performances were acquired. The first result was that the MCF did not correlate well with the YS or tensile elongation but it was found an almost linear relationship with the UTS (Fig. 1.18a,b). Moreover, the use of the true fracture strain resulted to give a clear cut off for cracking/no cracking conditions and a near linear deterioration in the crash rating with a decrease in the fracture strain (Fig. 1.18d). The work is also focused on the importance of the quenching properties on the crash rating. Two main concepts have been proven: on the one hand, having an increase in the recrystallized surface layer and an increase in the grain size of this layer leads to an increase in the crash grade of the profile (decrease in the crash performances). On the other hand, the water quenching resulted in an increase in the true fracture strain of the component, decreasing the crash grade (increase in the crash performances). In more detail, the use of air quenching allows the coarsening of the grains and Mg_2Si precipitates which resulted in a reduction

the grain boundary strength. For this reason, if the goal is to produce an extruded profile optimized for crash application, the water quenching must be used after the extrusion process (Fig. 18c,e,f).

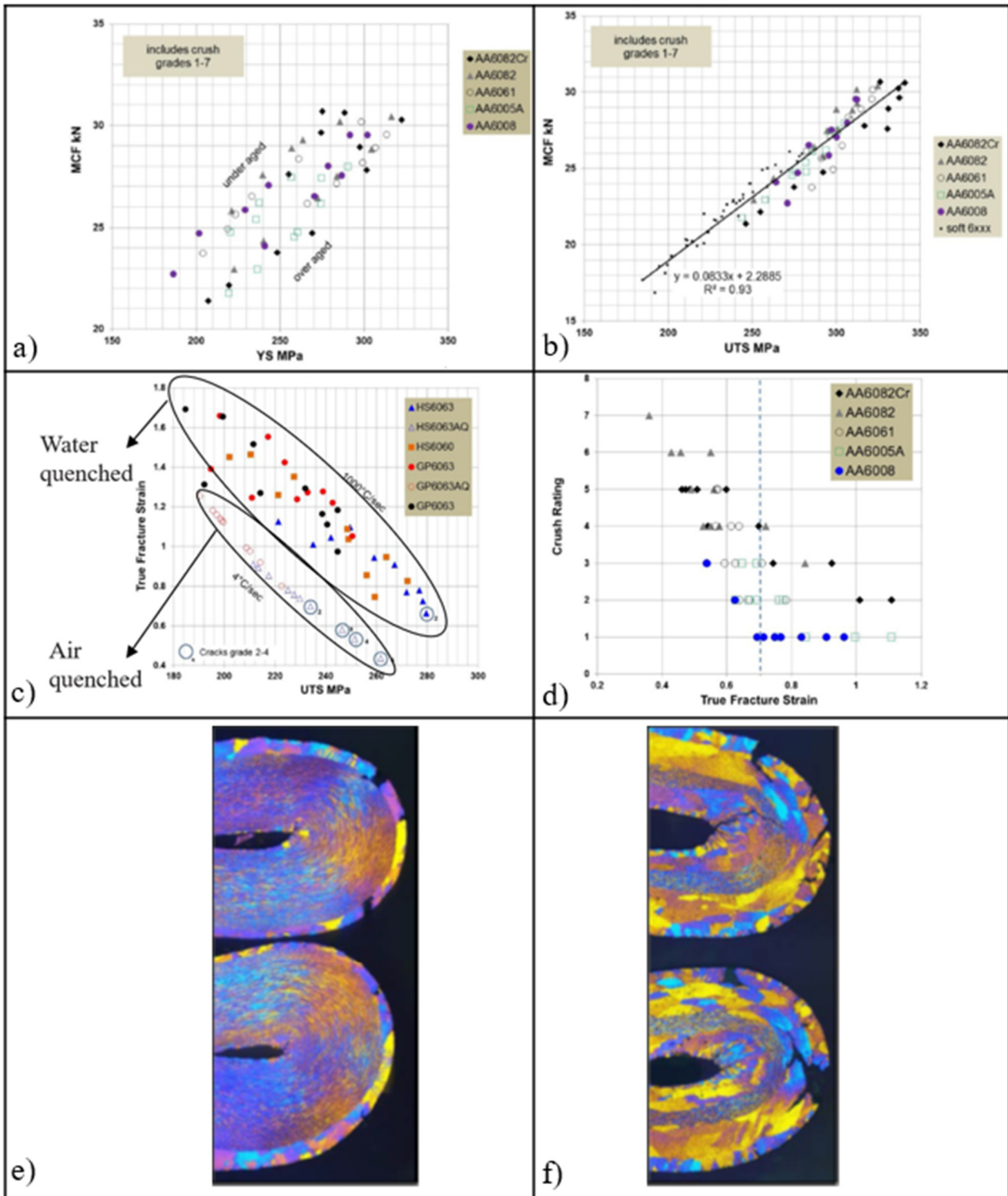


Figure 1.18: a) Correlation between MCF and YS, b) correlation between MCF and UTS, c) correlation between true fracture strain and UTS, d) correlation between crush rating and true fracture strain, e) folds with water quenched profiles (small recrystallized layer), folds with air quenched profiles (huge recrystallized layer) [24].

The microstructure may also be the cause of aesthetic defects in extruded profiles [28-30]. In several applications such as the architectural one, surface appearance provide an important characteristic for high quality structures. In this contest, streak defects, which are aesthetic defects occurred in anodized profiles, prevent the applicability of the components. In 2009, Zhu H. et al. [29] investigated the possible causes of the streaking defects after the anodization process (Fig. 1.19). The first cause may be the chemical composition: in case of big pre-chamber, when there is the change of billet material, the welding area may have a mixture of different chemical compositions and, consequently, different microstructures. The second cause may be a non-uniform microstructure due to the thermal or strain field applied during the extrusion process. In addition to that, streaks may be also caused by the presence of charge/seam welds or billet skin particles that interact with the surface. Moreover, Babaniris S. et al. [30], investigated the streaks in the hot extrusion of AA6060 profiles. The authors found that the perceived lightness of an etched profile directly correlates with the roughness. This is primarily dependent on the size and distribution of grain etching steps, which in turn are related to the size of the etched grains (Fig. 1.20).

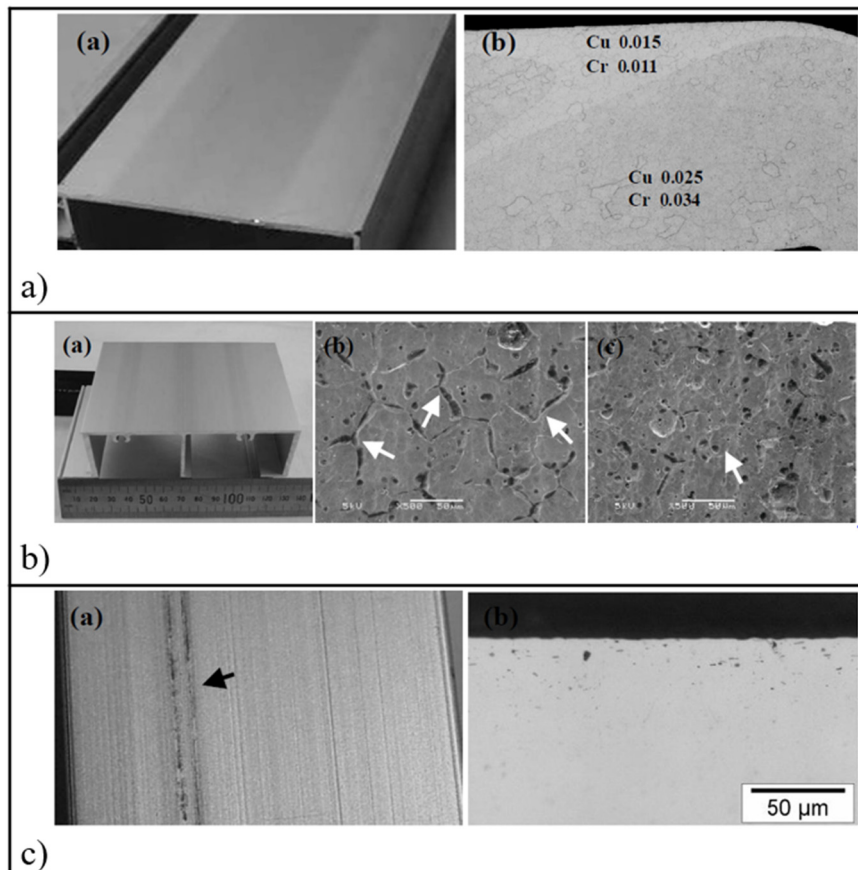


Figure 1.19: Streaks caused by: a) different chemical compositions, b) different microstructures, c) billet skin particle inclusions [28].

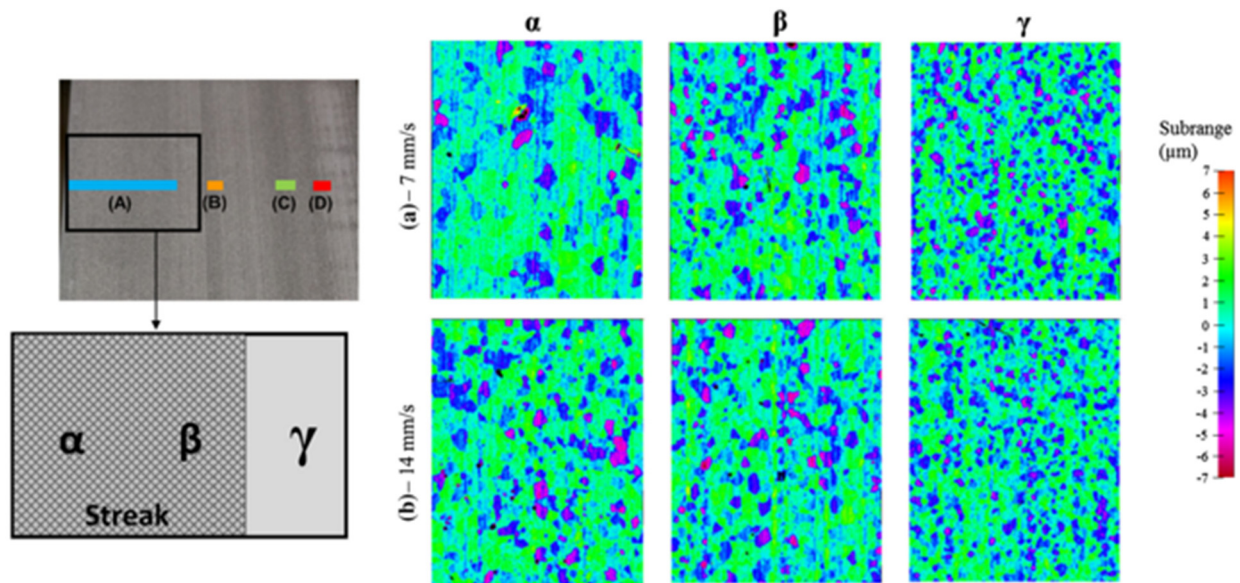


Figure 1.20: Influence of grain size on the streak defect [29].

The grain size is not the only microstructural factor that affects the properties of the material but also the texture of the extruded profile should be considered. This is because the texture has an important role in the definition of the mechanical properties of the material. The results of the work of Zhang L. et al. [31], in which is reported a detailed study of the mechanical properties, texture and microstructural evolution of an AA6111 aluminum alloy subject to rolling deformation, show that the shear and recrystallization texture mainly influence the anisotropy of the tensile elongation along the three directions of 0° , 45° and 90° with respect to the rolling direction. However, this effect on the anisotropy was not detected for the yield stress. On the contrary, the rolling texture has an influence on the yield stress along the three directions but less effect on the anisotropy of the elongation. In addition, the results of the work of Liao Q. et al. [19], in which is reported the analysis of microstructure, mechanical properties and texture evolution in extruded and rolled sheets, shows that the texture has less effect on the yield stress if compared to the grain refinement, but the finer-grains with relatively weak basal texture display randomness on grain orientation resulted in an increase in the ductility of the material. Westermann I. et al. [32] studied the effect of microstructure and texture on bendability. Three-point plane-strain bending tests were performed on AA7108 alloy with different microstructures: as-cast, homogenized, fibrous extruded, cold rolled and recrystallized. The results of this work show that the texture influences the bendability of the alloy by initiation of the shear bands. As-cast and homogenized material performed very poorly in the test mainly due to large grains and constituent particles aligned on grain boundaries and in the dendritic as-cast structure. An increase of 10 pct was found when the banding angle (BA) was aligned with the extrusion direction

(ED) or 45° to the ED with respect to the force observed when the BA was aligned to the transversal direction (TD): this force anisotropy may be a consequence of the crystallographic texture. The cold rolled and recrystallized material with a very weak texture, on the other hand, exhibits a nearly isotropic behaviour.

The reported literature review has been made to demonstrate the importance of the microstructure in the characterization of the properties of extruded profiles. Consequently, in order to optimize these properties and allow the application of these profiles in structural and automotive fields, it is mandatory to consider and control the evolution of the microstructure during the plastic deformation and heat treatment processes.

References

- [1] P.K. Saha (2000) Aluminum extrusion technology, ASM International, Materials Park, OH, USA.
- [2] T. Sheppard (1999) Extrusion of aluminum alloys, Springer, Boston, MA, USA.
- [3] Aluminum Extruders Council (2018) Aluminum Extrusion Manual. 4.2 Edition.
- [4] P.K. Saha (1998) Thermodynamics and tribology in aluminum extrusion, *Wear* 218: 179-190.
- [5] A. Lawal, D.M. Kalyon (1997) Nonisothermal extrusion flow of viscoplastic fluids with wall slip, *International Journal of Heat and Mass Transfer* 40: 3883-3897.
- [6] L. Zhu, K.A. Narh, K.S. Hyun (2005) Investigation of mixing mechanisms and energy balance in reactive extrusion using three-dimensional numerical simulation method, *International Journal of Heat and Mass Transfer* 48: 3411-3422.
- [7] ASTM E112-13, Standard Test Methods for Determining Average Grain Size, ASTM International, West Conshohocken, PA, 2013, <https://www.astm.org>.
- [8] F.J. Humphreys, M. Hatherly (2008) Recrystallization and Related Annealing Phenomena, 2nd edn. Elsevier, Oxford.
- [9] A. Rivas, P. Muñoz, S. Camero, O. Quintero (1999) Effect of the microstructure on the mechanical properties and surface finish of an extruded aa-6063 aluminum alloy, *Advanced Materials Science and Technology* 2(1): 15-23.
- [10] J.R. Hirsch, T. Al-Samman (2013) Superior light metals by texture engineering: Optimized aluminum and magnesium alloys for automotive applications, *Acta Materialia* 61(3): 818-846.
- [11] T. Sheppard (2006) Prediction of structure during shaped extrusion and subsequent static recrystallisation during the solution soaking operation, *Journal of Materials Processing Technology* 177: 26–35.
- [12] A.R. Bandar, S.R., Claves, J. Lu, K. Matous, W.Z. Misiolek, A.M. Maniatty (2004) Microstructural Evaluation of 6xxx Aluminum Alloys for Computer-Simulated Texture Prediction, *Proceedings of the Aluminum Extrusion Technology Seminar, ET 2004, Orlando, FL, 1: 169-176.*
- [13] J.F. Shackelford (2009) Introduction to Materials Science for Engineers, Pearson Education, New Jersey.
- [14] J.D. Verhoeven (1994) Fundamentals of Physical Metallurgy, Wiley, Inc., New York.
- [15] W.D. Callister (2011) Materials Science and Engineering - An Introduction, Wiley, New York, Weinheim.

- [16] A Tetelman, C.R. Barrett, W.D. Nix (2005) *The Principles of Engineering Materials*, Prentice-Hall, Englewood Cliffs, NJ.
- [17] R. Ambriz, D. Jaramillo (2014) *Mechanical Behavior of Precipitation Hardened Aluminum Alloys Welds*. In: Monteiro, W. A. , editor. *Light Metal Alloys Applications* [Internet]. London: IntechOpen.
- [18] C.Y. Lin, T.S. Lui, L.H. Chen, F.Y. Hung (2014) Hall-Petch Tensile Yield Stress and Grain Size Relation of Al5Mg0.5Mn Alloy in Friction-Stir-Processed and Post-Thermal-Exposed Conditions, *Materials Transactions* 55(2): 357-362.
- [19] Q. Liao, W. Hu, Q. Le, X. Chen, K. Hu, C. Cheng, C. Hu (2020) Microstructure, Mechanical Properties and Texture Evolution of Mg–Al–Zn–La–Gd–Y Magnesium Alloy by Hot Extrusion and Multi Pass Rolling, *Acta Metallurgica Sinica* 33: 1359-1368.
- [20] D. Zander, C. Schnatterer, C. Altenbach, V. Chaineux (2015) Microstructural impact on intergranular corrosion and the mechanical properties of industrial drawn 6056 aluminum wires, *Materials and Design* 83: 19-59.
- [21] Ø. Bøger, T. Furu (2010) Results from Field Testing of Aluminium Extrusions on a Truck for Six Years. Comparisons with Accelerated Corrosion Testing, *Proceedings of the 12th International Conference on Aluminium Alloys*, September 5-9 Yokohama, Japan. 1: 1498-1503.
- [22] A. Turnbull, E.R. De Los Rios (1995) The effect of grain size on fatigue crack growth in an aluminium magnesium alloy, *Fatigue Fracture Engineering Material Structure* 18(11): 1355–1366.
- [23] T.M. Yue, H.U. Ha, N.J. Musson (1995) Grain size effects on the mechanical properties of some squeeze cast light alloys, *Journal of Materials Science* 30: 2277-2283.
- [24] N. Parson, J. Fourmann, J.F. Beland (2017) *Aluminum Extrusions for Automotive Crash Applications*, SAE Technical Papers 1–16.
- [25] U. Tundal, O. Reiso, S. Skerjvold, A.D. Kubiak (2013) Al-Mg-Si Aluminium Alloy with Improved Properties, PCT Application WO 2013/162374.
- [26] Miller, W.S., et al., Recent development in aluminium alloys for the automotive industry. *Materials Science and Engineering: A*, 2000. 280(1): p. 37-49.
- [27] M. Rosefort, R. Baumgart, C. Matthies, H. Koch (2014) Influence of Microstructure on the Folding Behavior of Crash Relevant Aluminum Extrusion Parts, *Light Metal Age* 56: 201-205.
- [28] H. Zhu, J.C. Malcolm, A.K. Dahle (2012) Effect of Process Variables on the Formation of Streak Defects on Anodized Aluminum Extrusions: An Overview, *High Temperature Material Proceedings* 31: 105-111.
- [29] H. Zhu, X. Zhang, J.C. Malcolm, A.K. Dahle (2009) Classification of Streaking Defects on Anodized Aluminium Extrusions, *Materials Science Forum* 618-619: 349-352.

- [30] S. Babaniaris, A.G. Beer, M.R. Barnett (2019) Optical and Microstructural Origins of Thermomechanical Streaking Defects in Hot Extruded AA6060, *Metallurgical and Materials Transactions A* 50: 5483-5493.
- [31] L. Zhang, Y. Wang, X. Yang, K. Li, S. Ni, Y. Du, M. Song (2017) Texture, Microstructure and Mechanical Properties of 6111 Aluminum Alloy Subject to Rolling Deformation, *Materials Research* 20(5): 1-9.
- [32] I. Westermann, K.E. Snilsberg, Z. Sharifi, O.S. Hopperstad, K. Marthinsen, B. Holmedal (2011) Three-Point Bending of Heat-Treatable Aluminum Alloys: Influence of Microstructure and Texture on Bendability and Fracture Behavior, *Metall. Mater. Trans A* 42: 3386-3398.

2. Recrystallization During the Extrusion of 6XXX Aluminum Alloys

2.1 Introduction

The deformation of metals affects the microstructure in several ways. Firstly, it influences the shape and distribution of the grains, modifying the total area of the grain boundaries [1-4]. This occurs because some of the dislocations formed due to plastic deformation are accumulated in the grain boundaries. Secondly, even the smallest grain structures such as dislocation cells or subgrains also change their shape. The sum of accumulated dislocations represents the energy stored in the material and this stored energy is the driving force for recrystallization.

Furthermore, during plastic deformation, the shape and orientations of the grains of a polycrystalline metal vary by changing direction. This change will be dependent on the components of the stress applied to our base material. As a consequence, grains can acquire a particular shape and a preferential orientation, called Texture, which also affects the stored energy of the deformed material [5-6].

There are different mechanisms investigated in literature that describe the recrystallization kinetics of metals and, in particular, 6XXX aluminum alloys during the hot deformation. The most general classification distinguishes dynamic recrystallization (DRX) from static recrystallization (SRX) [7-10]. The dynamic recrystallization kinetics depend on the properties of the investigated material and involves, for LSFE (Low Stacking Fault Energy) materials, nucleation and growth of new grains during deformation or, for HSFE (High Stacking Fault Energy) materials such as aluminum alloys, different mechanisms that are still under investigation from the research community. The static recrystallization mechanism may occur after the deformation causing the rearrangement of the microstructure through nucleation and growth. Moreover, there are other recrystallization mechanisms that led to the loss of some of the energy stored during the deformation that must be considered: Recovery and Grain Growth [1,11,12]. The first occurs as a rearrangement of the dislocations into more stable substructures, forming Low Angle Grain Boundaries (LAGB) and subgrains. The second mechanism leads to the growth of the grains, decreasing the total amount of grain boundary area.

2.2 Recrystallization during the extrusion process of 6XXX aluminum alloys.

In Fig. 2.1 is reported the schematization of the microstructural evolution during the hot extrusion process of aluminum alloys. In more detail, Fig. 2.1a shows the microstructure of the starting billet

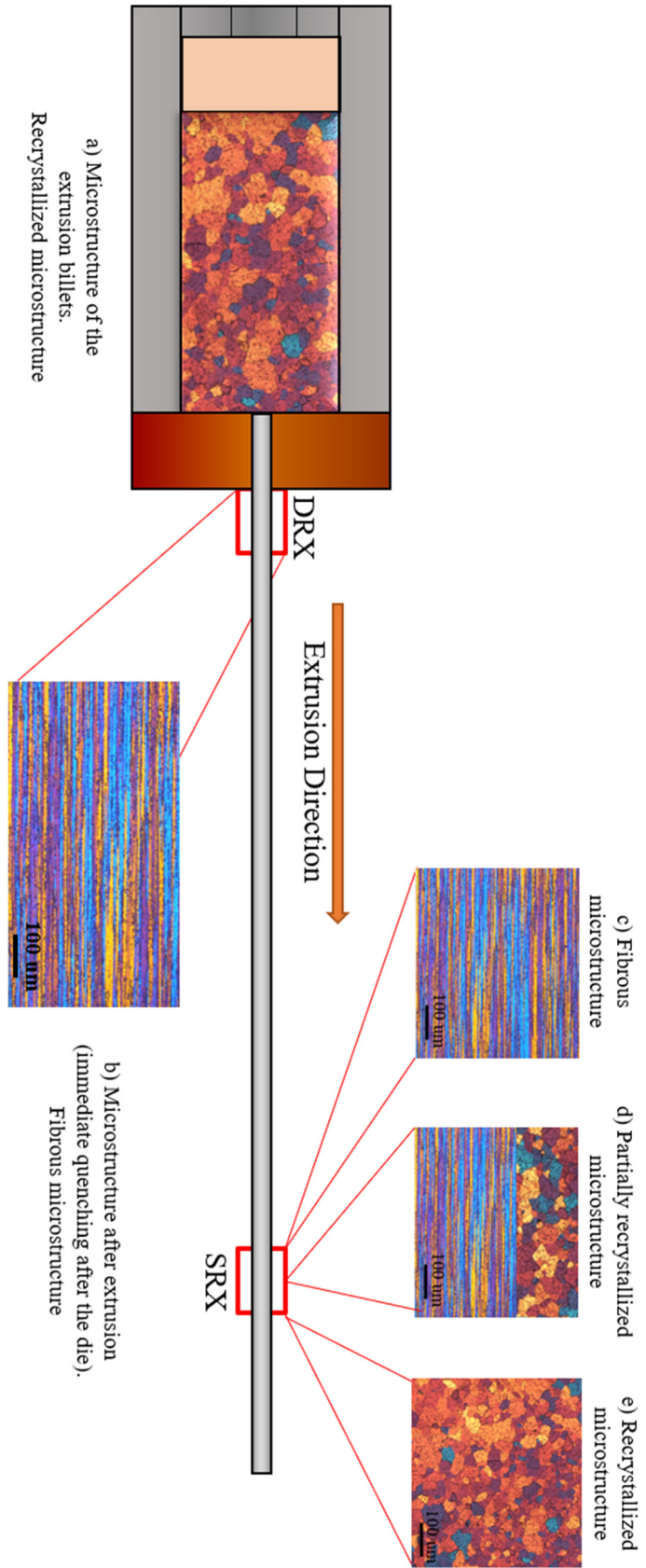


Figure 2.1: Microstructure evolution during extrusion process.

material, which is fully recrystallized due as consequence of the casting phase and further homogenization process. Once the extrusion begins, the dynamic recrystallization (DRX) may occur as a result of the strain field applied to the material and the high frictional coefficients. This evolution leads to the condition reported in Fig. 2.1b, where an example of fibrous microstructure is reported. The fibrous grains are marked by a dimension along the extrusion direction several times greater than the width and thickness. After the extrusion, depending on several factors such as the exit temperature, the level of strain applied during extrusion, the chemical composition of the alloy and the quenching conditions (media and time), the static recrystallization (SRX) may also occur. This phenomenon involves the nucleation and growth of new grains. The static recrystallization may be total (Fig. 2.1c), partial (Fig. 2.1e) or absent (Fig. 2.1d).

Moreover, in the specific case of the extrusion process, the phenomenon of Abnormal Grain Growth (AGG) or Peripheral Coarse Grain (PCG) may occur as a disproportionate growth of some grains located on the surface of the profiles (PCG, Fig. 2.2) or on the inner parts of the profile material, typically in welding zones (AGG) [13-14]. These mechanisms may cause a degradation in mechanical, crash, corrosion, fracture and surface quality properties thus precluding their applicability in the automotive sector.

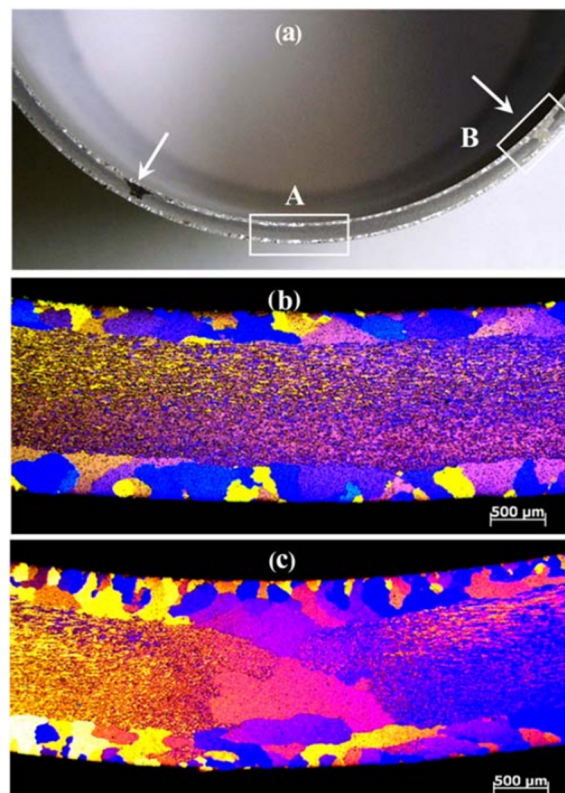


Figure 2.2: Transverse section of the tube extruded from alloy A. Higher magnification view of (b) region A and (c) region B in part (a). Arrows indicate the weld seams. [14]

2.3 Dynamic and Static Recovery

Recovery is a softening mechanism which occurs in metals as a microstructural reorganization to release some of the stored energy accumulated during the deformation [15-22]. If recovery occurs during the deformation of the metal, then it is referred to as “Dynamic” (DRV), while if it occurs after the material processing is called “Static”. Its main effect is the lowering of the flow stress due to the rearrangement of the dislocations in more stable substructures, increasing the ductility of the investigated material. The presence of alloying elements or impurities may reduce the improvement of ductility in DRV metals due to the pinning effect on dislocations.

Materials with High Stacking Fault Energy (HSFE) such as aluminum alloys, alpha-iron and ferritic steels frequently exhibit dislocation climb, cross-slip and glide, which are the main mechanisms of dynamic recovery, resulting in the formation of low angle boundaries and subgrains (Fig 2.3, 2.4) [1]. From a microscopical point of view, this rearrangement led to an increase in the size of the substructures in the hot worked materials and, consequently, to an increase in ductility and a decrease in the flow stress.

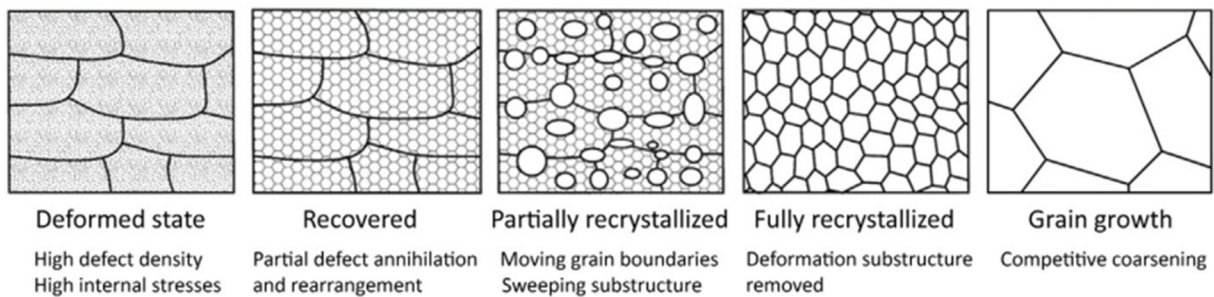


Figure 2.3: Schematization of the recrystallization mechanism [23]

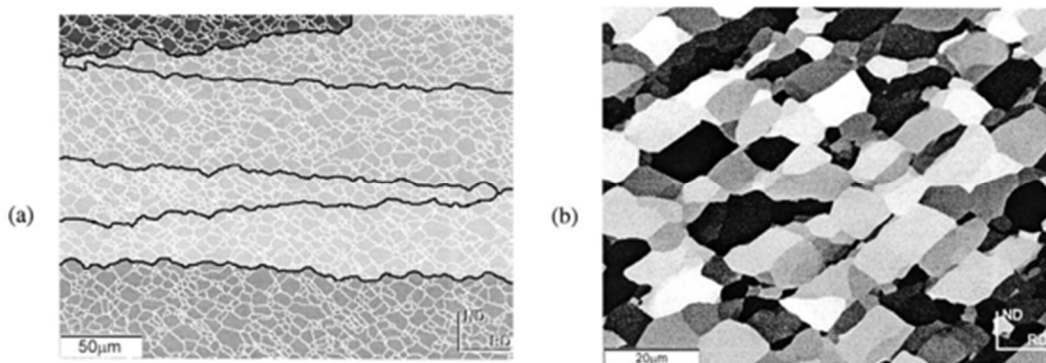


Figure 2.4: Al-01%Mg deformed in plane strain compression. a) EBSD map showing LAGBs (white) and serrated HAGBs (black); (b) SEM channeling contrast image showing the subgrain structure [1].

During the hot deformation of metals, dislocations interact, grow and increase as the driving pressure and the rate of recovery. In the same period, the low angle grain boundaries and the subgrains develop and grow. At a certain level of strain, the rates of the work hardening and recovery reach a dynamic state of equilibrium [1]. As a result, the steady-state flow stress remains almost constant as shown in Fig. 2.4. It must be noticed that, if the heat generated by the processing of the material cannot be removed from the specimen, it may result in a further decrease in the flow stress of the material at high strains and strain rates larger than 1 s^{-1} .

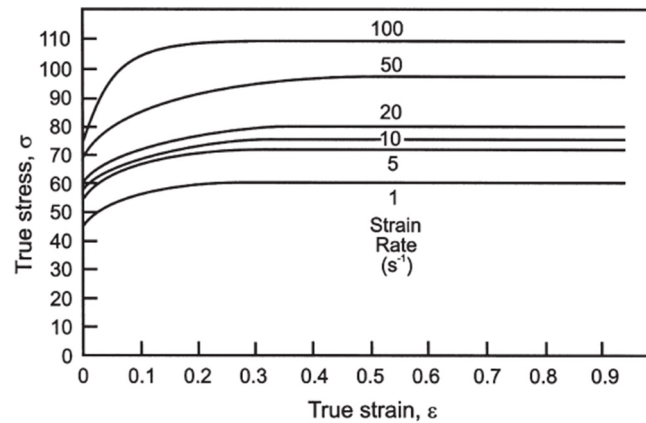


Figure 2.5: Flow stress curves at different strain rates [24]

Static recovery can be observed as a decrease in the fraction of the residual strain hardening shown in Fig. 2.5. It occurs as the reorganization of the dislocation substructures due to the internal elastic stresses of the material caused by the prior plastic deformation. More in detail, the recovery led to the annihilation of the point defects and dislocations associated with the higher mobility, forming the subgrain and grain boundaries without any nucleation stage or modification in the grain structure (High Angle Grain Boundaries HAGB). This mechanism produced a modest and gradual reduction in hardness and internal stress fields.

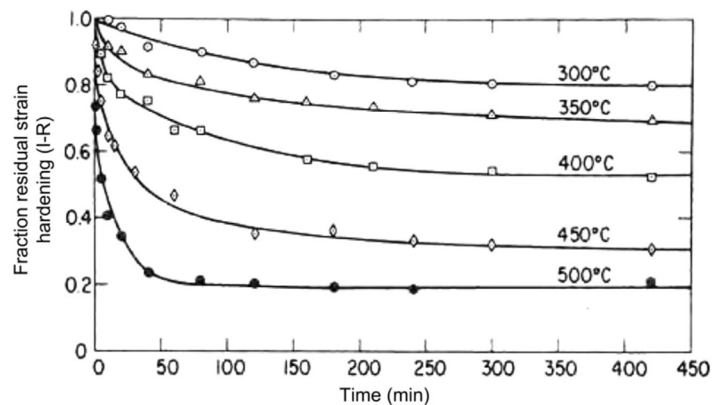


Figure 2.6: Fraction residual strain hardening behaviours after time at different temperatures [25]

2.4 Dynamic Recrystallization (DRX)

Dynamic recrystallization is a complex mechanism which may occur on materials due to plastic deformation processes; it depends on a number of influencing factors: the Stacking Fault Energy (SFE), the thermo-mechanical conditions of the manufacturing process, the initial grain size in the billet material, the chemical composition of the alloy in terms of chemical elements and precipitates [26-28].

For materials with low stacking fault energy (LSFE) such as Cu, Ni, discontinuous dynamic recrystallization (DDRX) usually occurs, involving the nucleation and growth of new equiaxed grains during deformation as shown in Fig. 2.7 [26]. The discussion on this mechanism will not be further detailed in this work since it is rarely reported in aluminum alloys, although it has been occasionally observed in Al alloys as AA7050 or AA7055 [29, 30].

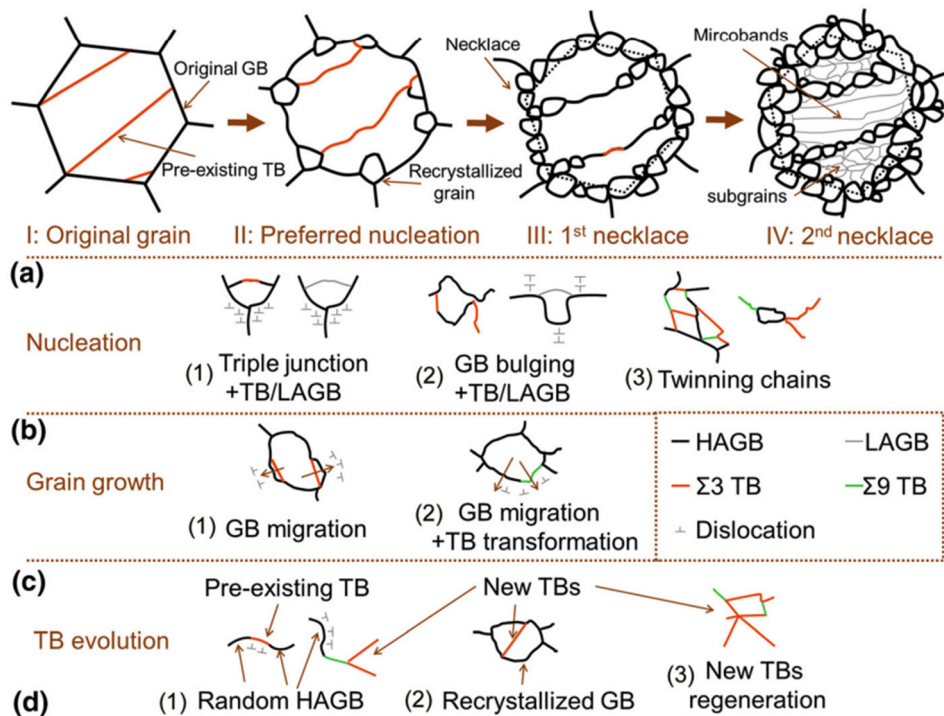


Figure 2.7: Schematization of DDRX mechanism. [31]

However, for materials with high stacking fault energy (HSFE), such as aluminum alloys, there are different theories proposed in literature which explain the microstructural evolution under plastic deformation conditions. In this work, the following three types of DRX will be considered: Geometric Dynamic Recrystallization (gDRX), Continuous Dynamic Recrystallization (cDRX) and Joint Dynamic Recrystallization (jDRX).

The gDRX mechanism was first theorized by McQueen [32] in 1985. The research involved a campaign of torsion tests on pure aluminum specimens exposed to high deformations. The geometric dynamic recrystallization was also observed by a number of researchers in different materials: copper [33], Al-Mg alloys [34, 35], AA5083 [36], AA6015 [37], magnesium alloys [38-40], α -Zr [41]. All the cited works refer to experiments in which the materials were subjected to high compressive or torsion deformations. During these experiments, the formation of new subgrains involves the evolution of HAGBs toward the distortion of boundaries caused by the applied strain field [42-44]. According to this theory, the original grain is deformed during the manufacturing process and, when the thickness becomes about 2-3 times the subgrain size, the opposite subgrain boundaries approach and contact thus splitting the grain into two new grains (“pinch-off”). In Fig. 2.8, the mechanism of gDRX is schematically reported. In Fig. 2.9, the influence of the strain level on the occurrence of the gDRX is shown. At lower strains (Fig. 2.9a), the flattened old grains containing subgrains are seen, but at large strains (Fig. 2.9b), the microstructure shows that almost equiaxed grains have formed in the whole sample area.

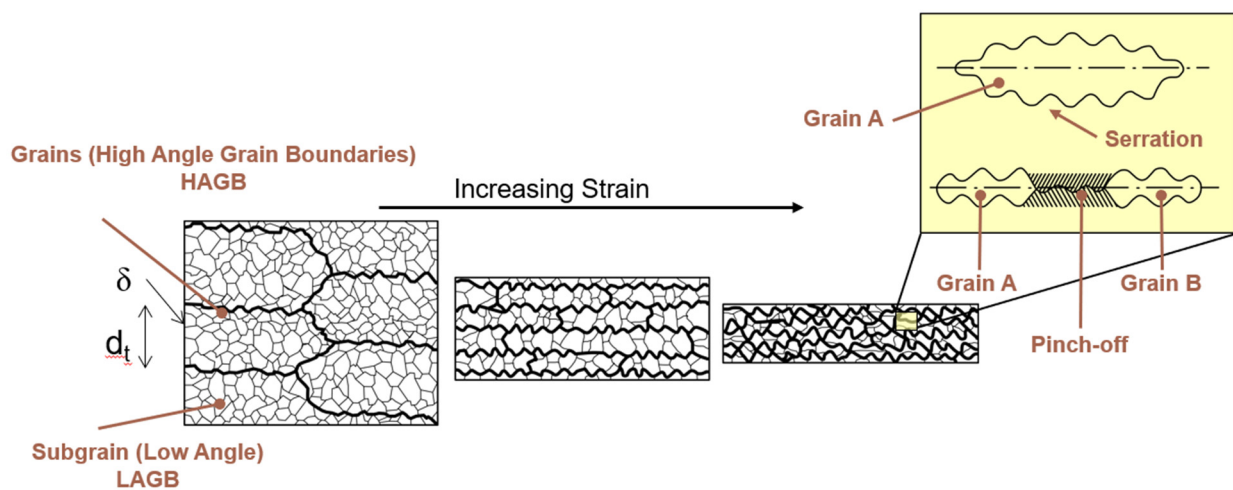


Figure 2.8: Schematization of the gDRX mechanism. Black lines represent HAGBs while grey lines are the LAGBs (subgrains).

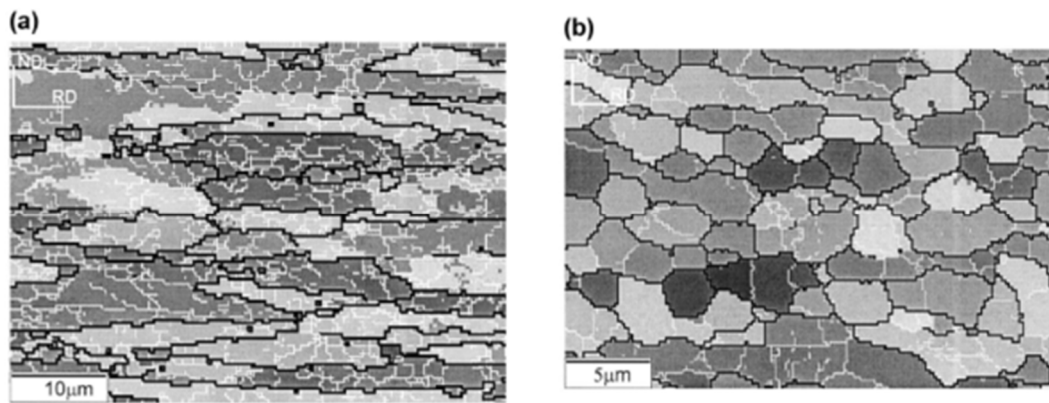
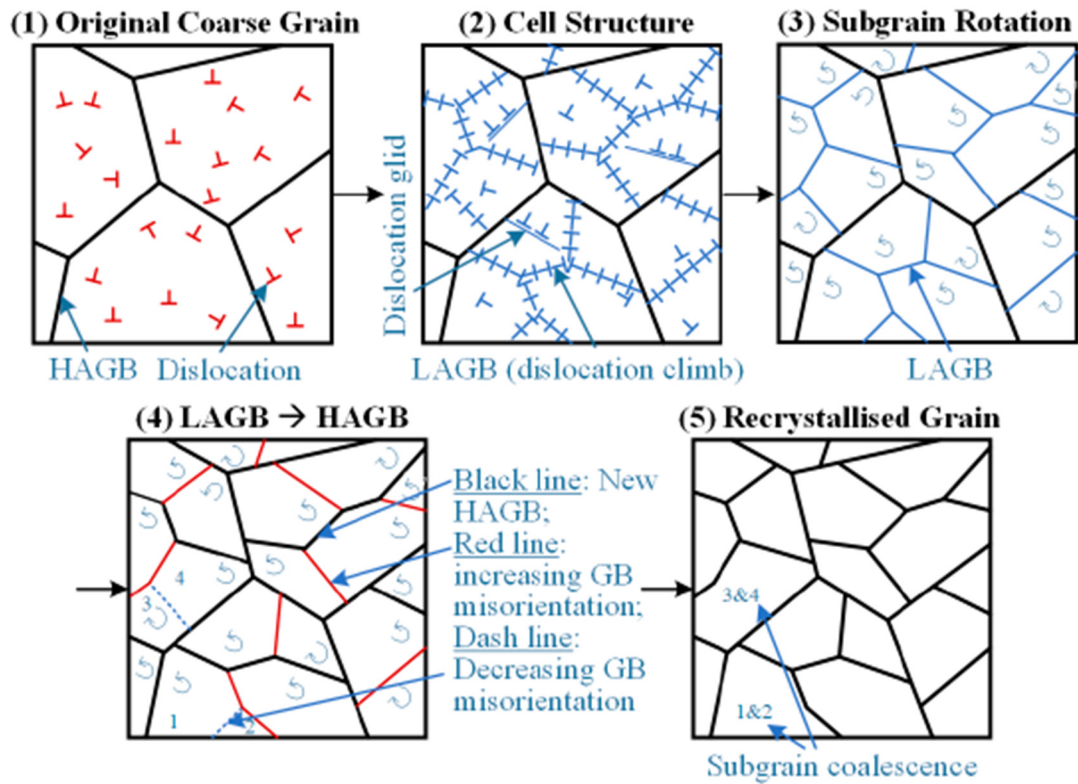


Figure 2.9: EBSD maps showing geometric dynamic recrystallization in an Al-3Mg-0.2Fe alloy deformed at 350°C in plane strain compression: (a) lower strain values; (b) higher strain values. HAGBs are shown in black and LAGBs in white [34].

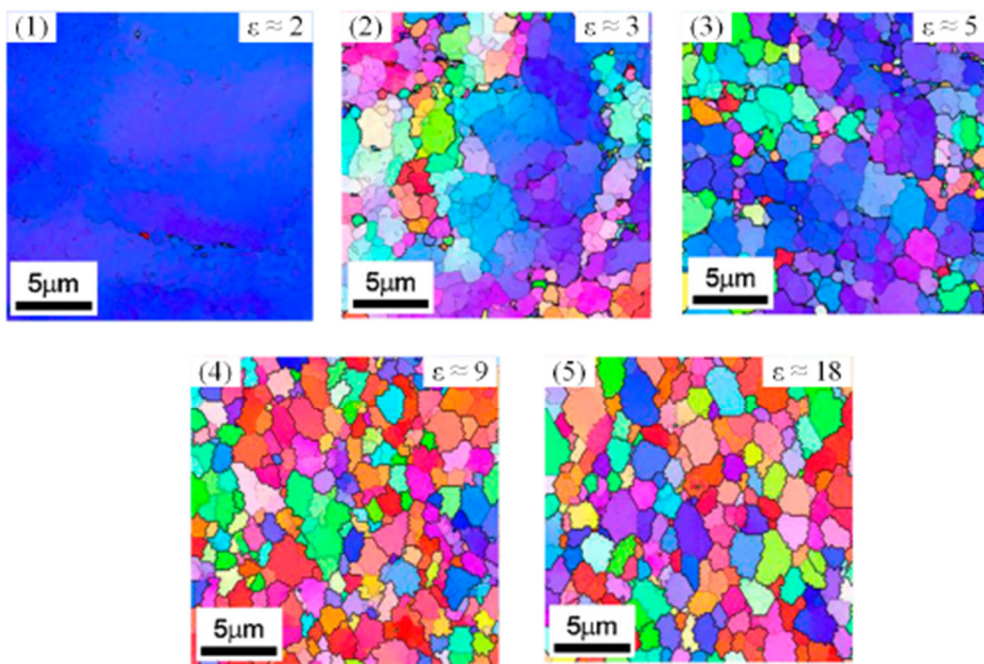
The recent review by Huang and Logè [42] summarizes the main characteristics of gDRX and a brief summary is provided below:

- gDRX is found in materials with high stacking energies (HSFE), strained at high temperatures and low strain rates.
- Subgrains are formed when a certain strain threshold is exceeded and remain constant as the strain varies. The stationary dimensions of the substructures decrease with the increase in the Zener-Hollomon parameter [44].

The cDRX mechanism theorized by Gourdet S. et al. [28] in 2003, proposed that the formation of new grains during the deformation is caused by the evolution of the misorientation angle of subgrains, which increase till the LAGB (low angle grain boundaries, which surround the subgrains within the grain) become HAGB (high angle grain boundaries, which surround the grains). An example is given in Fig. 2.10.



(a)



(b)

Figure 2.10: Development of new grains during CDRX: (a) schematic illustration, (b) experimental observation (EBSD IPF maps) of as-annealed pure Al (99.99%) deformed by high-pressure torsion at room temperature. [27]

According to “A Review of Microstructural Evolution and Modelling of Aluminium Alloys under Hot Forming Conditions” [27], the cDRX is the most active mechanism for the hot forming processes in aluminum alloys. The gDRX sometimes is interpreted as a cDRX since both involve the absence of nuclei and a continuous increase in the area of HAGB. The main difference between the two theories is the evolution of LAGB misorientation due to the applied strain field. Moreover, in manufacturing processes which involve large deformation, for example the porthole extrusion, the gDRX was observed to be a secondary mechanism in addition to the cDRX [45].

The third investigated mechanism is the jDRX, theorized by De Pari L. and Misiolek W. [46] and further investigated by Donati L. et al. [44], which combines the gDRX and cDRX into a unified model validated in the hot rolling process of an AA6061 aluminum alloy. More in detail, both the nucleation of new subgrains and the thinning of the grains as the deformation proceeds are contemplated, for this reason it has been defined as a "joint" (Fig. 2.11).

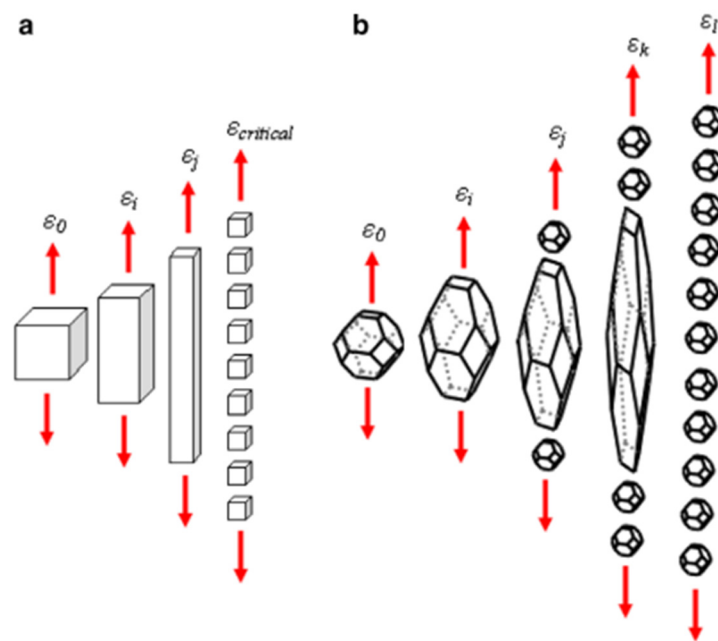


Figure 2.11: Schematization of new grains formation during the dynamic recrystallization according to the jDRX theory [46].

2.5 Stored Energy and Zener-Drag Pressure

In order to study the nucleation and growth in aluminum alloys after hot deformation or during annealing processes, the driving and retarding forces for the recrystallization must be investigated.

During the manufacturing of metals, such as extrusion, a small amount of the deformation work is stored in the material in the form of point defects and dislocations [26, 47]. With the increase in the deformation, material grains change their shape, leading to an increase in the total grain boundary

area. The rate of growth in this area depends on the mode of deformation (Fig. 2.12, Fig. 2.13). This is due to the incorporation of a part of the dislocations that are created during the process. Moreover,

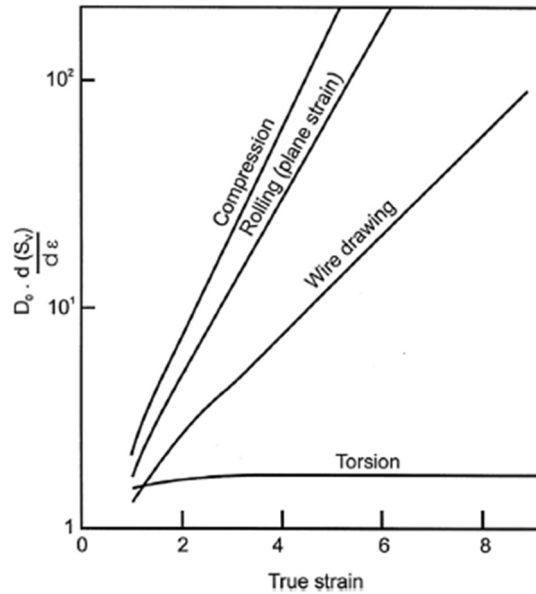


Figure 2.22: Rate of growth of grain boundary area per unit volume S_v for different deformation processes assuming an initial cubic grain of size D_0 [48].

another consequence of the accumulation of dislocation is the appearance of internal structures called subgrains. This sum of energy contribution of dislocations and new interfaces represents the driving force for the recrystallization and it is called Stored Energy [49]. This energy accumulation is the reason for the property changes typical in deformed metals as a consequence of the energy absorption of point defects and dislocation generated during the manufacturing process.

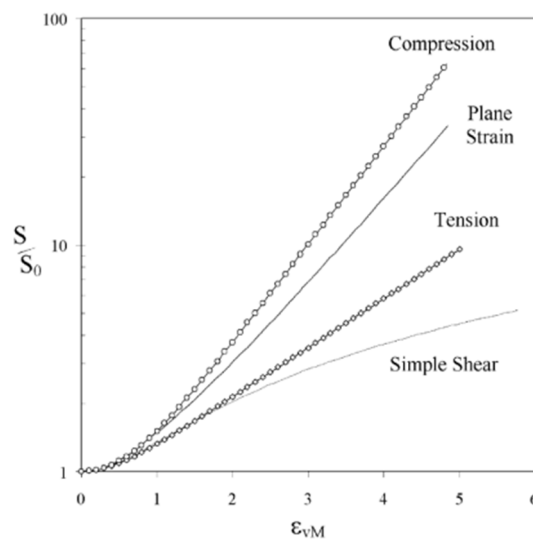


Figure 2.13: Grain boundary area S compared to the original grain boundary area S_0 assuming spherical initial grains as a function of the total strain. [50]

If the dislocation density and formation during the deformation provide the driving force for the recrystallization, the presence of secondary particles (i.e. dispersoids) or atoms in solid solution could provide a retard in the nucleation and boundary migration [51]. The reason is their pinning effect on grain boundaries thus limiting the boundary mobility. This force that suppresses the recrystallization was first investigated by Smith and Zener and it is known as Zener-Drag Pressure. The main contribution to the pinning force is given by nanometre sized dispersoids according to their fraction volume and size [52].

The homogenization parameters, such as heating rate, soak temperature and cooling rate together with the alloy chemical composition have a direct effect on the size and distribution of dispersoids (Fig. 2.14). It has been proven that the presence of alloying elements such as Mn, Cr or Zr may lead to the precipitation of dispersoids during the homogenization process [53-57]. This presence not only affects the recrystallization behaviour of the alloy during and after the extrusion process, but also the work hardening behaviour, fracture toughness and quench sensitivity in aluminum alloys.

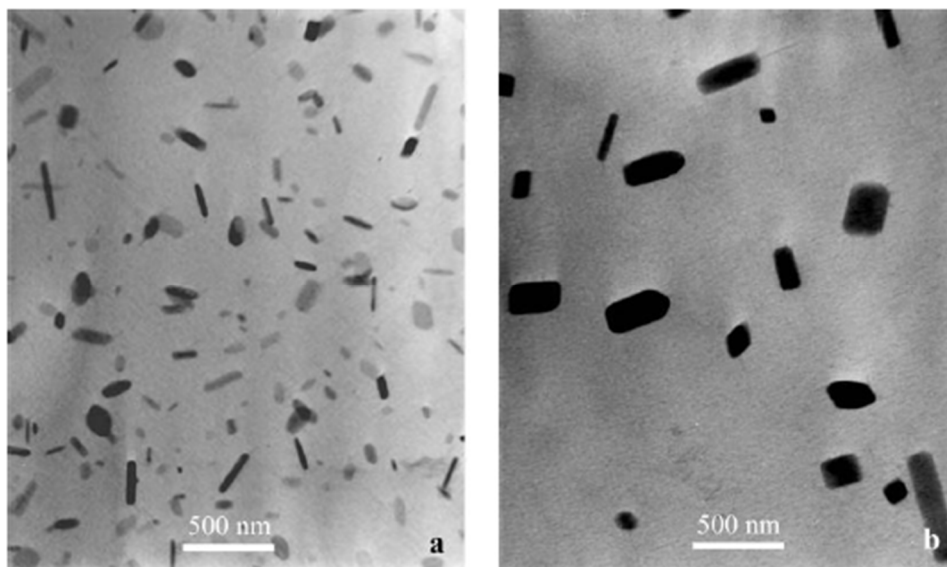


Figure 2.14: TEM images of 6082 alloy showing Mn containing dispersoids homogenized for 2 hours at (a) 520 °C and (b) 585 °C [58]

2.6 Static Recrystallization (SRX)

The static recrystallization mechanism is defined as a process in which a deformed material is transformed into a "strain free" structure thanks to the succession of phases of nucleation and growth of new grains promoted by a thermal gradient, with the aim of achieving a condition of energy stability [1,59,60]. This mechanism may occur if the material temperature is higher than the recrystallization temperature of the investigated aluminum alloy. The achievement of the condition of total static recrystallized structure and grain size are influenced by several factors: material

conditions in terms of temperature and holding time, strain and strain rate of the deformation process, size of the sub-grains [61], chemical composition of the investigated alloy [62] and distribution of precipitates and dispersoids [63]. Therefore, the final microstructure is thermodynamically more stable with a lower dislocation density if compared to the pre-recrystallized one.

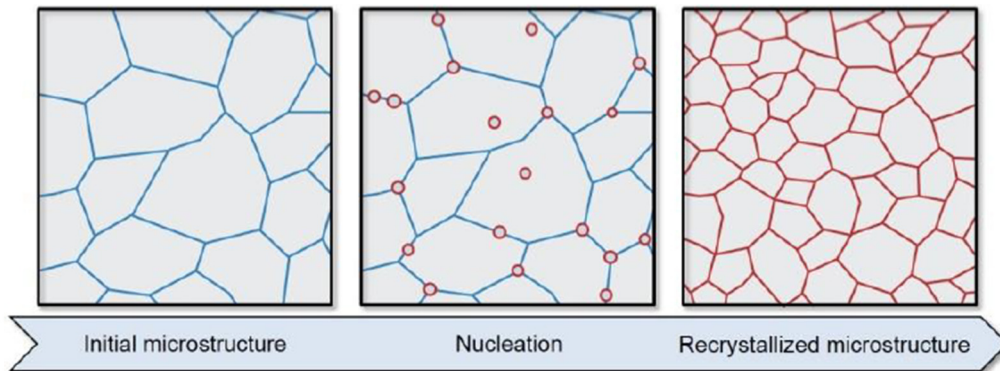


Figure 2.15: Schematization of nucleation and growth

During the nucleation phase in deformed materials, small regions called critical embryos grow as new strain-free grains. Nuclei are not homogeneously distributed in the material but their position depends on different factors. The new grains form and grow in the deformed matrix by boundary migration and they are of a central importance because, together with the orientation, they determine the microstructural evolution in terms of grain size, shape and texture of the fully recrystallized structure.

There are different mechanisms responsible for the nucleation [1]: Strain-Induced Boundary Migrating (SIBM) involves a portion of pre-existing HAGB bulging, and leaving a relative dislocation-free region behind the migrating boundary (Fig. 2.16). If the bulge is sufficiently large, it will become a nucleus.

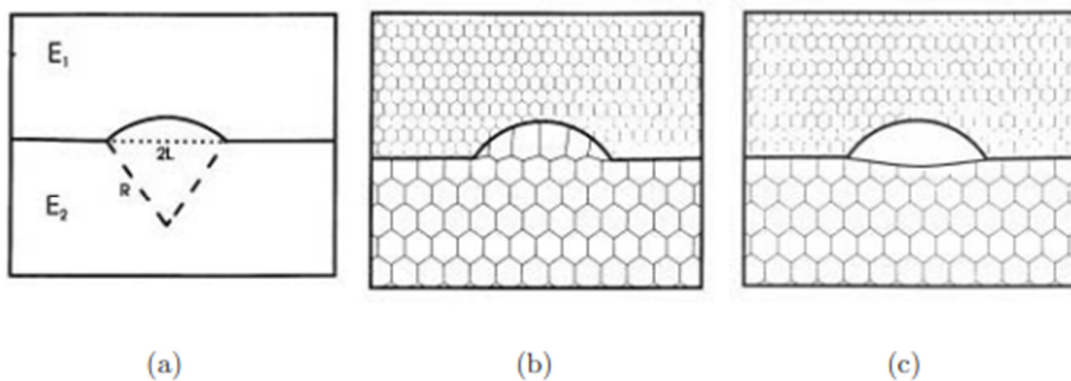


Figure 2.16: Critical embryo creation by strain induced boundary migration (SIBM). A part of the HAGB bulges out into the grain with the higher stored energy and, if the driving force is high

enough, it will keep bulging until it reaches the size of a critical embryo. (a) Initial bulge on a HAGB; (b) multiple subgrain SIBM; and (c) single subgrain SIBM [1].

Another mechanism of nucleation is called Subgrain Coalescence (Fig. 2.17). According to this theory, two or more subgrains merge by reducing the LAGB energy into one larger subgrain which may become a new embryo.

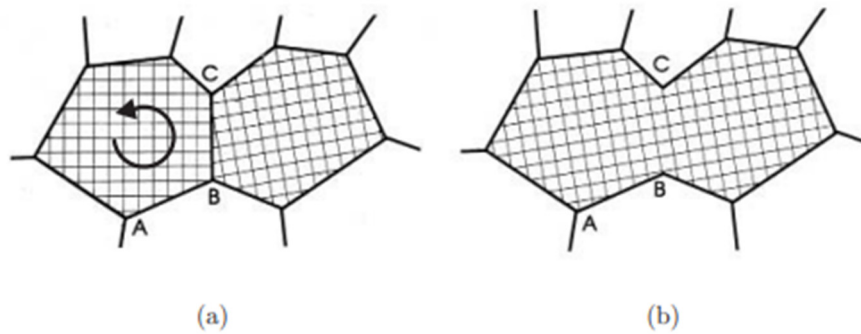


Figure 2.17: Embryo formation by subgrain coalescence. The LAGB (B to C) disappears due to the rotation of a subgrain: (a) Two subgrains divided by a LAGB; (b) The subgrains have coalescence into one bigger subgrain (embryo) [1].

Moreover, Subgrain Coarsening is an alternative mechanism according to which a new embryo may occur by the merging of two or more close subgrains (Fig. 2.18). This merging is caused by the migration of the LAGB, which may be absorbed by a closer grain boundary. This mechanism has been proven to be the main nucleation type in regions with large orientation gradients.

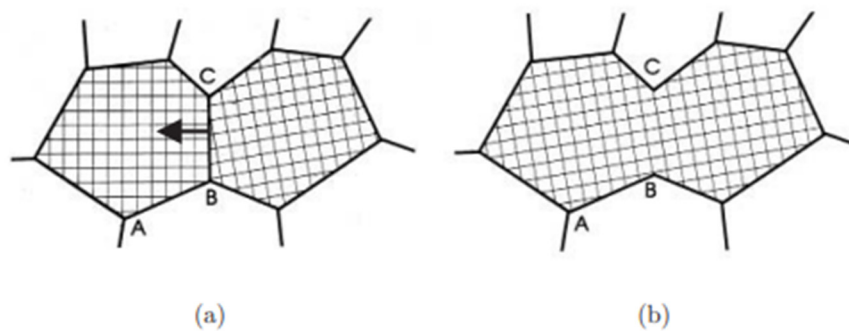


Figure 2.3: Embryo formation by subgrain coarsening: The LAGB (line from B to C) moves (see arrow) through the left subgrain, eventually being absorbed in the left boundary. (a) Two subgrains divided by a LAGB; (b) The two subgrains have coarsened into one bigger subgrain (embryo) by LAGB migration [1].

In order to describe nucleation mechanisms that may occur in HSFE materials such as aluminum alloys, another type should be added to the ones previously described, which is the Particle Stimulated Nucleation (PSN). If smaller particles, with an average diameter lower than 1 μm , act retarding the recrystallization as inhibitors of the grain boundary mobility, particles larger than 1 μm may act in

favour of the nucleation as they can produce, when the material is deformed, local concentration of stored energy and large misorientation in boundaries. In fact, during deformation, the microstructure tends to rotate around particles during deformation and create an increase in the local misorientation, depending on the strain values. If the strained region is larger than a critical nucleus size, nuclei may form. The critical size of the particles was investigated by Eivani in the hot deformation of Al-4.5Zn-1Mg alloy finding out that this size and the density of nuclei are dependent on the deformation temperature and strain rate (Fig. 2.19).

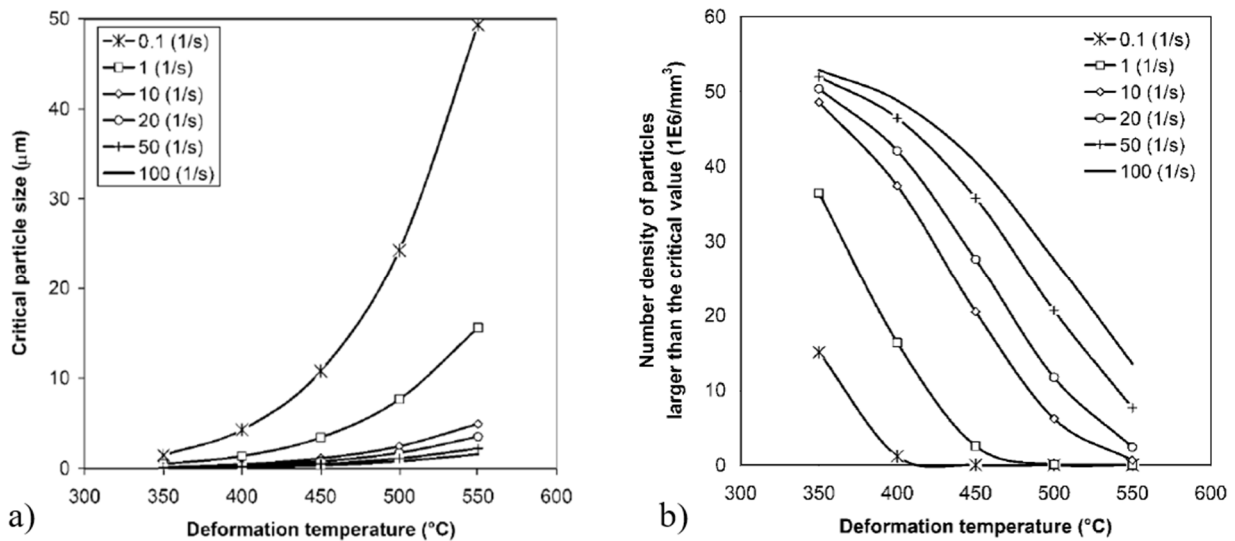


Figure 2.19: Critical particle size and number density of particles depending on deformation temperature and strain rate [61]

Grain growth occurs after the hot deformation or during the annealing process to reduce the residual internal energy. This growth is based on the migration of the HAGB driven by the mobility of boundaries and the stored energy for the recrystallization (Fig. 2.20). The mobility can be reduced by the presence of solute atoms, impurities or second-phase particles.

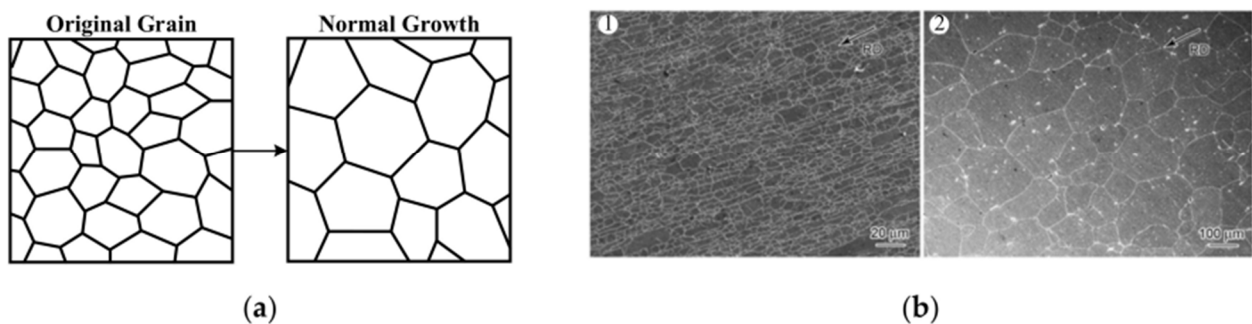


Figure 2.20: Grain growth of aluminium alloys. (a) Schematic and (b) corresponding experimental observation for normal grain growth [64].

Several authors investigated the SRX in the hot deformation processes of 6XXX aluminum alloys, focusing on how the different material and process parameters may affect the recrystallization behaviour. Sellars C.M. and Zhu Q. [65] proposed a model able to evaluate all the internal variables, such as dislocation density, subgrain size or misorientation angle between subgrains, which influence the static recrystallization of the investigated material. Vatne H.E. et al. [66] calculated the SRX grain size as a function of the nucleation, according to which depends on the sum of three contributions: the particle stimulated nucleation, the cube bands nucleation and the grain boundaries nucleation. The evaluation of these three nucleation contributions was further investigated by Eivani A.R. et al. [61] in the hot deformation of Al-4.5Zn-1Mg aluminum alloy. Moreover, several studies have been carried out to validate the modeling of the recrystallization behaviour in the extrusion of aluminum alloy by means of FEM codes comparing the results of the simulations to the experimental trials [44, 62, 67-70].

2.7 Peripheral Coarse Grain (PCG) and Abnormal Grain Growth (AGG)

The hot extrusion of Al-Mg-Si alloys is a manufacturing process increasingly used for the production of complex lightweight profiles with high functional and mechanical properties. These properties may be affected by the presence of the Peripheral Coarse Grain (PCG), which occurs as a surface recrystallized layer especially during the extrusion of medium-strength alloys such as AA6082 [69], or Abnormal Grain Growth (AGG), which typically occur in welding zones in aluminum alloy extruded hollow profiles. Unfortunately, the control over the formation of the AGG/PCG structure is extremely difficult because of the high number of factors that influences the defect behaviour. Both of these phenomena involve the fast grain growth of a few grains within a matrix of fine grains thus forming strong microstructural heterogeneities that may affect the properties of the material. Especially in the automotive sector, the profiles must avoid the presence of PCG structure because it greatly affects the crash behaviour and, therefore, determines its applicability.

In the extrusion process of aluminum alloy, the PCG formation is typically related to higher extrusion temperatures, high ram speeds, high extrusion ratios and low cooling rates [71]. Moreover, the defect is affected by the presence of dispersoids and alloying elements in solid solution which may act as pinning particles for subgrain, grain boundaries or growing recrystallized grains, retarding the formation of the PCG in favour of a complete fibrous structure. These small particles are formed mainly during the homogenization of the billets as a consequence of the presence of particular alloying elements such as Mn, Cr or Zr. While it seems quite clear how these particles affect recrystallization and PCG formation, i.e. considering a direct proportionality between volume fraction

and the inverse of size with the retarding force for the recrystallization [52], there is a lack of knowledge on which are the main parameters responsible for the PCG formation. In addition, it is still not clear how the typical PCG structure with smaller grains on the external surface and coarser grains in the internal part is formed. Several authors investigated the PCG formation and different theories have been proposed. Van Geertruyden W.H. et al. [72] carried out theoretical studies showing that high peripheral strain rates ($\dot{\epsilon} > 45 \text{ s}^{-1}$) may lead to the increase in the energy stored and, consequently, to the formation of PCG. Parson N. et al. [73] studied the influence of different die geometries, billet temperatures and ram speed during the extrusion of an AA6082 aluminum alloy round bar, founding out that the presence of a choke angle act in opposition to the PCG formation. A similar study was conducted by Mahmoodkhani et al. [74], further proving the retarding effect on the recrystallization of the choke angle. De Peri Jr L. and Misiolek W.J. [75] and Van Geertruyden W.H. et al. [76] proposed that the defect behaviour may be related to a very fine grain structures produced in the external layer due to the Geometric Dynamic Recrystallization (gDRX) or Continuous Dynamic Recrystallization (cDRX), which under certain conditions lead to the formation of large grains at the surface of the extruded profiles. Eivani A.R. et al. [71] suggested an improvement to this theory: due to a combination of large second-phase particles, high strains and strain rates at the surface layer of the extruded profiles, static recrystallized (SRX) grains may nucleate. These SRX grains, together with the DRX grains formed due to the high strain field, may grow with the difference that the SRX grains boundaries enlarge faster than the DRX grains, justifying the existence of finer grains at the surface and coarser grains in the inner part of the PCG layer. Furthermore, Charit I. and Mishra R.S. [77] investigated the Abnormal Grain Growth (AGG) in the friction stir welding of 7xxx aluminum alloy suggesting that the dissolution of Mg-Zn particles allows the reduction of the local pinning pressure (Zener-Drag pressure) thus leading to a fast recrystallization and grain growth.

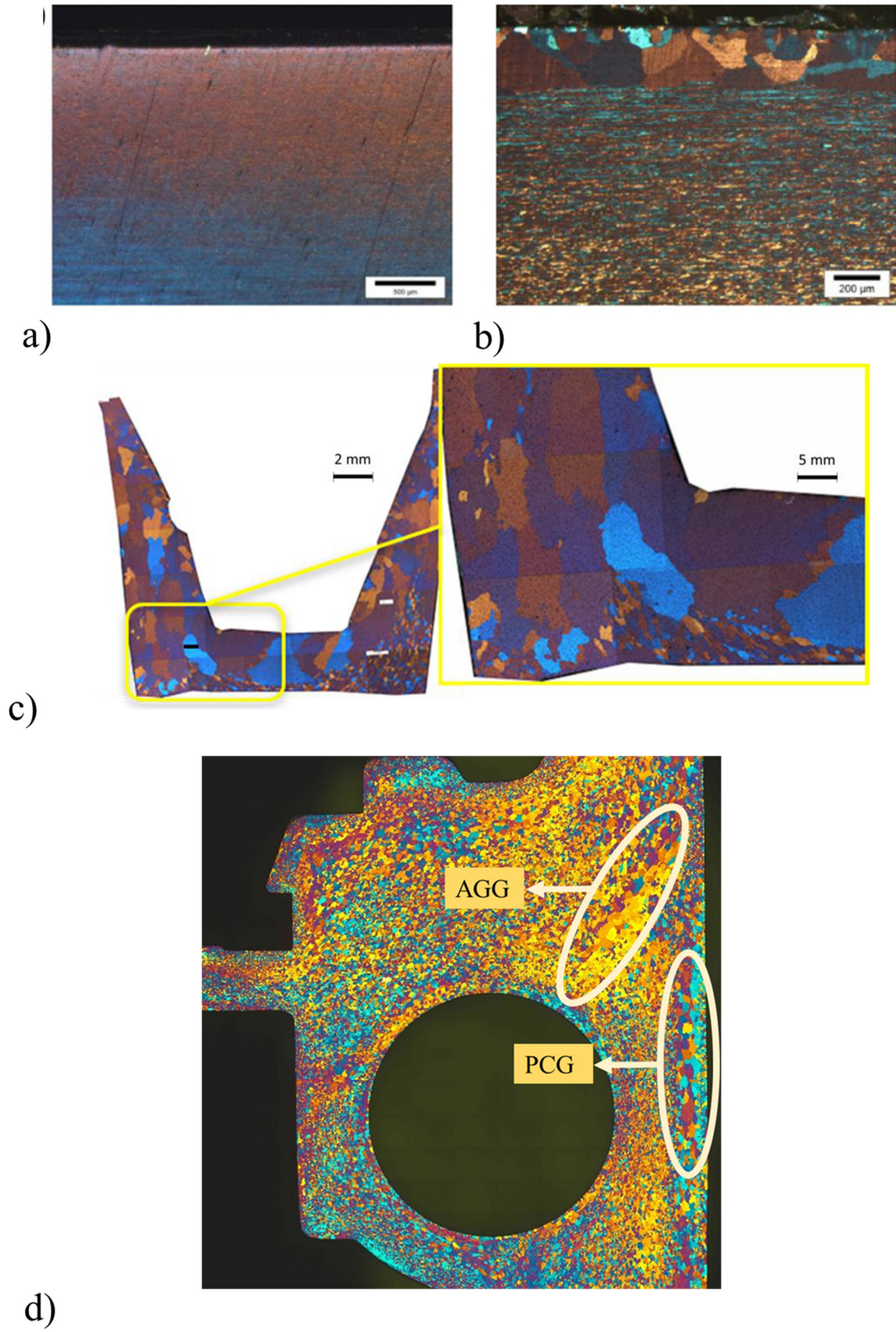


Figure 2.21: Example of PCG/AGG formations.

2.8 Modeling of the Recrystallization Mechanisms

From the analytical perspective, several studies have been carried out in order to investigate the recrystallization modeling of AA6XXX series aluminum alloy.

2.8.1 Modeling of the Dynamic Recrystallization

In 1990, Castro-Fernandez [78] proposed a model for the evaluation of the subgrain size validated over a compression test of an Al-1Mg-1Mn alloy. According to this study, the Zener-Hollomon parameter Z and the subgrain size δ are calculated as follow:

$$Z = \dot{\epsilon} \exp\left(\frac{Q}{RT}\right) \quad (2.1)$$

$$\frac{1}{\delta} = A \ln(Z) - B \quad (2.2)$$

where R is the universal gas constant (8.341 J/mol), Q is the activation energy of the aluminum alloy, T is the temperature and $\dot{\epsilon}$ is the strain rate. A and B are material constants, which are calculated as $0.165 \cdot 10^6 \text{ m}^{-1}$ and $3.87 \cdot 10^6 \text{ m}^{-1}$, respectively, for the Al-1Mg-1Mn alloy. However, there is a problem with the Eq. 2 since, for Z values lower than the asymptotic value $Z = \dot{\epsilon} \exp(B/A)$, return negative values of the subgrain size.

In 1995, Nes et al. [79] suggested an innovative equation for the subgrain evaluation which solve the mentioned problem of Eq. 2. This model was further validated in 1996 by Vatne et al. [66] in a hot torsion test of AA3004 and AA1050 samples. The subgrain is calculated as:

$$\frac{1}{\delta} = \frac{RT}{A^*} \ln\left(\frac{Z \delta^2}{B^*}\right) \quad (2.3)$$

where A^* and B^* are material constants (0.026 and 0.06, respectively).

The problem of Eq. 2 was also solved by the model proposed by Donati et al. [44] in 2013. In the work, hot torsion tests were performed on a AA6060 aluminum alloy and the following subgrain model was suggested:

$$\frac{1}{\delta} = C (\ln Z)^n \quad (2.4)$$

where C and n are material constants with a value of $C=3.36 \cdot 10^{-9} \text{ m}^{-1}$ and $n=5.577$.

In Fig. 2.22, the difference between the subgrain size predictions made according to different models is reported and compared to the data collected from the experimental campaign described in the work of McQueen et al. [80]. As clearly visible from the figure, the model of Donati (represented with the line in red).

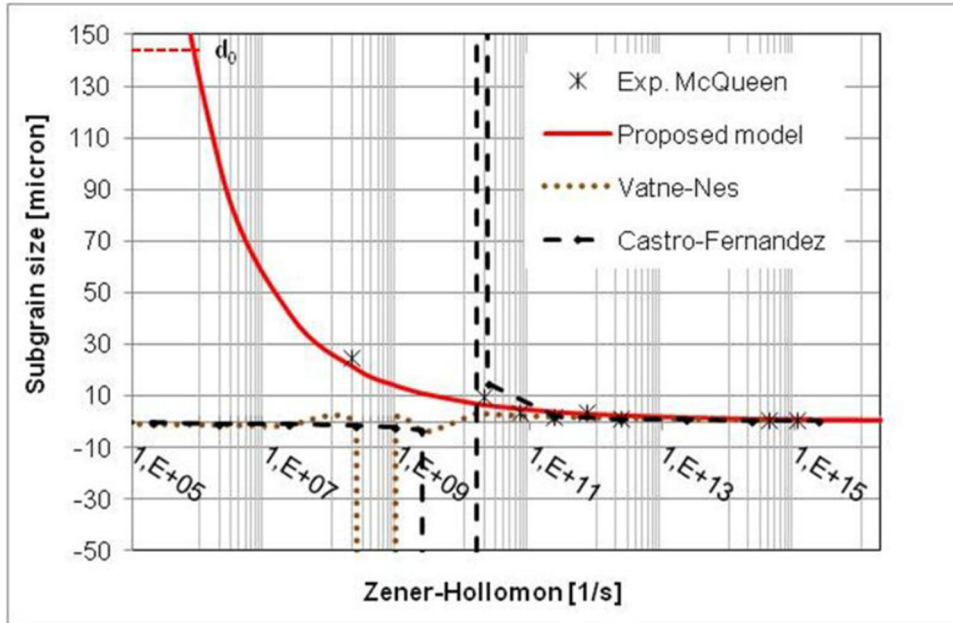


Figure 2.22: Relationship between subgrain size and Zener-Hollomon parameter according to different models [44].

Many authors in literature proposed analytical models for the prediction of the dynamic recrystallization during the hot deformation of aluminum alloys.

In 2002, Gholinia et al. [34] used the following model validated in the hot compression test of an Al-3Mg-0.2Fe alloy, for the calculation of the DRX:

$$\varepsilon = \ln \left(\frac{d_0}{d_{drx}} \right) \quad (2.5)$$

$$\varepsilon_c = \ln \left(\frac{d_0}{\delta} \right) \quad (2.6)$$

If $d_{drx} < \delta$ then $d_{drx} = \delta$

where d_0 is the grain size before the deformation, d_{drx} is the dynamic recrystallized grain size, ε is the strain and ε_c is the critical strain after which the pinch-off mechanism takes place. According to the modeling, if d_{drx} is lower than the subgrain size δ , then $d_{drx} = \delta$ (Fig. 2.23).

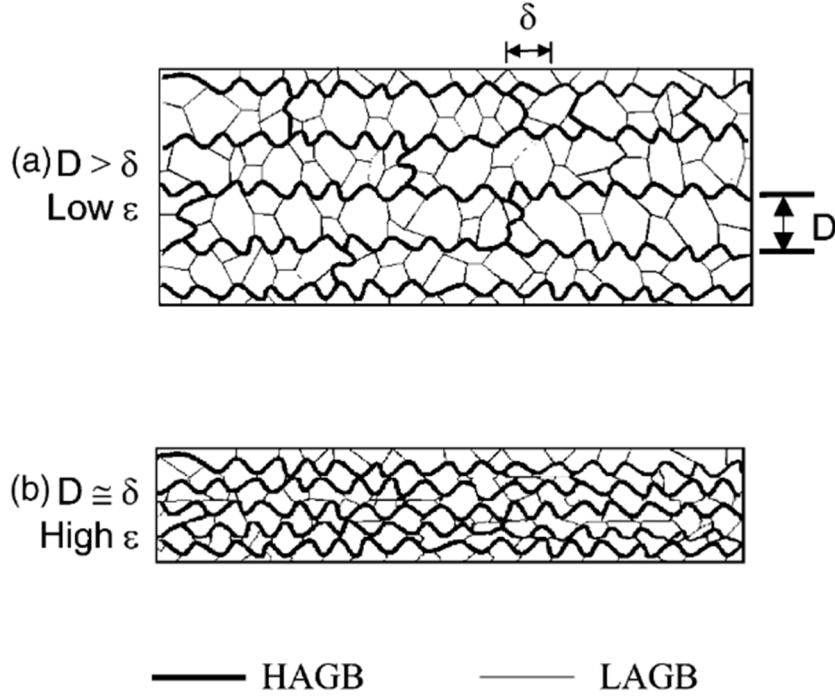


Figure 2.23: Schematic representation of the strain influence on grain thickness D and sub-grain size d , where HAGBs and LAGBs are shown as heavy dark and light lines, respectively [34].

In 2006, Fluher et al. [81] suggested a DRX model within the DEFORM software environment which was further investigated by Donati et al. in 2008 [82]. The investigated equation was the same one used to describe the DDRX in LSFE materials. It was adjusted and tested for the description of the dynamic recrystallization behaviour of HSFE materials as AA6060 [45] and AA6082. The modeling was made as follows:

$$d_{drx} = a_8 d_0^{h_8} \varepsilon^{n_8} \dot{\varepsilon}^{m_8} \exp\left(\frac{Q}{RT}\right) + c_8 \quad (2.7)$$

$$\text{If } d_{drx} > d_0 \text{ then } d_{drx} = d_0$$

where a_8, h_8, n_8, m_8, c_8 , are experimental material constants.

In 2008, De Pari et al. [46] Proposed a jDRX model further investigated by Donati et al. [44] in 2013 (Fig. 2.24). According to the latter, the dimensions of length and thickness of the dynamically recrystallized grains after the hot extrusion of aluminum alloy can be calculated as follow:

$$d_t = (d_0 - 2.5 * \delta_{ss}) * (k_1)^{\bar{\varepsilon}} + 2.5 * \delta_{ss} \quad (2.8)$$

$$d_l = k_2 \bar{\varepsilon}^2 - k_3 \bar{\varepsilon} + d_0 \quad \text{if } \varepsilon < \varepsilon_p \quad (2.9)$$

$$d_l = k_4 \bar{\varepsilon}^{-m} + 10\delta_{ss} \quad \text{if } \varepsilon > \varepsilon_p \quad (2.10)$$

where d_t and d_l are the average thickness and length of the grains immediately after the bearings zone, ε_p is the critical level of strain for the pinch-off onset which corresponds to a value of 3, δ_{ss} is the subgrain size at the steady-state condition ($\delta_{ss} = 8.4 \mu\text{m}$) and m, k_1, k_2, k_3, k_4 are material constants ($m=4.75, k_1=0.4, k_2=85.192, k_3=14.88, k_4=1.68 \cdot 10^5$ [44]).

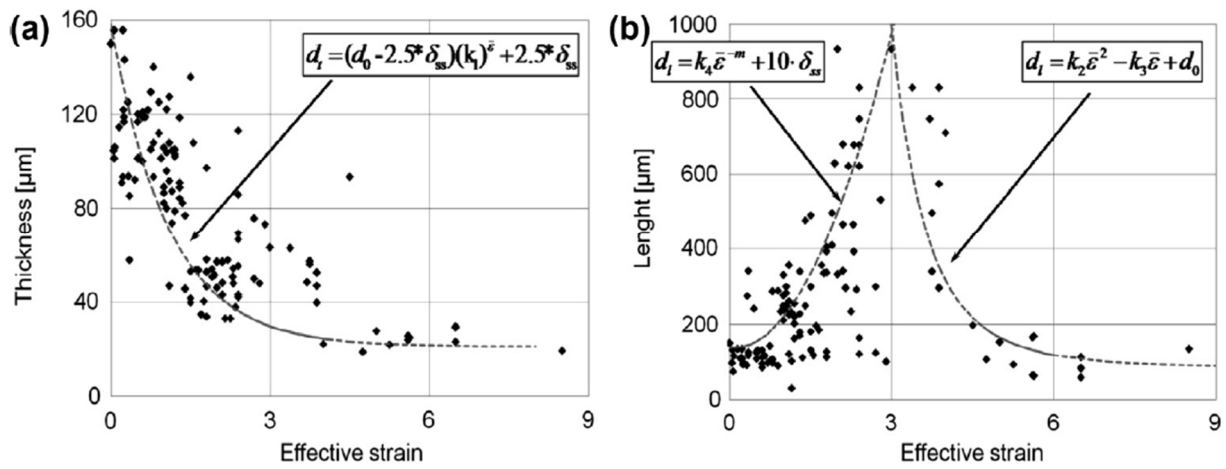


Figure 2.24: (a) Grain thickness and (b) grain length predictions (lines) vs experimental data (dots) [44]

In order to investigate the dynamic recrystallization, the following equation investigated by Schikorra in 2008 [45] was used to predict the percentage of DRX occurred in an extruded profile:

$$X_{DRX} = 1 - \exp \left[-\beta \left(\frac{\varepsilon - \varepsilon_c}{\varepsilon_s} \right)^m \right] \quad (2.11)$$

where ε_c is critical strain corresponding to the beginning of DRX, ε_s is the saturated strain meaning that the DRX completely occurred, β and m are material constants ($\beta=1.823$ and $m=1.109$ [9]).

2.8.2 Modeling of the Static Recrystallization

Several authors proposed analytical models to describe and predict the static recrystallization behaviour after the hot deformation of aluminum alloy.

In 1941, Avrami M. et al. [83] proposed the Kolmogorov-Johnson-Mehl-Avrami (JMAK) equation validated over hot rolling processes. The JMAK calculates the fraction of statically recrystallized surface and it can be expressed as follow:

$$X_{rex} = 1 - \exp \left\{ -0.693 * \left(\frac{t}{t_{50}} \right)^k \right\} \quad (2.12)$$

where X_{rex} is the percentage of SRX, t_{50} is the time needed to have the 50% of static recrystallization, t is the time and k is the Avrami coefficient.

In 1979, Sellars and Whiteman [84] proposed a new SRX model validated over hot deformation tests of steels with low carbon content. This model is described as follow:

$$t_{50} = c_1 d_0^C \varepsilon^{-n} Z^{-K} \exp \left(\frac{Q}{RT} \right) \quad (2.13)$$

$$d_{srx} = c_2 d_0^{C'} \varepsilon^{-n'} Z^{-K'} \quad (2.14)$$

where c_1, c_2, C, C', K, K' are material constants.

In 1996, Vatne et al. [66] suggested an innovative model for the prediction of the grain size after recrystallization considering the sum of three nucleation contributions:

$$D_{rex} = DN^{-1/3} \quad (2.15)$$

$$N = N_{PSN} + N_{GB} + N_C \quad (2.16)$$

where D is a material calibration constant and N is the nucleation density. N was considered as sum of different nucleation components: N_{PSN} , N_{GB} and N_C . N_{PSN} is the nucleation occurred on large particles (larger than the critical particle size) around which the deformation zones may form. It is frequently the main nucleation mechanism in the commercial alloys which contains large undeformable particles, and involves the growth of nuclei in turbulent deformation zones with random orientations. N_{GB} is the nucleation from old grain boundaries and N_C is the nucleation from retained cube grains, present in the initial material, which survived the applied deformation. Both N_{GB} and N_C are dependent on the subgrain size and density, grain boundary area per volume and grain size before deformation.

According to [66], these three contributions were calculated as follows:

$$N_{PSN} = C_{PSN} \exp\left(\frac{-A_{PSN}}{(Pd - Pz)}\right) \quad (2.17)$$

$$N_{GB} = C_{GB} \delta A(\varepsilon) S_{GB} \quad (2.18)$$

$$N_C = C_C \delta A(\varepsilon) S_C \quad (2.19)$$

where C_{PSN} , A_{PSN} , C_{GB} and C_C are the material constants, Pd is the Stored Energy and Pz the Zener Drag Pressure. $A(\varepsilon)$ is the grain boundary area per volume at a given strain and S_{GB} , which can be assumed as $S_{GB}=S_C=S$ [66], is the number of subgrain larger than a critical subgrain size δ^* , calculated as followed:

$$\delta^* = \frac{4 \gamma}{Pd - Pz} \quad (2.20)$$

According to what reported in literature [66], $A(\varepsilon)$ was modeled as:

$$A(\varepsilon) = \frac{1}{d_0} [(\exp(\varepsilon) + \exp(-\varepsilon) + 1)] \quad (2.21)$$

In 1999, Furu et al. [85] proposed a SRX model validated over compression tests of a Al-1Mg alloy. The calculation of the final grain size is the same as in Eq. 15 but the total nucleation contribution is calculated as follow:

$$N_v = \left(\frac{C_d}{\delta^2}\right) S_v(\varepsilon) \quad (2.22)$$

$$S_v(\varepsilon) = \frac{2}{d_0} [(\exp(\varepsilon) + \exp(-\varepsilon) + 1)] \quad (2.23)$$

where C_d is a material constant and $S_v(\varepsilon)$ is the equivalent of the grain boundary area per volume $A(\varepsilon)$ calculated in [66]. Moreover, the authors suggested the following equations for the calculation of the time needed to have the 50% of static recrystallization t_{50} :

$$\gamma_{SB} = \left(\frac{Gb}{4\pi(1-\nu)}\right) \vartheta \left(1 + \ln\left(\frac{\vartheta_c}{\vartheta}\right)\right) \quad (2.24)$$

$$\Gamma = \frac{1}{2}Gb^2 \quad (2.25)$$

$$P_D = \frac{\alpha\gamma_{SB}}{\delta} + \rho_i\Gamma \quad (2.26)$$

$$t_{50} = \frac{C_t}{M_{GB}P_D} \left(\frac{1}{N_v}\right)^{\frac{1}{3}} \quad (2.27)$$

where is C_t, M_{GB}, α are material constants, G is the material shear modulus (2.05×10^{10} Pa), b the Burgers vector (2.86×10^{-10} m), ρ_i the dislocation density, δ the subgrain size, θ the misorientation angle and θ_c the misorientation angle limit (15°).

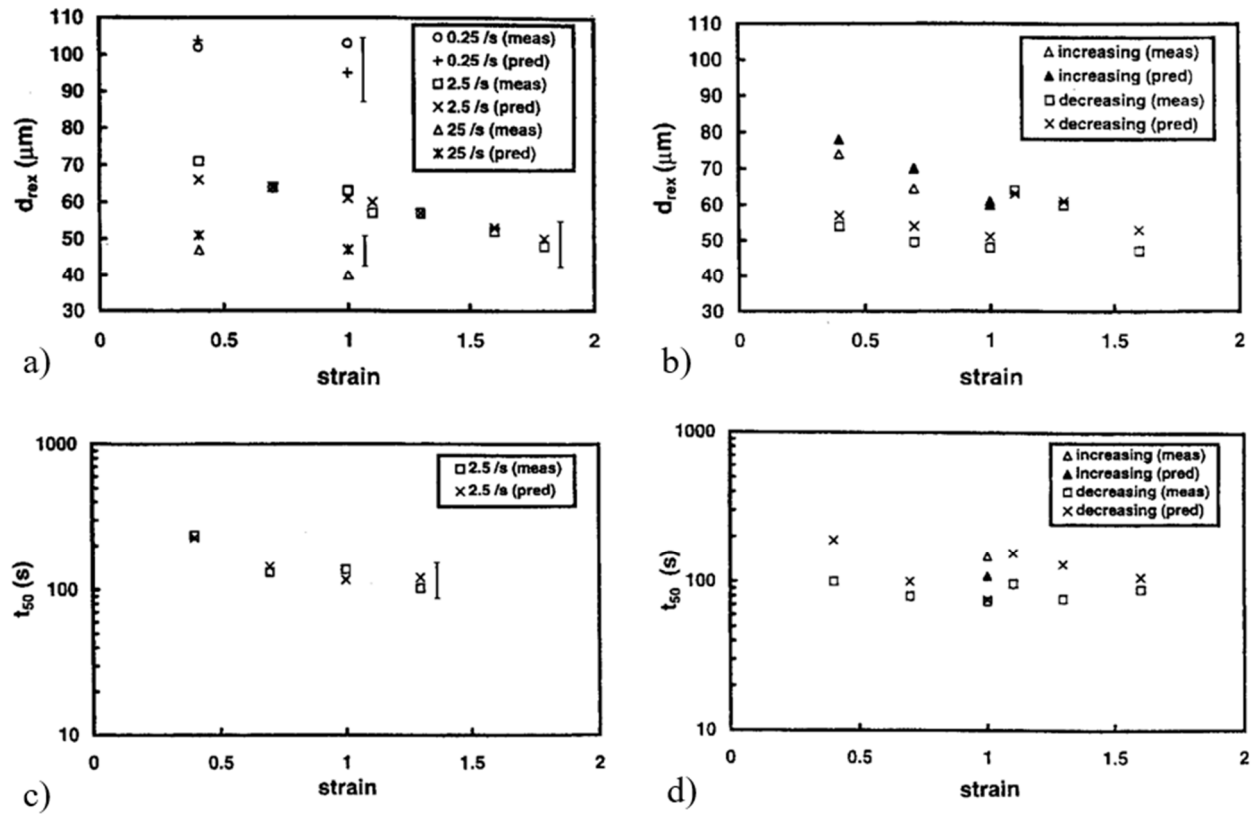


Figure 2.25: Predicted and measured recrystallized grain size after being deformed at (a) constant strain rate; (b) varying strain rate. Typical uncertainty in the model is shown by the error bars. Predicted and measured time to 50% recrystallized t_{50} following tests at: (a) constant strain rate; (b) varying strain rate. Typical uncertainty in the model is shown by the error bar [85].

In 2000, Sellars C.M. and Zhu Q. [65] proposed the following equation for the Stored Energy computation:

$$Pd = \frac{Gb^2}{10} \left[\rho_i (1 - \ln(10b\rho_i^{0.5})) + \frac{2\theta}{b\delta} \left(1 + \ln\left(\frac{\theta c}{\theta}\right) \right) \right] \quad (6.1)$$

where G is the material shear modulus (2.05×10^{10} Pa), b the Burgers vector (2.86×10^{-10} m), ρ_i the dislocation density, δ the subgrain size, θ the misorientation angle and θc the misorientation angle limit (15°).

In 2002, Sheppard and Duan [86] used a simplified formula to calculate the dimension of the grain after static recrystallization validated over the hot rolling of AA5083 samples:

$$d_{rex} = \frac{4.79 d_0 Z^{-0.075}}{3.72 + \bar{\epsilon}^2} \quad (2.28)$$

In 2013, Donati et al. [44] introduced in the nucleation formula the variables d_t and d_l calculated with Eq. 2.8-2.10 (Fig. 2.26, 2.27). The following model was proposed:

$$D_{rex} = DN_v^{-1/3} \quad (2.29)$$

$$N_v = \frac{C_d}{\delta^2} \left(\frac{4}{d_t + d_l} \right) [(\exp(\epsilon) + \exp(-\epsilon) + 1)] \quad (2.30)$$

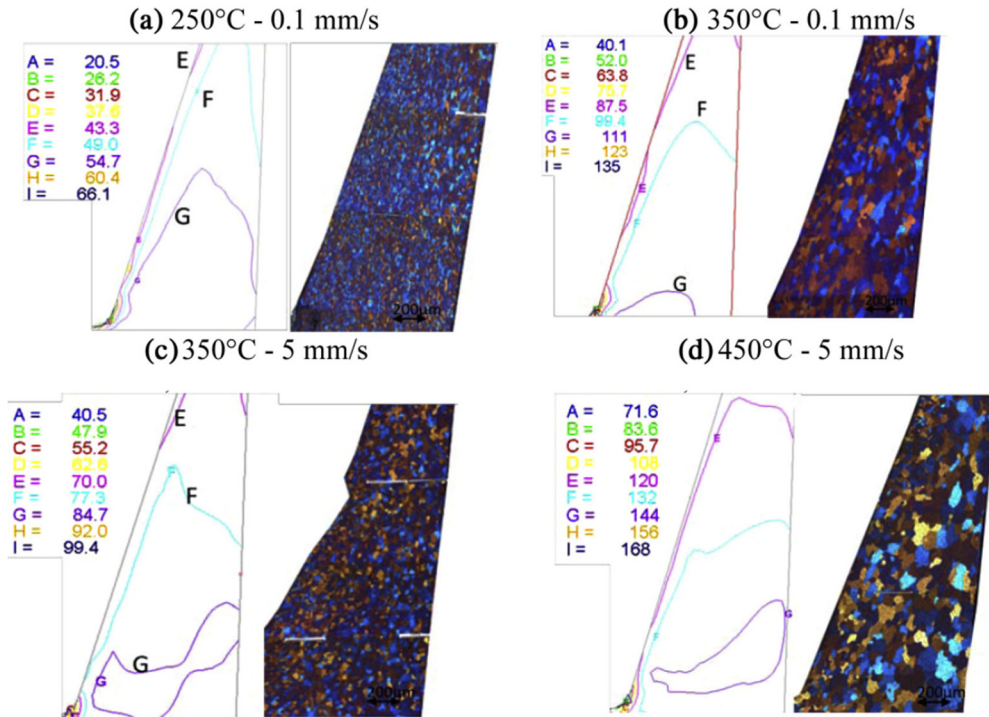


Figure 2.26: Prediction of the grain size in different deformation conditions [44]

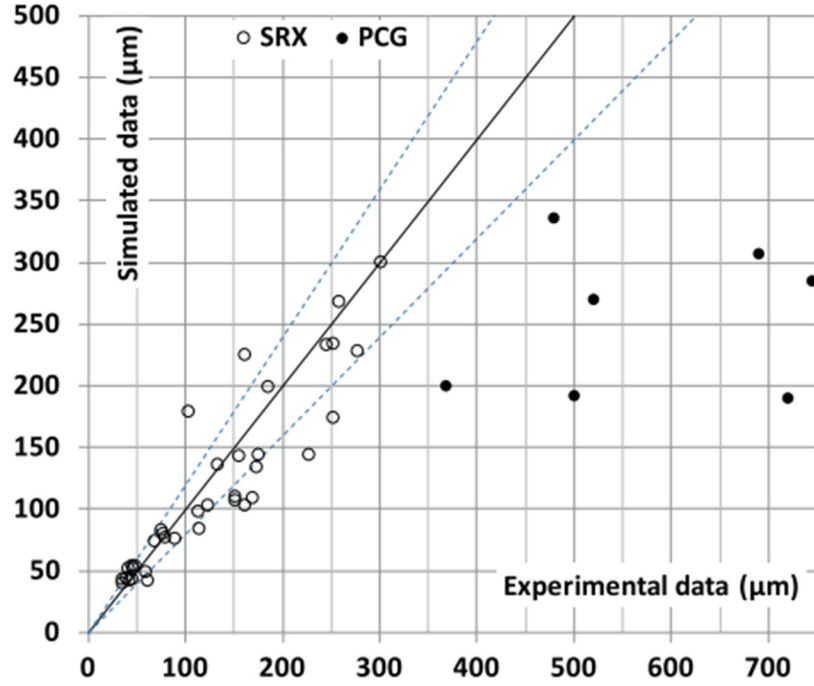


Figure 2.27: Comparison between experimental and numerical grain size [44]

In 2016, Furu T. et al. [62], investigated the recrystallization kinetics using the standard JMAK (Johnson-Mehl-Avrami-Kolmogorov) theory. In this work, the following modeling was used to evaluate the fraction of the recrystallized grain after a hot deformation process:

$$\frac{dX_{rex}}{dt} = N(1 - X_{rex})4\pi r_{(t)}^2 G_{(t)} \quad (2.31)$$

$$G_{(t)} = \frac{dr_{(t)}}{dt} = M(P_D - P_Z) \quad (2.32)$$

$$M = \frac{M_0}{C_{SS}RT} \exp\left(-\frac{U_{GB}}{RT}\right) \quad (2.33)$$

where X_{rex} is the fraction of recrystallized grains, N is the total contribution for nucleation, $r_{(t)}$ and $G_{(t)}$ are the radius and the growth rate of recrystallized grains, M is the mobility, $M_0 = 0.5 \cdot 10^3 \frac{m^4}{s}$ is the constant value for the mobility calculated for an AA6060 alloy [87], C_{SS} is the effective solid solution concentration based on individual element concentrations after homogenization and U_{GB} is the activation energy for grain boundary migration.

The modeling of the recrystallization behaviour used for the numerical analysis reported in this thesis was developed starting from the models described in the current analysis. The subgrain size evolution and the dynamic recrystallization kinetics were calculated according to the modeling of Donati L. et al. [44] while the impact of the static recrystallization in the microstructure evolution was calculated according to the modeling of Sellars C.M. and Zhu Q. [65] and Vatne et al. [66] with different improvements reported in paragraph 4.2, 5.2, 6.1.2 and 6.2.2.

References

- [1] F.J. Humphreys, M. Hatherly (2008) *Recrystallization and Related Annealing Phenomena*, 2nd edn. Elsevier, Oxford.
- [2] H. Hallberg (2011) Approaches to Modeling of Recrystallization, *Metals* 1:16-48.
- [3] C.M. Adam, A. Wolfenden (1978) The influence of microstructure on the energy stored in deformed aluminium and aluminium alloys, *Acta Metallurgica* 26(9): 1307-1315.
- [4] T. Sakai, A. Belyakov, R. Kaibyshev, H. Miura, J.J. Jonas (2014) Dynamic and post-dynamic recrystallization under hot, cold and severe plastic deformation conditions, *Progress in Materials Science*, 60: 130-207.
- [5] G. Guiglionda, A. Borbély, J.H. Driver (2008) Orientation-dependent stored energies in hot deformed Al-2.5%Mg and their influence on recrystallization, *Acta Materialia*, 52(12): 3413-3423.
- [6] G.E. Lloyd, A. B. Farmer, D. Mainprice (1997) Misorientation analysis and the formation and orientation of subgrain and grain boundaries, *Tectonophysics*, 279: 55-78.
- [7] J. Yu, G. Zhao, C. Zhang, L. Chen (2017) Dynamic evolution of grain structure and microtexture along a welding path of aluminum alloy profiles extruded by porthole dies, *Mater. Sci. Eng. A* 682: 679-690.
- [8] G. Xiao, J. Jiang, Y. Liu, Y. Wang, B. Guo (2019) Recrystallization and microstructure evolution of hot extruded 7075 aluminum alloy during semi-solid isothermal treatment, *Materials Characterization*, 156(109874): 1-13.
- [9] C. Zhang, C. Wang, R. Guo, G. Zhao, L. Chen, W. Sun, X. Wang (2019) Investigation of dynamic recrystallization and modeling of microstructure evolution of an Al-Mg-Si aluminum alloy during high-temperature deformation, *Journal of Alloys and Compounds* 773: 59-70.
- [10] P. Sperry (1984) Correlation of microstructure in 6xxx extrusion alloys with process variables and properties. *Proceedings of the 3th International Aluminum Extrusion Technology Seminar* 1:21-29.
- [11] R.D. Doherty, D. A. Hughes, F. J. Humphreys, J.J. Jonas, D.J. Jensen, M. E. Kassner, A. D. Rollett (1997) Current issues in recrystallization: a review, *Materials Science and Engineering: A* 238: 219-274.
- [12] K. Huang, R. E. Logé (2016) A review of dynamic recrystallization phenomena in metallic materials. *Materials & Design* 111: 548-574.
- [13] A.R. Eivani, *Modeling of Microstructural Evolution during Homogenization and Simulation of Transient State Recrystallization leading to Peripheral Coarse Grain Structure in Extruded Al-4.5Zn-1Mg Alloy*. PhD Thesis, Delft University of Technology, Delft, NL (2010).

- [14] Y. Birol (2014) Effect of Cr and Zr on the grain structure of extruded EN AW 6082 alloy. *Met. Mater. Int.* 20: 727–732.
- [15] M.F. Ashby, J. Harper, and J. Lewis (1969) The interaction of crystal boundaries with second-phase particles, *Trans Met Soc AIME* 245(2): 413-420
- [16] F.J. Humphreys, A network model for recovery and recrystallisation, *Scripta Metallurgica et Materialia*, Volume 27, Issue 11, 1992, 1557-1562
- [17] E.A. Holm, M.A. Miodownik, A.D. Rollett (2003). On abnormal subgrain growth and the origin of recrystallization nuclei, *Acta Mater.* 51:2701–2716.
- [18] M. Ferry, F.J. Humphreys (1996) Discontinuous subgrain growth in deformed and annealed {110} (001) aluminium single crystals, *Acta Mater.* 44:1293–1308.
- [19] L. Himmel (Ed.) (1962) *Recovery and Recrystallization of Metals*. AIME. published by Interscience Publishers.
- [20] C. Shi, J. Lai, X.G. Chen, (2013) Microstructural Evolution and Dynamic Softening Mechanisms of Al-Zn-Mg-Cu Alloy during Hot Compressive Deformation, *Materials* 7: 244-264.
- [21] R.D. Doherty, R.W. Cahn (1972) Nucleation of new grains in recrystallization of cold worked metals, *J. Less Common Met.* 28(2): 279–296.
- [22] T. Furu, K. Marthinsen, E. Nes (1993) Particle Effects on Recrystallization of Metals, *Materials Science Forum*, 113–115: 41–54.
- [23] D. Raabe (2014) *Recovery and Recrystallization: Phenomena, Physics, Models, Simulation*, *Physical Metallurgy*, 2291–2397.
- [24] E.S. Puchi, J. Beynon, C.M. Sellars (1988) Simulation of hot rolling operations on commercial aluminum alloys, *Proc. Int. Conf. On Physical Metallurgy of Thermomechanical Processing of Steels and Other Metals: THERMC'88*, 572–579.
- [25] W.C. Leslie, J.T. Michalak, F.W. Aul (1963). *Iron and Its Dilute Solid Solutions*, Spencer, Wemer, (Eds.), 1963c., 119. Interscience, New York.
- [26] H.J. McQueen (2004) Development of dynamic recrystallization theory, *Materials Science and Engineering A* 387: 203–208.
- [27] J. Lv, J. Zheng, V.A. Yardley, Z. Shi, J. Lin (2020). A Review of Microstructural Evolution and Modelling of Aluminium Alloys under Hot Forming Conditions, *Metals* 10(1516): 1-33.
- [28] S. Gourdet, F. Montheillet (2003) A model of continuous dynamic recrystallization, *Acta Materialia* 51: 2685-2699.

- [29] J. Zhao, Y. Deng, J. Tan, J. Zhang (2018) Effect of strain rate on the recrystallization mechanism during isothermal compression in 7050 aluminum alloy. *Mater. Sci. Eng. A* 734: 120–128.
- [30] B. Liao, X. Wu, L. Cao, G. Huang, Z. Wang, Q. Liu (2019) The microstructural evolution of aluminum alloy 7055 manufactured by hot thermo-mechanical process, *J. Alloy. Compd.* 796: 103–110.
- [31] X. Zhong, L. Huang, F. Liu (2020) Discontinuous Dynamic Recrystallization Mechanism and Twinning Evolution during Hot Deformation of Incoloy 825, *J. of Materi Eng and Perform* 29: 6155–6169.
- [32] H.J. McQueen, O. Knustad, N. Ryum, J. K. Solberg (1985) Microstructure Evolution in Al Deformed to Strains of 60 at 400°C, *Scripta Metallurgica* 19: 73-78.
- [33] A.M. Wusatowska-Sarnek, H. Miura, T. Sakai (2002) Nucleation and microtexture development under dynamic recrystallization of copper, *Materials Science and Engineering: A* 323: 177-186.
- [34] A. Gholinia, F.J. Humphreys, P.B. Prangnell (2002) Production of ultra-fine grain microstructures in Al–Mg alloys by conventional rolling, *Acta Materialia* 50: 4461-4476.
- [35] G.A. Henshall, M.E. Kassner, H.J. McQueen (1992) Dynamic restoration mechanisms in Al-5.8 At. Pct Mg deformed to large strains in the solute drag regime, *Metallurgical Transactions A* 23: 881-889.
- [36] W. Blum, Q. Zhu, R. Merkel, H.J. McQueen (1996) Geometric dynamic recrystallization in hot torsion of Al-5Mg-0.6 Mn (AA5083), *Materials Science and Engineering: A* 205: 23-30.
- [37] E.V. Konopleva, H.J. McQueen, E. Evangelista (1995) Serrated grain boundaries in hot-worked aluminum alloys at high strains, *Materials Characterization* 34: 251-264.
- [38] H.J. McQueen, M.M. Myshlyaev, A. Mwembela (2003) Microstructural evolution and strength in hot working of ZK60 and other Mg alloys, *Canadian metallurgical quarterly* 42: 97-76-112.
- [39] M.M. Myshlyaev, H.J. McQueen, A. Mwembela, E. Konopleva (2002) Twinning, dynamic recovery and recrystallization in hot worked Mg–Al–Zn alloy, *Materials Science and Engineering: A* 337: 121-133.
- [40] A.R. Eivani, J. Zhou, J. Duszczyk (2014) Numerical modeling of subgrain growth of hot extruded Al–4.5Zn–1Mg alloy in the presence of nanosized dispersoids, *Computational Materials Science* 86: 9-16.
- [41] M.T. Perez-Prado, S.R. Barrabes, M.E. Kassner, E. Evangelista (2005) Dynamic restoration mechanisms in α -zirconium at elevated temperatures, *Acta Materialia* 53: 581-591.
- [42] K. Huang, R.E. Logé (2016) A review of dynamic recrystallization phenomena in metallic materials, *Materials & Design* 111: 548-574.

- [43] H.J. McQueen, M.E. Kassner (2004) Comments on 'a model of continuous dynamic recrystallization' proposed for aluminum, *Scr. Mater.* 51: 461–465.
- [44] L. Donati, A. Segatori, M. El Mehtedi, L. Tomesani (2013) Grain evolution analysis and experimental validation in the extrusion of 6XXX alloys by use of a lagrangian FE code, *International Journal of Plasticity* 46: 70-81.
- [45] M. Schikorra, L. Donati, L. Tomesani, A. E Tekkaya (2008) Microstructure analysis of aluminum extrusion: Prediction of microstructure on AA6060 alloy, *Journal of Materials Processing Technology*: 201:156-162.
- [46] L. De Pari, W.Z. Misiolek (2008) Theoretical predictions and experimental verification of surface grain structure evolution for AA6061 during hot rolling, *Acta Materialia* 56: 6174–6185.
- [47] A. Baczmanski, K. Wierzbanowski, A. Benmarouane, A. Lodini, P.Lipinski, B. Bacroix (2007) Stored energy and recrystallization process, *Materials Science Forum* 539-543: 3335-3340.
- [48] J. Gil Sevillano, P. Van Houtte, E. Aernoudt (1980) Large strain work hardening and textures, *Prog. Mater. Sci.* 25: 69-134.
- [49] H.E. Vatne, R. Ørsund, K. Marthinsen, E. Nes (1996) Modeling recrystallization kinetics, grain sizes, and textures during multipass hot rolling, *Metallurgical and Materials Transactions A* 27(12): 4133-4144.
- [50] P.S. Bate, W.B. Hutchinson (2005) Grain boundary area and deformation, *Scripta Materialia* 52: 199-203.
- [51] A.R. Eivani, S. Valipour, H. Ahmed, J. Zhou, J. Duszczuk (2011) Effect of the Size Distribution of Nanoscale Dispersed Particles on the Zener Drag Pressure, *Metall Mater Trans A* 42: 1109–1116.
- [52] P. Rios, F. Siciliano, H. Sandim, R. Lesley, A. Padilha (2005) Nucleation and growth during recrystallization, *Materials Research* 8(3): 225-238.
- [53] Z. Li, J. Qin, H. Zhang, X. Wang, B. Zhang, H. Nagaumi (2021) Improved Distribution and Uniformity of α -Al(Mn,Cr)Si Dispersoids in Al-Mg-Si-Cu-Mn (6xxx) Alloys by Two-Step Homogenization, *Metall Mater Trans A* 52: 3204–3220.
- [54] F. Schmid, I. Weißensteiner, M.A. Tunes, T. Kremmer, T. Ebner, R. Morak, P.J. Uggowitzer, S. Pogatscher (2021) Synergistic alloy design concept for new high-strength Al–Mg–Si thick plate alloys, *Materialia* 15:100997 1-13.
- [55] R. Hu, T. Ogura, H. Tezuka, T. Sato, Q. Liu (2010) Dispersoid Formation and Recrystallization Behavior in an Al-Mg-Si-Mn Alloy, *Journal of Materials Science & Technology*, Volume 26(3): 237-243.
- [56] K. Strobel, E. Sweet, M. Easton, J.F. Nie (2010) Couper M. Dispersoid Phases in 6xxx Series Aluminium Alloys, *Materials Science Forum* 654–656:926–9.

- [57] E. Elgallad, K. Liu, Z. Zhang, X.G. Chen (2020). Effect of transition elements on dispersoid formation and elevated-temperature mechanical properties in 6082 aluminum alloy, *Philosophical Magazine* 101: 1-21.
- [58] P.A. Rometsch, S.C. Wang, A. Harriss, P.J. Gregson, M.J. Starink (2002) The effect of homogenizing on the quench sensitivity of 6082, *Mater. Sci. Forum* 396-402: 655–660.
- [59] D.J. Srolovitz, G.S. Grest, M.P. Anderson (1986) Computer simulation of recrystallization— I. Homogeneous nucleation and growth, *Acta metallurgica* 34: 1833-1845.
- [60] F.J. Humphreys (1997) A unified theory of recovery, recrystallization and grain growth, based on the stability and growth of cellular microstructures—I. The basic model, *Acta Materialia* 45(10): 4231-4240.
- [61] A.R. Eivani, J. Zhou, J. Duszczyk (2013) Grain boundary versus particle stimulated nucleation in hot deformed Al-4.5Zn-1Mg alloy, *Materials Science and Engineering* 29: 517–528.
- [62] T. Furu, R. Østhus, N. Telioui, R. Aagård, M. Bru, O.R. Myhr (2016) Modeling the Effect of Mn on Extrudability, Mechanical Properties and Grain Structure of AA6082 Alloys, *Proceedings of the Eleventh International Aluminum Extrusion Technology Seminar ET '16* 1: 567-590.
- [63] F.J. Humphreys (1997) A unified theory of recovery, recrystallization and grain growth, based on the stability and growth of cellular microstructures-II. The effect of second-phase particles, *Acta materialia* 45: 5031-5039.
- [64] Y. Xiong, N. Li, H. Jiang, Z. Li, Z. Xu, L. Liu (2014) Microstructural evolutions of AA7055 Aluminum alloy under dynamic and quasi-static compressions, *Acta Metall. Sin.* 27: 272–278.
- [65] C.M. Sellars, Q. Zhu (2000) Microstructural modelling of aluminium alloys during thermomechanical processing, *Materials Science and Engineering: A* 280: 1-7.
- [66] H.E. Vatne, T. Furu, R. Orsund, E. Nes (1996) Modelling recrystallization after hot deformation of aluminum, *Acta Materialia* 11: 4463–4473.
- [67] Z. Peng, T. Sheppard (2004) Prediction of Static Recrystallisation after Extrusion of Shaped Aluminium Sections, *Materials Science Forum* 467–470: 407–420.
- [68] A. Güzel, A. Jäger, F. Parvizian, H.G. Lambers, A.E. Tekkaya, B. Svendsen, H.J. Maier (2012) A new method for determining dynamic grain structure evolution during hot aluminum extrusion, *Journal of Materials Processing Technology*, Volume 212(1): 323-330.
- [69] Y. Mahmoodkhani, J. Chen, M.A. Wells, W.J. Poole, N. Parson (2019) The Effect of Die Bearing Geometry on Surface Recrystallization During Extrusion of an Al-Mg-Si-Mn Alloy, *Metallurgical and Materials Transactions A* 50: 5324–5335.
- [70] A.R. Eivani, H.R. Jafarian, J. Zhou, J. Simulation of peripheral coarse grain structure during hot extrusion of AA7020 aluminum alloy, *Journal of Manufacturing Processes* 57: 881-892.

- [71] A. R. Eivani, J. Zhou, J. Duszczyk (2016) Mechanism of the formation of peripheral coarse grain structure in hot extrusion of Al-4.5Zn-1Mg, *Philosophical Magazine* 96(12): 1188-1196.
- [72] W.H. Van Geertruyden, W.Z. Misiolek, P. T. Wang (2005) Evolution of surface recrystallization during indirect extrusion of 6xxx aluminum alloys. *Metall. Mater. Trans.* 36: 1049–1056.
- [73] N. Parson, A. Maltais, C. Jowett, (2012) The Influence of Die Bearing Geometry on Surface Recrystallisation of 6xxx Extrusions, *Proceedings of the Tenth International Aluminum Extrusion Technology Seminar ET2012* 1: 19-32.
- [74] Y. Mahmoodkhani, J. Chen, M.A. Wells, W.J. Poole, N. Parson (2019) The Effect of Die Bearing Geometry on Surface Recrystallization During Extrusion of an Al-Mg-Si-Mn Alloy, *Metallurgical and Materials Transactions A* 50: 5324–5335.
- [75] L. De Peri Jr., W.J. Misiolek (2008) Theoretical prediction and experimental verification of surface grain structure evolution for AA6061 during hot rolling, *Acta Materialia*, 56: 6174-6185.
- [76] W. Misiolek, W.H. Van Geertruyden (2009) Combined Numerical Simulation and Microstructure Characterization for Prediction of Physical Properties in Extruded Aluminum Alloys. *Key Engineering Materials* 424: 1-8.
- [77] I. Charit, R.S. Mishra (2008) Abnormal grain growth in friction stir processed alloys, *Scripta Materialia* 58(5): 367-371.
- [78] F.R. Castro-Fernandez, C.M. Sellars, J.A. Whiteman (1990) Changes of flow stress and microstructure during hot deformation of Al–1Mg–1Mn, *Materials Science and Technology* 6: 453-460.
- [79] E. Nes (1995) Recovery revisited, *Acta Metallurgica et Materialia* 43(6): 2189-2207.
- [80] H.J. McQueen, S. Spigarelli, M.E. Kassner, E. Evangelista (2011) *Hot Deformation and Processing of Aluminum Alloys*. CRC Press, Taylor and Francis Group, Boca Raton FL, USA.
- [81] J. Fluhner (2006) *DEFORMTM 3D User's Manual Version 6.0*, Scientific Forming Technologies Corporation.
- [82] L. Donati, J.S. Dzwonczyk, J. Zhou, L. Tomesani (2008) Microstructure Prediction of Hot-Deformed Aluminium Alloys, *Key Engineering Materials* 367: 107-116.
- [83] M. Avrami (1941) Kinetics of Phase Change. III. Granulation, Phase Change, and Microstructure, *Journal of Chemical Physics* 9(2): 177–184.
- [84] C.M. Sellars, J.A. Whiteman (1979) Recrystallization and grain growth in hot rolling, *Metal Science* 13: 187-194.

- [85] T. Furu, H.R. Shercliff, G.J. Baxter, C.M. Sellars (1999) The influence of transient deformation conditions on recrystallization during thermomechanical processing of an Al-1% Mg alloy, *Acta Materialia* 47(8): 2377-2389.
- [86] T. Sheppard, X. Duan (2002) Modelling of static recrystallisation by combining FEM with empirical models, *Journal of materials processing technology* 130: 250-253.
- [87] C.O. Paulsen (2015) Recrystallization Behaviour in Extruded Profile of Non-Dispersoid Containing Al-Mg-Si Alloys, PhD Thesis, Department of Materials Science and Engineering NTNU-Trondheim, Materials Science and Engineering.

3. FEM Simulation of the Extrusion Process

The "Finite Element Method" (FEM) was born in the second half of the XX century for structural analysis and then applied for the approximate solution of differential equations systems.

The main advantage of this method is the capability of solving complex problems despite the high computational time required to obtain solutions that satisfy adequate criteria of accuracy and precision. This problem of the calculation time is relatively solved thanks to the use of modern workstations which, due to a constant improvement of the computing calculation power over the years, have made it possible to use and apply the FEM method in various fields of engineering [1-4]. The FEM method allows to solve several problems (for example structural, thermal, etc.) expressed by systems of very complex differential equations and, also through simplifying hypotheses, to reach a sufficiently accurate solution.

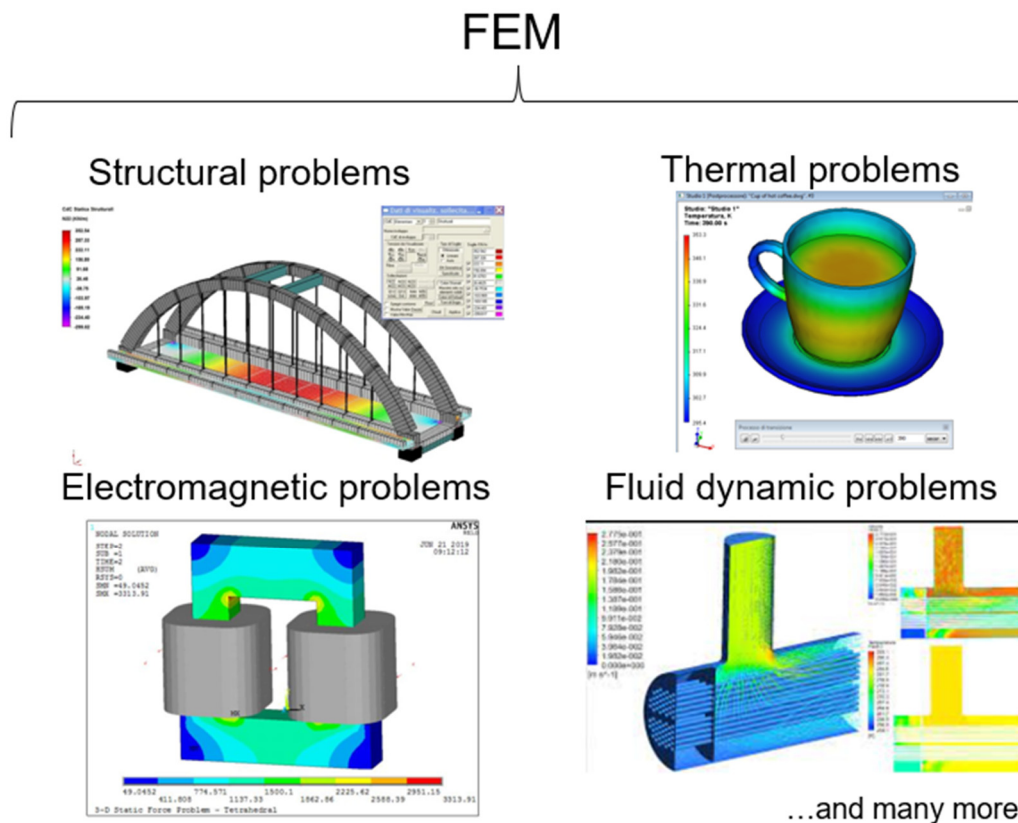


Figure 3.1: Application fields of the FEM method.

3.1 FEM simulation of manufacturing processes

The FEM method is particularly suitable for the investigation of manufacturing processes, as it allows the calculation and prediction of displacements, distortions, stresses, strains, temperatures, heating and cooling phases and the possible onset of local defects [5-7].

3.2 Approaches of FEM Codes

The application and development of FEM codes to plastic deformation processes is possible because of the high versatility and ability to simulate even complex cases with various boundary conditions (heat treatments, external loads, friction conditions, etc.) in a short period of time. As previously mentioned, several numerical codes are available on the market, each one of them uses different simulation methodologies and approaches. In general, three main types of simulation approaches can be distinguished [1, 2, 6]:

- Lagrangian approach: it deals with individual particles and calculates each particle separately (Fig. 3.2). By using this approach in plastic deformation problems, the mesh is deformed as the material flow during the manufacturing process. Despite a great accuracy in the simulation, it is difficult to use a pure Lagrangian approach in the simulation of processes which involve large deformation because of the high computational time. This is because, once the elements are severely deformed, an operation called “remeshing” is needed. For this reason, if the process led to high deformations, the number of remeshing phases increases as the simulation time. Examples of codes that use this type of approach are Deform and QForm.

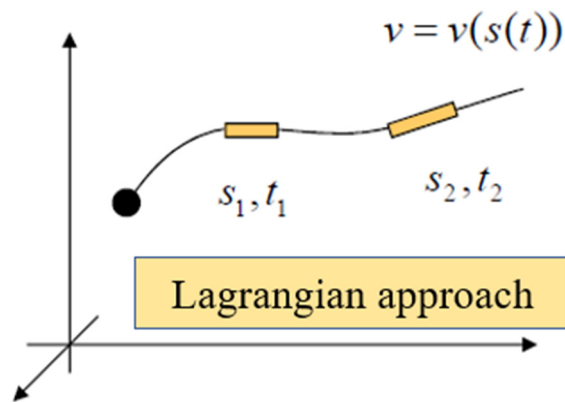


Figure 3.2: Lagrangian approach: the elements of the mesh move (with respect to the fixed reference system) and deform together with the material flow.

- Eulerian approach: it deals with the calculation of the problem variable in a fixed control volume (Fig. 3.3). Consequently, the mesh is fixed while the material is deforming and act as a background grid. As a consequence, is a simpler approach if compared to the Lagrangian one but it requires the knowledge of the final geometry of the product in order to be applied.

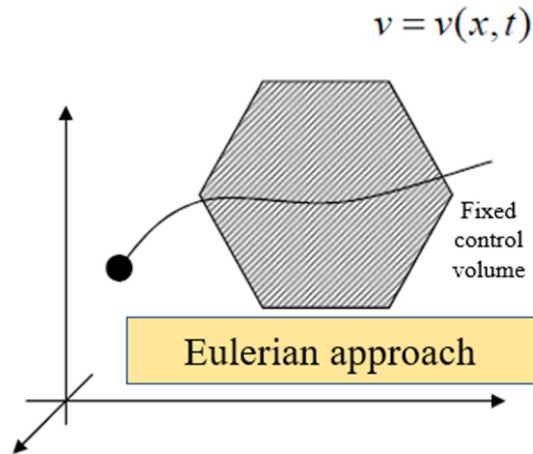


Figure 3.3: Eulerian approach: the elements of the mesh remain fixed (with respect to the fixed reference system) while they are crossed by the flow of material in deformation.

- Arbitrary-Lagrangian-Eulerian approach (ALE): using this combined approach, the computational mesh inside the domains moves arbitrarily in order to optimize the elements shape, while the mesh on the boundaries and interfaces of the domains can move along with materials to precisely track the boundaries and interfaces of a multi-material system. It represents a suitable choice for the simulation of the manufacturing process because it requires less computational time if compared to the pure Lagrangian approach.

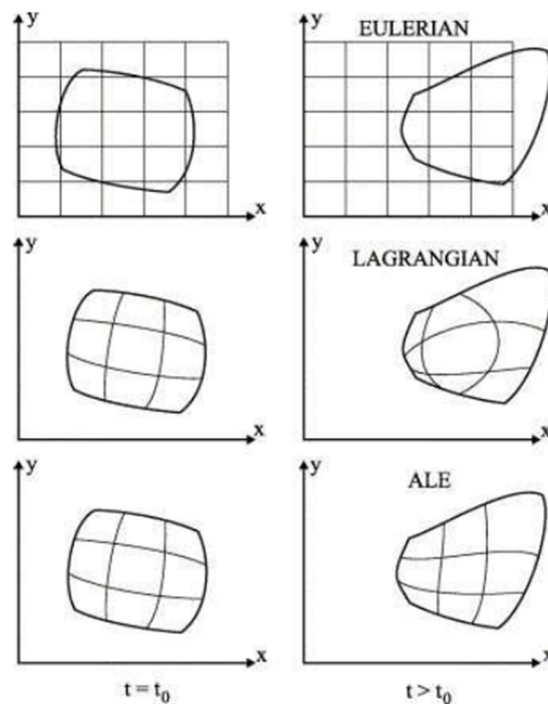


Figure 3.4: Schematization of the Eulerian, Lagrangian and Lagrangian-Eulerian (ALE) approach [1].

3.3 Qform UK® software

Qform UK is one of the commercial codes capable of simulating plastic deformation processes, such as forging and rolling. In particular, the Qform Extrusion tool is optimized to simulate the extrusion process [8, 9]. The program is able to perform coupled simulations between the material flow and the die (thermal and mechanical problems).

The software adopts two types of approaches in order to simulate the extrusion processes: the Lagrangian and the Arbitrary-Lagrangian-Eulerian. As mentioned earlier, if the user chooses to simulate the process with a pure Lagrangian approach, it will be possible to simulate all the various phases of the process (including the die filling) at the expense of a high computational time. If, on the other hand, an ALE approach is chosen, the billet and the outgoing profile will be simulated with a mesh that deforms according to the material flow, while the material inside the die (because of the constant flow volume) is simulated considering an Eulerian approach, where the mesh is fixed and material velocities and stresses are calculated in the fixed nodes of the domains. In this way, it is possible to save computational time for the simulation.

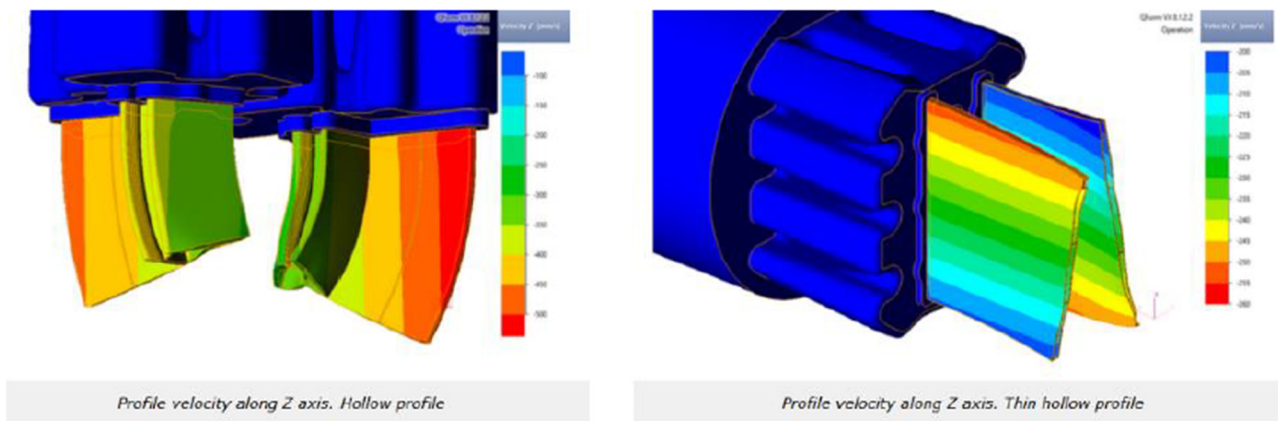


Figure 3.5: Qform extrusion: example of the simulation results.

Over the last 10 years, the code has released some updates which have made it more precise in modeling (for example in friction, heat exchange, flow stress setups) and have made it increasingly versatile and full of options to obtain a large number of information, both on the material under deformation and the tools.

3.3.1 Numerical Modeling of the Extrusion Process using Qform Extrusion

In this work, the ALE simulation of the extrusion process is analysed. By selecting “Extrusion” in the “Operation type” listed in Qform (Fig. 3.6), the user chooses to perform the ALE simulation which automatically involves the calculation of the viscous-plastic deformation of the material, the thermal

problem, the heat transfer to the workpiece with tool and environment, the heat conductivity and the heat generation as a result of deformation and friction.

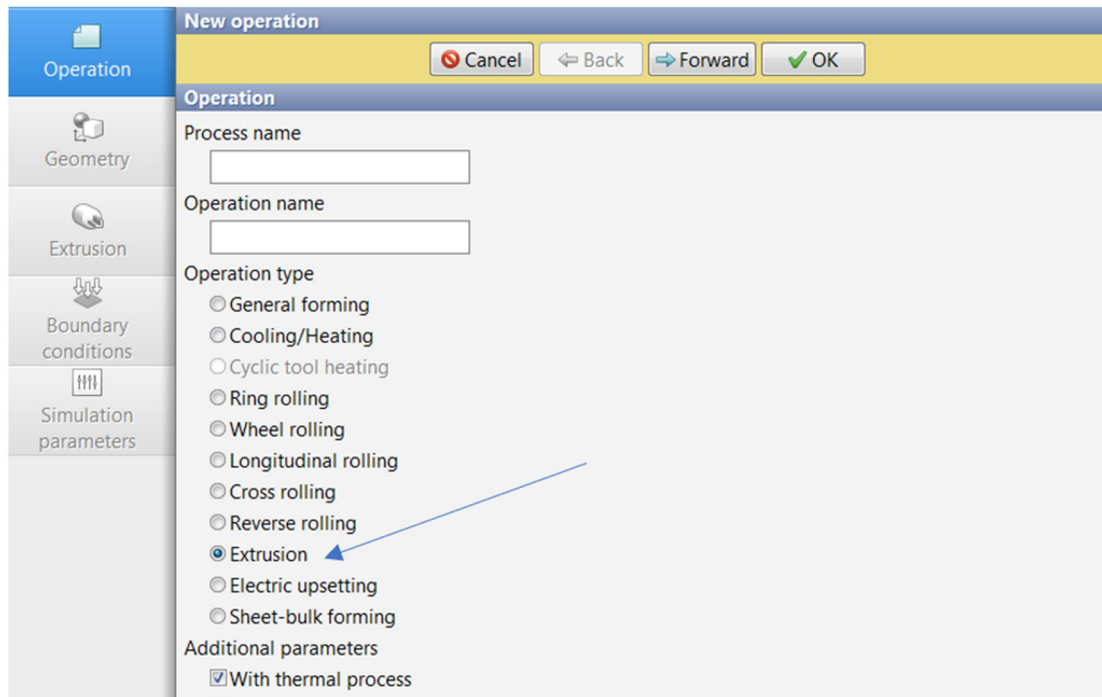
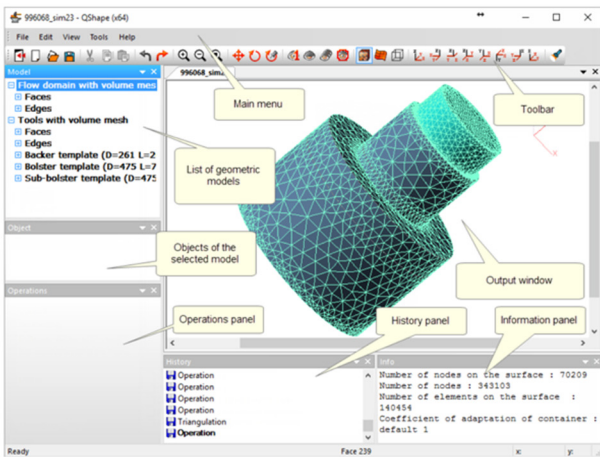


Figure 3.6: Operations in Qform.

The second step of the modeling is the meshing phase. In order to simulate the extrusion process, it is required to merge die plate, mandrel and backer into a single body. Once the CAD geometry is ready, it has to be imported into the Qform meshing tool called Qshape. This software is capable of generating and optimizing the mesh of the tool in order to perform the simulation of the extrusion process achieving the required level of accuracy. If a great precision is needed, the mesh should be finer, if the user needs to perform quick simulations saving computational time, it should be made with bigger finite elements. In any case, the structure of the mesh is always constant and consists of tetrahedral elements in all the parts but the exit profile, where the elements are prismatic.



Main menu	Contains menu options with the list of commands
Toolbar	Icons of the Windows standard object control commands, etc.
List of geometric models and objects (Model window)	List of all geometrical models, edges and faces describing these models, etc
Geometrical object display window (Output window)	Used for visualization of geometrical models and objects.
Structure of selected object (Object window)	List of all edges or faces referred respectively to the selected face or edge as well as (in case the mesh has some defects). The list of bad elements and open chains of edges are also displayed here.
Operations field	Here commands applicable to a given object should appear depending on the type of a selected object.
History of operations	List of all operations performed in the process of the geometry setup.
Information	Detailed information about selected model in Model window.

Figure 3.7: Qshape interface.

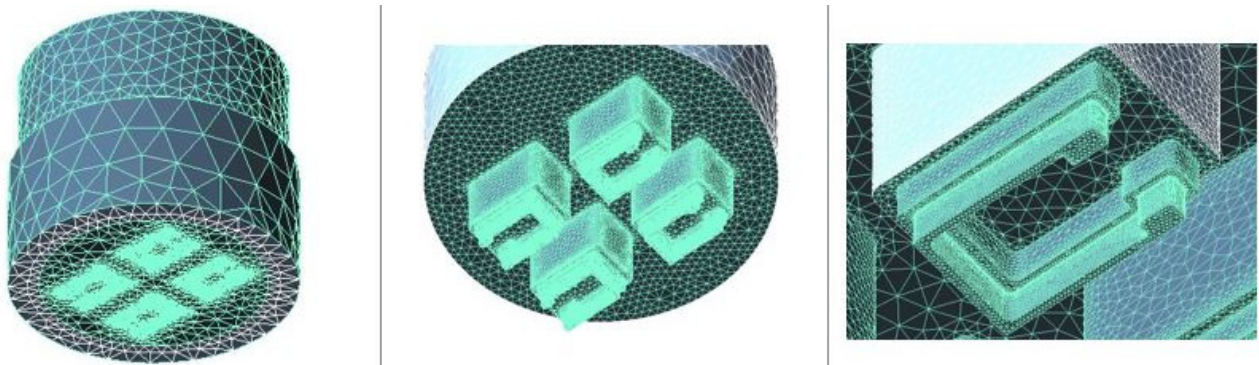


Figure 3.8: Example of meshing with Qshape.

During the meshing step, the tool allows the parametrization of the bearings lengths, with allows the user to easily modify these parameters to get the required balance in the profile exit speed. Moreover, it is also possible to insert choke/relief angles.

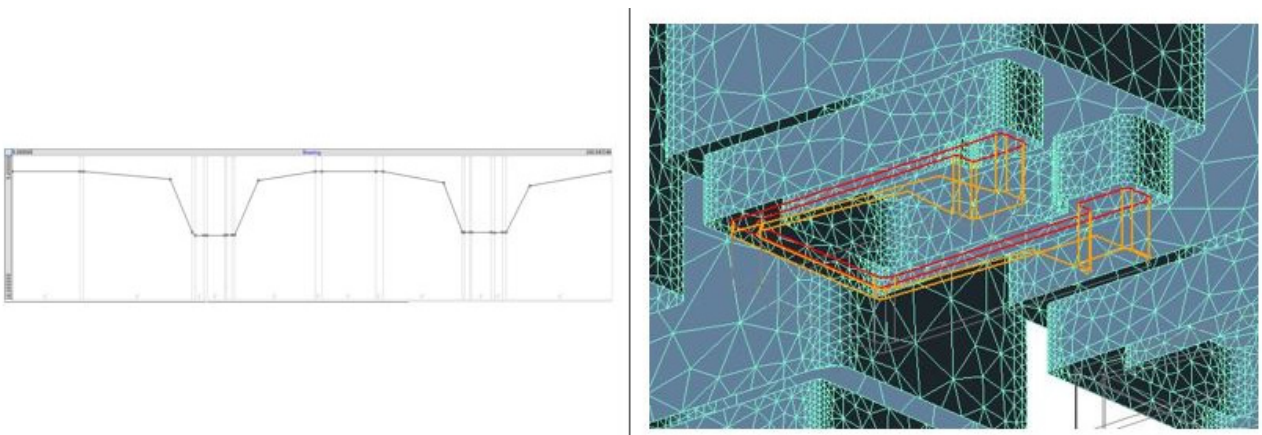


Figure 3.9: Bearings parametrization with Qshape.

It is important to specify that the meshing phase is done automatically by Qshape software, with element size generated according to geometrical gradients of the components (for high gradients, the

dimensions of the elements are reduced and consequently their number increases) and without the possibility to arbitrary modify the mesh properties in selected zones. However, it is possible to adjust specific parameters (adjustable rates of meshing) during the mesh preparation which allows the generation of a finer or bigger mesh in pre-selected regions (bearings, welding chamber, etc.).

Once the mesh is prepared, it can be imported into the project and the modeling of the extrusion process begins.

As shown in Fig. 3.10, several input variables need to be defined.

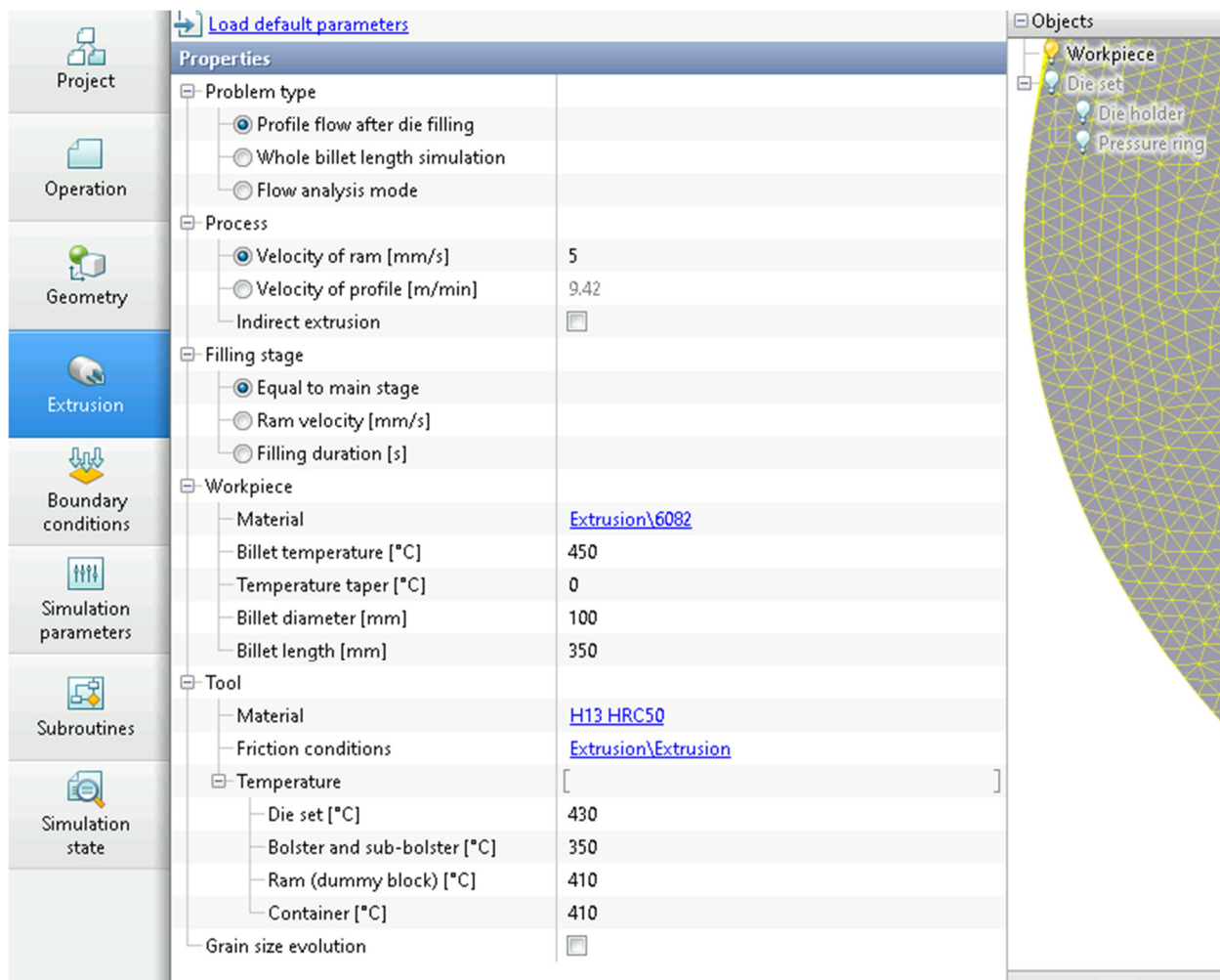


Figure 3.10: Extrusion process parameters in Qform extrusion.

- Problem type: different types of problems are available. The first is called “Profile flow after die filling” and refers to the stage where the die is already filled with the workpiece material. It can be used for the prediction of the material flow at the velocity steady-state stage of the process. The second is called “whole billet length simulation”, it calculates from the start of the ram stroke and is generally used to evaluate the extrusion load graph

and optimize the temperature-velocity mode. The last one called “Flow analysis mode” allows the animation of the material flow through the tool cavities.

- **Process:** in this section the user defines the velocity of the ram or the profile to be used in the simulation. If “Velocity of ram” is selected, the program will automatically determine the exit speed of the profile based on the extrusion ratio and vice versa. There is also the option to simulate the indirect extrusion by adding the container velocity.
- **Filling stage:** in this section the user defines the type of filling of the die that the program must simulate. “Equal to main stage” means that the ram velocity does not change between before and after the die is completely filled. “Ram velocity” allows the user to define a different ram speed for the die filling stage. “Filling duration” should be selected if the filling time is known in advance.
- **Workpiece:** in the current section the workpiece properties must be defined. The user can choose to use one of the material models already present in the database or create a new material with customized properties such as flow stress law (formula, table function, constant value), density, thermal conductivity, specific heat, Young module, Poisson coefficient, Thermal expansion and also additional properties as damage or recrystallization models (Fig. 3.11). After this step, the user must define the billet temperature, diameter and length and the taper parameters (if present). The taper is a temperature gradient between the front and the back of the billet often used in the industrial practice to avoid an excessive increase in the exit temperature of the profile in the last part of the extrusion ram stroke and, consequently, achieve a stability in the exit temperature of the profile.

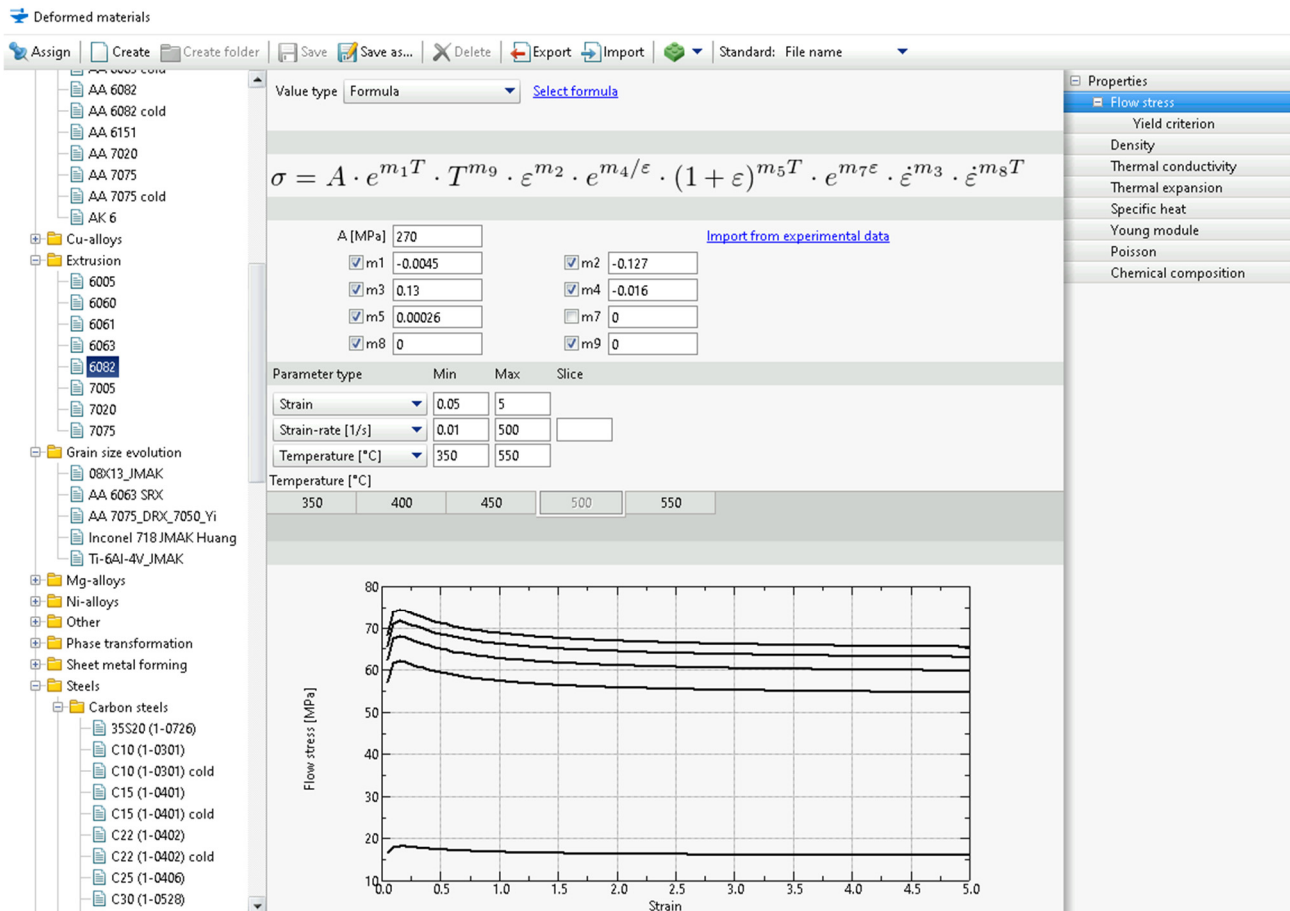


Figure 3.11: Material parameters.

- Tool: in this current section the user selects the tool material and temperatures with the same modulus operandi seen in “Workpiece”. Moreover, the user select the fiction conditions from the standard database: the user may select between Siebel, Levanov, Coulomb or Hybrid friction laws.

The Coulomb friction law is modelled as follows:

$$\tau = \mu \cdot \sigma_n \quad 3.2$$

where τ is the shear stress, μ the friction coefficient ($0 < \mu < \frac{1}{\sqrt{3}}$) and σ_n is the normal contact pressure. This model should be used if the friction condition depends only on the contact pressure between two bodies and, consequently, when the pressures are low. It is used mainly in processes when there is no plastic deformation.

The Siebel friction law is modelled as follows:

$$\tau = m \cdot \frac{\sigma_{eq}}{\sqrt{3}} \quad 3.3$$

where m is the friction factor ($0 < m < 1$) and σ_{eq} is flow stress of the material. This model describes the case in which, considering a strong level of pressures acting between two materials, the sliding occurs by plastic deformation and not by splitting of the weld areas created between the extremities in contact with the two bodies. For this reason, this modeling is preferred to the Coulomb one for the simulation of plastic deformation processes.

The Levanov friction law combines the Coulomb and the Siebel approaches and is modelled as follows:

$$\tau = m \cdot \frac{\sigma_{eq}}{\sqrt{3}} \cdot (1 - e^{-n \cdot \frac{\sigma_n}{\sigma_{eq}}}) \quad 3.4$$

where n is the Levanov coefficient ($0 < n < 1,25$). Using this model the friction law is accurate both for high and low values of pressure between two bodies. The difference in the trends of Coulomb, Siebel and Levanov laws is reported in Fig. 3.12.

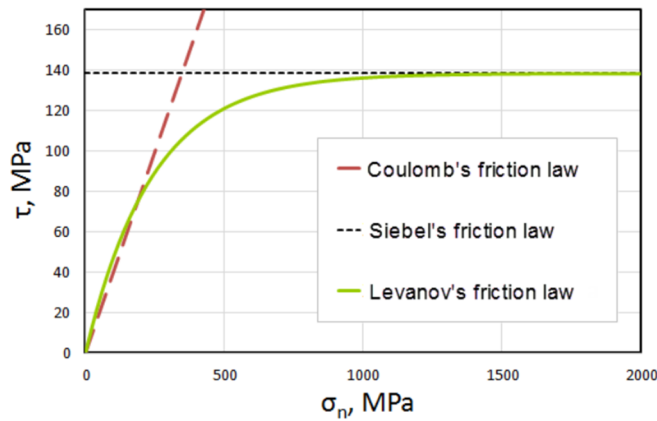


Figure 3.12: Shear stresses versus normal contact pressure according to Siebel and Levanov friction laws ($m=0.8$, $\sigma_s=300$ MPa, $n=1.25$), and Coulomb law ($\mu=0.4$).

It is also possible to use a Hybrid friction law which is a generalization of the Coulomb and Siebel. Coulomb law is used until a specific pressure is not exceeded, after that Siebel law occurs.

$$\tau = \left\{ \begin{array}{ll} \mu \cdot \sigma_n & (\mu \cdot \sigma_n < m \cdot \frac{\sigma_{eq}}{\sqrt{3}}) \\ m \cdot \frac{\sigma_{eq}}{\sqrt{3}} & (\mu \cdot \sigma_n > m \cdot \frac{\sigma_{eq}}{\sqrt{3}}) \end{array} \right\} \quad 3.5$$

After setting all the extrusion parameters, the boundary conditions must be defined. Although the temperatures of the tools are defined in the Extrusion tab, the user can introduce the temperature and heat transfer of die holder, pressure ring and define the heat transfer with the environment. There are also other settings that may be introduced such as boundary conditions of load, velocity, pressure, heat transfer, rotation or pusher on the workpiece setup and also the possibility to add sprayer group.

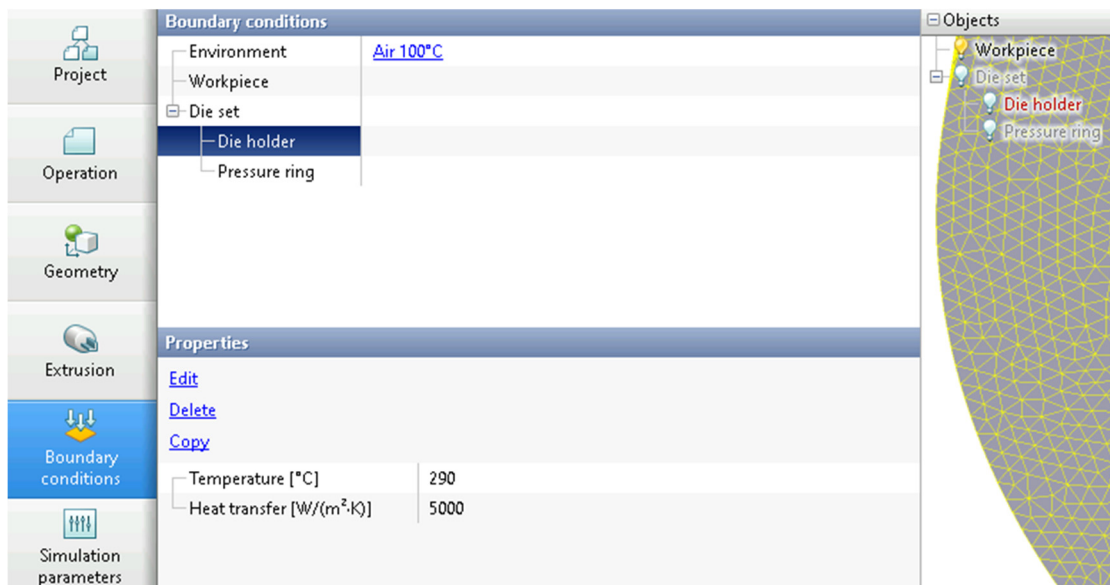


Figure 3.13: Boundary conditions.

After the definition of the boundary condition, the user needs to set up the simulation parameters. In this section, the user is able to customize the simulation stop conditions by defining the records count, activating the steady-state criterion and defining a limit value for its application. Moreover, it is possible to define:

- the accuracy of the thermal problem solving;
- the convergence parameters which are the velocity norm, the stress norm and the maximum number of iterations;
- the mesh adaptation factor and acceleration coefficient which affect the number of finite elements in volume of the workpiece (by increasing the adaptation factor, the elements are proportionally increased);
- the weight consideration option;

- the coupled tools simulation which allows the combined simulation between deflection of the die and deformation of the workpiece;
- the direct recalculation of the nodal loads option which may increase the accuracy in the “whole billet length simulation”;
- the iteration parameters of the tool for the simulation of the elastic problem (it should be mentioned that the software calculates the tools only by solving the elastic problem).

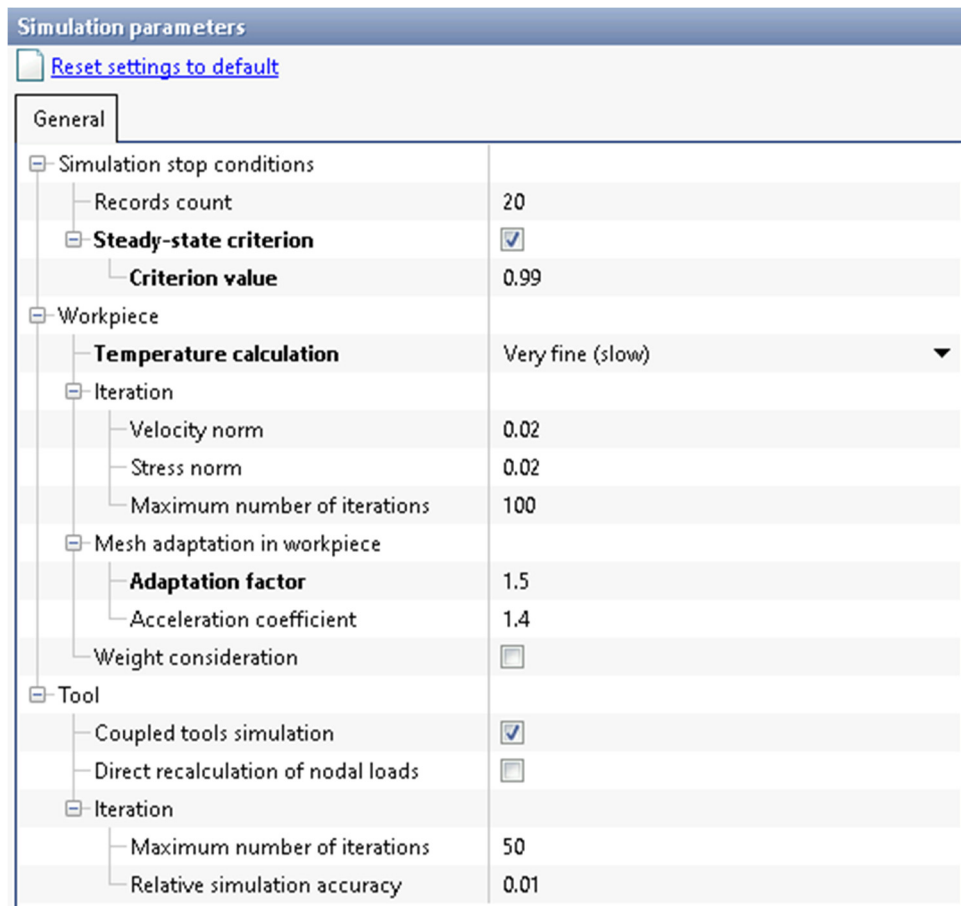


Figure 3.14: Simulation parameters.

3.3.2 Post-Process Analysis through the Use of Sub-Routines

A useful feature of Qform software is the capability of developing subroutines, which are models to calculate user-defined quantities and variables otherwise not considered in the program. There are two types of subroutines:

- processing subroutines which are run during the main simulation;
- post-processing subroutines which are run after the main simulation.

There are some standard subroutines already developed by the Qform research group which calculate some parameters specific to each investigated process. In the extrusion case, the standard subroutines are reported in Fig. 3.15.

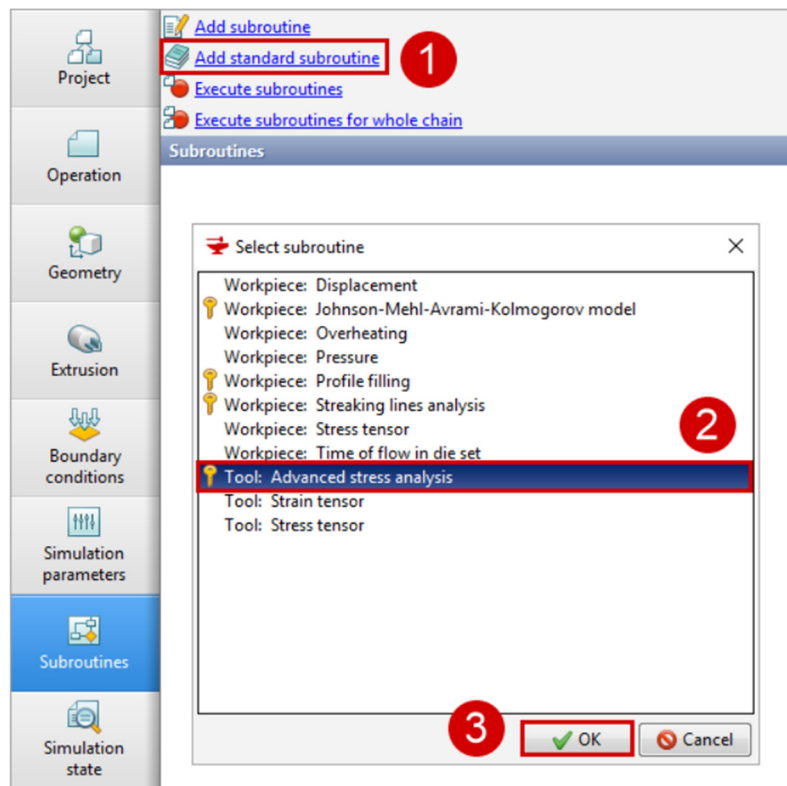


Figure 3.15: Standard subroutines.

The only requirement for implementing a user-defined subroutine in QForm is that it must be written in the Lua programming language. Lua is a very simple and extremely flexible programming and scripting code, created by the programmer Roberto Ierusalimschy in 1993. Lua is normally used to extend run-time applications. It is widely used in the PSP (PlayStation Portable) environment and many game and 3D graphics programs.

The user has the ability to recall and use fields already calculated by the code during the main simulation of the process both referring to workpiece and tools and using them as new inputs (Fig. 3.16).

Post-processing subroutines can correctly interact with the software following the reported steps:

- indicate the object of the simulation: workpiece (*set_target_workpiece ()*), profile (*set_extrusion_trace ()*) and tools (*set_target_tool ()*);
- specify user-defined fields by the function *result ()*;
- specify additional input parameters by the function *parameters ()*;

- create functions in which user-defined fields are computed *UserFields ()*.

As an example, a user-subroutine that calculates the heating/cooling rate of a forged part during the deformation is reported in Fig. 3.18 while another user-subroutine that calculates the maximum strain rate reached during the material flow from the billet to the extruded profile is reported in Fig. 19.

Variable	Name in QForm interface 10	Description	Unit of meas. in Lua
Available in subroutines			
t	Time	Time at current point location along the trace	sec
dt	Step	Time step between current and previous point locations along the trace	sec
T	Temperature	Temperature	°C
stress_mean	Mean Stress	Mean Stress	Pa
stress_flow	Effective stress	Flowstress (Mises criterion)	Pa
strain	Plastic strain	Strain intensity	—
strain_rate	Strain rate	Strain rate intensity	1/sec
x, y, z	—	Coordinates of the FE node	m
disp_x, disp_y, disp_z	Displacement	Elastic displacements	m
v_x, v_y, v_z	Velocity	Velocity components of FE node	m/s
node_id	—	Number of FE node	—
bearing_z	—	zentry level of bearings	m
stream_id	Material streams	Indication of each stream	—
stream_border	Material streams borders	Welding seam indicator	—
trace_id	—	Unique trace identifier. Equal to trace number in interface	—
extr_pressure	Contact pressure	Contact pressure	Pa
stress_xx, stress_yy, stress_zz, stress_xy, stress_yz, stress_xz	Stress tensor	Stress tensor components	Pa
stress_1, stress_2, stress_3	Principal stresses	Principal stresses	Pa
Available in postprocessor subroutines for workpiece target only			
strain_xx, strain_yy, strain_zz, strain_xy, strain_yz, strain_xz	Strain tensor	Strain tensor components	Pa
strain_1, strain_2, strain_3	Principal strain	Principal strain	—
normal_x, normal_y, normal_z	—	Components of a unit normal vector for a surface node	—

Figure 3.16: Variables table for Lua subroutines.

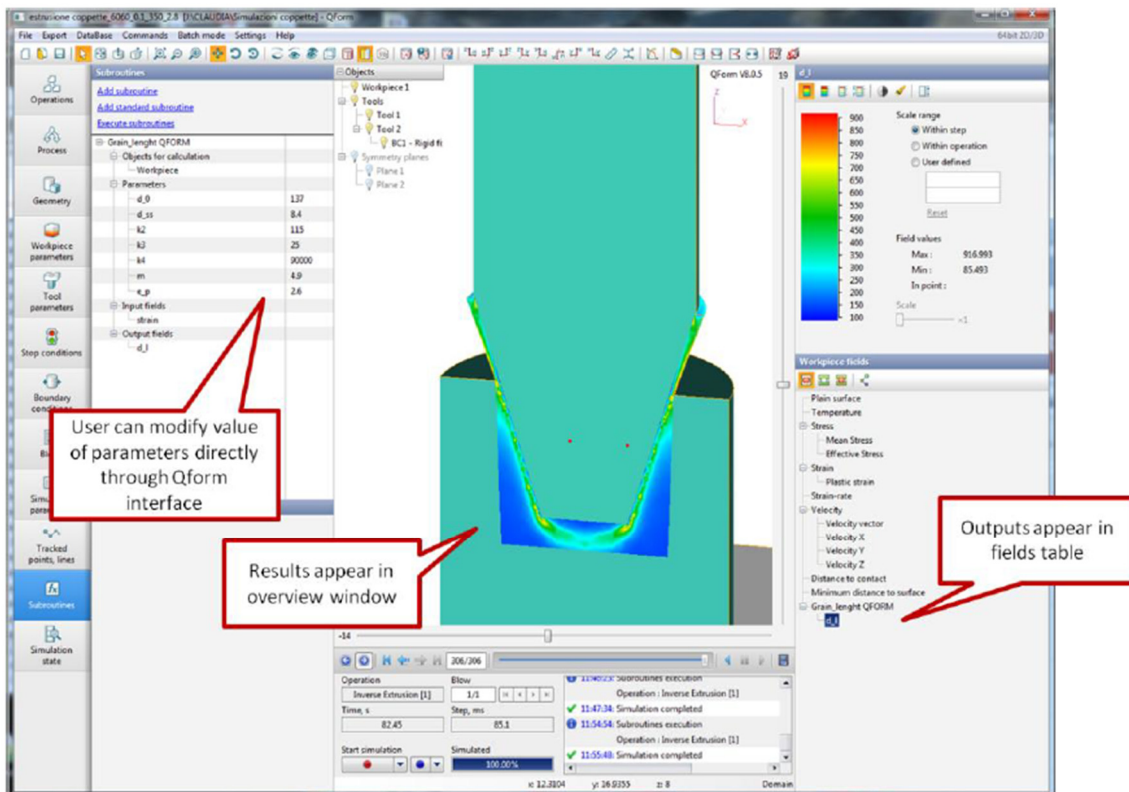


Figure 3.17: Visualization of the subroutines results.

```

1  set_target_extrusion_trace()
2  scale = parameter("scale", 1)
3  rate_of_T = result("rate_of_T", 0)
4  function UserFields(T, prev_T, dt)
5    local rT = scale*(T - prev_T)/dt
6    store(rate_of_T, rT)
7  end

```

Figure 3.18: Example of a user-subroutine for the computation of the heating/cooling rate of a forged part during the deformation.

```

set_target_extrusion_trace()

MAX_StrainRate = result("MAX_StrainRate")

function fact(m)
  if m==0 then
    return 1
  else
    return m*fact(m-1)
  end
end

function UserFields (strain_rate, prev_MAX_StrainRate, t, T)

  T = T + 273.15

  if t > 1e-10 then
    if strain_rate > S_max then
      S_max = strain_rate
    else
      S_max = prev_MAX_StrainRate
    end
  else
    S_max = -1e30
  end

  b = S_max
  store (MAX_StrainRate, S_max)
end

```

Figure 3.19: Example of a user-subroutine that calculates the maximum strain rate reached during the material flow from the billet to the extruded profile.

3.4 Validation of the FEM code in the extrusion of aluminum alloys

The Qform code has been extensively tested in order to validate the results of the extrusion simulation in the work of Bandini C. [10]. In this work, viscoplasticity experimental tests were conducted at the "Institute of Forming Technology and Lightweight Construction" of the University of Dortmund (Germany) with the aim of obtaining data on the flow trend of the AA6060 alloy in the extrusion processes and determining the optimized settings that foresee the experimental conditions and use them to validate the QForm software. Moreover, several extrusions were performed in a temperature-controlled condition. Thermocouples were used to acquire data on the thermal evolution

in the die/container/ram and the profile exit temperature was also acquired. These data were then used to validate the code in the evaluation of the heat exchanges and temperatures reached during the process.

References

- [1] J. Hu'etink (1986) On the simulation of thermomechanical forming processes. PhD thesis, University of Twente.
- [2] T.J.R. Hughes, W.K. Liu, T.K. Zimmermann (1981) Lagrangian-Eulerian finite element formulation for incompressible viscous flows, *Computer Methods in Applied Mechanics and Engineering* 29(3): 329-349.
- [3] P.M. Muessig (2008) Thermal-efficient products through computer simulation software, In *Proceedings of the ninth international aluminium extrusion technology seminar*.
- [4] G. Fang, J. Zhou, J. Duszczuk (2009) FEM simulation of aluminium extrusion through two-hole multi-step pocket dies, *Journal of Materials Processing Technology* 209(4): 1891-1900.
- [5] J. Proudian (2012) *Simulating Residual Stress in Machining, from Post Process Measurement to Pre-Process Predictions* (Doctoral dissertation, KTH Royal Institute of Technology).
- [6] J. Donea, S. Giuliani, J.P. Halleux (1982) An arbitrary lagrangian-eulerian finite element method for transient dynamic fluid-structure interactions, *Computer Methods in Applied Mechanics and Engineering* 33(1-3): 689, 1982.
- [7] F. Klocke, T. Beck, S. Hoppe, T. Krieg, N. Müller, T. Nöthe, H.W. Raedt, K. Sweeney (2002) Examples of FEM application in manufacturing technology, *Journal of Materials Processing Technology* 120(1-3): 450-457.
- [8] A. Biba, A. Lishnij, A.Vlasov (1998) Simulation of coupled problem of electric upsetting, *Journal of Materials Processing Technology* 80: 184-187.
- [9] S. Stebunov, A. Lishnij, N. Biba, S. Bellotti, P. Fazzinni (2009) Development and industrial verification of QForm-Extrusion program simulation profile extrusion, *Proceeding of International Conference on Extrusion and Benchmark, Dortmund*.
- [10] C. Bandini (2017) *Previsione dell'evoluzione della microstruttura in processi industriali di estrusione delle leghe di alluminio serie AA6XXX*. PhD thesis, University of Bologna.

4. Modeling of the Recrystallization Behaviour of AA6063 Aluminum Alloy Extruded Profiles

The control over the microstructure during the aluminum alloy extrusion is of primary importance if mechanical, crash, corrosion and aesthetic properties need to be guaranteed. To date, the relation between extrusion parameters and grain structure evolution is not fully understood due to the high number of factors that affects the final microstructure of the profile. For this reason, the scientific community is pooling its efforts to investigate the laws that regulate the recrystallization of aluminum profiles during the extrusion process and, consequently, to develop reliable models for the prediction of the profile microstructure.

In the last decades, different studies have been carried out to validate the modeling of the recrystallization behaviour in the extrusion of aluminum alloy by means of FEM codes comparing the results of the simulations to the experimental trials. However, none of these works proposed a combined DRX/SRX simulation of the evolution of grain size after the extrusion and of the profile recrystallization thickness after the static recrystallization. In addition to that, the proposed models were not extensively tested on industrial-scale or complex geometry profiles, thus limiting the strain and strain rate fields for the modeling validation.

In this work, the experimental campaign involved the extrusion of three different AA6063 profiles. The first solid profile was extruded with different billet temperatures and ram speeds in order to have a reliable amount of data for the model calibration, the other two industrial-scale profiles, one solid and one hollow, were used for the model validation. The numerical simulations involving Finite Element (FE) analysis of the three experimental extrusions were performed with the commercial Qform Extrusion® code. An innovative recrystallization model was developed and optimized by comparing the results of DRX/SRX simulations with the microstructural data experimentally acquired. The final aim of this work reported in this chapter was to propose, optimize and validate a reliable recrystallization model for the prediction of the microstructural behaviour in the hot extrusion of AA6063 aluminum alloy profiles.

4.1 Experimental Investigation

The AA6063 profile was extruded by Hydro plant in Finspång (Sweden) with a 10 MN extrusion press. In Fig. 4.1, the geometries of profile and die are shown. In Table 4.1, the extrusion process and the tool geometry parameters of the two profiles are reported.

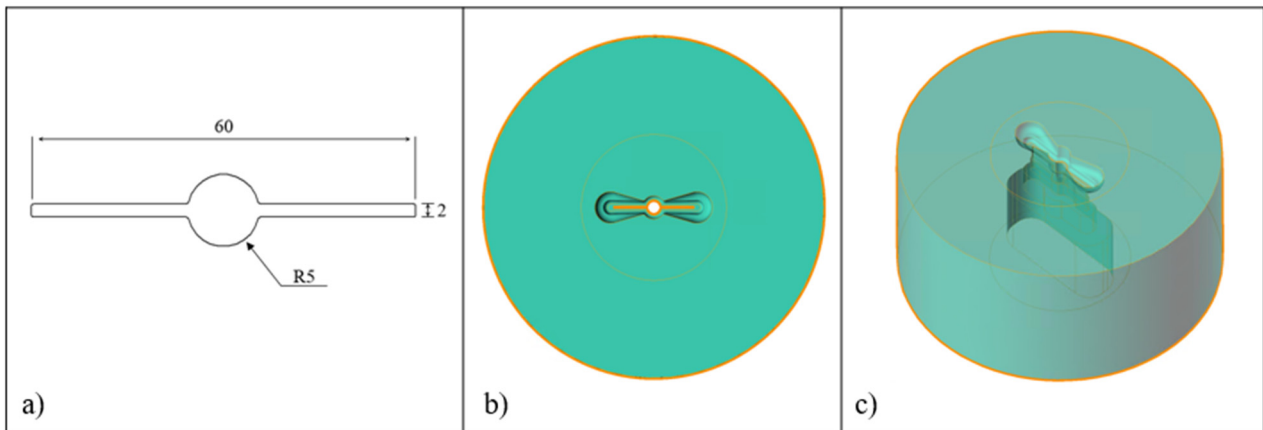


Figure 4.1: Investigated profiles and die geometries. a) profile geometry; b,c) die geometry (from CAD)

Table 4.1: Process parameters and geometry tolerances

Process parameters and geometry tolerances	Profile <i>Hydro</i>
Aluminum alloy	AA6063
Extrusion ratio	46
Ram speed [mm/s]	1.1 / 2.1 / 9.2 / 10.4
Container temperature [°C]	400
Billet temperature [°C]	420 / 490
Die temperature [°C]	400
Ram acceleration time [s]	5
Billet length [mm]	270
Billet diameter [mm]	100
Container diameter [mm]	107
Billet Rest length [mm]	15

The profile *Hydro* experimental campaign involved the extrusion of 20 billets: a combination of four ram speeds (1.1 mm/s, 2.1 mm/s, 9.2 mm/s and 10.4 mm/s) and two different billet temperatures (420 °C and 490 °C) were tested. After the extrusion, part of the profiles were water-quenched while the other part was not quenched. In order to collect data on the grain size of the profiles, samples were grinded, polished and then etched with electrolytical etching. For each profile, two different microstructures are shown, one taken from the beginning of each extruded length (“front” in Fig. 4.2) and one from the end (“back” in Fig. 4.2). Through the use of a pyrometer, the profile temperature trends at the exit of the extrusion die were recorded. The temperature was measured in the centre of the solid round part of the profile (this point is evidenced by the start of the blue arrows in Fig.

4.10b,d). These data were used to validate the numerical simulations. Fig. 4.2a,b represent the grain structures result from the extrusion made with a billet temperature of 420°C and a ram speed of 1,1 mm/s. Fig. 4.2c,d represent the grain structures result from the extrusion made with a billet temperature of 480°C and a ram speed of 2,1 mm/s. Fig. 4.2e,f represent the grain structures result from the extrusion made with a billet temperature of 480°C and a ram speed of 9.2 mm/s. Fig. 4.2g,h represent the grain structures result from the extrusion made with a billet temperature of 480°C and a ram speed of 10.4 mm/s. In Fig. 4.3a, the microstructure of the billet is reported, with an average grain size of 137 μm . As clearly visible from the images, Fig. 4.2a,b present a partially recrystallized microstructure, while all other cases present a fully recrystallized grain structure. Twenty points were chosen for measurement for each acquired microstructure: in each point, the grain size was measured according to the ASTM-E112 regulation, using the ImageJ software. Ten of these measurements were used as calibration data, in order to optimize the recrystallization model described in the Numerical Modeling section. The other ten measurements were used to check and validate the model accuracy by comparing the data with the results of the numerical prediction.

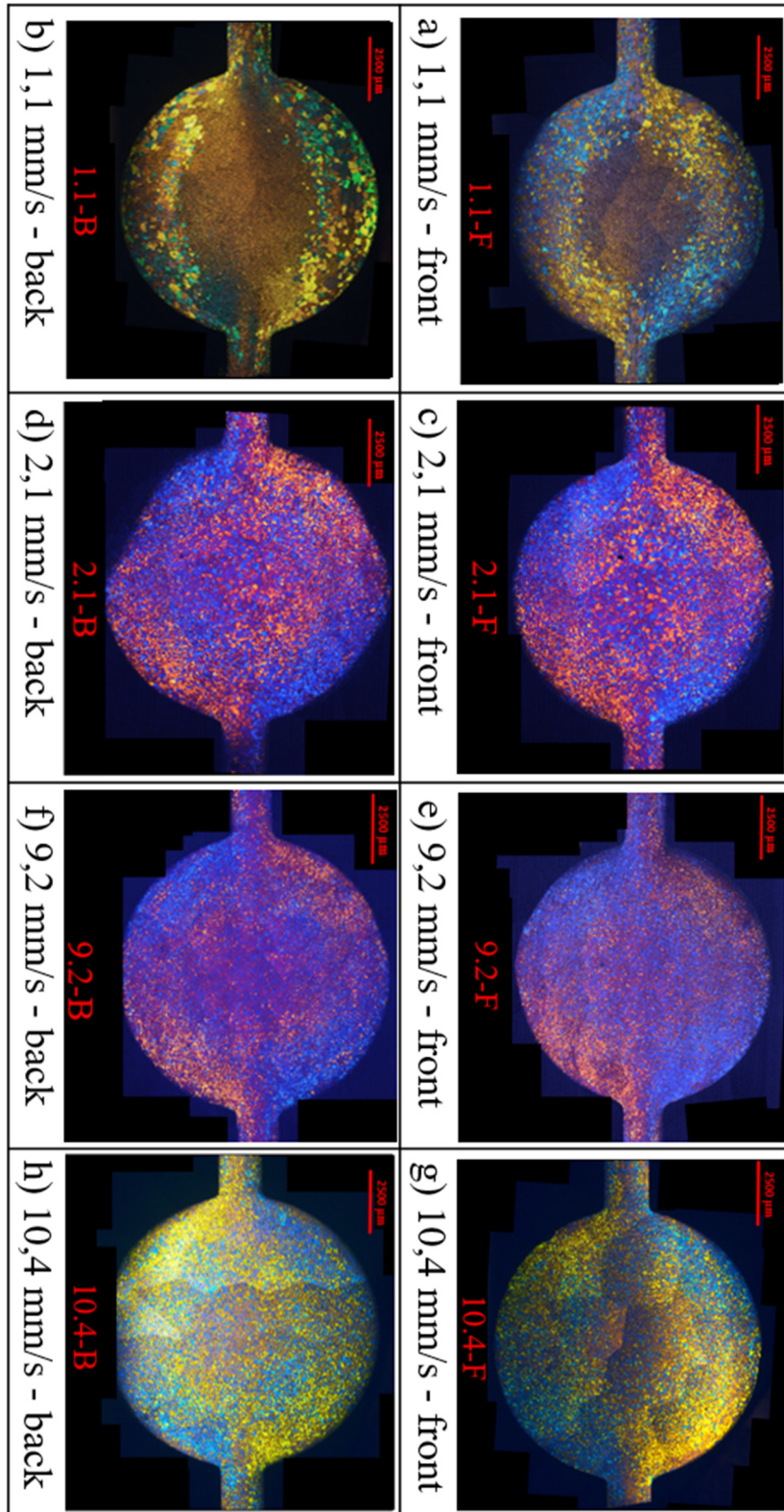


Figure 4.2: Microstructures of the *Hydro* extruded profiles

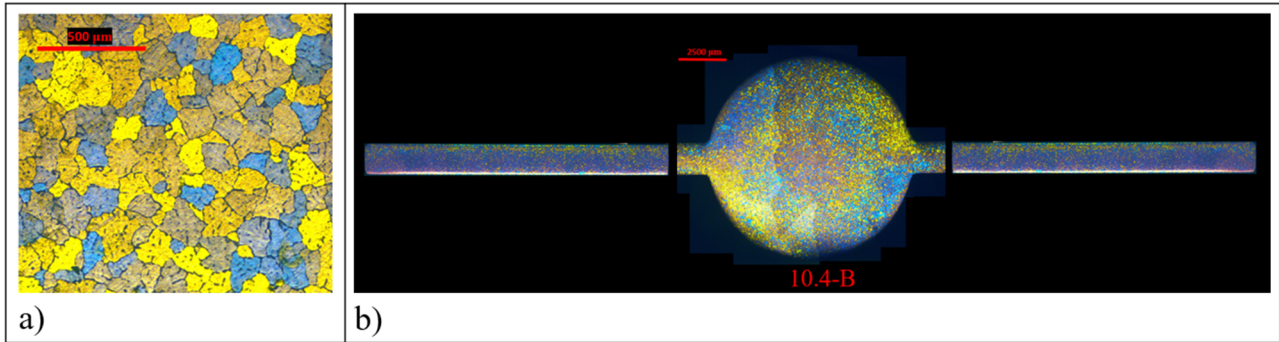


Figure 4.3: a) Microstructure of the billet, b) microstructure of the entire *Hydro* profile

In order to ensure the reliability of the model, the results of the recrystallization prediction were validated not only on the *Hydro* case, but also on two other industrial-size AA6063 profiles. The data of the grain size of profile *a* were taken from the work of Gamberoni A. et al. [1], while, for profile *b*, were experimentally acquired. The two extrusions reveal different characteristics in terms of temperatures, profile shapes, dimensions and extrusion ratios, thus producing a reliable amount of data for the numerical model validation. The extrusion parameters are reported in Table 4.2.

Table 4.2: Process parameters and geometry tolerances of Profile *a* and Profile *b*

Process parameters and geometry tolerances	Profile <i>a</i>	Profile <i>b</i>
Aluminum alloy	AA6063	AA6063
Extrusion ratio	9.6	44
Ram speed [mm/s]	8.5	6.44
Container temperature [°C]	420	430
Billet temperature [°C]	470	530
Die temperature [°C]	450	450
Ram acceleration time [s]	5	5
Billet length [mm]	815	670
Billet diameter [mm]	247	254
Container diameter [mm]	257	264
Billet Rest length [mm]	55	15

In Fig. 4.4, the geometries of the investigated profiles are reported together with the CAD image of the dies.

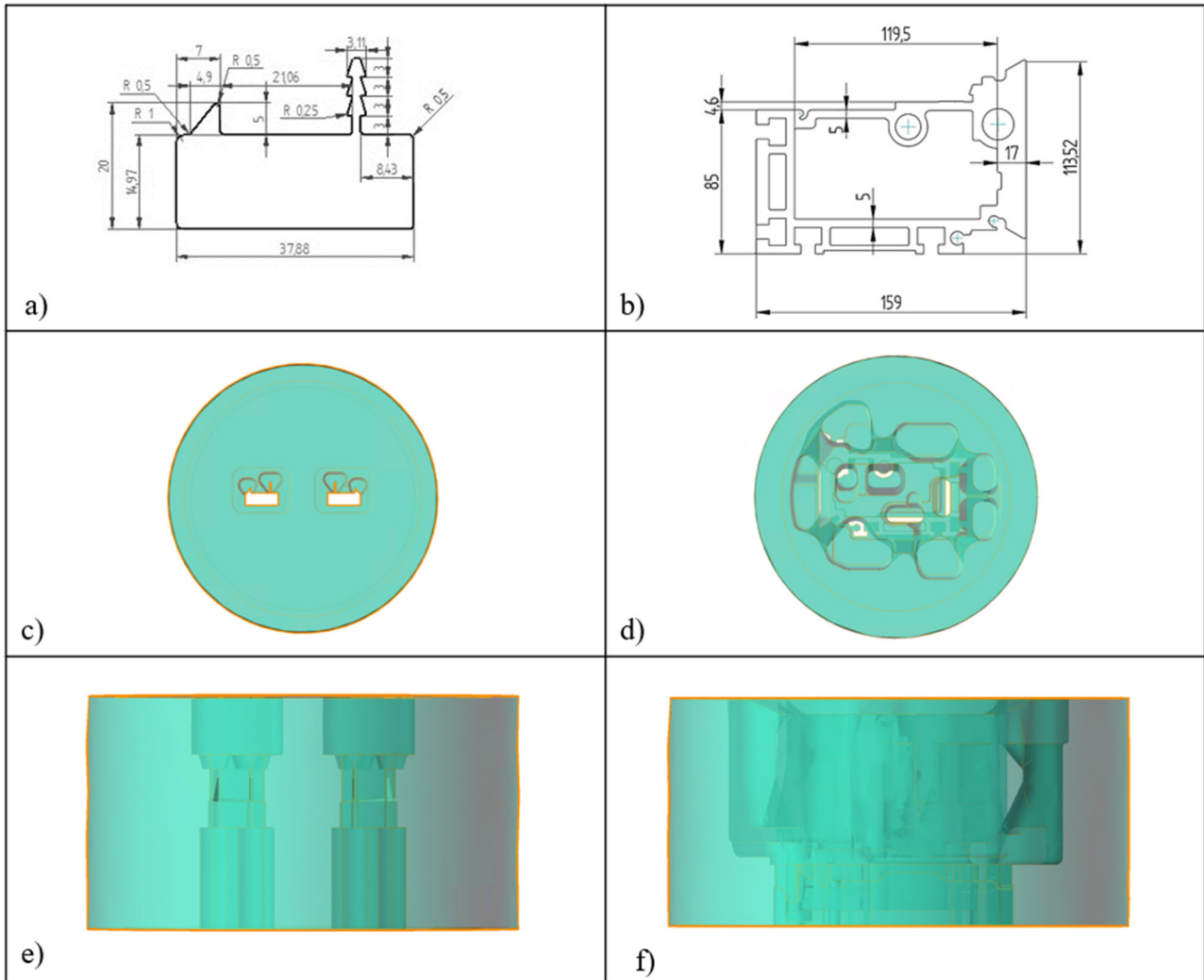


Figure 4.4: Investigated profiles and die geometries: a) profile a, b) profile b, c) top view of profile a, d) top view of profile b, e) side view of die for profile a, f) side view of die for profile b.

The microstructure of profile *a* is shown in detail in Fig. 4.5: the image was acquired by using polarized light microscopy of electrolytical etched samples. Each measurement of the average grain dimension was carried out according to the ASTM-E112 regulation. The analysed samples were taken at the middle length of the extrusion profile once the process has achieved the thermal steady-state condition. As for profile *a*, a merge of the different micrographs is reported, revealing a completely recrystallized microstructure, within a minimum grain dimension of 55 μm (top-right part of Fig. 4.5c). The maximum grain dimension (around 500 μm) is detectable where the profile shows PCG, as revealed in Fig. 4.5e, and AGG (Abnormal Grain Growth) structures, localized in the seam welds (Fig. 1b). This structure is characterized by coarse grains with respect to the dimension of the surrounding grains which may reduce crash, mechanical, corrosion and fracture properties.

The microstructure of profile *b* is shown in detail in Fig. 4.6a-e. The figure clearly shows a completely recrystallized structure, within an average dimension range from 40 μm to 170 μm .

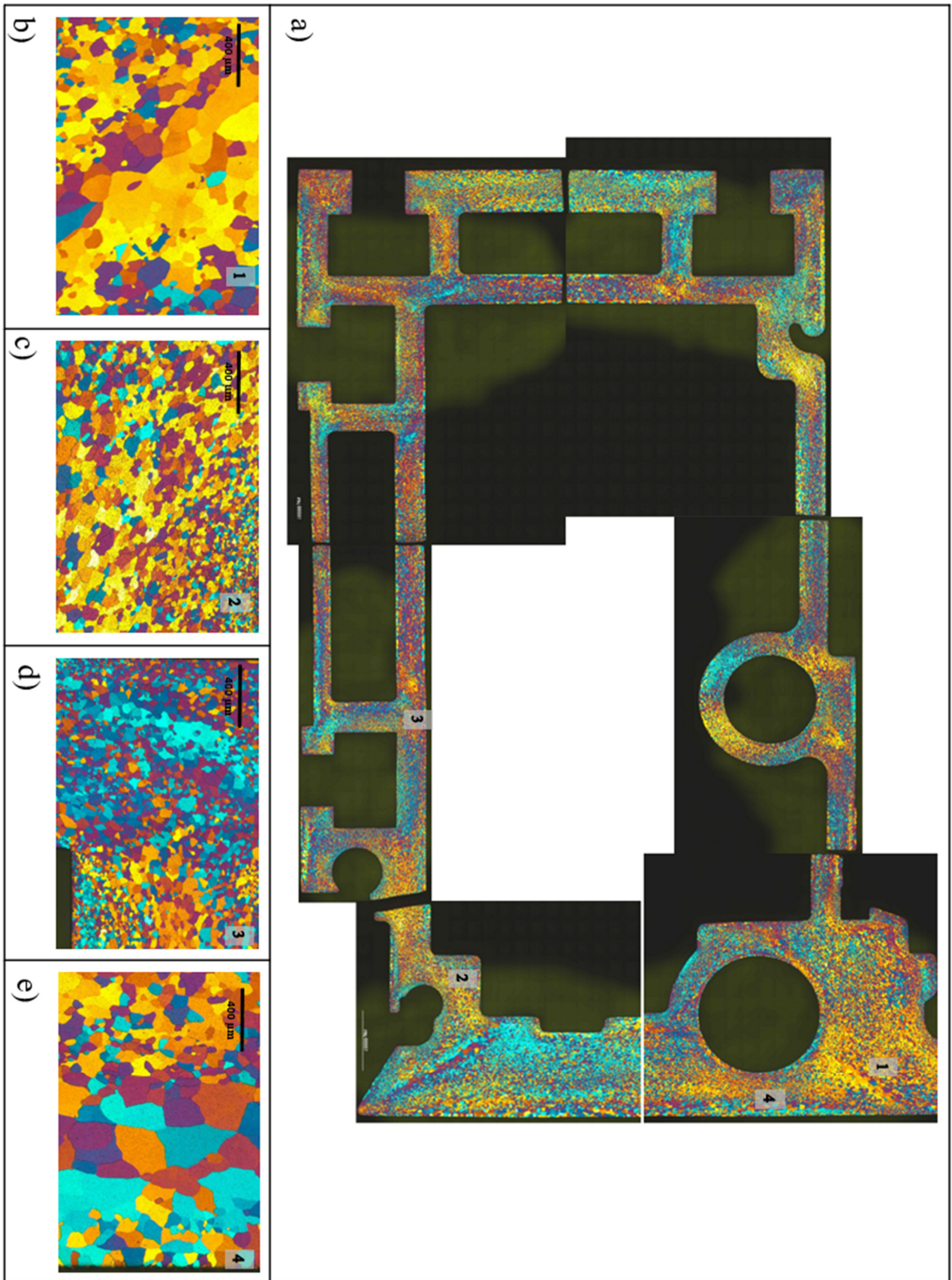


Figure 4.5: Microstructure of profile *a*: a) overview of the microstructure of the entire profile, b) focus on zone 1, c) focus on zone 2, d) focus on zone 3, e) focus on zone 4.

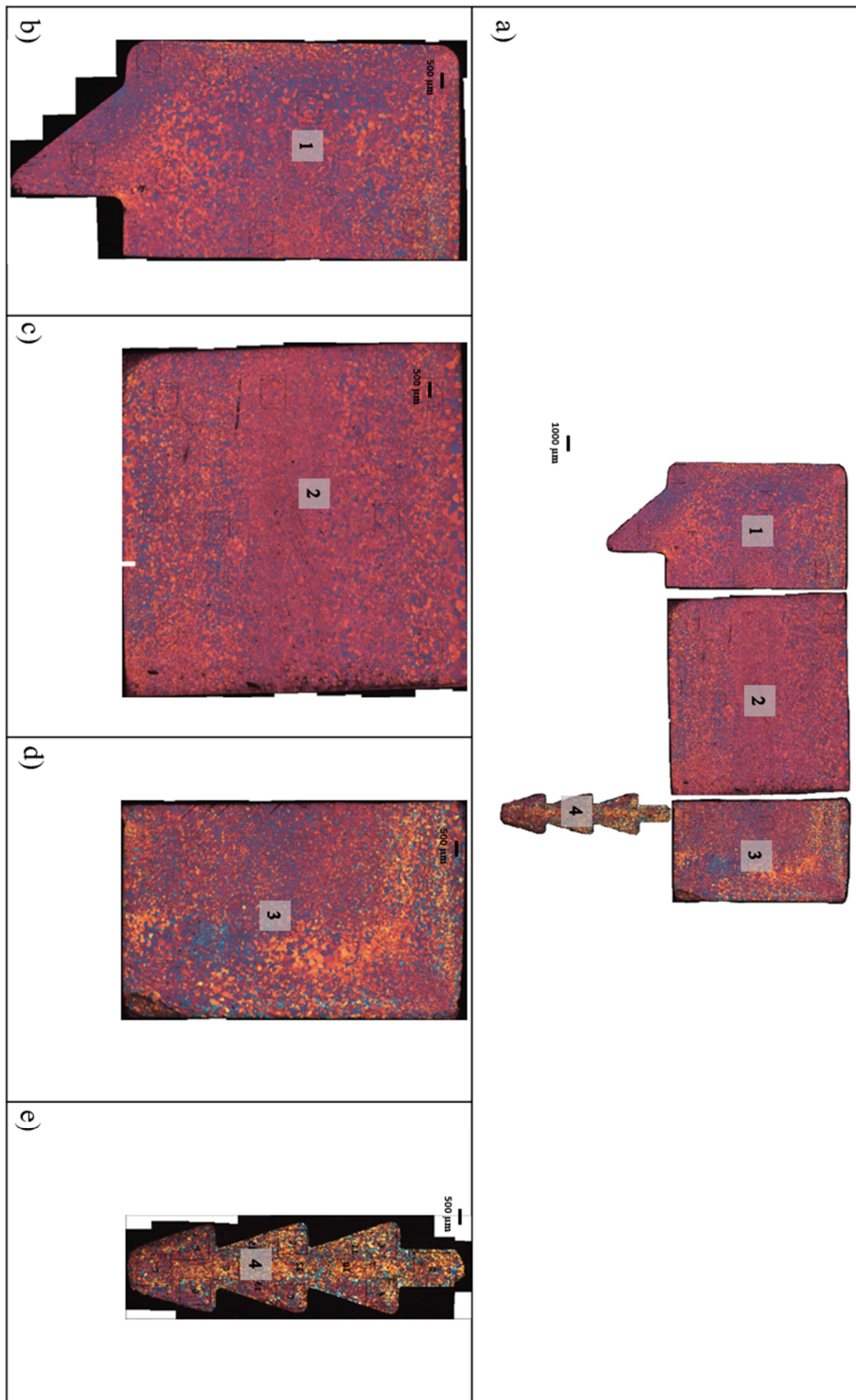


Figure 4.6: Microstructure of profile *b*: a) overview of the microstructure of the entire profile, b) focus on zone 1, c) focus on zone 2, d) focus on zone 3, e) focus on zone 4

4.2 Modeling of the AA6063 Recrystallization Behaviour

The static recrystallization of a 6XXX aluminum alloy was modelled according to Vatne et al. [2]:

$$D_{rec} = DN^{-1/3} \quad (4.1)$$

$$N = N_{PSN} + N_{GB} + N_C \quad (4.2)$$

where D is a material calibration constant and N is the nucleation density. N was considered as sum of different nucleation components: N_{PSN} , N_{GB} and N_C . N_{PSN} is the nucleation occurred on large particles (larger than the critical particle size) around which the deformation zones may form. It is frequently the main nucleation mechanism in the commercial alloys which contains large undeformable particles, and involves the growth of nuclei in turbulent deformation zones with random orientations. N_{GB} is the nucleation from old grain boundaries and N_C is the nucleation from retained cube grains, present in the initial material, which survived the applied deformation. Both N_{GB} and N_C are dependent on the subgrain size and density, grain boundary area per volume and grain size before deformation.

According to [2], these three contributions were calculated as following:

$$N_{PSN} = C_{PSN} \exp\left(\frac{-A_{PSN}}{(Pd - Pz)}\right) \quad (4.3)$$

$$N_{GB} = C_{GB} \delta A(\epsilon) S_{GB} \quad (4.4)$$

$$N_C = C_C \delta A(\epsilon) S_C \quad (4.5)$$

where C_{PSN} , A_{PSN} , C_{GB} and C_C are the material constants. These constants need to be calculated in order to optimize the model for the particular investigated 6XXX alloy.

Pd is the Stored Energy and Pz the Zener Drag Pressure. The Stored Energy, driving force for recrystallization, acts in the form of dislocation substructures and concentrations of vacancies [3]. The Zener Drag Pressure, retarding force for recrystallization, depends on the alloying elements in solid solution and dispersoids size and density [4]. Pd and Pz were calculated according to [3, 5]:

$$Pd = \frac{Gb^2}{10} \left[\rho_i (1 - \ln(10b\rho_i^{0.5})) + \frac{2\theta}{b\delta} * \left(1 + \ln\left(\frac{\theta c}{\theta}\right) \right) \right] \quad (4.6)$$

$$Pz = \frac{3 * f * \gamma}{4 * r} \quad (4.7)$$

where G is the material shear modulus (2.05×10^{10} Pa), b the Burgers vector (2.86×10^{-10} m), ρ_i the dislocation density, δ the subgrain size, θ the misorientation angle and θc the misorientation angle limit (15°). The dislocation density ρ_i and the misorientation angle θ were calculated according to [3]. The dislocation density depends on the strain ε and Zener-Hollomon parameter Z (Fig. 4.7a). The misorientation angle depends on the strain rate $\dot{\varepsilon}$, the temperature T and the strain ε (Fig. 4.7b).

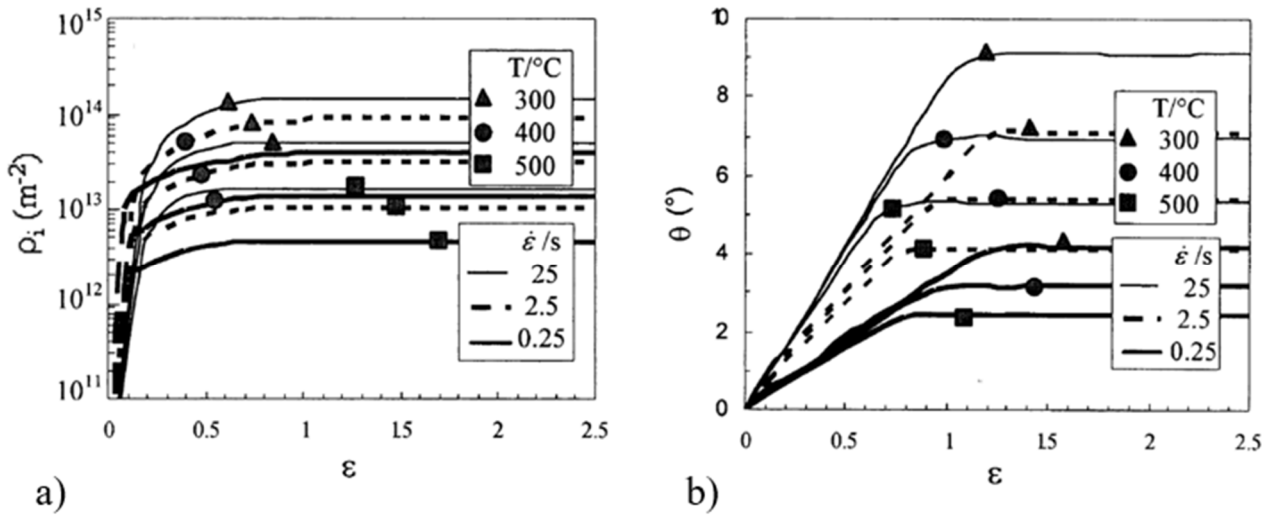


Figure 4.7: a) Dislocation density [3], b) Misorientation angle [3].

The subgrain size and the Zener-Hollomon parameter were calculated according to [15]:

$$\frac{1}{\delta} = C (\ln Z)^n \quad (4.8)$$

$$Z = \dot{\varepsilon} \exp\left(\frac{Q}{RT}\right) \quad (4.9)$$

where $C=3.36 \times 10^{-9} m^{-1}$, $n=5.577$, Q is the activation energy of the AA6063 ($232350 J/mol \cdot K$), R is the universal gas constant ($8.341 J/mol$) and $\dot{\varepsilon}$ is the maximum strain rate for each point of material flow during the extrusion deformation path.

In the Zener Drag pressure calculation (Eq. 7), f and r are the fraction area and the mean size of the dispersoids, respectively, and γ is the grain boundary energy ($0.3 \frac{J}{m^2}$ [6]). In this work, values for f and r were taken from [7], where the microstructures of different 6XXX were analysed. In the AA6063 aluminum alloy, obtaining an average value of 0.023% for the fraction area and around 60 nm for the mean size of the dispersoids.

$A(\epsilon)$ is the grain boundary area per volume at a given strain and S_{GB} , which can be assumed as $S_{GB}=S_C=S$ [19], is the number of subgrain larger than a critical subgrain size δ^* , calculated as followed:

$$\delta^* = \frac{4 \gamma}{Pd - Pz} \quad (4.10)$$

According to what reported in literature [2], $A(\epsilon)$ was modeled as:

$$A(\epsilon) = \frac{1}{D_0} [(\exp(\epsilon) + \exp(-\epsilon) + 1)] \quad (4.11)$$

Considering Eq. 4.11, since this equation was investigated in rolling processes with stain values lower than 10 [8], it has been noticed that for strain values higher than 10 (Fig. 4.8a), typical of industrial-scale extrusion processes, unreasonably high values of $A(\epsilon)$ are obtained and,

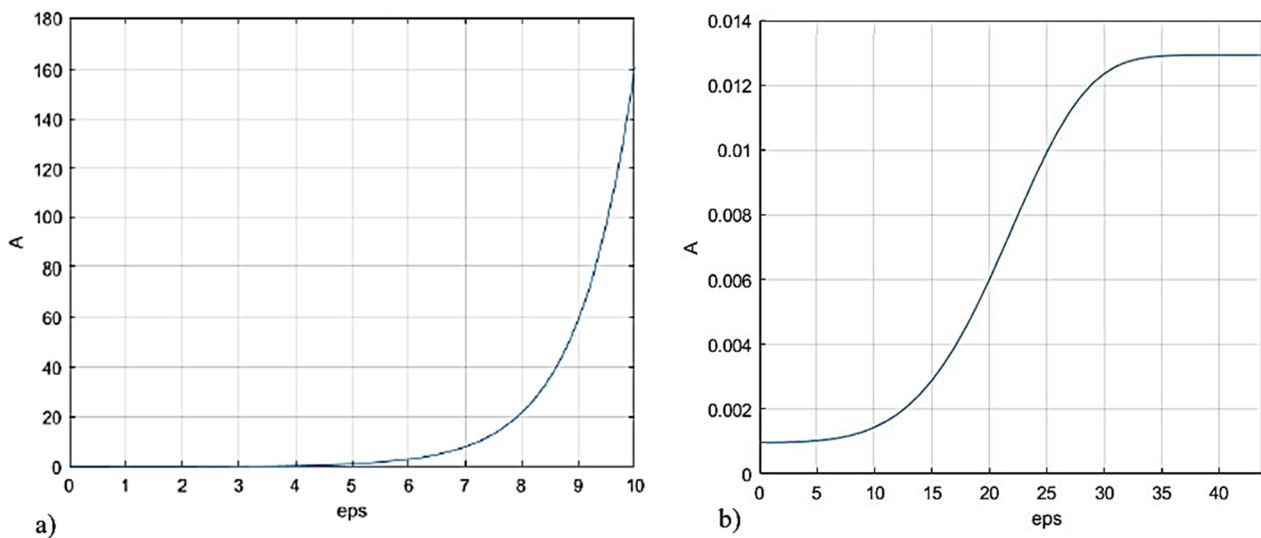


Figure 4.8: a) $A(\epsilon)$ calculated according to Eq. 4.11, b) schematic behaviour of $A(\epsilon)$ calculated according to Eq. 4.12

consequently, of N_{GB} and N . For this reason, $A(\varepsilon)$ has been calculated according to eq. 4.12, limiting the growth of the parameter to a maximum value (Fig. 4.8b):

$$A(\varepsilon) = \frac{1}{D_0} [p_1 - p_2 e^{p_3 \varepsilon^{p_4}}] \quad (4.12)$$

where p_1, p_2, p_3, p_4 are material constants which depend on the investigated 6XXX alloy.

Regarding the dynamic recrystallization, in accordance with the work of Donati L. et al. [9], the average thickness d_t and length d_l of the grains immediately after the bearing zone was calculated as following:

$$d_t = (d_0 - 2.5 * \delta_{ss}) * (k_1)^{\bar{\varepsilon}} + 2.5 * \delta_{ss} \quad (4.13)$$

$$d_l = k_2 \bar{\varepsilon}^2 - k_3 \bar{\varepsilon} + d_0 \quad \text{if } \varepsilon < \varepsilon_p \quad (4.14)$$

$$d_l = k_4 \bar{\varepsilon}^{-m} + 10\delta_{ss} \quad \text{if } \varepsilon > \varepsilon_p \quad (4.15)$$

where ε_p is the critical level of strain for the pinch-off onset, which correspond to a value of 3, δ_{ss} is the subgrain size at the steady-state condition ($\delta_{ss} = 8.4 \mu\text{m}$) and m, k_1, k_2, k_3, k_4 are material constants ($m = 4.75, k_1 = 0.4, k_2 = 85.192, k_3 = 14.88, k_4 = 1.68 * 10^5$ [9]).

4.3 Numerical Simulation of the Extrusion Processes

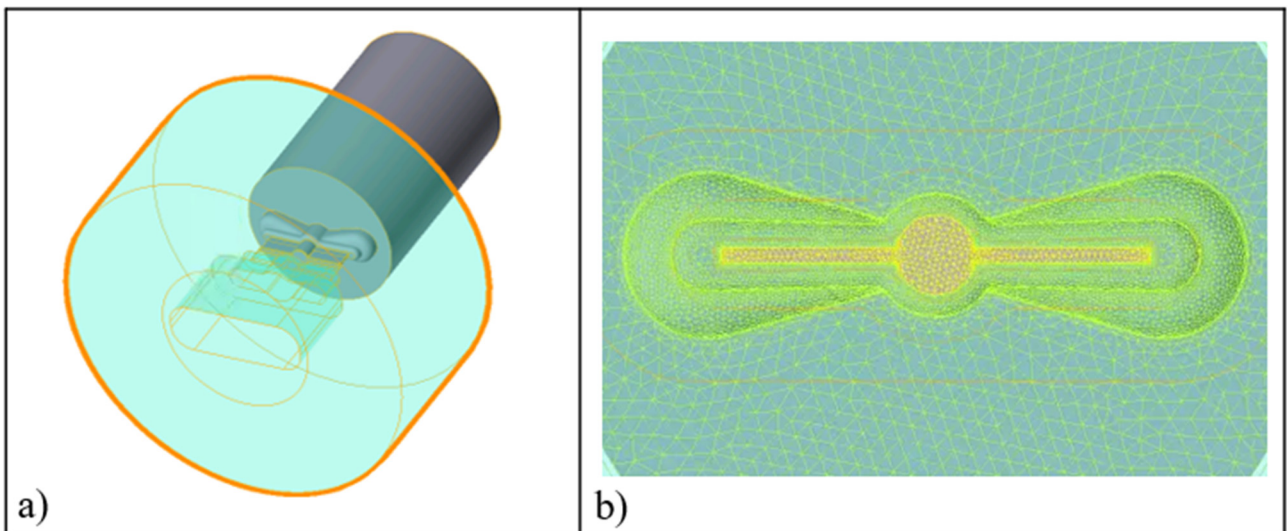


Figure 4.4: FEM simulation of the extrusion process

The simulations of the investigated extrusions were performed using Qform Extrusion®, an Arbitrary Lagrangian Eulerian FEM code. The constitutive model used for the description of the AA6063 flow stress was proposed by Hensel-Spittel [10]: according to the equation, the material flow stress $\bar{\sigma}$ depends on the contribution of strain $\bar{\epsilon}$, strain rate $\dot{\bar{\epsilon}}$ and temperature T:

$$\bar{\sigma} = A \cdot e^{m_1 T} \cdot \bar{\epsilon}^{-m_2} \cdot \dot{\bar{\epsilon}}^{-m_3} \cdot e^{\frac{m_4}{\bar{\epsilon}}} \cdot (1 + \bar{\epsilon})^{m_5 T} \cdot e^{m_7 \bar{\epsilon}} \cdot \dot{\bar{\epsilon}}^{m_8 T} \cdot T^{m_9} \quad (4.16)$$

The values of the Hensel-Spittel constants (m1-m9) and material properties are reported in Tab. 4.3 and Tab. 4.4.

Table 4.3: Hensel-Spittel and for the AA6063 aluminum alloy [11].

Parameters	AA6063
A	1014.7 [MPa]
m1	-0.00438 [K ⁻¹]
m2	0.2425
m3	-0.0965
m4	-0.000438
m5	-0.000766 [K ⁻¹]
m7	0.002939
m8	0.000291 [K ⁻¹]
m9	0

Table 4.4: Material parameters for the AA6063 aluminum alloy

Material Properties	AA6063
Density [Kg/m ³]	2690
Specific heat [J/kg K]	900
Thermal conductivity [W/m K]	200
Thermal expansivity [m/K]	2.34*10 ⁻⁵
Young's modulus [GPa]	68.9
Poisson's ratio	0.33

The friction conditions between workpiece and tools during the manufacturing process were set according to the default values optimized for extrusion in the Qform database (Tab. 4.5).

Table 4.5: Friction conditions.

Surface	Friction condition
Billet-Container	Sticking condition
Billet-Ram	Sticking condition
Billet-Die	Sticking condition
Bearings	Levanov model ($m = 0.3, n = 1.25$)

In order to validate the results of the numerical analysis, the predicted extrusion load and profile exit temperature were compared to the experimental ones. In Fig. 4.10, the results of the simulation of profile *Hydro* are reported: Fig. 4.10a and 4.10c show the investigations of the extrusion peak loads for the extrusions made with a ram speed of 1.1 mm/s and 10.4 mm/s, respectively. In the low ram speed condition (Fig. 4.10a), the experimental peak was found at 3.47 MN while the numerical at 3.20 MN. In the high ram speed condition (Fig. 4.10c), the experimental peak was found at 4.77 MN while the numerical at 4.69 MN. About the profile exit temperature at a thermal steady state condition, in the low ram speed condition (Fig. 4.10b), the acquired experimental value was 433°C while the numerical 438°C. In the high ram speed condition (Fig. 4.10d), the acquired experimental value was 551°C while the numerical 546°C. The average error in the extrusion load and temperature prediction was found below the 3.5%, thus proving the reliability of the simulations. A similar accuracy was found for the numerical analysis of all the other process conditions of profile *Hydro*, profile *a* and profile *b*.

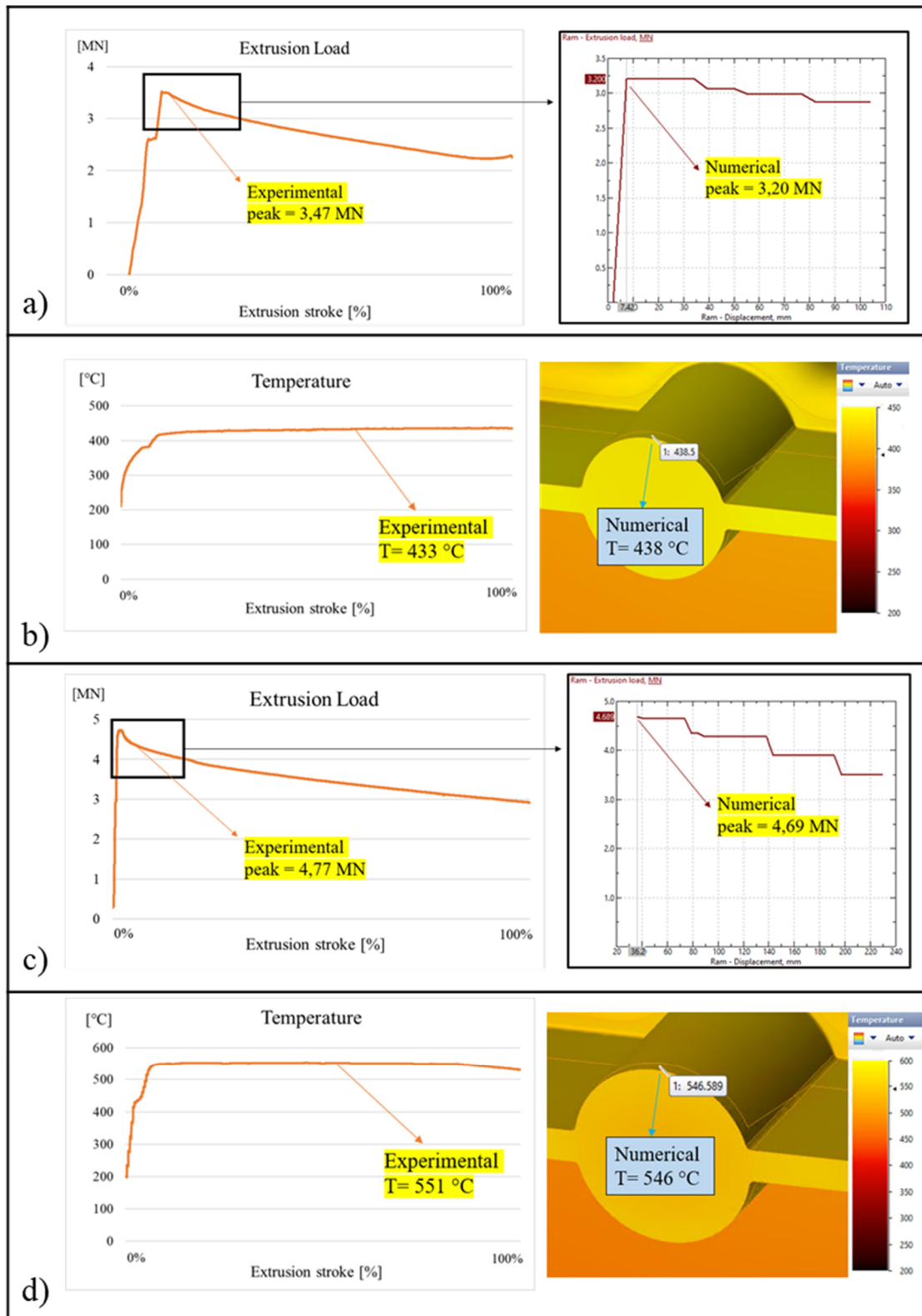


Figure 4.10: Profile *Hydro* simulation: a) comparison between experimental and numerical extrusion load in the extrusion with ram speed of 1.1 mm/s, b) comparison between experimental and numerical exit temperature in the extrusion with ram speed of 1.1 mm/s, c) comparison between experimental and numerical extrusion load in the extrusion with ram speed of 10.4 mm/s, d) comparison between experimental and numerical exit temperature in the extrusion with ram speed of 10.4 mm/s.

4.4 Comparison Between Numerical and Experimental Results

The model material constants were found using an optimization algorithm, the Levenberg-Marquardt non-linear regression algorithm [12]. As input variables, the calibration set of measurements was used together with the values of strain, strain rate and temperature from the simulation of the extrusion process. The AA6063 material constants are summarized in Tab. 4.6.

Table 4.6: Recrystallization model material constants AA6063

Material constants	AA6063
C_{PSN}	4.99962 e^{13}
A_{PSN}	864686
C_{GB}	0.00022279
C_C	0.00022279
p_1	1.9
p_2	1.06
p_3	1 e^{-7}
p_4	6

After calculating these constants, the model was implemented within the Qform Extrusion environment for the recrystallization analysis.

Since the profile extruded with ram speed of 1.1 mm/s present a partially recrystallized microstructure, the analysis of the dimensions of the fibrous grains in the inner part of the profile was carried out in order to acquire the data of the grains after DRX and check the accuracy of the dynamic recrystallization model. In Fig. 4.11 and Fig 4.12, the comparison between experimental and numerical grain size after the dynamic recrystallization, immediately after the bearing zone is shown. The numerical results of Fig. 4.11a, 4.11c are compared with the experimental data taken from Fig. 4.11b, 4.11d. The results of this comparison are reported in Fig. 4.12. A number of points were taken randomly on the fibrous part of the investigated profile. In these points, both numerical and experimental data were compared and collected in the graph shown in Fig. 4.12a (for the grain thickness prediction) and Fig. 10b (for the grain length prediction). In this figure, the x-axis and the y-axis represent the experimental and numerical dimensions of the grain size, respectively. Consequently, the red 45° line corresponds to the 100% matching between numerical and experimental values. The more the numerical prediction differs from the experimental values, the more the red dots diverges from the red line. In addition, two green lines corresponding to an error of $\pm 25\%$ were reported. $\pm 25\%$ was selected as the error range considering both the high number of

metallurgical and process factors that affect the final grain size and the approximations deriving from the measurement methodology chosen for the experimental analysis of the average grain diameter. For these reasons, this range, also used by Donati L. et al. in [9] for the investigation of a laboratory-scale extruded profile microstructure prediction, is considered an excellent accuracy range. As evidenced by the graphs of Fig. 4.12a and Fig. 4.12b, the 100% of the points is the $\pm 25\%$ error lines for both the prediction of length and thickness of the fibrous grains, thus confirming the good reliability of the model for the DRX evaluation.

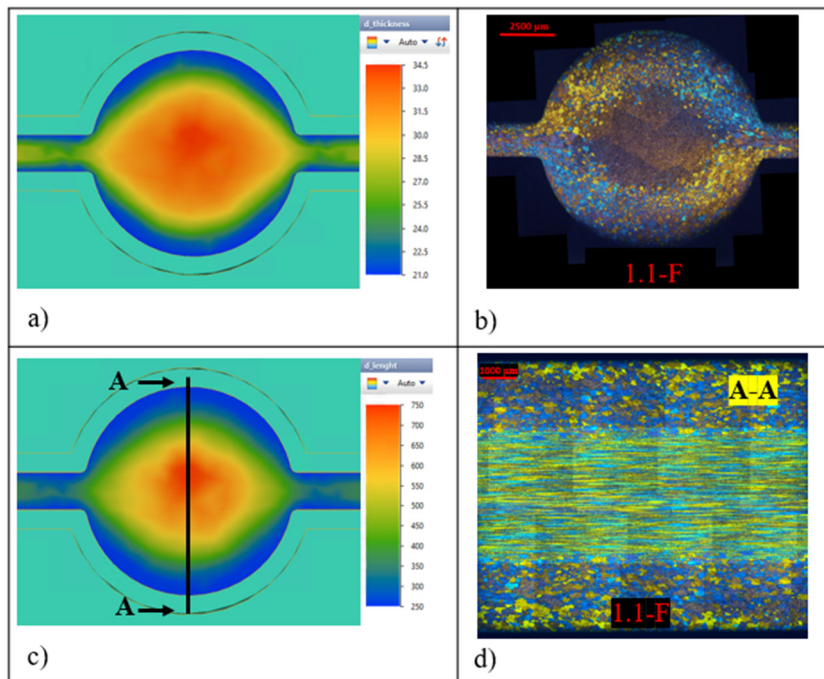


Figure 4.11: Profile *Hydro*: a) numerical grain thickness b) experimental microstructure (cross section) numerical grain length d) experimental microstructure (longitudinal section)

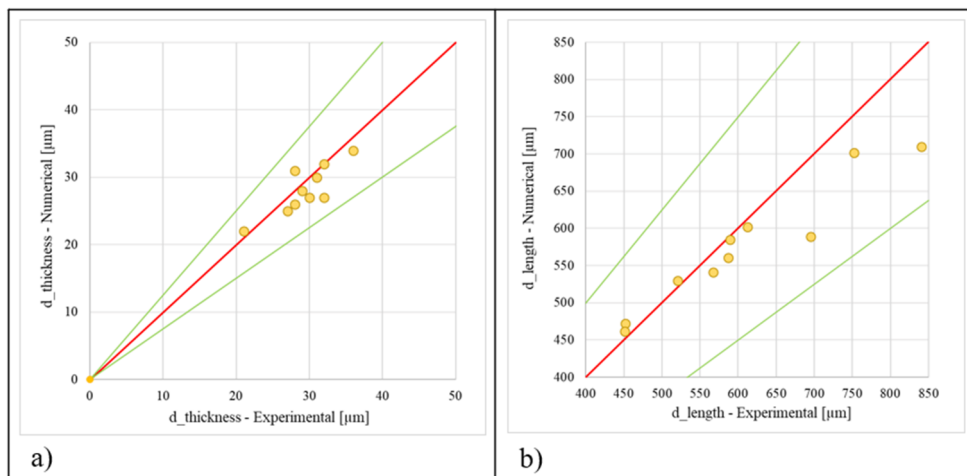


Figure 4.12: DRX analysis: a) comparison between experimental and numerical grain thickness of profiles *Hydro*, b) comparison between experimental and numerical grain length of profiles *Hydro*

In Fig. 4.13, the outputs of the simulation involving the recrystallization thickness prediction are reported and compared to the experimental microstructures. The area in red indicates the part of the profile where the static recrystallization occurred, while the area in blue where the grain structure remains fibrous. Since the microstructure of the “front” samples is almost the same as the “back” samples (Fig. 2), only the images of the “front” part are reported for the comparison. In AA6063 aluminum alloy, due to a low or absent dispersoids concentration [13], SRX is extremely likely to occur after the profile exits the die. Consequently, all the investigated profiles present a completely recrystallized structure except the one shown in Fig. 4.13a, where is partially recrystallized. In that case, the simulation reports, in agreement with the experimental evidence, a partially recrystallized microstructure (Fig. 4.13b). In the remaining cases, always in accordance with what was experimentally reported, the expected microstructure is completely recrystallized.

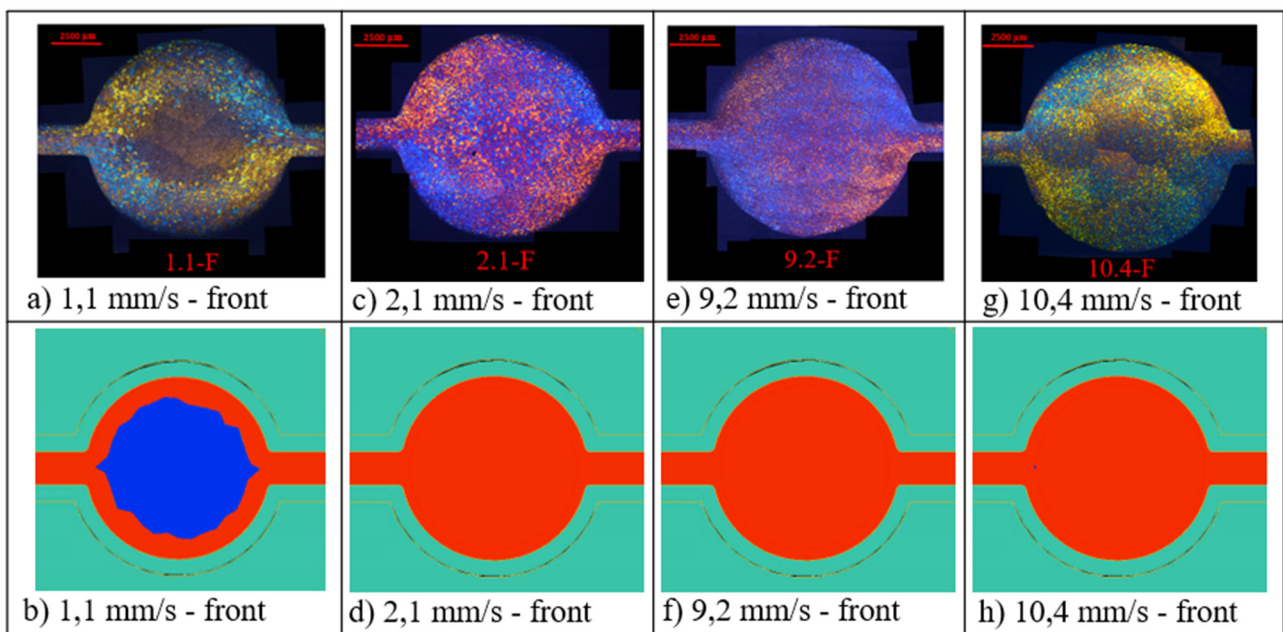


Figure 4.13: Recrystallization thickness analysis: a), c), e), g) experimental, b), d), f), h) numerical (red area = SRX area, blue area = No SRX area)

After the SRX thickness investigation, the comparison between the predicted and experimental grain size was carried out. In Fig. 4.14, the data about profile *Hydro* are reported: Fig. 4.14a, Fig. 4.14c and Fig. 4.14e show the microstructures of the extrusions made with a billet temperature of 480°C and a ram speed of 2.1 mm/s, 9.2 and 10.4 mm/s, respectively. The images shown under each microstructure (Fig. 4.14b, Fig. 4.14d and Fig. 4.14f) report the results of the grain size prediction simulation. In these figures, the values of the average diameter are reported, with a scale bar range from 40 µm (blue) to 110 µm (red). Consequently, the red areas represent the points where the predicted grain size has higher dimension while the green/blue areas the lower dimension. In

accordance with the experimental tests, the numerical predictions show that the sample extruded with a ram speed of 2.1 mm/s present the coarser grain size in the inner area (Fig. 4.14b), while the sample extruded with a ram speed of 9.2 mm/s the smaller (Fig. 4.14d), thus proving the good accuracy of the numerical computation.

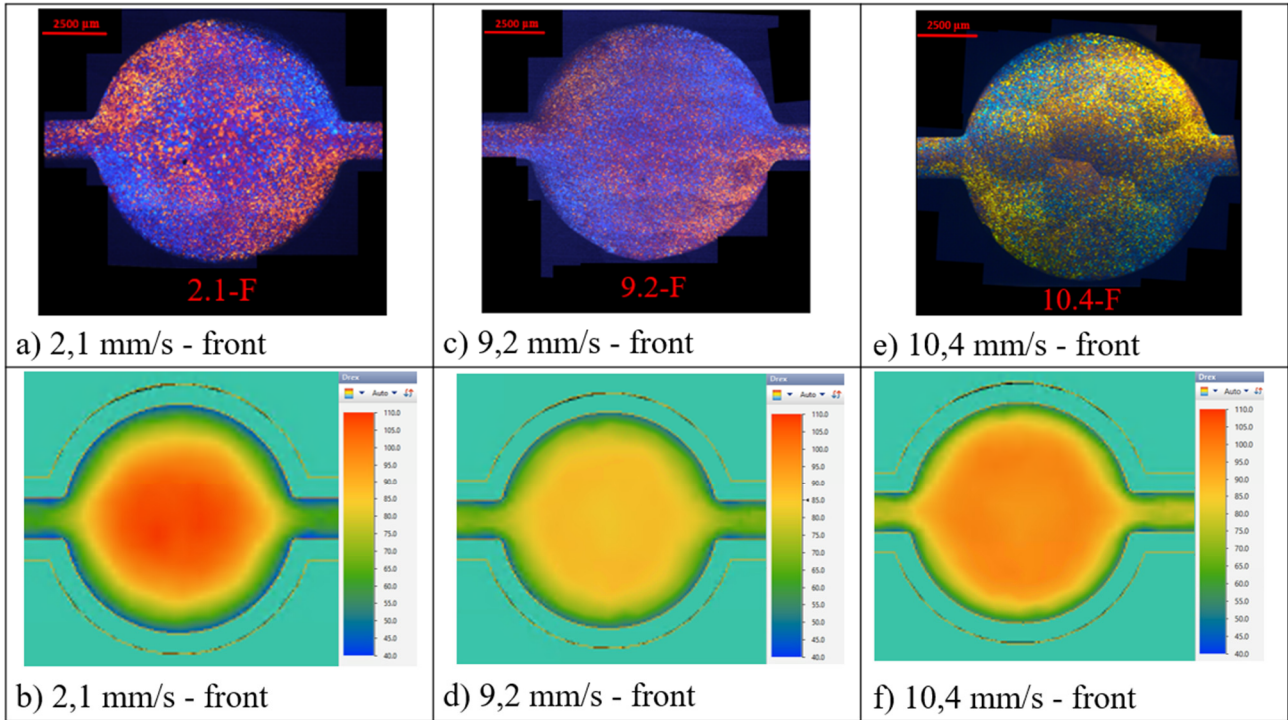


Figure 4.14: Grain size analysis after SRX: a), c), e) experimental grain size, b), d), f) numerical grain size

Using the same numerical model, the grain size prediction was carried out both for Profile *a* and Profile *b*: the results are shown in Fig. 4.15 and Fig. 4.16, respectively. As clearly visible by comparing Fig. 4.15b with Fig. 4.15c-f, a good matching between zones with smaller and coarser grains was found. Moreover, the good correlation is also highlighted by the comparison between Fig. 4.15b, 4.15d, 4.15f with Fig. 4.16a, 4.16c, 4.16e. In Fig. 4.16, the numerical simulation was capable of predicting the bigger grains in the massive zones of the profile close to the round hole (Figs.4.16c-d) rather than in the thinner section (Figs. 4.16e-f). The only areas where the numerical prediction is less accurate, as in Fig. 4.16c zone A-B, are characterized by the phenomenon of PCG (Peripheral Coarse Grain) or AGG (Abnormal Grain Growth), grain growth mechanisms not modelled in the algorithm used for the grain size forecast.

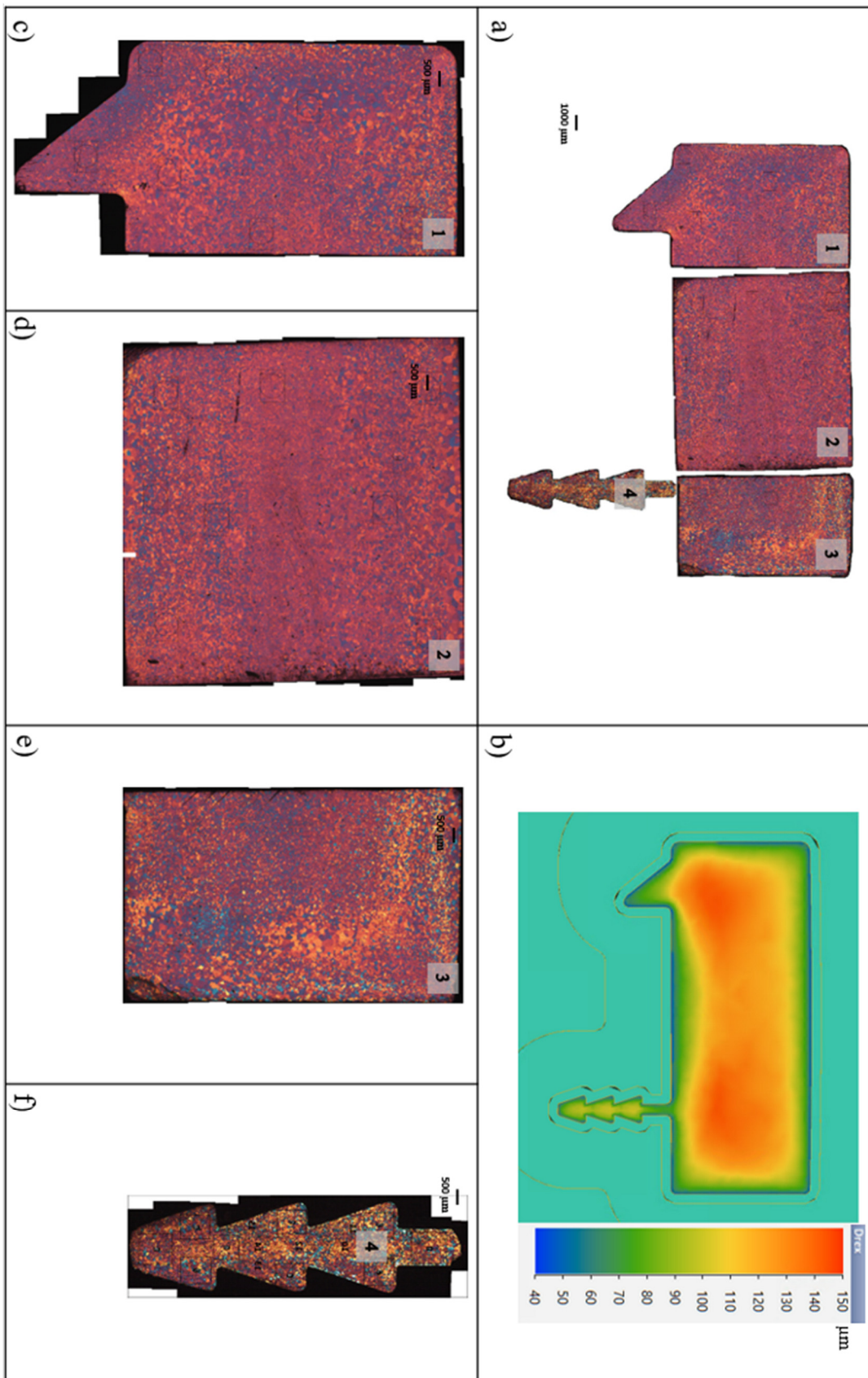


Figure 4.15: Comparison between experimental and numerical grain size of profile *a*: a) experimental, b) numerical, c) focus on zone 1, d) focus on zone 2, e) focus on zone 3, f) focus on zone 4

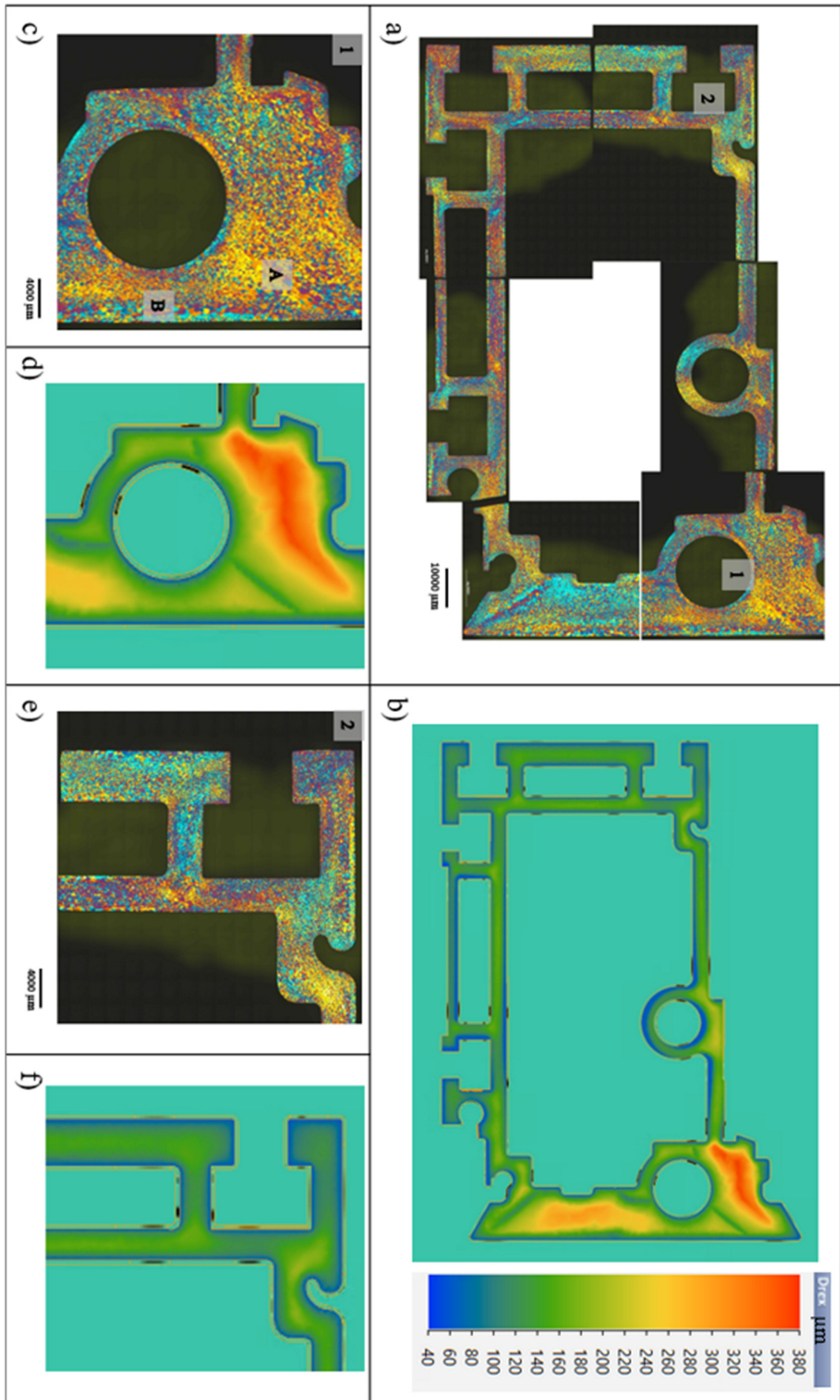


Figure 4.16: a), c), e) Experimental and b), d), f) numerical grain size of profile *b*

Together with the qualitative analysis, a quantitative analysis, similar to the one reported in Fig. 4.17, was carried out on the predictions of the diameters of the recrystallized grain for the *Hydro*, *a* and *b* profiles. A considerable number of points taken randomly on the profiles investigated were selected. The yellow dots represent the investigated points on the profiles and the blue dots the points taken from PCG/AGG areas. If the blue dots are excluded from the analysis, almost the entire amount of the dots is within the $\pm 25\%$, thus proving the excellent accuracy and reliability of the numerical model for the grain size prediction.

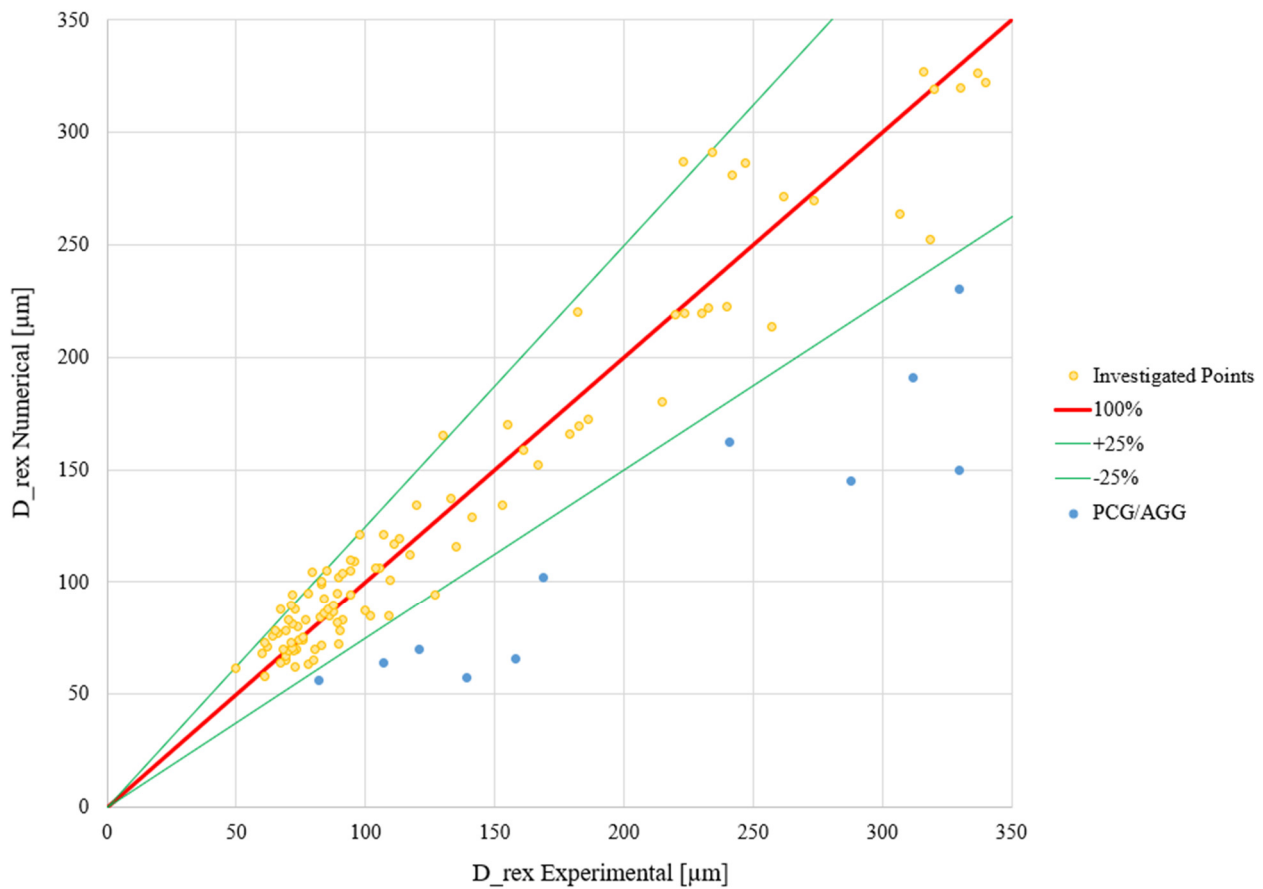


Figure 4.17: Comparison between experimental and numerical grain size of profiles *a*, *b*, *Hydro*

4.5 Remarks

In the present work, the development of the recrystallization model of the AA6063 aluminum alloy was carried out together with the FEM simulation of three industrial-scale extrusions using Qform Extrusion FEM code. The microstructural analysis of the three profiles were performed and the collected data were used for the validation of the proposed model. The microstructural data of the *Hydro* profile were used to calibrate the AA6063 recrystallization model, then it was validated over

two other industrial-scaled extruded AA6063 profiles. The main outcomes of this work can be summarized as follows:

- The results of the extensive experimental analysis on the recrystallization of a AA6063 aluminum alloy were collected and discussed: the microstructures of the *Hydro* profile were used for the calibration of the model while the microstructures of Profile *a* and *b* for the model validation.
- An innovative static recrystallization model was developed and optimized for the prediction in AA6063 aluminum alloys.
- FEM simulation of the analysed extrusion processes were carried out with an average error in the extrusion load and temperature prediction below the 3.5%, thus proving the reliability of the simulations.
- An excellent experimental-numerical agreement was achieved in terms of recrystallization thickness and grain size prediction: In the DRX modeling, the analysed points reveal an error between measured and predicted length and thickness of the fibrous grains always below the $\pm 25\%$, thus confirming the reliability of the model for the dynamic recrystallization evaluation. In the static recrystallized thickness, an almost perfect matching between experimental and numerical data was found, as for the prediction of the static recrystallized grain size, which present an error always below $\pm 25\%$. However, the grain size prediction of AGG/PCG grains needs to be further improved to increase the accuracy and the reliability of the proposed model.

References

- [1] A. Gamberoni, L. Donati, B. Reggiani, M. Haase, L. Tomesani, A.E. Tekkaya (2015) Industrial Benchmark 2015: Process Monitoring and Analysis of Hollow EN AW-6063 Extruded Profile, *Materials Today: Proceedings* 2(10): 4714-4725.
- [2] H.E. Vatne, T. Furu, R. Orsund, E. Nes (1996) Modelling recrystallization after hot deformation of aluminum, *Acta Materialia* 11: 4463–4473.
- [3] C.M. Sellars, Q. Zhu (2000) Microstructural modelling of aluminium alloys during thermomechanical processing, *Materials Science and Engineering: A* 280: 1-7.
- [4] P. Rios, F. Siciliano, H. Sandim, R. Lesley, A. Padilha (2005) Nucleation and growth during recrystallization, *Materials Research* 8(3): 225-238.
- [5] F.J. Humphreys, M. Hatherly (2004) *Recrystallization and related annealing phenomena*, Second edition, Elsevier, Oxford, UK.
- [6] C.O. Paulsen (2015) *Recrystallization Behaviour in Extruded Profile of Non-Dispersoid Containing Al-Mg-Si Alloys*, PhD Thesis, Department of Materials Science and Engineering NTNU-Trondheim, Materials Science and Engineering.
- [7] M.S. Remøe, I. Westermann, K. Marthinsen (2019) Characterization of the Density and Spatial Distribution of Dispersoids in Al-Mg-Si Alloys, *Metals* 9(1): 26-46.
- [8] A.R. Eivani, J. Zhou, J. Duszczuk (2013) Grain boundary versus particle stimulated nucleation in hot deformed Al–4.5Zn–1Mg alloy, *Materials Science and Technology* 29: 517-528.
- [9] L. Donati, A. Segatori, M. El Mehtedi, L. Tomesani (2013) Grain evolution analysis and experimental validation in the extrusion of 6XXX alloys by use of a lagrangian FE code, *International Journal of Plasticity* 46: 70-81.
- [10] A. Hensel, T. Spittel (1978) *Kraft und Arbeitsbedarf bildsamer Formgebungsverfahren*, 1. Auflage, Leipzig: VEB Deutscher Verlag für Grundstoffindustrie.
- [11] M. Negrozio, R. Pelaccia, L. Donati, B. Reggiani, T. Pinter, L. Tomesani (2021) Finite Element Model Prediction of Charge Weld Behaviour in AA6082 and AA6063 Extruded Profiles, *Journal of Materials Engineering and Performance* 30: 4691–4699.
- [12] P.E. Gill, W. Murray (1978) Algorithms for the Solution of the Nonlinear Least-Squares Problem, *SIAM Journal on Numerical Analysis* 15(5): 977–992.
- [13] N. Parson, J. Fourmann, J.F. Beland (2017) *Aluminum Extrusions for Automotive Crash Applications*, SAE Technical Papers 1–16.

5. Modeling of the Recrystallization Behaviour of AA6060 Aluminum Alloy Extruded Profiles

In order to extend the work made on the AA6063 aluminum alloy reported in chapter 4, the same experimental-numerical type of activity was made for a AA6060 extruded profile.

In this work, an industrial-scale extrusion of AA6060 aluminum alloy hollow profile was investigated. Numerical activities involving Finite Element (FE) simulation of the extrusion were performed with the commercial Qform Extrusion® code. Moreover, an innovative recrystallization model was developed, comparing the achieved results with the microstructural data experimentally collected for the industrial-scale profile. The final aim of this work was to propose a reliable model able to accurately predict the microstructural behaviour in the hot extrusion of AA6060 aluminum alloy profiles.

5.1 Experimental Investigation

The geometry of the profile under investigation is reported in Fig. 5.1. It was produced by the Profilati SpA plant of Medicina (Italy). The production batch involved the extrusion of 17 billets and the data about profile exit temperature and extrusion load were acquired during the whole process and used to validate the numerical simulation results. The analyzed sample comes from the extrusion of the seventh billet in order to have steady-state conditions in the tool-die set.

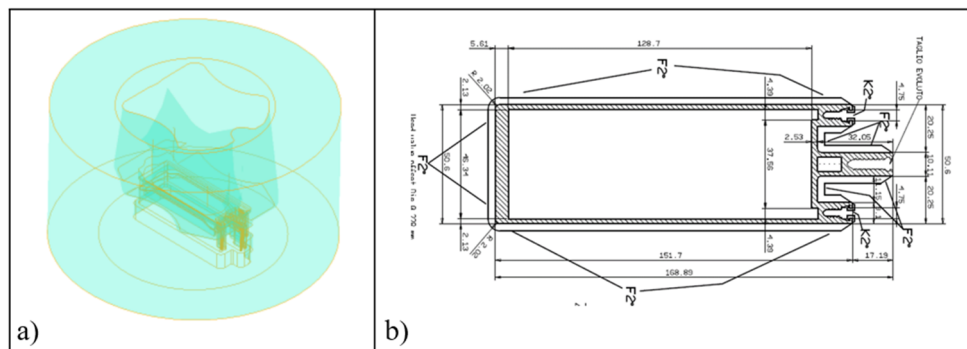


Figure 5.1: Investigated profiles and die geometries: a) die, a) cross-section of the extruded profile.

In Table 5.1, the extrusion process and the geometry parameters of billet and tools are reported.

The microstructure of the profile is reported in Fig. 5.2b-g: the images of the anodized samples were acquired by using polarized light microscopy and the measurement of the average grain dimension was carried out according to the ASTM-E112 regulation. The images of Fig. 5.2 clearly show a fully recrystallized microstructure, within an average dimension range of 45 μm to 110 μm . The analysed samples were taken at the middle length of the extrusion profile, corresponding to a

ram stroke of 475 mm. From the entire cross-section of the profile, six zones were selected (Fig. 5.2b-g). From each zone, 10 points were extracted and in each of these, the dimensions of the statically recrystallized diameter were measured. Half of these points were used for the model calibration and the other half for the validation.

Table 5.2: Process parameters and geometry tolerances

Process parameters and geometry tolerances	Profile
Aluminum alloy	AA6060
Extrusion ratio	27
Ram speed [mm/s]	8
Container temperature [°C]	430
Billet temperature [°C]	480
Die temperature [°C]	510
Ram acceleration time [s]	5
Billet length [mm]	950
Billet diameter [mm]	203
Container diameter [mm]	211
Billet Rest length [mm]	44

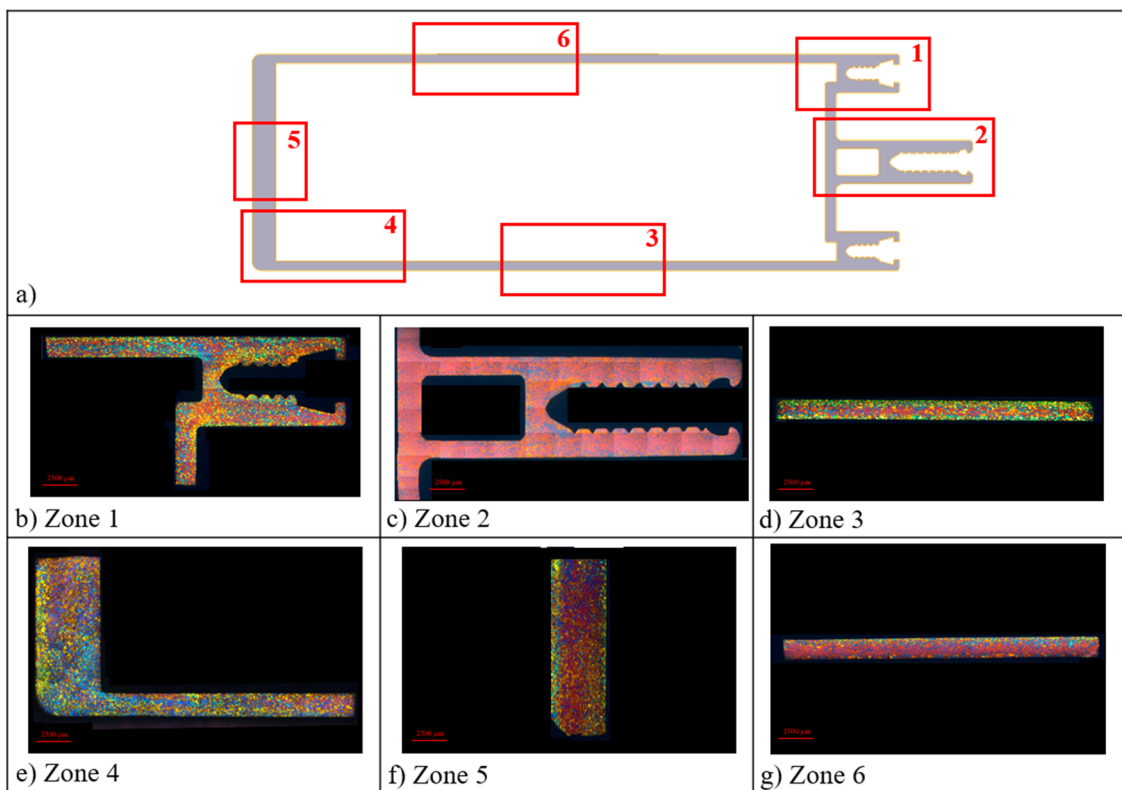


Figure 5.2: Microstructure of the investigated AA6060 profile

5.2 Modeling of the AA6060 Recrystallization Behaviour

The modeling of the AA6060 aluminum alloy was the same to the one reported in the 4.2 paragraph.

5.3 Numerical Simulation of the Extrusion Processes

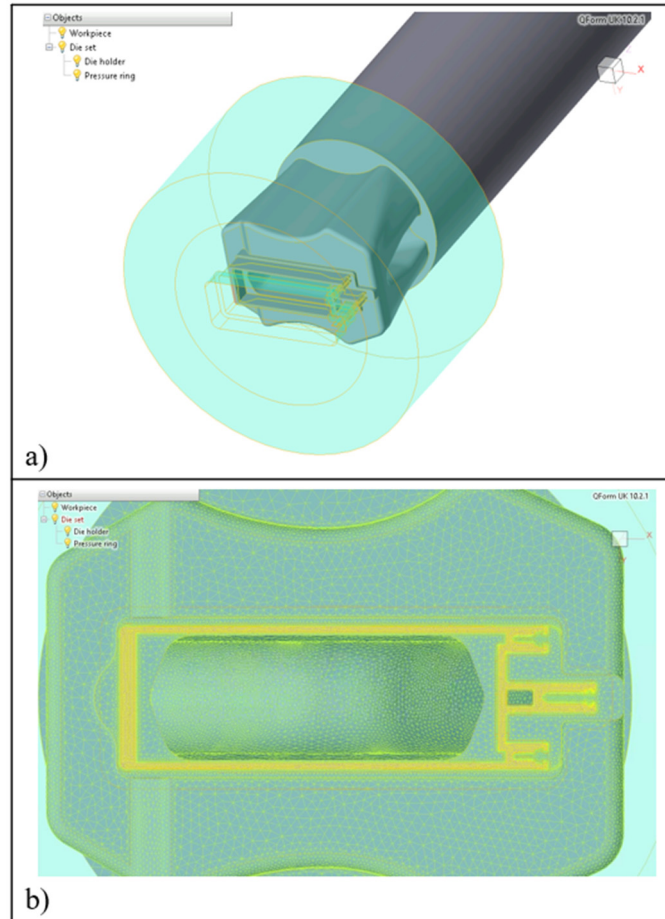


Figure 5.3: FEM simulation of the extrusion process

The simulation of the analysed extrusion process was performed using Qform Extrusion®, a commercial ALE (Arbitrarian Lagrangian Eulerian) FEM code. The constitutive model used for the description of the AA6060 flow stress was proposed by Hensel-Spittel [1]. According to the proposed equation (Eq. 5.1), the material flow stress $\bar{\sigma}$ depends on the contribution of strain $\bar{\epsilon}$, strain rate $\dot{\bar{\epsilon}}$ and temperature T:

$$\bar{\sigma} = A \cdot e^{m_1 T} \cdot \bar{\epsilon}^{-m_2} \cdot \dot{\bar{\epsilon}}^{-m_3} \cdot e^{\frac{m_4}{\bar{\epsilon}}} \cdot (1 + \bar{\epsilon})^{m_5 T} \cdot e^{m_7 \bar{\epsilon}} \cdot \dot{\bar{\epsilon}}^{m_8 T} \cdot T^{m_9} \quad (5.1)$$

The values of the Hensel-Spittel constants (m1-m9) used for the simulation of the AA6060 aluminum alloy, reported in Tab. 5.2, were taken from the Qform material database.

Table 5.2: Hensel-Spittel and for the AA6060 aluminum alloy.

Parameters	AA6060
A	280 [MPa]
m1	-0.00461 [K ⁻¹]
m2	-0.16636
m3	0.12
m4	-0.02056
m5	0.00036 [K ⁻¹]
m7	0
m8	0 [K ⁻¹]
m9	0

The friction conditions between workpiece and tools were also taken from the software database according to the default values optimized for extrusion (Tab. 5.3).

Table 5.3: Friction conditions.

Surface	Friction condition
Billet-Container	Sticking condition
Billet-Ram	Sticking condition
Billet-Die	Sticking condition
Bearings	Levanov model (m = 0.3, n = 1.25)

The values of the material properties used in the simulation are reported in Tab. 5.4.

Table 5.4: Material parameters for the AA6060 aluminum alloy.

Material Properties	AA6060
Density [Kg/m ³]	2690
Specific heat [J/kg K]	900
Thermal conductivity [W/m K]	200
Thermal expansivity [m/K]	2.34*10 ⁻⁵
Young's modulus [GPa]	68.9
Poisson's ratio	0.33

In order to validate the results of the simulation, the values of the numerical extrusion load and profile exit temperature were compared to the experimental ones (Fig. 5.5). With regard to the extrusion load, the experimental peak value was found at 23.4 MN while the numerical one at 23.3 MN. Consequently, the numerical error in the extrusion load prediction was under the 1%. Moreover, the experimental exit temperature of the profile was experimentally found at 557 °C (through the use

of a pyrometer pointed in the point indicated in Fig. 5.5b by the start of the red arrow) while the numerical one at 562 °C, with a prediction error close to the 1%. As a result, the average error in the extrusion load and temperature prediction was found below the 1%, thus proving the reliability of the simulation.

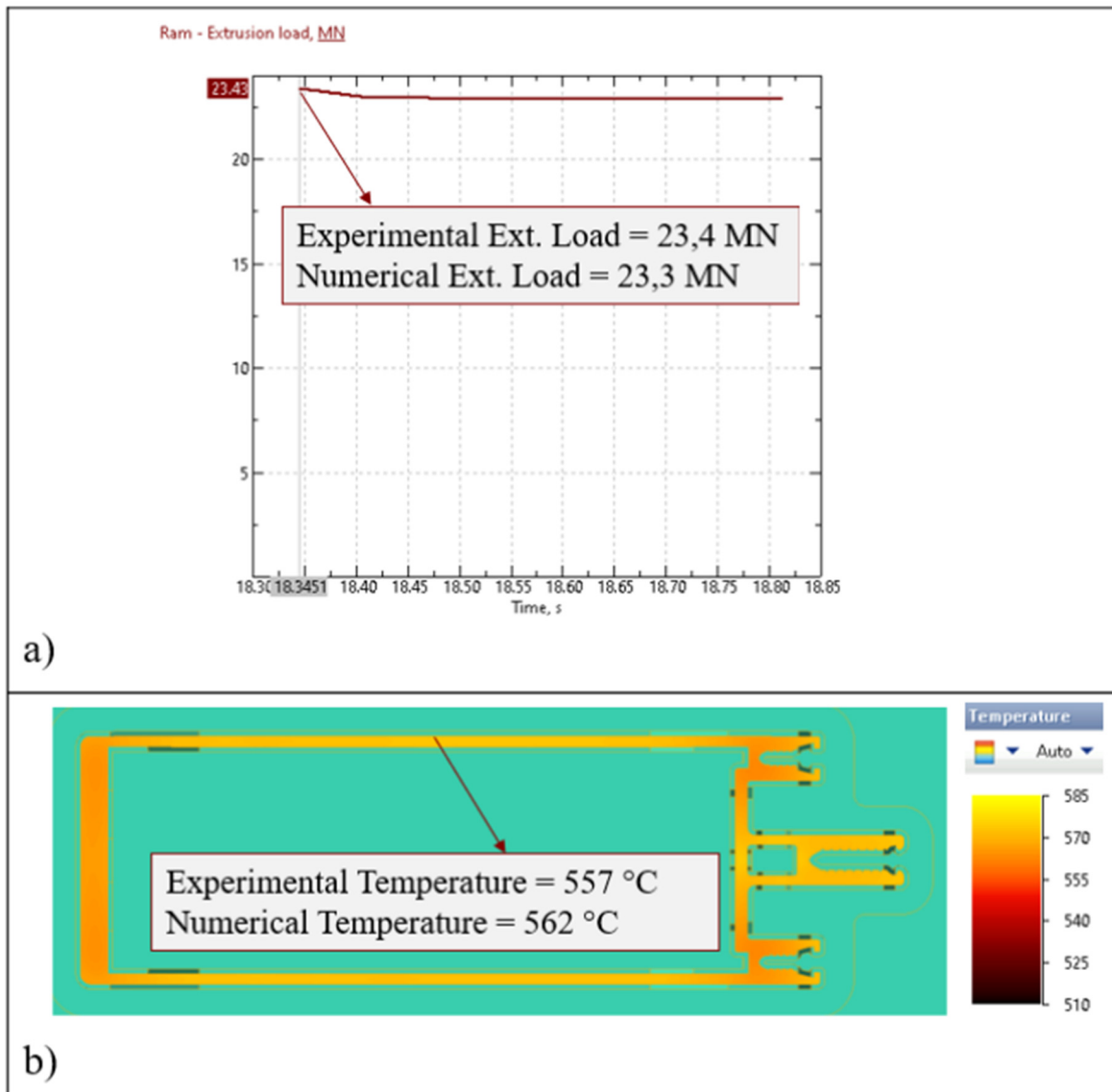


Figure 5.5: Experimental-numerical comparison between extrusion load and profile exit temperature.

5.4 Comparison Between Numerical and Experimental Results

According to the methodology reported in paragraph 4.4, the material constants of the recrystallization model were obtained by applying the Levenberg-Marquardt non-linear regression algorithm [2], implemented in Matlab®, using as input data the “calibration set” of points in which the grain size was experimentally calculated. For each considered point, the values of temperature,

strain and maximum strain rate were calculated by the FEM simulation using Qform software. A different set of points (“validation set”) were used to validate the results of the numerical microstructure prediction.

The outputs of the non-linear regression method are summarized in Tab. 5.5. After acquiring these values, the model was implemented into Qform Extrusion and used to calculate the average grain size of the extruded profile. The values of p_1 , p_2 , p_3 , p_4 were taken from the optimization of the AA6063 aluminum alloy reported in paragraph 4.4.

Table 5.5: Recrystallization model material constants AA6060

Material constants	AA6060
C_{PSN}	5.00021 e^{13}
A_{PSN}	872954
C_{GB}	0.0002145
C_C	0.0002145
p_1	1.9
p_2	1.06
p_3	1 e^{-7}
p_4	6

In Fig. 5.6, the simulated trends of the profile exit temperature, maximum value of strain rate and plastic strain are reported. The acquired values are similar to the ones obtained in the same analysis for the AA6063 aluminum alloy reported in paragraph 4.4. This result confirms the reliability of the methodology, since is reasonable to assume similar recrystallization behaviours in alloys (AA6063 and AA6060) with low or absent dispersoids content.

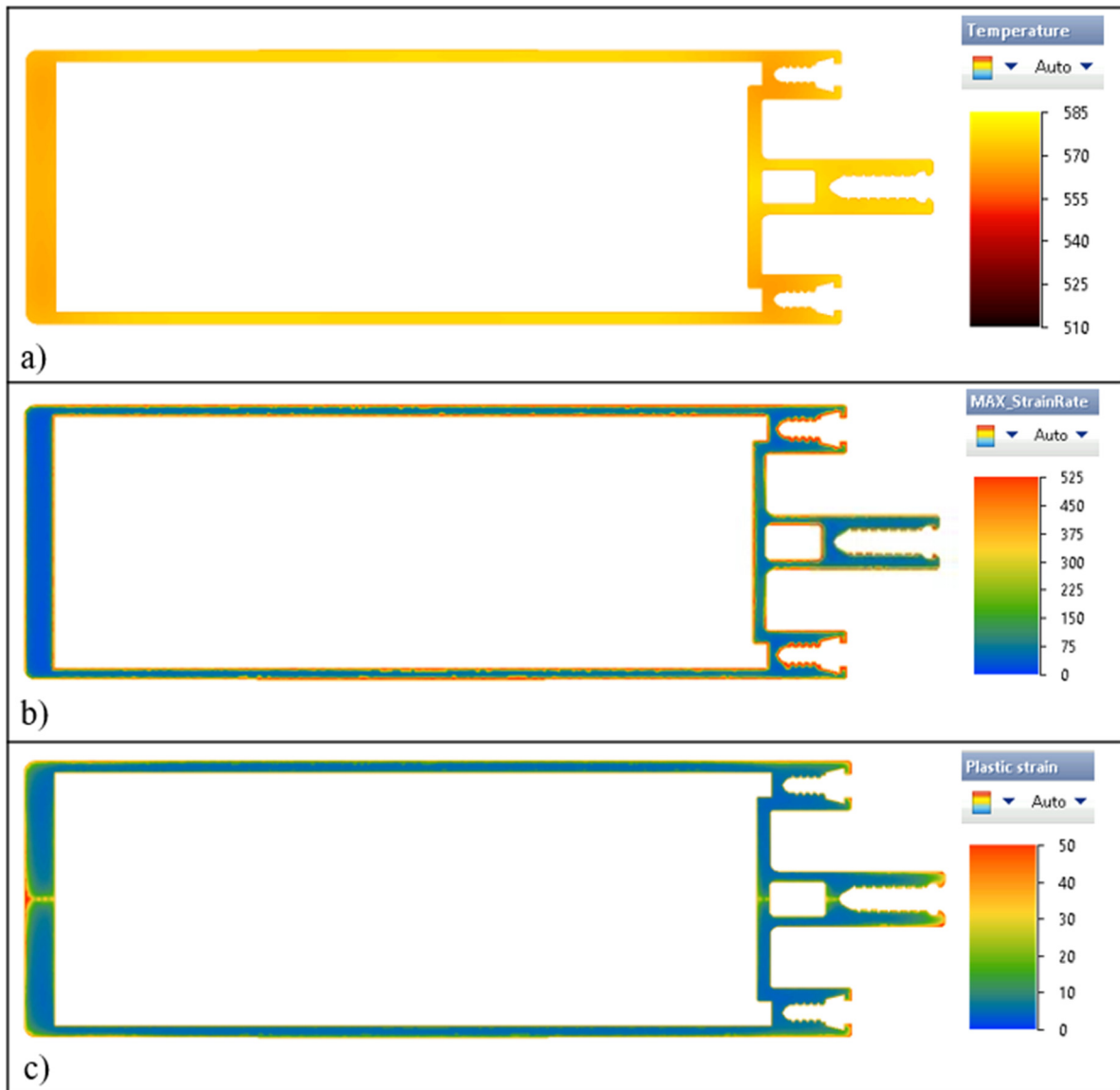


Figure 5.6: a) Profile exit temperature, b) maximum value of strain rate and c) plastic strain simulations.

In Fig. 5.7, the numerical simulation of the grain size after the complete SRX is reported. Red and blue areas correspond to the part of the profile in which the grain size has higher and lower dimensions, respectively. The numerical range of grain size dimensions resulted between 52 μm and 96 μm . Fig. 5.8 shows a visual comparison between the predicted and the experimental microstructures.

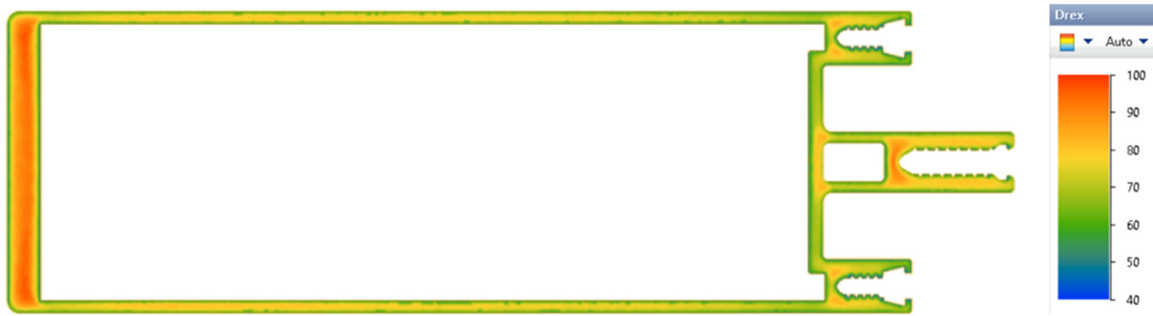


Figure 5.7: Numerical average grain size of the investigated extruded profile.

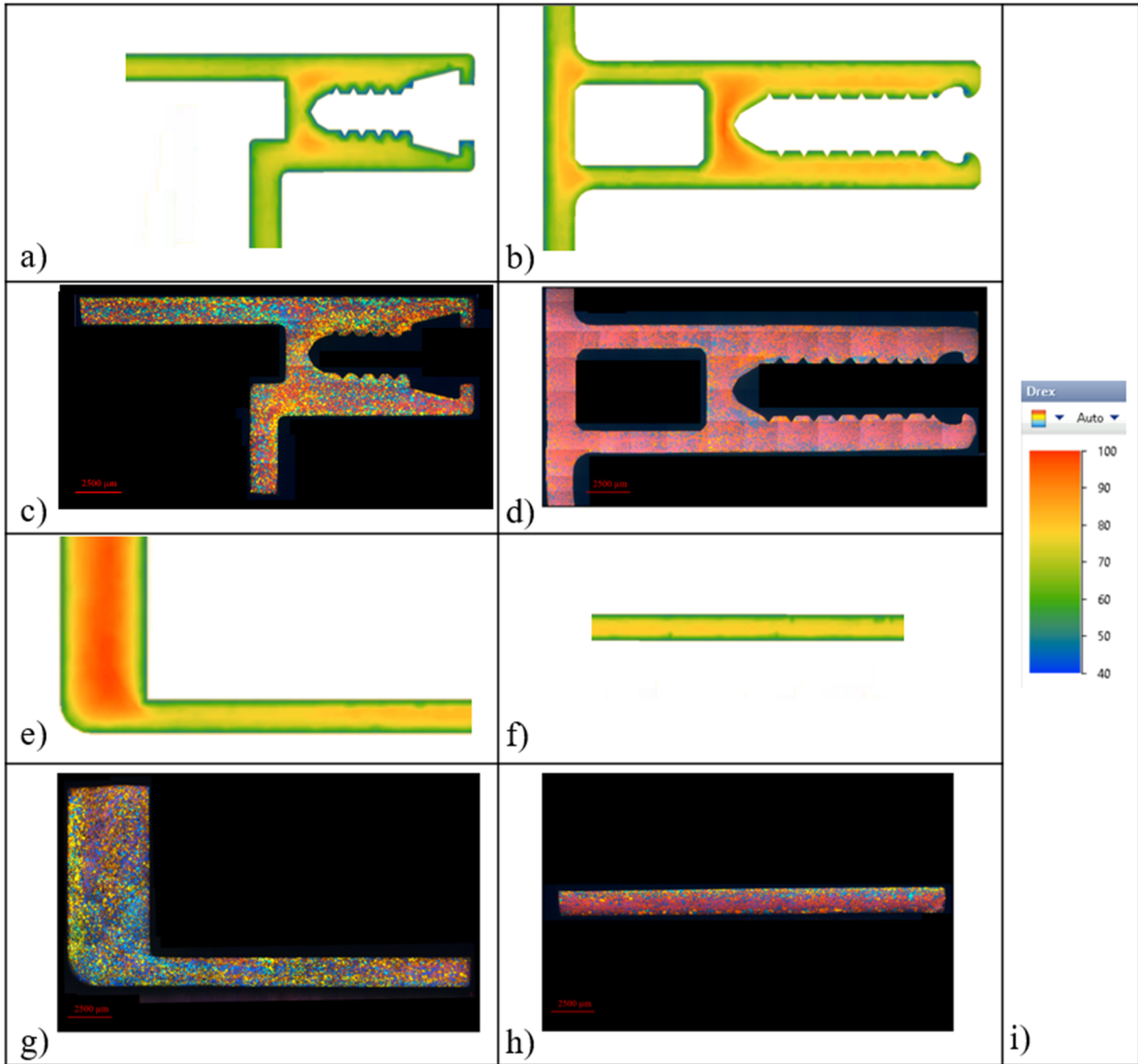


Figure 5.8: Visual comparison between the predicted and the experimental microstructures.

In Fig. 5.9, the quantitative comparison between experimental and numerical grain size calculated in the “validation set” of points is reported. In detail, the x-axis represents the diameter of grains experimentally measured while the y-axis represents the numerically predicted dimensions. Consequently, if the numerical measure perfectly matches the experimental one, the point is expected

to be exactly on the 45° green line. In order to facilitate the understanding of the prediction accuracy, two additional red lines were reported corresponding to a $\pm 25\%$ of error. Since the high number of both process and metallurgical factors affecting the final grain size, the industrial complexity of the analysed extruded geometries and the approximations deriving from the selected measurement methodology for the experimental analysis of the grain dimension, the range of $\pm 25\%$ of error, also used by Donati L. et al. in [3] for the analysis of a laboratory-scale extruded profile, should be considered as a range of excellent prediction accuracy. As can be seen in Fig. 5.9, over the 95% of the blue dots fall within the red lines, thus proving the accuracy of the developed recrystallization model.

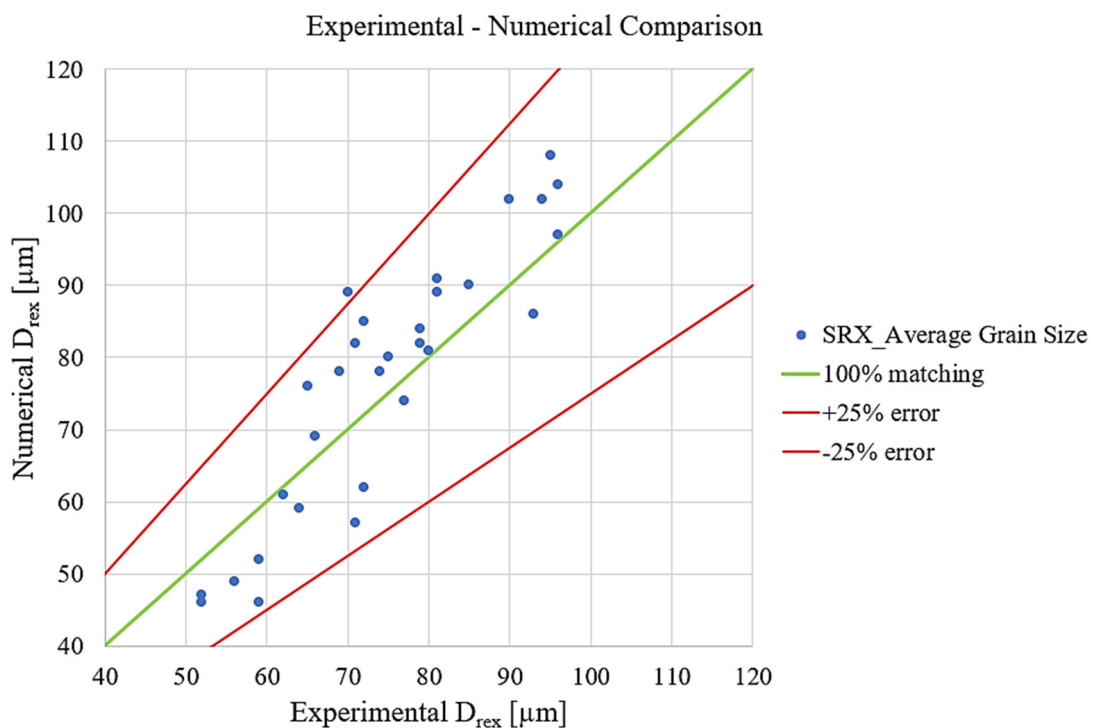


Figure 5.9: Comparison between experimental and numerical grain size.

5.5 Remarks

In the present work, the development of the recrystallization model of the AA6060 aluminum alloy was carried out together with the FEM simulation using Qform Extrusion FEM code. The microstructural analysis of the profile was performed and the collected data were used for the calibration of the proposed AA6060 recrystallization model. The main outcomes of this work can be summarized as follows:

- The final microstructure of the AA6060 hollow profile was experimentally analysed.

- An innovative static recrystallization model was developed and optimized using the data experimentally acquired from the investigate AA6060 extruded profile.
- FEM simulation of the analysed extrusion processes were carried out with an average error in the extrusion load and temperature prediction below the 1%, thus proving the reliability of the simulations.
- The prediction error of the average grain size in over the 95% of the analysed points remain below the $\pm 25\%$ thus proving the good experimental-numerical agreement and the reliability of the proposed model. Further investigations with profiles extruded with different die designs and process conditions are still needed to validate the model in different AA6060 extruded profiles.

References

- [1] A. Hensel, T. Spittel (1978) Kraft und Arbeitsbedarf bildsamer Formgebungsverfahren, 1. Auflage, Leipzig: VEB Deutscher Verlag für Grundstoffindustrie.
- [2] P.E. Gill, W. Murray (1978) Algorithms for the Solution of the Nonlinear Least-Squares Problem, SIAM Journal on Numerical Analysis 15(5): 977–992.
- [3] L. Donati, A. Segatori, M. El Mehtedi, L. Tomesani (2013) Grain evolution analysis and experimental validation in the extrusion of 6XXX alloys by use of a lagrangian FE code, International Journal of Plasticity 46: 70-81.

6. Modeling of the Recrystallization Behaviour of AA6082 Aluminum Alloy Extruded Profiles

The hot extrusion of Al-Mg-Si alloys is a manufacturing process increasingly used for the production of complex lightweight profiles with high functional and mechanical properties. These properties may be affected by the presence of the Peripheral Coarse Grain (PCG), which occurs as a surface recrystallized layer, especially during the extrusion of medium-strength alloys such as AA6082. Unfortunately, the control over the formation of the PCG structure is extremely difficult because of the high number of factors which influences the defect behaviour.

It is worth noting that all of the experimental investigations reported in 2.7 paragraph are carried out on laboratory round bar extrusions, thus limiting the range of analyzed process conditions for the experimental validation of the proposed theories. Moreover, only a few studies performed FEM simulations of the extrusion processes to study the parameters which lead to the PCG layer. As for the reported experimental investigations, all of these numerical works are conducted on simple extruded round bars and none of these proposed a unified modeling for the PCG prediction using the FEM simulation.

In this context, aim of the work presented in this chapter was to investigate the conditions that lead to the formation of the PCG and propose a theory that explains the defect kinetics. Together with the experimental investigation, purpose of this activity was also to develop a reliable model for the PCG prediction by means of FEM simulations.

In this work, experimental and numerical activities were carried out. Two cases were analysed. In the first case, the analytical modeling of the stored energy evolution in the extrusion of a AA6082 profile under different processing conditions was developed and discussed. The experimental tests were performed by Parson N et al. [1] and involved the analysis of the microstructures of AA6082 round bar profiles extruded with different bearings geometries, pre-heating temperatures, ram velocities and quenching conditions. The final aim of this work was to assess the influence of different die designs on the extruded profile, implement the developed stored energy evaluation model in the commercial FEM code Qform Extrusion®, apply the model in the extrusion of AA6082 aluminum alloy round bars and compare the numerical results with the experimental microstructures reported in [1]. In addition, the work proposed an innovative approach to determine the recrystallization behaviour of aluminum alloys extruded profiles by the modeling of the stored energy and the Zener Drag Pressure.

In the second case, two different profiles with industrial complexity were extruded, one solid and one hollow profile, both with the same AA6082 aluminum alloy. A huge range of process conditions was investigated: for each condition, data and images of the microstructure were collected and analysed in order to calibrate and validate the numerical modeling. Moreover, Scanning Electron Microscope (SEM) analysis were conducted to study the dispersoids distributions both in the billet and in the extruded profiles. After the experimental analysis, a new theory was proposed which may explain the role of all the analysed parameters in the PCG formation. From the numerical point of view, the simulation of the extrusions was carried out using the commercial FEM code Qform UK Extrusion®, which is an Arbitrary Lagrangian Eulerian (ALE) software optimized for the investigated process. Furthermore, an innovative model for the dynamic recrystallization and PCG prediction was developed and validated, comparing the numerical and the experimental results.

6.1 Case 1

6.1.1 Experimental Investigation

Different die geometries with various bearing lengths, choke lengths and choke angles were tested in the extrusion of round bar with a 25 mm diameter made by AA6082 aluminum alloy (Mg: 0.70 wt%, Si: 1.00 wt%, Fe: 0.17 wt%, Mn: 0.5wt%) and the data of the microstructure were collected and discussed. In Fig. 6.1, images of the dies together with data of the bearings geometries (Tab. 6.1) are described. For the purpose of this work, the microstructural data of the profiles extruded with the R6 -1.5° , R12 $+1^\circ$, R25 $+0^\circ$ and R35 $+3^\circ$ dies are considered and then compared with the results

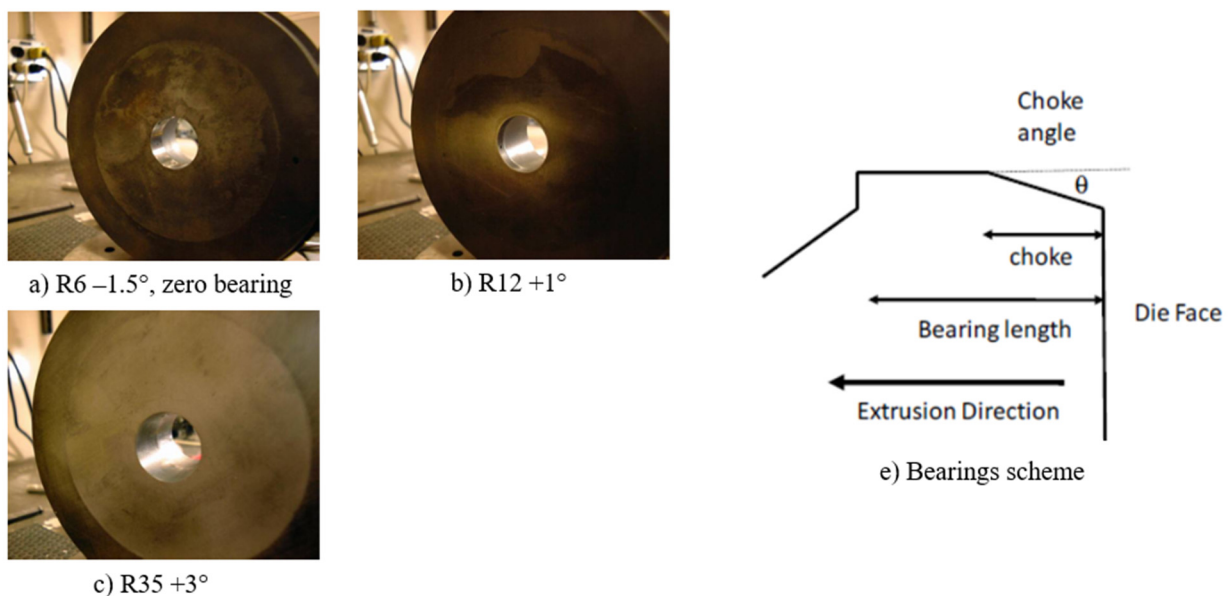


Figure 6.1: images and scheme of the die geometries [1]

Table 6.1: bearings data [1]

ID	Bearing Length [mm]	Choke Length [mm]	Angle deg.
R6 - 1.5°	6	Zero bearings	-1.5
R12 +1°	12	6	+1
R25 +0°	25	Flat	0
R35 +3°	35	17.5	+3

of the developed simulations. The experimental campaign consisted of extrusion with two billet pre-heating temperatures T_b (350 °C and 500 °C) and four ram speeds (5 mm/s, 20 mm/s, 30 mm/s, 40 mm/s). For the extrusion made at $T_b=350$ °C, the tools (die, bolster and container) were pre-heated at 330 °C, while, for the extrusions made at $T_b=500$ °C the tools were heated at 480 °C. In Fig. 6.2 and Fig. 6.3, all the microstructures of the different extruded profiles are reported both in the press-quenched condition (without any solution treatment) and after the solution treatment (30 min at 540°C using a salt bath). Specimens were taken at the middle of the length of the extruded profiles. The x-axis reports the type of bearing geometry tested during the extrusion while the y-axis the ram speed. As it can be seen from the pictures, all the profiles extruded with $T_b=350$ °C and press-quenching (Fig. 3a) present a fibrous microstructure. The profiles extruded with $T_b=500$ °C and press-quenching (Fig. 3b) are also fibrous except for $T_b=500$ °C with dies R6 -1.5° and R25 +0° at higher speeds (over 20 mm/sec), where a surface recrystallized layer (PCG) is visible. For the extrusion made at a pre-heating temperature of 350 °C, the solution treatment greatly impacted on the static recrystallization behaviour. All of the specimens' microstructures changed from fibrous (Fig. 6.2a) to partially or fully recrystallized (Fig. 6.3a). For the extrusions made at a pre-heating temperature of 500 °C, the situation is completely different. In this case, the experimental evidence shows that the solution treatment did not affect the recrystallization of the specimens, as there is no difference in terms of microstructure between Fig. 6.2b and Fig. 6.3b.

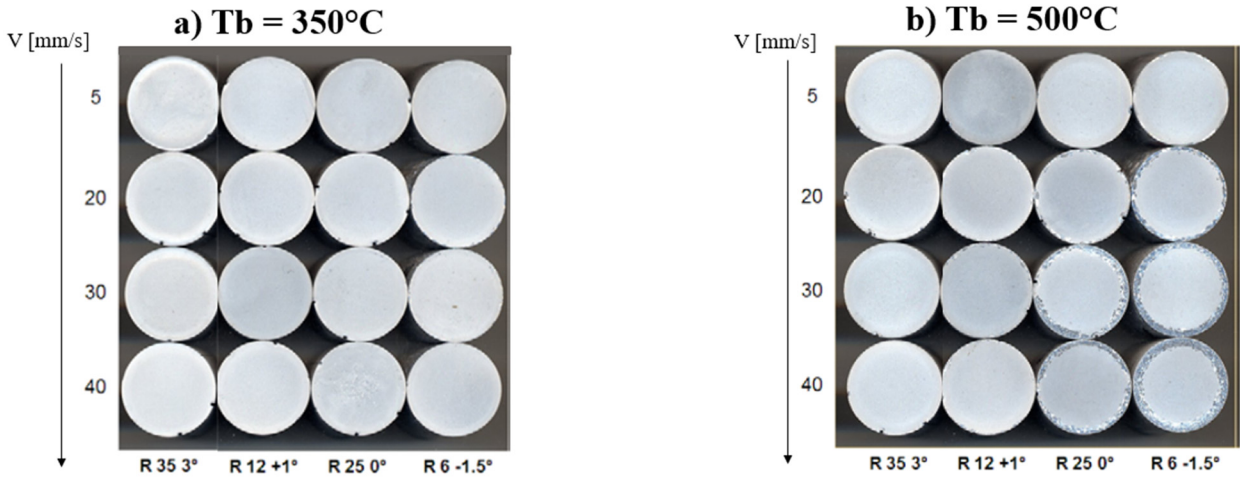


Figure 6.2: microstructures of the press quenched specimens [25].

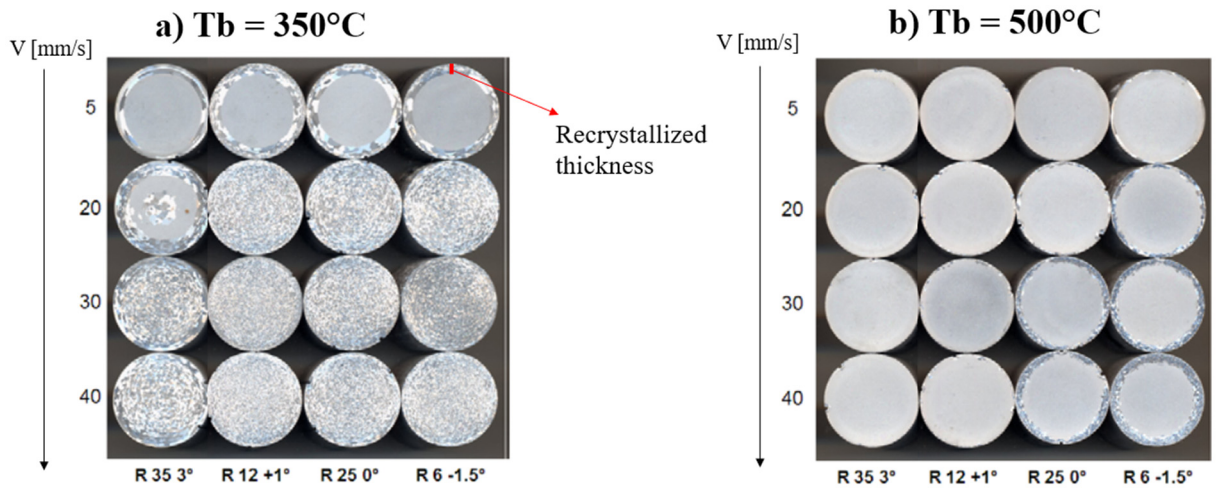


Figure 6.3: microstructures of the solution treated specimens [1].

6.1.2 Recrystallization Modeling in AA6082 Aluminum Alloy

According to the work of [2], the formation and growth of new grains in 6XXX aluminum alloy profiles after the extrusion process is related to the difference between driving force and retarding force for the recrystallization. During the manufacturing processes, a part of the deformation energy is stored in the material in the form of dislocations and point defects. This energy, called Stored Energy, acts in favour of the recrystallization and it can be calculated as follow [3]:

$$Pd = \frac{Gb^2}{10} \left[\rho_i(1 - \ln(10b\rho_i^{0.5})) + \frac{2\theta}{b\delta} \left(1 + \ln\left(\frac{\theta c}{\theta}\right) \right) \right] \quad (6.1)$$

where G is the material shear modulus (2.05×10^{10} Pa), b the Burgers vector (2.86×10^{-10} m), ρ_i the dislocation density, δ the subgrain size, θ the misorientation angle and θc the misorientation angle

limit (15°). The dislocation density ρ_i and the misorientation angle θ were calculated according to [4]. The dislocation density depends on the strain ε and Zener-Hollomon parameter Z (Fig. 6.4a). The misorientation angle depends on the strain rate $\dot{\varepsilon}$, the temperature T and the strain ε (Fig. 6.4b).

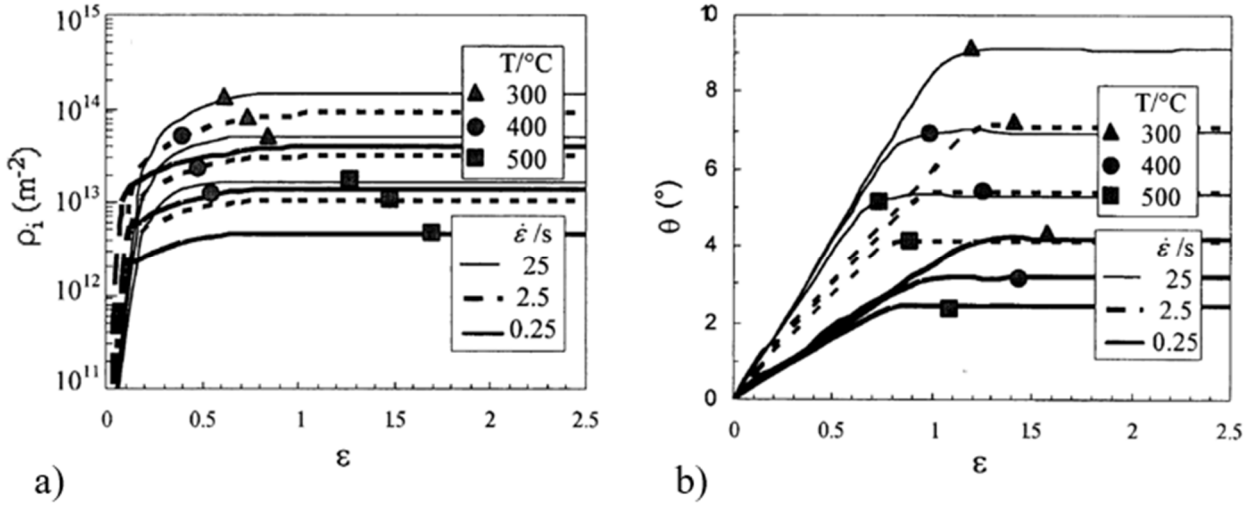


Figure 6.4: a) Dislocation density [4], b) Misorientation angle [4].

The subgrain size and the Zener-Hollomon parameter were calculated according to [5]:

$$\frac{1}{\delta} = C (\ln Z)^n \quad (6.2)$$

$$Z = \dot{\varepsilon} \exp\left(\frac{Q}{RT}\right) \quad (6.3)$$

where $C=3.36 \times 10^{-9} \text{ m}^{-1}$, $n=5.577$, Q is the activation energy of the AA6082 (182000 J/mol*K [6]), R is the universal gas constant (8.341 J/mol) and $\dot{\varepsilon}$ is the maximum strain rate for each point of material flow during the extrusion deformation path.

The retarding force for the recrystallization is due to dispersoids, i.e. Zener Drag Pressure, and alloying elements in solid solution, which pin the nucleated grains and prevent growth from occurring [2]. According to the work of [7], the Zener Drag Pressure calculation resulted in:

$$P_Z = \frac{3 * f * \gamma}{4 * r} \quad (6.4)$$

where f and r are the fraction area and the mean size of the dispersoids, respectively, and γ is the grain boundary energy. At coarse approximation, it is possible to extend the Eq. 1 of retarding force given by dispersoids to the retarding force due to solute atoms. In this case, the atom fraction and

atomic radius are used instead of volume fraction and dispersoid average. However, it is very difficult to correctly evaluate the total value of the retarding force for two main reasons: on the one hand, the concentration of dispersoids is not homogeneous within the material and is not always stable from the homogenized billet to the extruded profile as proved by the experimental investigation. On the other hand, it is really hard to evaluate the atom fraction and atomic radius of the elements in solid solution. Moreover, the elements pinning effect depends on the velocity of the moving boundaries [2]. Since the microstructural data for the f and r evaluation were not available, the values of Pz have been supposed based on the comparison between stored energy and recrystallized thickness of the extrusions made under different process conditions, as explained in more detail in the following.

6.1.3 Numerical Simulation of the Extrusion Process

The numerical simulation of the extrusions was carried out using the Arbitrary Lagrangian Eulerian FEM code Qform Extrusion®. As constitutive model for the AA6082 aluminum alloy, the following Hensel-Spittel equation was selected to calculate the material flow stress $\bar{\sigma}$ which depends to the contribution of strain $\bar{\epsilon}$, strain rate $\dot{\bar{\epsilon}}$ and temperature T [8]:

$$\bar{\sigma} = A \cdot e^{m_1 T} \cdot \bar{\epsilon}^{-m_2} \cdot \dot{\bar{\epsilon}}^{-m_3} \cdot e^{\frac{m_4}{\bar{\epsilon}}} \cdot (1 + \bar{\epsilon})^{m_5 T} \cdot e^{m_7 \bar{\epsilon}} \cdot \dot{\bar{\epsilon}}^{m_8 T} \cdot T^{m_9} \quad (6.5)$$

The values of the material parameters (m1-m9) are reported in Tab. 6.2 according to [9].

Table 6.2: Hensel-Spittel parameters for the AA6082 aluminum alloy [9].

Material parameters	AA6082
A	568000
m1	-0.002117
m2	0.1059
m3	0.08299
m4	0.0009266
m5	-0.0005221
m7	0.02343
m8	0.00006741
m9	-1.208

The workpiece-tools friction conditions were set to the default values contained in the Qform Extrusion database (Tab. 6.3).

Table 6.3: Friction conditions.

Surface	Friction condition
Billet-Container	Sticking condition
Billet-Ram	Sticking condition
Billet-Die	Sticking condition
Bearings	Levanov model ($m = 0.3$, $n = 1.25$)

The extrusions process parameters collected from the experimental campaign and components geometry data are reported in Tab. 6.4 and Tab. 6.5.

Table 6.4: Process parameters.

Process Parameters	
Aluminum alloy	AA6082
Ram speeds [mm/s]	5/20/30/40 mm/s
Container/Billet/Die temperatures [°C]	380/480 °C
Ram acceleration time [s]	5

Table 6.5: Extrusion components geometry data.

Extrusion components geometry data	
Extrusion ratio	20
Billet length [mm]	384
Billet diameter [mm]	101
Container diameter [mm]	266
Billet Rest length [mm]	18

6.1.4 Comparison Between Numerical and Experimental Results

Fig. 6.5 and Fig. 6.6 report the results of the exit temperatures (highlighted values are taken at the middle profile radius for each specimen) and the stored energy predictions, respectively. The simulation of each case requires an average time of 29 min. In the extrusions made with $T_b=350^\circ\text{C}$, the exit temperatures of the profiles are between 400°C and 450°C and the stored energy is significantly higher if compared to the extrusions with $T_b=500^\circ\text{C}$, where the exit temperatures are between 530°C and 560°C . The FEM acquired data are taken at the medium value of the ram stroke because the microstructures reported in Fig. 6.2 and Fig. 6.3 were taken from the middle of the extruded profile length.

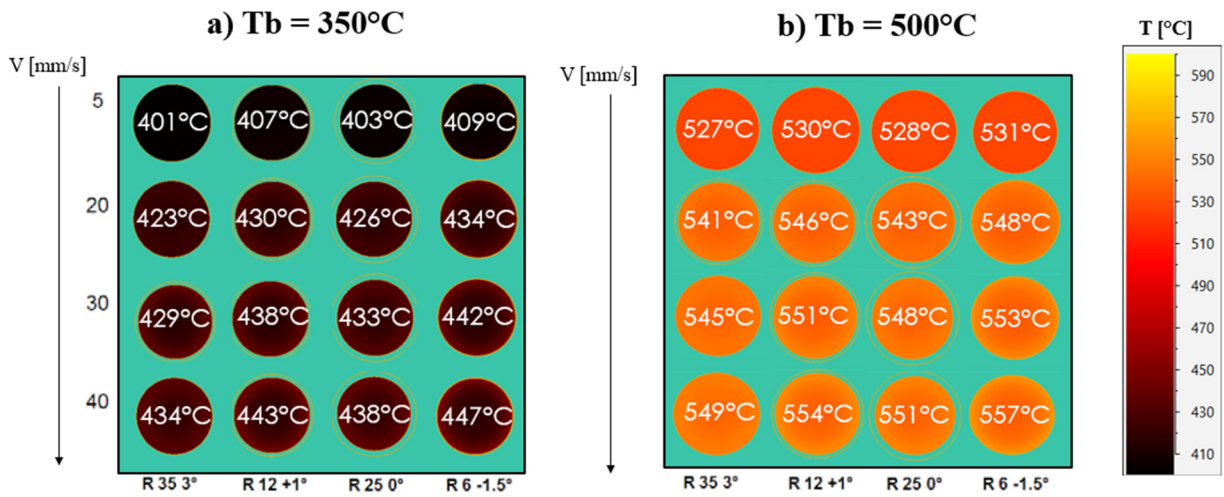


Figure 6.5: Exit temperature.

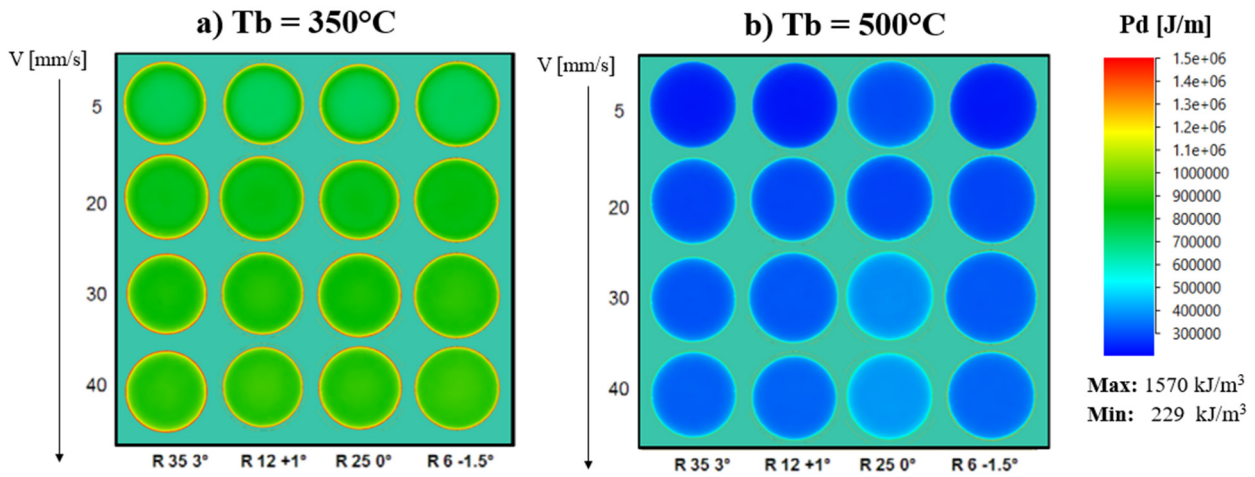


Figure 6.6: Stored energy predictions after extrusion.

The stored energy predictions are then compared with the microstructure for each tested condition in order to understand at what stored energy value the recrystallization occurs. As said, in the specimens extruded with $T_b=350\text{ }^\circ\text{C}$ in the press-quenched condition, no static recrystallization occurred. Therefore, according to what is reported in the literature [3], the stored energy must always be lower than P_z . For this reason, a P_z value higher than the highest value of P_d found on the simulation is assumed ($P_z > 1570\text{ kJ/m}^3$).

In the specimens extruded with $T_b=350\text{ }^\circ\text{C}$ after the solution treatment, a partially or fully static recrystallization occurred. Consequently, after selecting one extrusion condition for the calibration (in our case the extrusion made with the $R_{35} + 3^\circ$ die, extrusion speed 5 mm/s , Fig. 6.7), the value of P_z for the solution treated specimens was taken as the stored energy value in the point where the recrystallized begins ($P_z > 819\text{ kJ/m}^3$). The computation of the P_z evaluation process is detailed in Fig. 8 at the radius of $9,5\text{ mm}$.

In the extrusions made with $T_b=500\text{ }^\circ\text{C}$, the microstructure does not change between press quenched and solution treated specimens. For this reason, one single P_z value was assumed for the two conditions ($P_z=600\text{ kJ/m}^3$), using the same methodology applied to the case described before. The reason we adopted different P_z values for extrusions with different exit temperatures or solution treatment is because the Zener Drag Pressure is depending on the dispersoids distribution and size which, in turn, depends on the temperature. Consequently, with the purpose to model and predict the recrystallization behaviour, it is reasonable to assume that P_z may change with temperature and, consequently, in particular temperature conditions the SRX is more likely to occur. The validation of this approach and consequently of the assumed values for Zener drag Pressure, will be performed by comparing the recrystallized layer thickness of FEM predictions over experimental data.

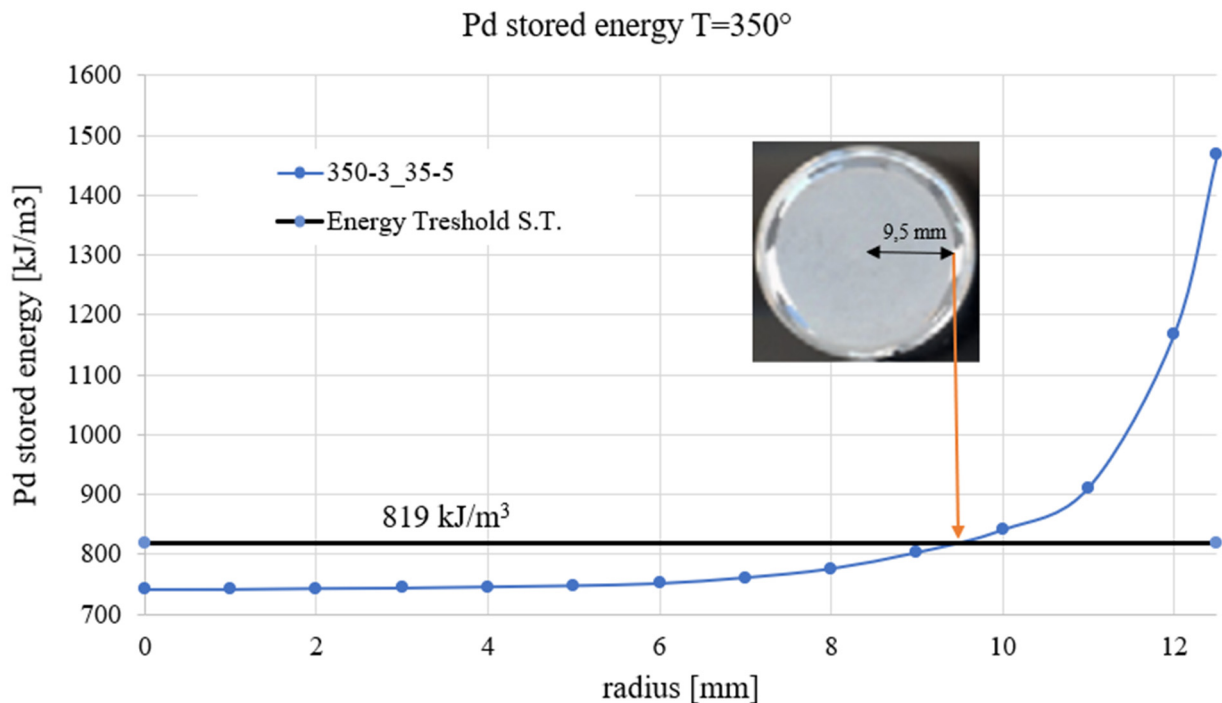


Figure 6.7: Zener Drag pressure evaluation process.

In Fig. 6.8 and Fig. 6.9, the stored energy behaviour along the radius of the specimens for the extrusions made with $T_b=350\text{ }^\circ\text{C}$ and $T_b=500\text{ }^\circ\text{C}$ were reported together with the supposed P_z values in the press-quenched and solution treated conditions.

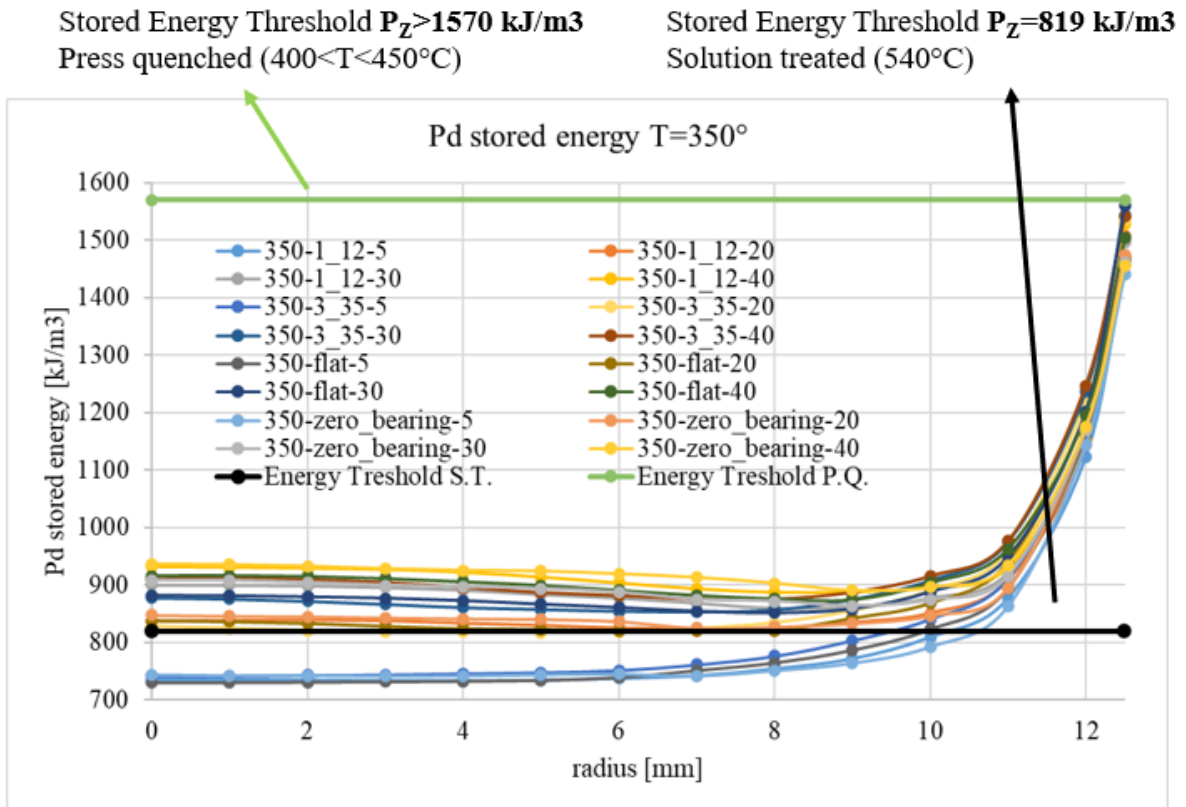


Figure 6.8: Stored energy and stored energy thresholds (P_z values) in the $T_b = 350^\circ\text{C}$ case.

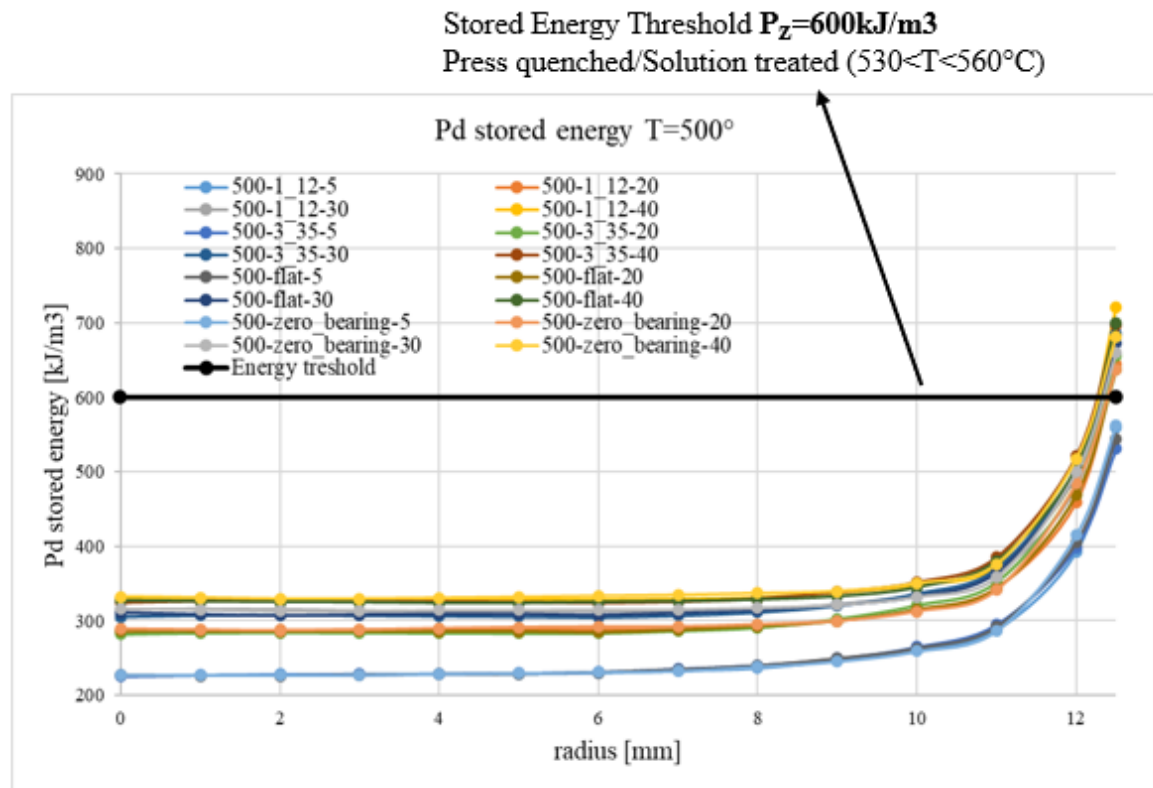


Figure 6.9: Stored energy and stored energy thresholds (P_z values) in the $T_b = 500^\circ\text{C}$ case.

The comparisons between experimental and numerical recrystallized thicknesses are shown in Fig. 6.10-6.17 for each bearing geometry and pre-heating billet temperature, in order to validate the methodology and the assumed critical values of Pz. In the left part of each figure, it is shown the stored energy evaluation along the extruded bar radius together with the estimated Pz value. In the right part of the figures, it is reported the comparison between numerical and experimental recrystallized thickness for the press-quenched and solution treated conditions. This comparison is shown by reporting experimental/numerical images and thickness measurements. The numerical recrystallized thickness values were obtained by comparing the predicted stored energy with the supposed value of Pz.

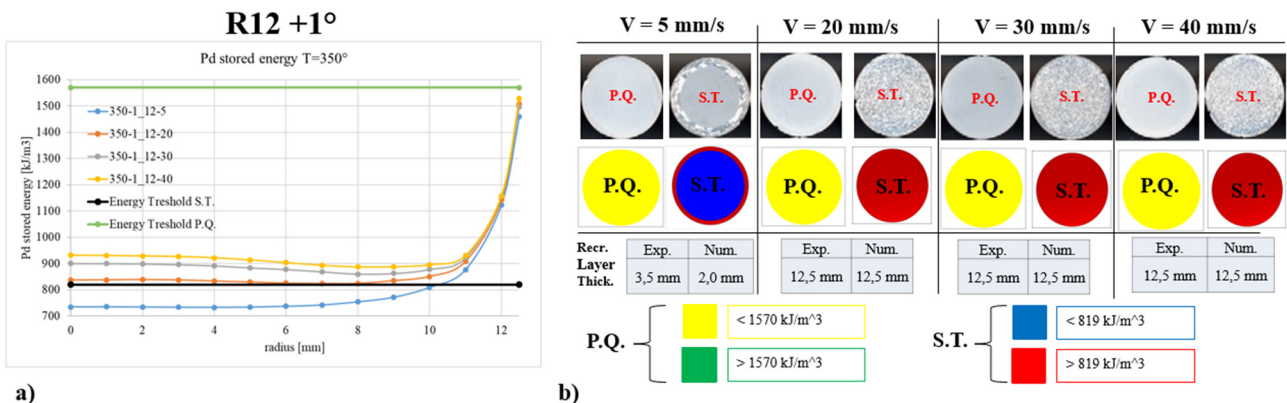


Figure 6.10: R12 +1° die, Tb=350°, all speeds. a) stored energy behaviors and comparison with estimated Pz values, b) comparison between numerical and experimental recrystallized thicknesses for Press Quenched (P.Q.) and Solution Treated (S.T.) conditions.

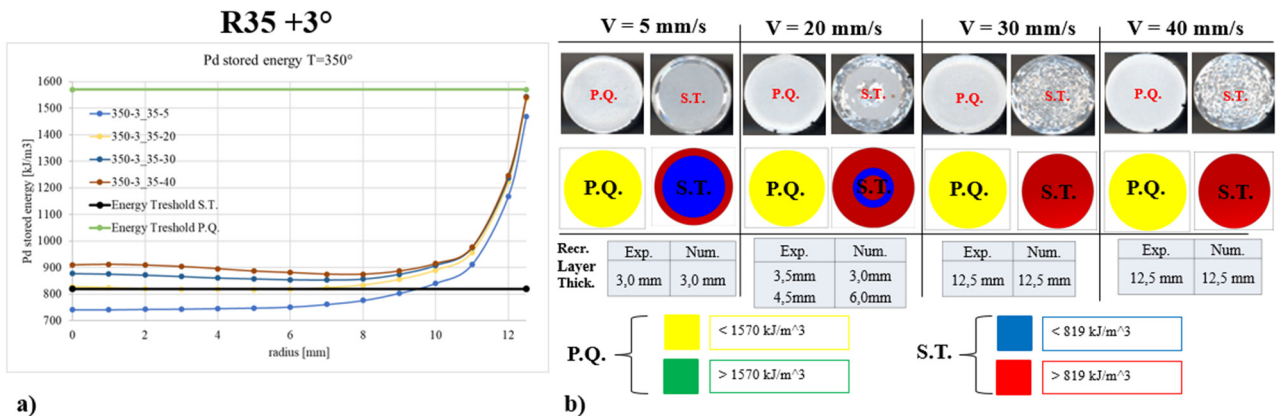
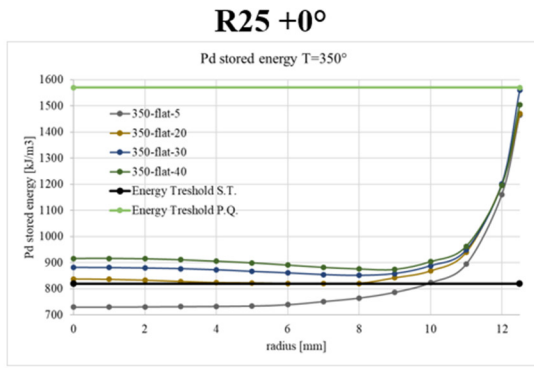
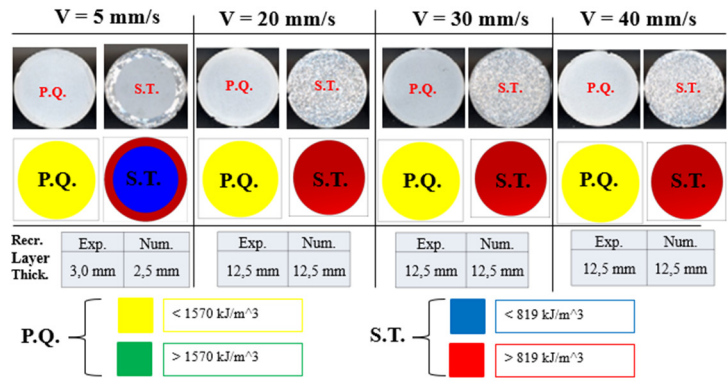


Figure 6.11: R35 +3° die, Tb=350°, all speeds. a) stored energy behaviors and comparison with estimated Pz values, b) comparison between numerical and experimental recrystallized thicknesses for Press Quenched (P.Q.) and Solution Treated (S.T.) conditions.

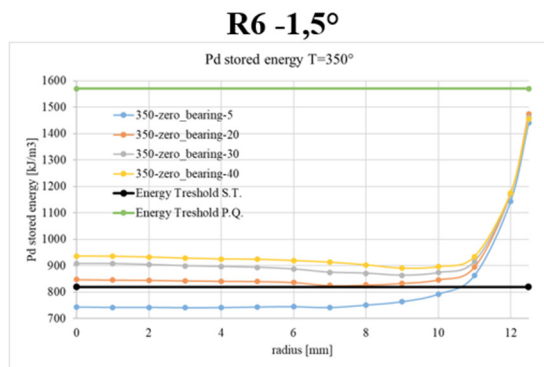


a)

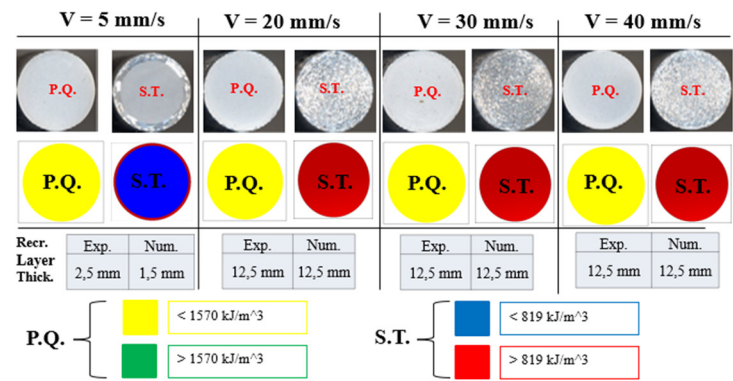


b)

Figure 6.12: R25 +0° die, Tb=350°, all speeds. a) stored energy behaviors and comparison with estimated Pz values, b) comparison between numerical and experimental recrystallized thicknesses for Press Quenched (P.Q.) and Solution Treated (S.T.) conditions.

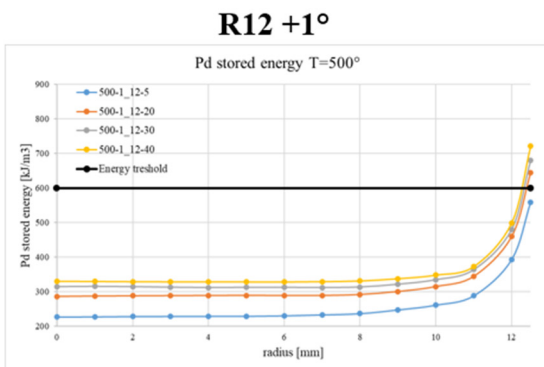


a)

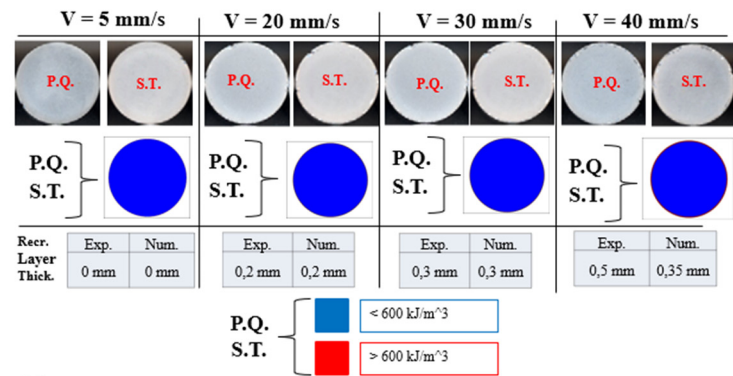


b)

Figure 6.13: R6 -1,5° die, Tb=350°, all speeds. a) stored energy behaviors and comparison with estimated Pz values, b) comparison between numerical and experimental recrystallized thicknesses for Press Quenched (P.Q.) and Solution Treated (S.T.) conditions.

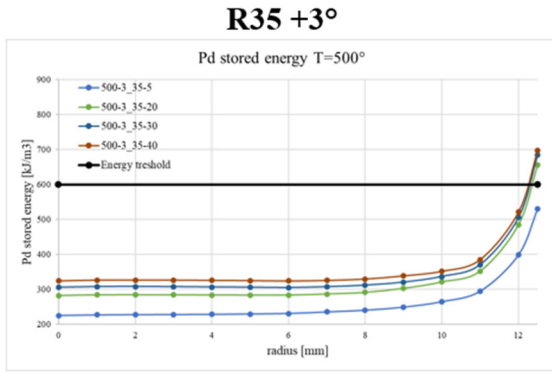


a)

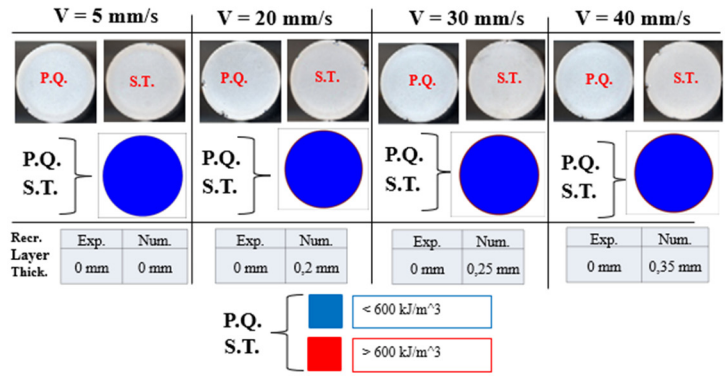


b)

Figure 6.14: R12 +1° die, Tb=500°, all speeds. a) stored energy behaviors and comparison with estimated Pz values, b) comparison between numerical and experimental recrystallized thicknesses for Press Quenched (P.Q.) and Solution Treated (S.T.) conditions.

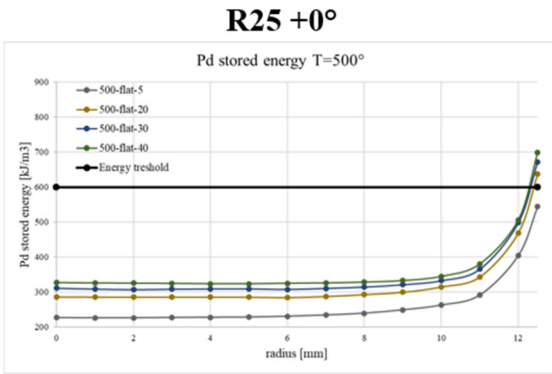


a)

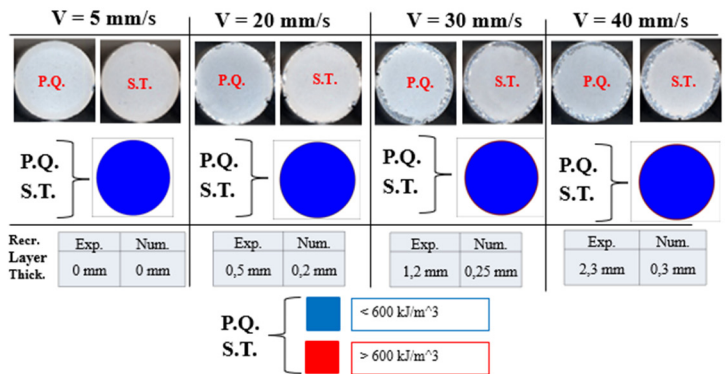


b)

Figure 6.15: R35 +3° die, Tb=500°, all speeds. a) stored energy behaviors and comparison with estimated Pz values, b) comparison between numerical and experimental recrystallized thicknesses for Press Quenched (P.Q.) and Solution Treated (S.T.) conditions.

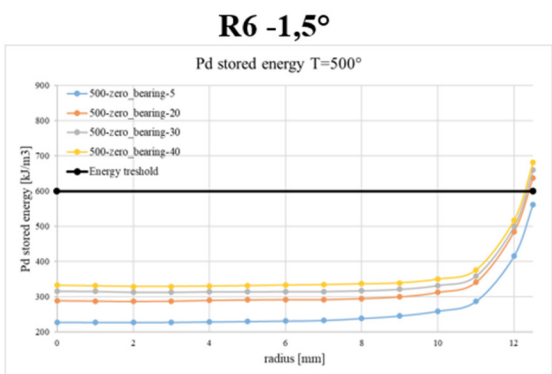


a)

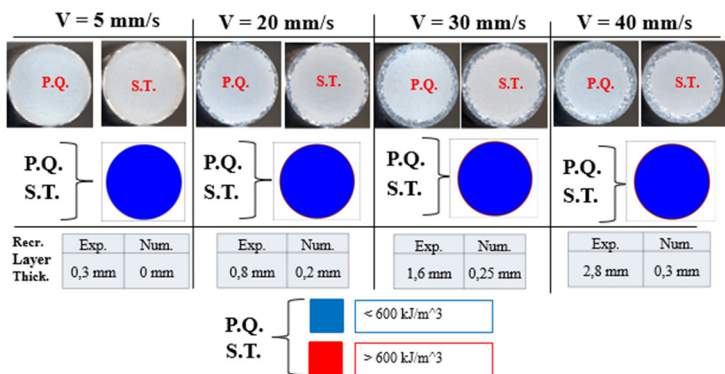


b)

Figure 6.16: R25 +0° die, Tb=500°, all speeds. a) stored energy behaviors and comparison with estimated Pz values, b) comparison between numerical and experimental recrystallized thicknesses for Press Quenched (P.Q.) and Solution Treated (S.T.) conditions.



a)



b)

Figure 6.17: R6 +1.5° die, Tb=500°, all speeds. a) stored energy behaviors and comparison with estimated Pz values, b) comparison between numerical and experimental recrystallized thicknesses for Press Quenched (P.Q.) and Solution Treated (S.T.) conditions.

These results show a good accuracy in the prediction of the recrystallized layers in almost all experimental conditions (Fig. 6.18). The accuracy is higher for the conditions tested with Tb=350 °C.

In this case, almost a perfect matching (with a maximum error of 1.5 mm) was found between numerical and experimental data of the specimens after solution treatment. In the $T_b=500\text{ }^\circ\text{C}$ case, the results are good in the extrusion made with the R 12 $+1^\circ$ die (with a maximum error of 0.15 mm) but there is an overestimation with the R35 $+3^\circ$ (with a maximum error of 0.35 mm) and an underestimation in the R25 $+0^\circ$ and R6 -1.5° (with a maximum error of 2.5 mm). This is probably due to the lack of profile exit temperature data in the experimental trials; for this reason, it was not possible to check the accuracy of the numerical exit temperatures, that in the $T_b=500\text{ }^\circ\text{C}$ case are very close and sometimes higher than the annealing temperature. Moreover, these inaccuracies may also be caused by the effect of the strain rate. Using the R35 $+3^\circ$ die, where the bearings are longer and the material entry into the bearings zone is less sharp, the profile shows no recrystallized layer even with high ram speed. Using an R6 -1.5° die, where the bearings are non-existent (zero bearings case) and the profile has a sharp entry into the bearing zone, the profile shows the highest value of recrystallized thickness. Considering that higher bearings and choke angles correspond to a decrease in the maximum strain rate value reached during the material flow, a dependence between maximum strain rate and surface recrystallization (PCG) should be further investigated together with the effect of the profile exit temperature.

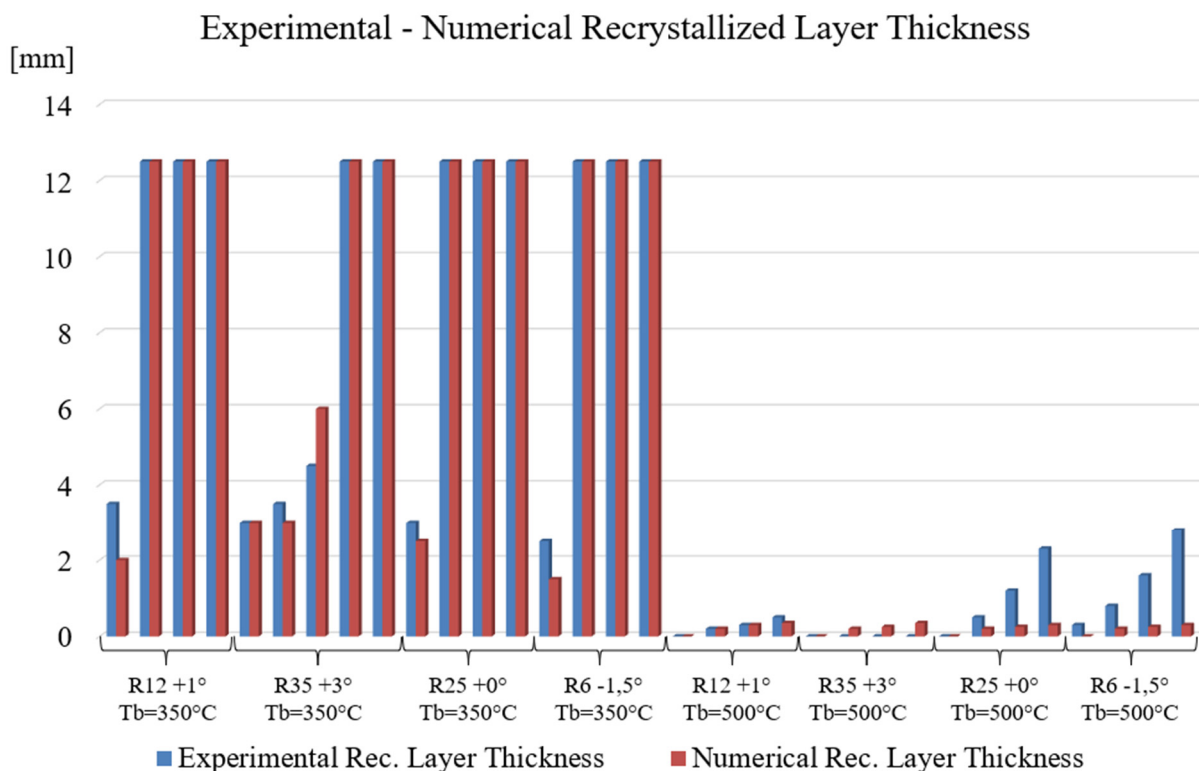


Figure 6.18: Comparison between experimental and numerical recrystallized layer thickness in all the investigated cases.

In Fig. 6.19, the assumed values of the Zener Drag Pressure are reported and correlated with the exit temperatures shown in Fig. 6.5 for the press-quenched conditions (from 401 °C to 447 °C for the extrusions with $T_b = 350$ °C and from 527 °C to 557 °C for the extrusions with $T_b = 500$ °C) and the annealing temperature of 540 °C for the solution treated conditions. The empty circles represent the P_z values assumed in the non-recrystallized specimens of the extrusions made with $T_b = 350$ °C in the press-quenched condition, in which case it was assumed as P_z the maximum stored energy value of 1570 kJ/m³ found in the simulation, even if it can be higher. The full green circle represents the P_z value of 819 kJ/m³ supposed in the extrusions made with $T_b = 350$ °C with solution treatment at 540 °C. The full orange circles represent the P_z value of 600 kJ/m³ supposed for the extrusions made with $T_b = 500$ °C, both for press-quenched and solution treated conditions.

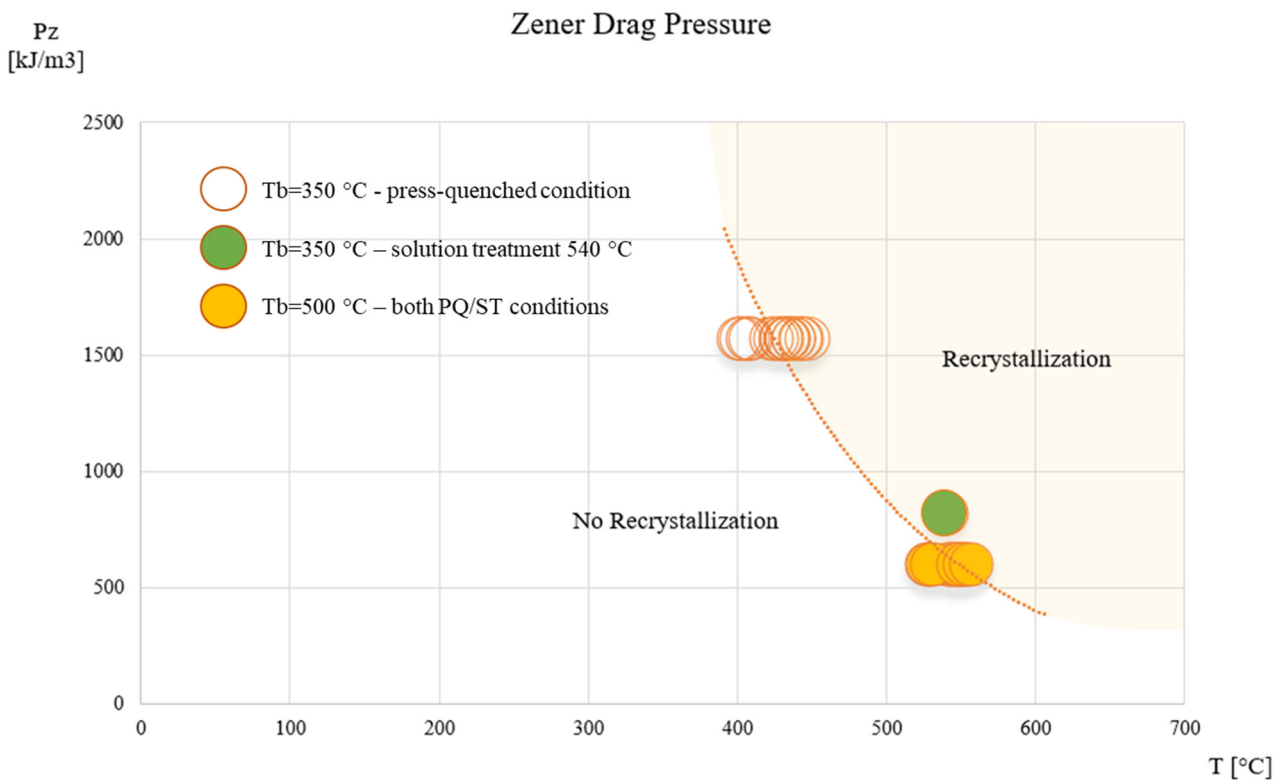


Figure 6.19: Estimated Zener Drag pressures and temperatures.

The graph in Fig. 6.19 divides the Zener Drag pressure/Temperature area into two zones: conditions on the left side of the dashed line (which was inserted in the figure to help understand the trend of P_z in relation to the temperature) promote fibrous structures while conditions on the right side of the line recrystallized ones. It is clear the existence of a correlation between the retarding forces for recrystallization and extrusion parameters such as temperature, die geometry and ram speed that needs to be investigated and modeled through further experimental trials and research activities.

6.1.5 Remarks

In the present work, the numerical modeling of the extrusion process and of the stored energy was carried out using Qform Extrusion FEM code. The experimental data were taken from the work of Parson N et al. [1], in which several industrial-scale extrusions of a AA6082 round bars were made by testing different die geometries and process conditions. The main outcomes of this work can be summarized as follows:

- The results of the various stored energy predictions of the extrusions reported in [1] were collected, compared and discussed. Consequently, by comparing the microstructures to the stored energy data, an estimation of the Zener Drag pressure was carried out. Finally, the results of the predicted recrystallized thickness were presented.
- A good correlation between numerical predictions and experimental data was found in the recrystallized thickness evaluation of the extruded profiles. In the $T_b=350\text{ }^\circ\text{C}$ case, almost a perfect matching was found between numerical and experimental data of the specimens. In the $T_b=500\text{ }^\circ\text{C}$ case, the results were almost perfectly in accordance with the experimental data in the extrusions made with the R 12 +1° die, but a slightly overestimation in the R 35 +3° case and a slightly underestimation in the R25 +0° and R6 -1.5° case was observed.
- An innovative approach for the evaluation of the recrystallized thickness in the extrusion of AA6082 aluminum alloys was proposed. In order to present a complete model able to compute stored energy, Zener Drag pressure and recrystallization behaviour according to the extrusion and annealing parameters, further investigations should be carried out.

Considering the results of the current work on the influence of the die design and process parameters on the microstructure and, therefore, on the extruded profile properties and considering the results of the numerical modeling and simulations of the AA6082 recrystallization behaviour, it was decided to continue the analysis through a specific experimental and numerical campaign dedicated to the study of the AA6082 microstructure evolution kinetics. This campaign is presented in the 6.2 paragraph.

6.2 Case 2

6.2.1 Experimental Investigation

The AA6082 profiles were extruded by Hydro plant in Finspång (Sweden) with a 10 MN extrusion press. In Fig. 6.20, the geometries of profiles and dies are shown. In Table 6.6 and Table 6.7, the AA6082 chemical composition and the extrusion process parameters of the two profiles are reported, respectively.

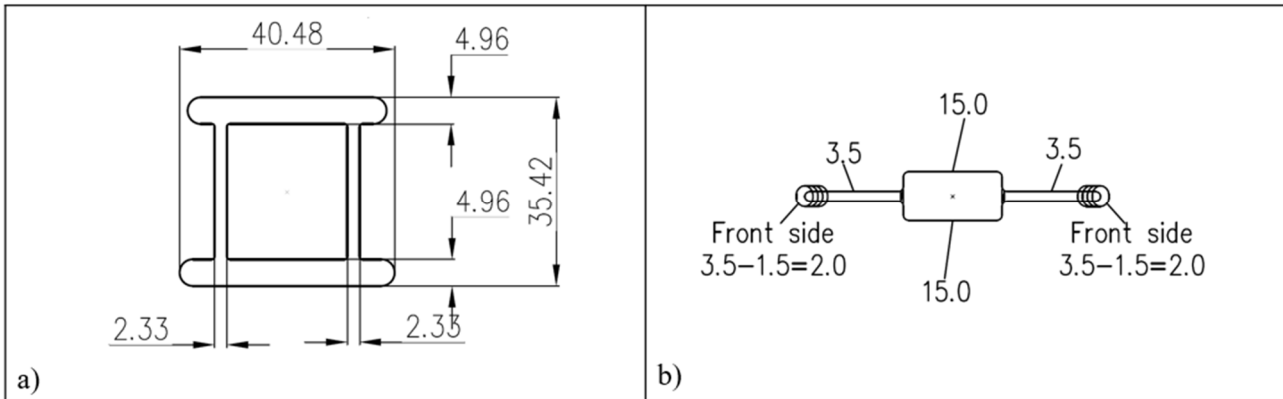


Figure 6.20: Investigated profiles and die geometries. a) Profile *a*. b) Profile *b*

Table 6.6: AA6082 chemical composition

Element [Wt %]	Si	Fe	Cu	Mn	Mg	Cr	Ni	Zn
	1.00	0.20	0.03	0.49	0.62	< 0.01	< 0.01	0.01

As shown in Tab. 6.2, Profile *a* was extruded with three different billet temperatures and three different ram speeds while Profile *b* with one billet temperature and five ram speeds. The large range of process conditions was selected in order to have a reliable amount of data for the correct understanding of the PCG kinetics and for the model validation. In this experimental campaign, the same billet material and homogenization cycle (565°C - 2h) was used for the two extrusions. All the data about profile exit temperatures and extrusion loads were collected during the extrusion of the two profiles in order to validate the numerical simulations. Moreover, the water quenching system was deactivated in order to avoid the contamination of the experimental results by its functioning (blocking the recrystallization after the extrusion) thus favouring the investigation of the effect of the billet temperature, ram speed, profile exit temperature and profile geometry on the microstructure evolution.

Table 6.7: Process parameters and geometry tolerances

Process parameters and geometry tolerances	Profile <i>a</i>	Profile <i>b</i>
Aluminum alloy	AA6082	AA6082
Extrusion ratio	18.2	31.5
Ram speed [mm/s]	2 / 5 / 10	2 / 5 / 10 / 15 / 20
Container temperature [°C]	410	410
Billet temperature [°C]	350 / 450 / 500	500
Die temperature [°C]	480	480
Ram acceleration time [s]	5	5
Billet length [mm]	400	350
Billet diameter [mm]	100	100
Container diameter [mm]	107	107
Billet Rest length [mm]	15	15
Billet Homogenization	565°C - 2h	565°C - 2h

In Fig. 6.21, the images of the anodized sample and the SEM analysis of the billet material are reported.

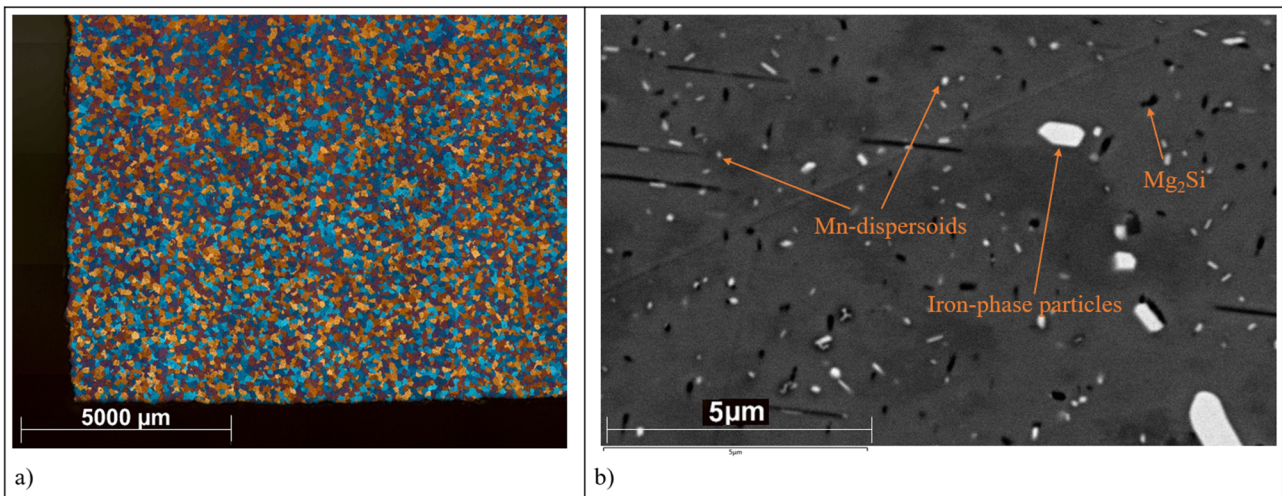


Figure 6.21: a) Microstructure of the billet, b) SEM analysis of the billet material.

The microstructure of Fig. 6.21a shows a complete recrystallized structure as consequence of the billet casting and further homogenization process with an average grain dimension of 121 μm. All the grain size measurements were performed according to the ASTM-E112 regulation. In Fig. 6.21b, the SEM acquired image of the billet material is shown, evidencing the secondary particles (Mn-dispersoids) characterized with small dimensions (typically 10-500 nm) and precipitated during the homogenization from alloying elements in solid solution, the primary particles (Iron-phase particles) solidified during the casting and the Mg₂Si constituent particles.

In Fig. 6.22, the microstructures of Profile *a* extruded with different process conditions are shown. The analysed samples were taken at the middle length of the extrusion profile where the process achieved the thermal steady-state condition. For each sample, the billet temperature “ T_b ”, the ram speed “ V_{ram} ” and the profile exit temperature “ T_{exit} ” acquired from a pyrometer are reported. The first result is that the investigated billet temperature range has a negligible influence on the PCG behaviour since the microstructures of the specimens with billet temperature of 450°C (Fig. 6.22a-c) and 500°C (Fig. 6.22d-f) are quite identical. Considering the extrusions made with both billet temperatures, the increase in ram speeds corresponds to the increase in exit temperature and the PCG thickness. In Fig. 6.23, the zoom-in images of the $T_b=450^\circ\text{C}$ specimens are reported in order to better show the evolution of the defect with the ram speed increase.

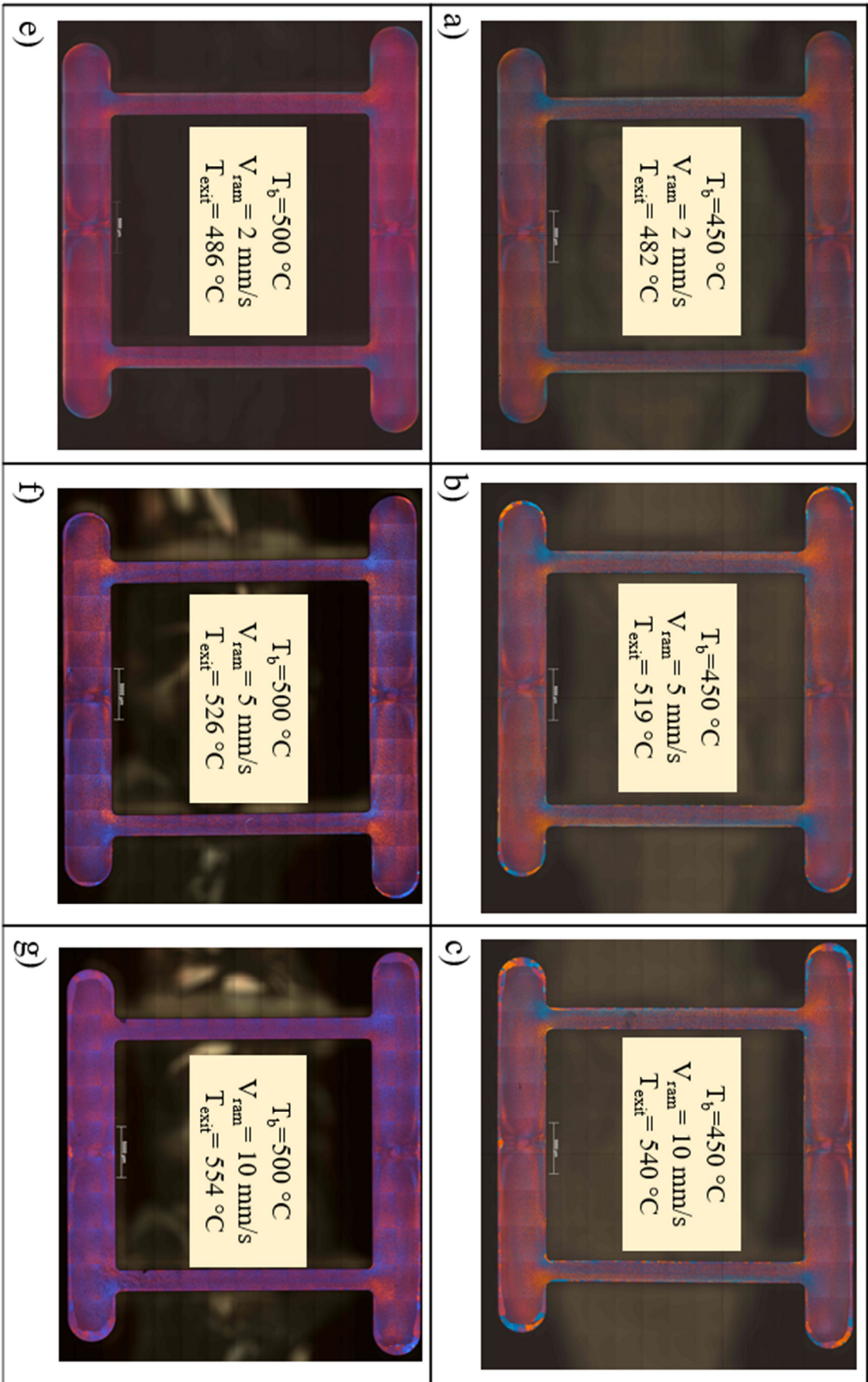


Figure 6.22: Microstructures of Profile *a* extruded with different process conditions.

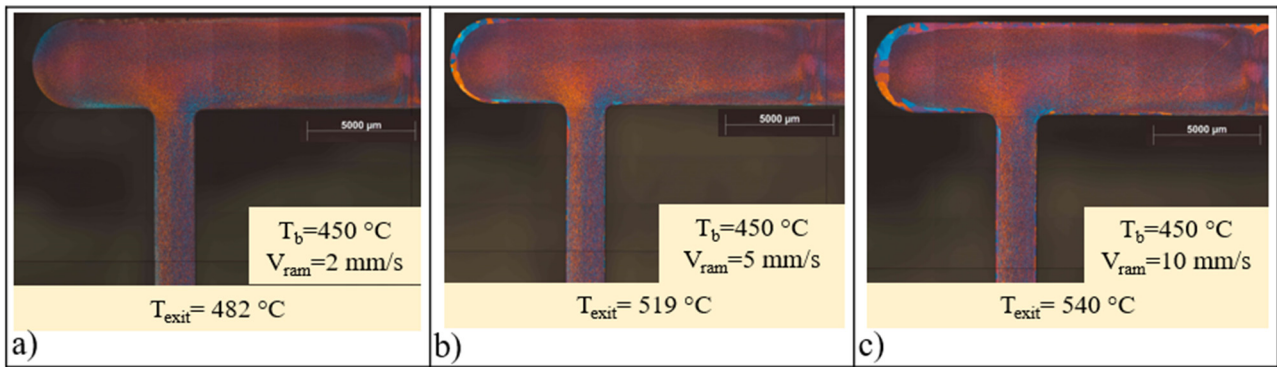


Figure 6.23: Microstructures of Profile *a* with $T_b = 450^\circ\text{C}$ extruded with different ram speeds (zoom-in images).

In Fig. 6.24, the microstructure of the PCG zones was further examined combining the results of cross and longitudinal sections in order to investigate the influence of the fibrous grains dimensions on the PCG zones. Fig. 6.24a shows the microstructure of the extruded profile at 2 mm/s, which is completely fibrous. From the analysis of Fig. 6.24b and Fig. 6.24c which correspond to sections A-A and B-B of Fig. 6.24a, it can be seen that the grains in the inner part of the material are elongated in extrusion direction, as can be reasonably expected due to the applied strain field, with a thickness average dimension of 20-40 μm and a length average dimension reaching values up to 50 times higher than the grain thickness. However, in Zone 1 (Fig. 6.24b) and Zone 2 (Fig. 6.24c), grains show a different shape, with a similar average thickness of 5-15 μm but a different average length of 20-40 μm , extremely lower if compared to the inner grains. This difference is caused by the very high strain values reached in Zone 1 and Zone 2 and, consequently, by the occurrence of the DRX kinetics. According to De Pari Jr. L. and Misiolek W.Z. [10], which theorized a combined gDRX–cDRX model called Joint Dynamic Recrystallization (jDRX), during the manufacturing process the grain is initially elongated along the main direction of deformation. As the strain increases, a critical value is reached and the original grain is divided into two grains. By further increasing the strain, these divisions multiply until the original elongated grain is converted into a set of fine equiaxed grains. In this context, Zone 1 (Fig. 6.24b) and Zone 2 (Fig. 6.24c) present fine grains thus proving the occurrence of the dynamic recrystallization. These DRX zones match with those in which the PCG occurs when ram speed is increased (Fig. 6.24c-e). This result is in accordance with several works [11-13], where it is proposed that highly DRX zones may lead to the formation of the PCG. This theory is also confirmed by the comparison between Fig. 6.24g and Fig. 6.24f, where the microstructures of the cross sections of Profile *a* extruded with ram speed of 2 mm/s (Fig. 6.24g) and 5 mm/s (Fig. 6.24h) are reported. The Surface Area 1 of Fig. 6.24g presents a layer of fine equiaxed grains at the edge of the profile, while the grains in Surface Area 2 are coarser and not equiaxed. It is reasonable to assume

that this is caused by the higher strain values and, consequently, higher DRX occurrence in grains of Surface Area 1 with respect to the grains of Surface Area 2 (assumption further confirmed by the numerical results of strain and DRX prediction summarized in the Results and Discussion paragraph). This difference led to the PCG formation in Surface Area 1 and not in Surface Area 2 when the ram speed is increased to 5 mm/s (Fig. 6.24h).

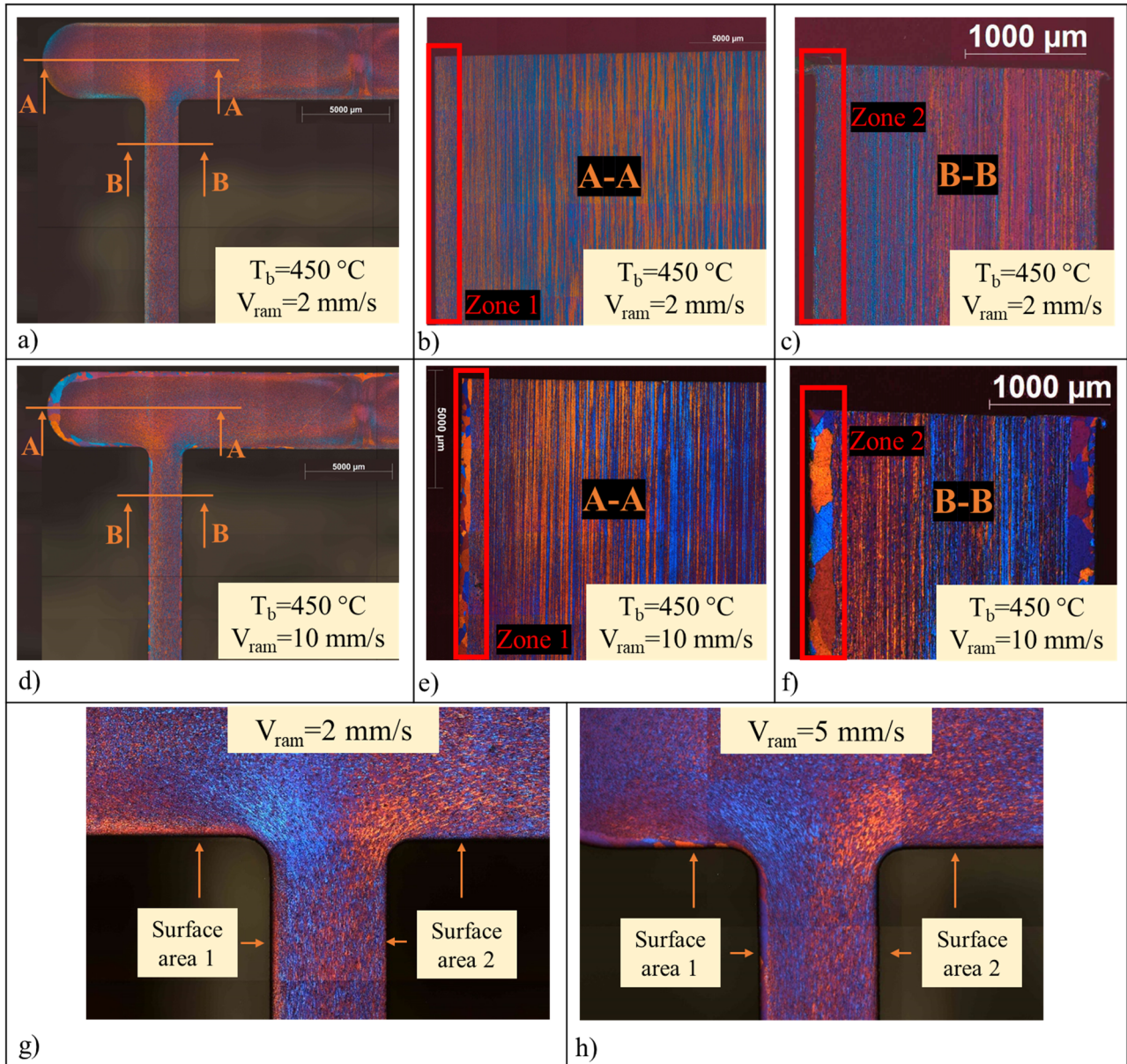


Figure 6.24: Microstructure investigations on Profile *a* extrusions.

In order to show some evolutions of the grains from the longitudinal section perspective, Fig. 6.25 and 6.26 are reported. In Fig. 6.25, the A-A section (see Fig. 6.24) of the profiles extruded with billet temperature of 450 °C and ram speeds of 2, 5 and 10 mm/s are shown in order to highlight the difference in the thickness and length of grains based only on the extrusion speed and, consequently,

on the strain rate reached during the process. In Fig. 6.26, it is reported the A-A section of the profile extruded with billet temperature of 500 °C and ram speed of 5 mm/s. In this figure, it is possible to see the difference between the grains of the inner material and the welding. In the latter, the dynamic recrystallization seems to strongly occur, causing the formation by DRX of small and equiaxed grains, similar to the one occurred in the surface zones when PCG does not occur (Fig. 6.24b).

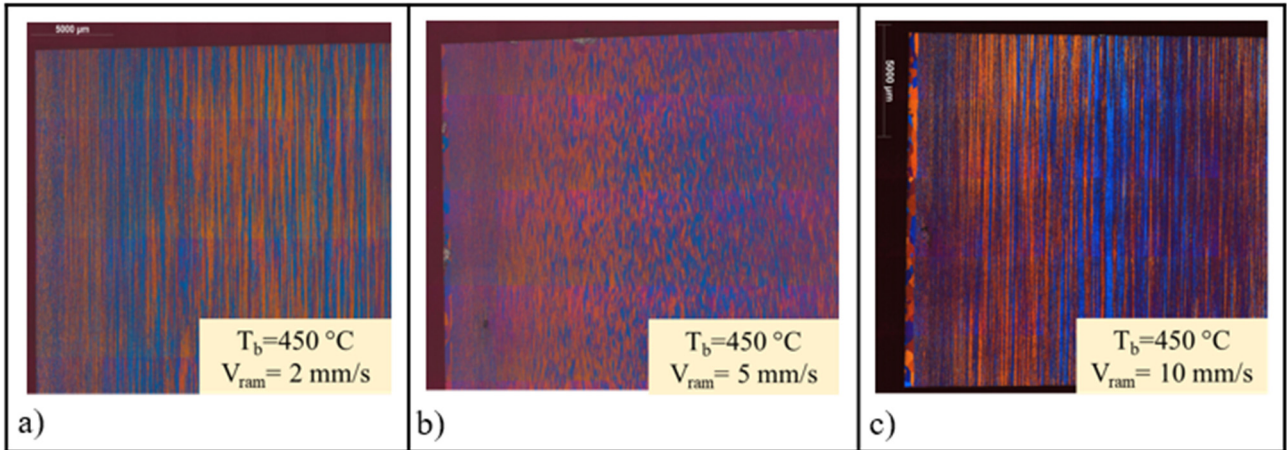


Figure 6.25: Microstructure of profiles extruded with billet temperature of 450 °C and ram speeds of 2, 5 and 10 mm/s.

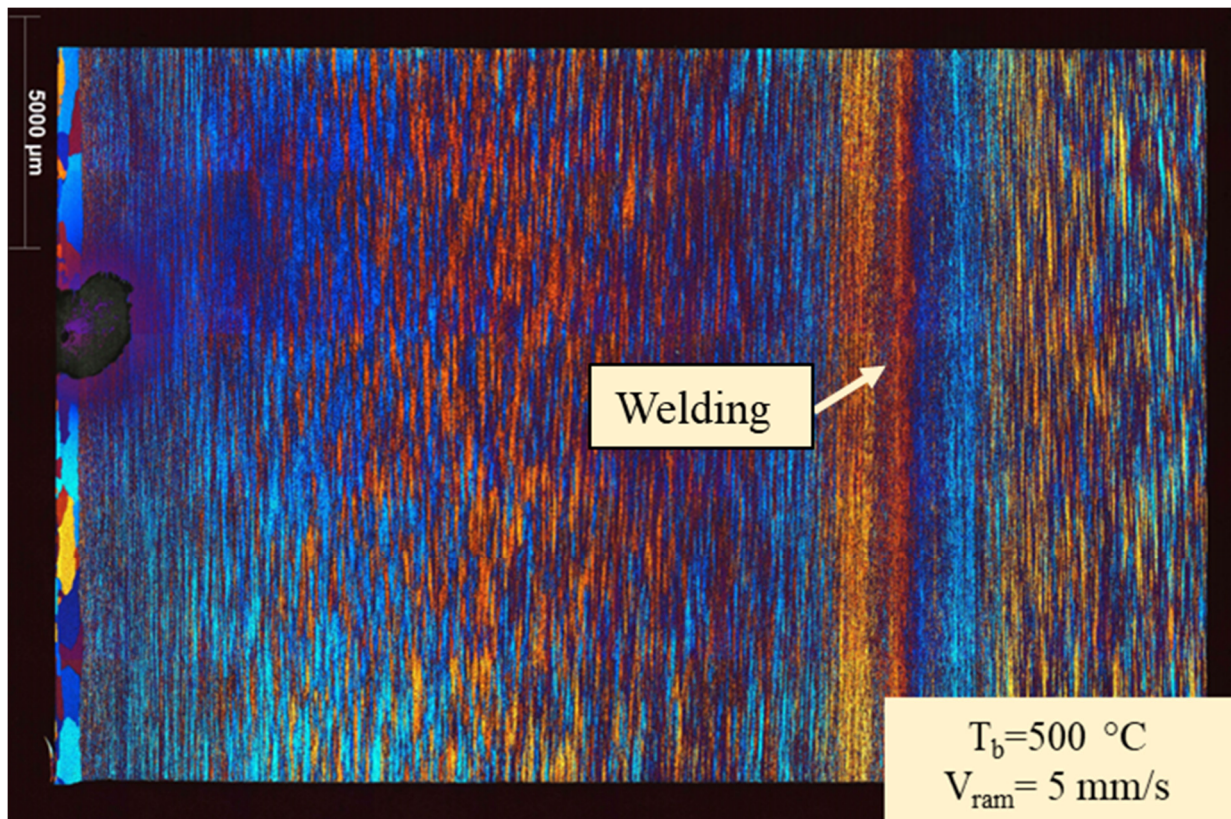


Figure 6.26: Microstructure of profiles extruded with billet temperature of 500 °C and ram speeds of 5 mm/s.

In order to understand which parameter between temperature and ram speed has the main influence on the PCG formation in the high DRX zones, two additional extrusions were performed with billet temperature of 350 °C and ram speeds of 5 mm/s and 10 mm/s. The results are shown in Fig. 6.27. Fig.6.27a reports the microstructure of the profile extruded with ram speed of 5 mm/s and billet temperature 450 °C, which is similar to the microstructure of Fig.6.27c, where the profile was extruded with the same ram speed but lower billet temperature and, consequently, lower profile exit temperature. The same match occurs for the profiles extruded with ram speed of 10 mm/s but different billet and exit temperatures (Fig. 6.27b and Fig.6.27d). Moreover, the profiles in Fig. 6.27a and Fig. 6.27d extruded with the same exit temperature but different ram speeds show different PCG thicknesses. After this comparison, the authors reasonably assumed two conclusions: on the one hand, there is a direct proportionality between the ram speed and PCG thickness. On the other hand, the temperature must be higher than a critical value to trigger the conditions necessary for recrystallization but it has less influence on the PCG formation if compared to the ram speed and, consequently, to the achieved strain rate.

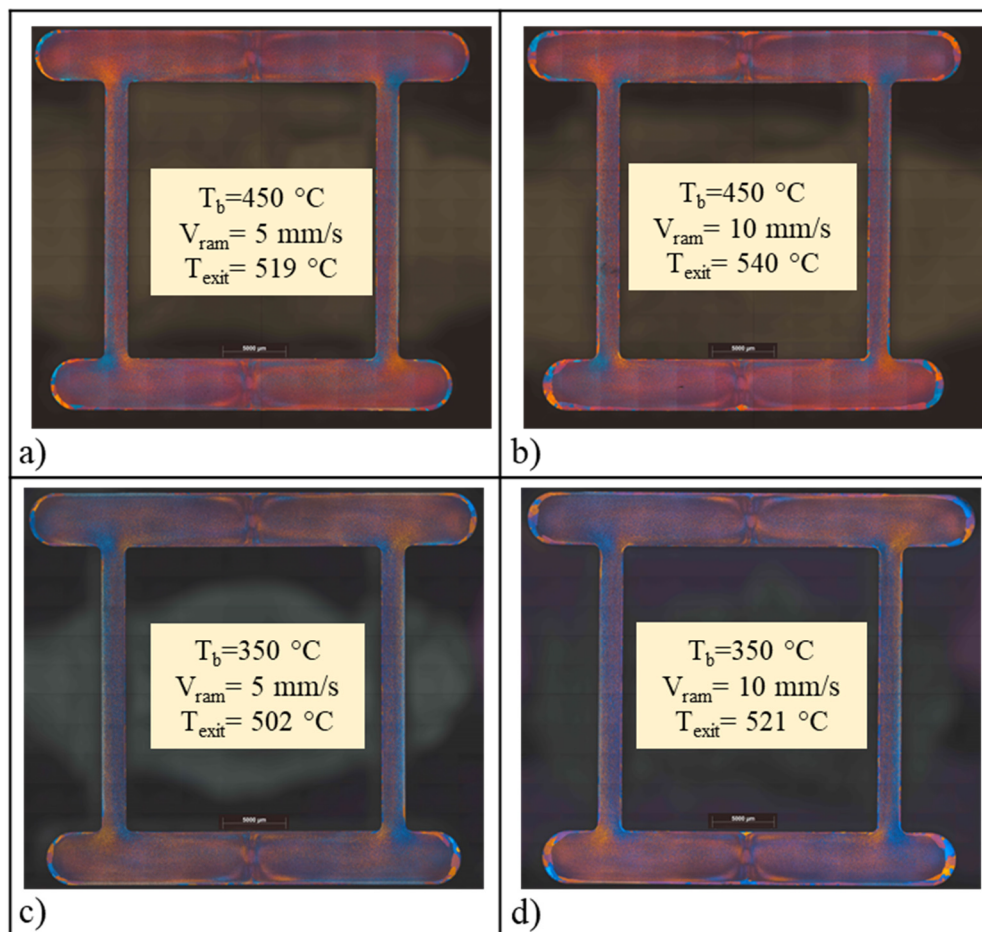


Figure 6.27: Microstructures of Profile *a* with $T_b= 450\text{ °C}$ and $T_b=350\text{ °C}$.

In Fig. 6.28, the SEM analysis of the Profile *a* extruded with billet temperature of 450 °C and ram speeds of 2 mm/s, 5 mm/s and 10 mm/s is reported. For each sample, two different points were investigated, one taken from the surface of the profile P1 and one from the inner part P2. In these points, the dispersoids analysis was carried out, in order to understand the influence of ram speed and exit temperature on the dispersoids fraction volume and size. As a result, no significant difference in the dispersoid distribution between P1 and P2 was found for all the analysed samples. However, with the increase in the ram speed and, consequently, the profile exit temperature, the dispersoids total number increase and the average dimension decrease (Fig. 6.28g), evidencing the precipitation of small Mn-dispersoids during the extrusion process with the increase in the profile exit temperature. In Fig. 6.29, the Energy Dispersive Spectroscopy (EDS) is reported, showing the composition of small dispersoids (Fig. 6.29d-f) and primary iron-phase particles (Fig. 6.29g-i).

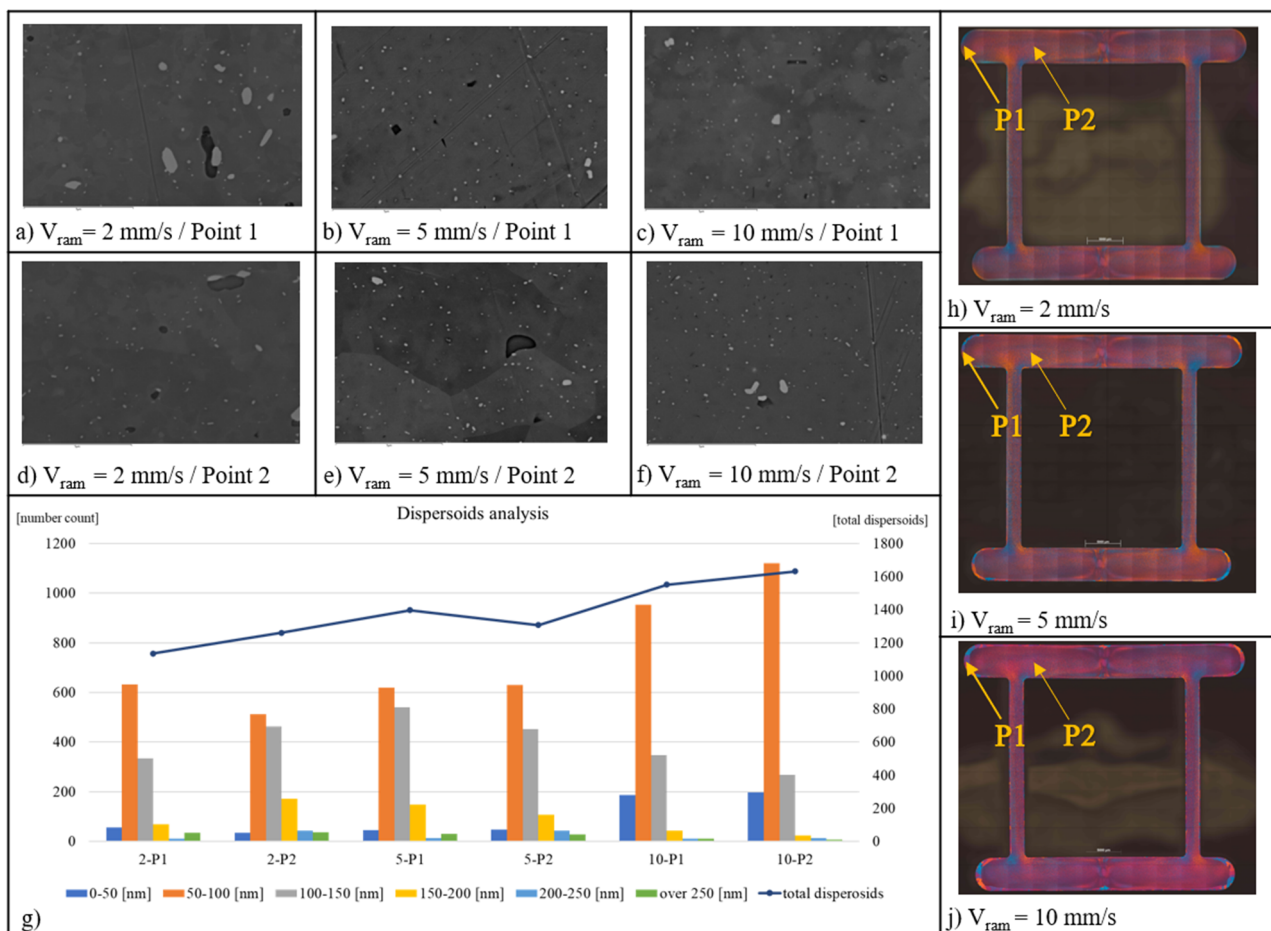


Figure 6.28: SEM analysis of dispersoids distribution of Profile *a* extrusions.

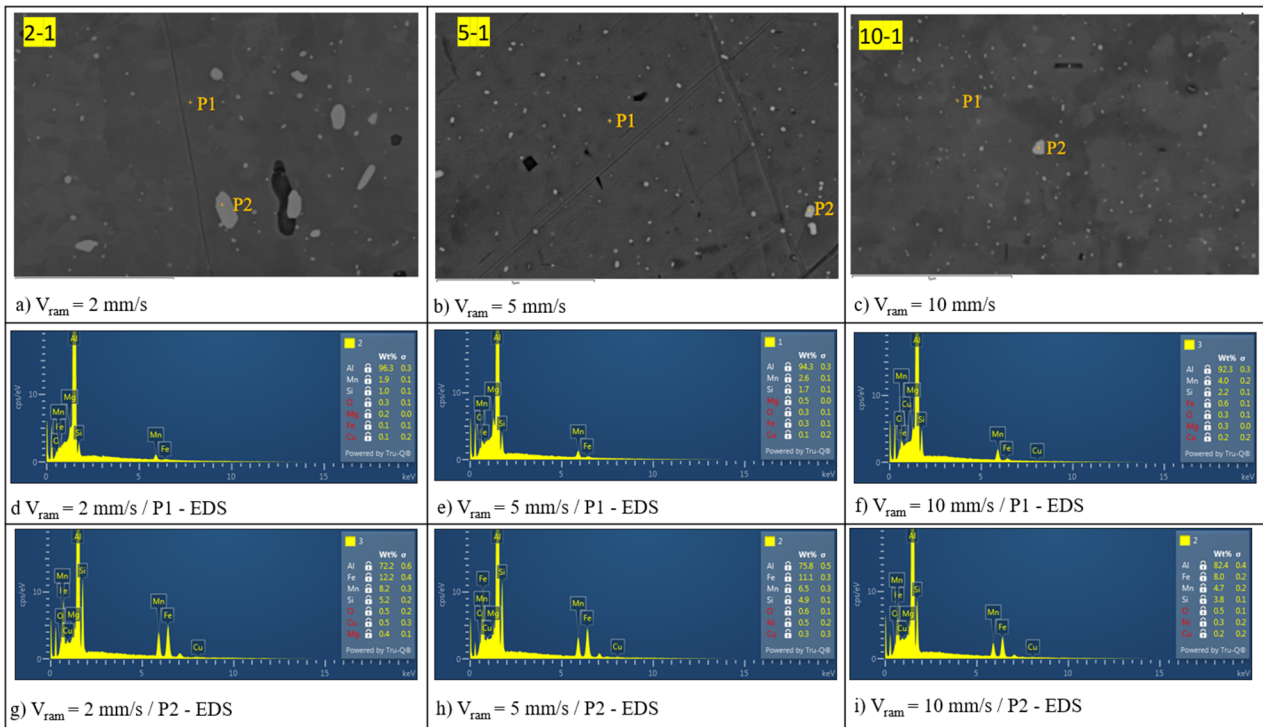


Figure 6.29: EDS analysis of Profile *a* extrusions.

In Fig. 6.30, the microstructures of Profile *b* extruded with billet temperature of 500 °C and different several ram speeds are reported. As for Profile *a*, the analysed specimens were taken at the middle length of the extrusion profile where the process achieved the thermal steady-state condition. In Fig. 6.30a, the profile extruded with 2 mm/s is reported, presenting a complete fibrous microstructure. With the increase in the ram speed, the PCG occurs and grows until it reaches a maximum thickness in the condition with ram speed of 10 mm/s (Fig. 6.30c). In the 15 mm/s and 20 mm/s ram speed conditions (Fig. 6.30d,e), the PCG thickness remains similar to the 10 mm/s condition.

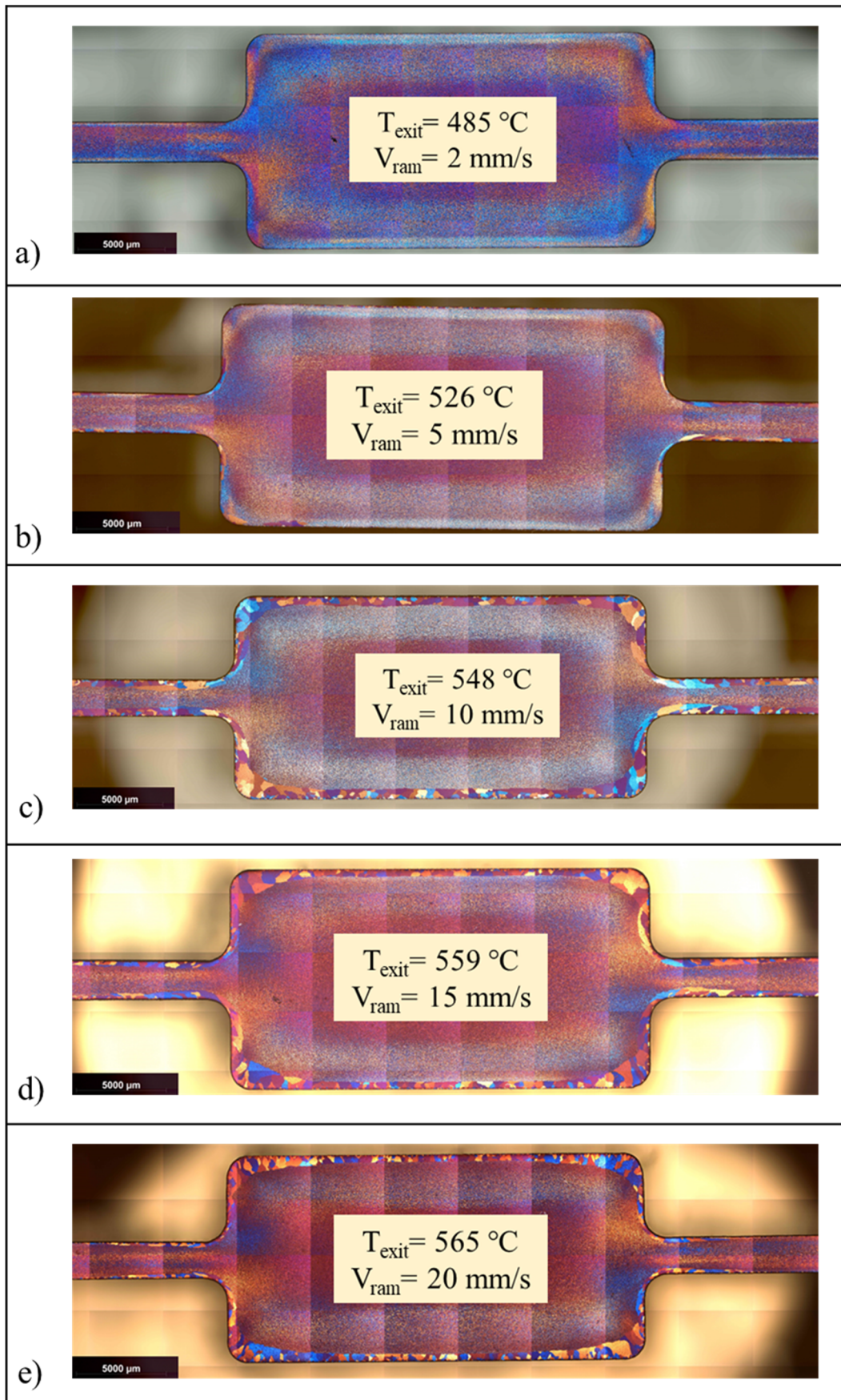


Figure 6.30: Microstructures of Profile *b* with $T_b = 500^{\circ}C$ extruded with different ram speeds.

In Fig. 6.31, a similar investigation to the one shown in Fig. 6.24 was carried out. Two different sections were analysed in order to investigate the fibrous grain dimensions in the inner material and in the edge material where the PCG occurred. As already described for Profile *a* in Fig. 6.24, the grains of Zone 1 (Fig. 6.31b) and Zone 2 (Fig. 6.31c) are finer and almost equiaxed, thus proving the incidence of the DRX in the high strain zones. In contrast with these zones, the grains on the inner part of the profile are elongated along the extrusion direction, with an average length dimensions several times greater than the average thickness.

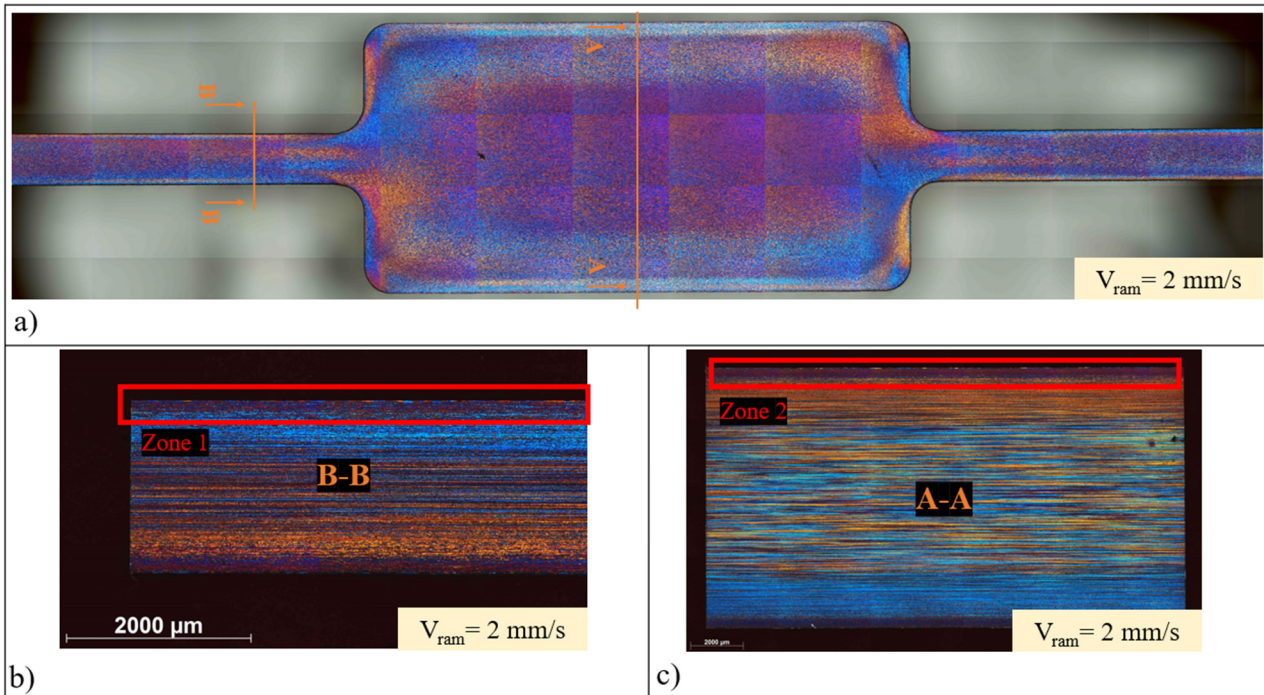


Figure 6.31: Microstructure investigations on Profile *b* extrusions.

6.2.2 PCG Modeling in AA6082 Aluminum Alloy

The modeling of the AA6082 recrystallization behaviour is the same as the one reported in the 6.1.2 paragraph. In addition to that model, according to the experimental evidence of case 2 which highlights a strong influence of the DRX on the surface recrystallization in AA6082 extruded profiles, some improvements were carried out.

In order to investigate the dynamic recrystallization, the following equation proposed by [14] was used to investigate the percentage of DRX occurred in the extruded profile:

$$X_{DRX} = 1 - \exp \left[-\beta \left(\frac{\varepsilon - \varepsilon_c}{\varepsilon_s} \right)^m \right] \quad (6.6)$$

where ε is the strain, ε_c is critical strain corresponding to the beginning of DRX, ε_s is the saturated strain where the DRX happens completely, β and m are material constants ($\beta=1.823$ and $m=1.109$ [14]).

According to the experimental evidence, the PCG formation is mainly caused by the combination of three conditions: high DRX zones, high temperature and high maximum strain rate reached during the deformation of the material. In the areas where these three conditions occur, the force that acts in favour of the recrystallization becomes greater than the retarding force and, consequently, the PCG occurs. Considering that the PCG increase with the exit temperature and ram speed and the stored energy decrease with the increase in the process temperature, it is reasonable to assume that the PCG is favoured because of a decrease in the retarding force for the recrystallization. In Fig. 6.32, a schematization of the principle of the PCG is schematized. A new parameter is introduced P_t which is the total pressure that acts in opposition to the recrystallization. As outlined in the figure, this pressure is lowered, in the high DRX zones, if high temperature and high maximum strain rate are reached. When the P_t value becomes lower than the Stored Energy P_d , which typically reaches the highest values in the profile surface areas, PCG is formed.

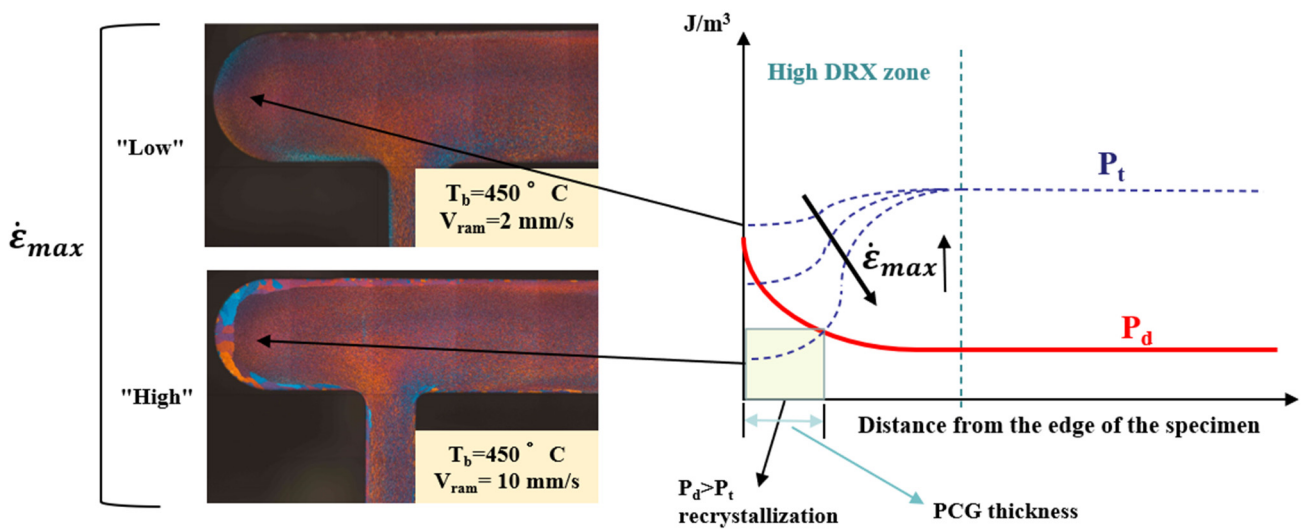


Figure 6.32: PCG modeling schematization.

The value of P_t was calculated as follow:

$$P_t = P_z * C_{sr} \quad (6.6)$$

$$C_{sr} = f(\dot{\varepsilon}_{max}) \quad (6.7)$$

where Csr is a variable which depends on the $\dot{\epsilon}_{max}$ and has a value between 0 and 1. This variable takes into consideration the decrease in the retarding energy for the recrystallization when high maximum strain rate values are reached in high DRX zones and when the processing temperature is higher than the material recrystallization temperature.

6.2.3 Numerical Simulation of the Extrusion Processes

The simulations of the investigated extrusions were performed using Qform Extrusion® (Fig. 6.33). The material properties used in the simulation are reported in Tab. 6.8.

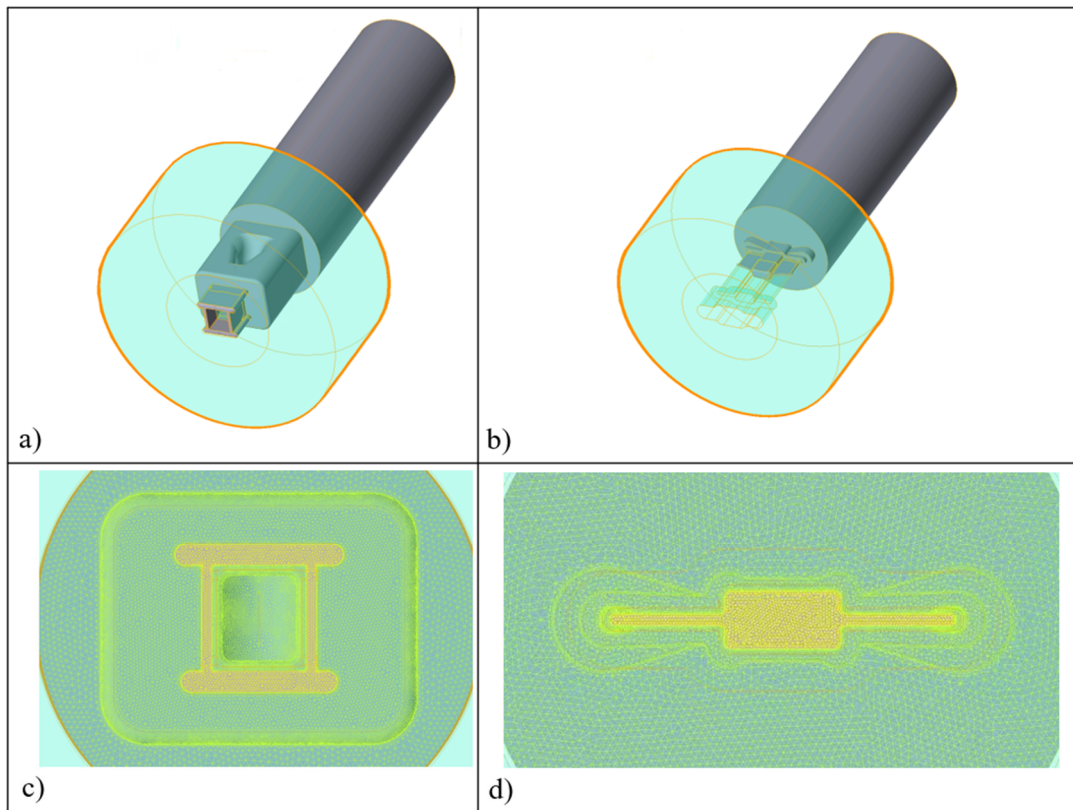


Figure 6.33: FEM simulations of the extrusion processes of Profile *a* and Profile *b*.

Table 6.8: Material parameters for the AA6063 aluminum alloy

Material Properties	AA6082
Density [Kg/m ³]	2690
Specific heat [J/kg K]	900
Thermal conductivity [W/m K]	200
Thermal expansivity [m/K]	$2.34 \cdot 10^{-5}$
Young's modulus [GPa]	68.9
Poisson's ratio	0.33

The constitutive model used for the description of the AA6082 flow stress was proposed by Hensel-Spittel (Eq. 6.5). The values of the Hensel-Spittel constants (m1-m9) are the same to the ones reported in Tab. 6.2.

The friction conditions between workpiece and tools during the manufacturing process were set according to the default values optimized for extrusion in the Qform database (Tab. 6.9).

Table 6.9: Friction conditions.

Surface	Friction condition
Billet-Container	Sticking condition
Billet-Ram	Sticking condition
Billet-Die	Sticking condition
Bearings	Levanov model (m = 0.3, n = 1.25)

In order to validate the results of the numerical simulations, the predicted extrusion load and profile exit temperature were compared to the experimental ones (Fig. 6.34, 6.35). The exit temperature was acquired by the use of a pyrometer pointed in the top-centre of profile *a* (the point is indicated in Fig. 6.35 by the start of the white arrows). The average error in the extrusion load and temperature prediction was in all cases found below the 5%, thus proving the reliability of the simulations.

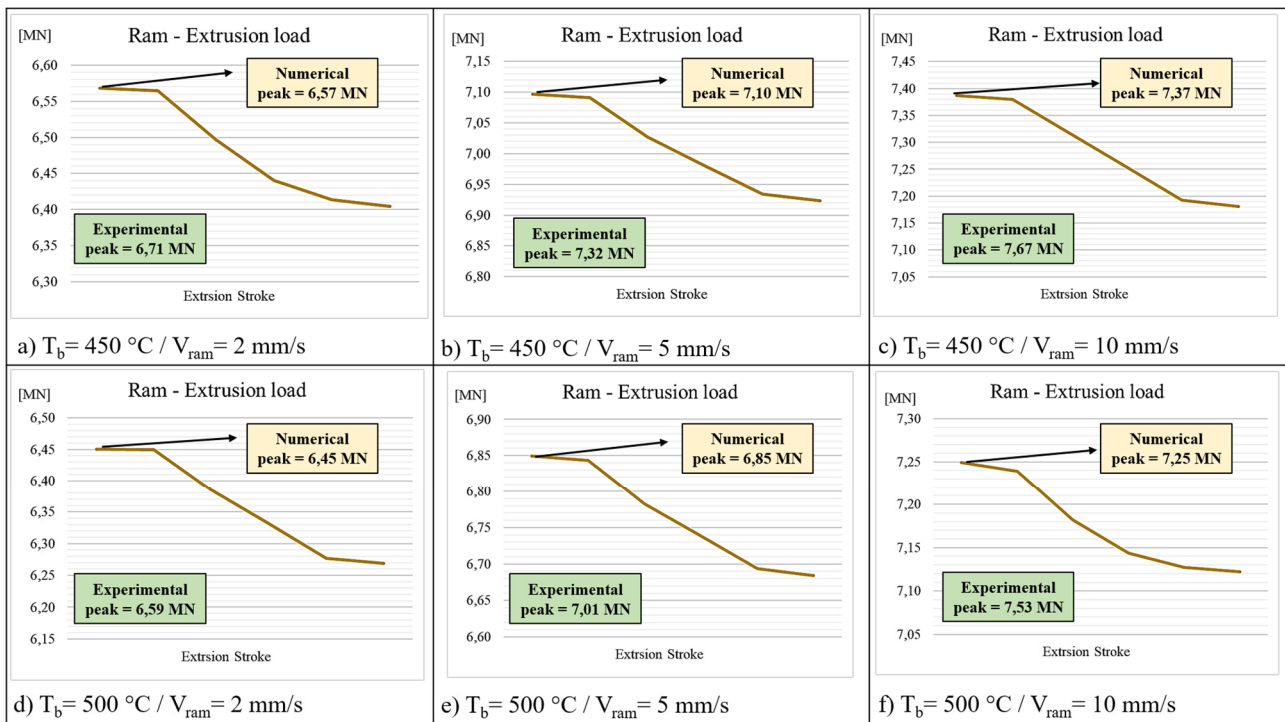


Figure 6.34: Experimental vs numerical peak extrusion load on the extrusion of Profile *a*.

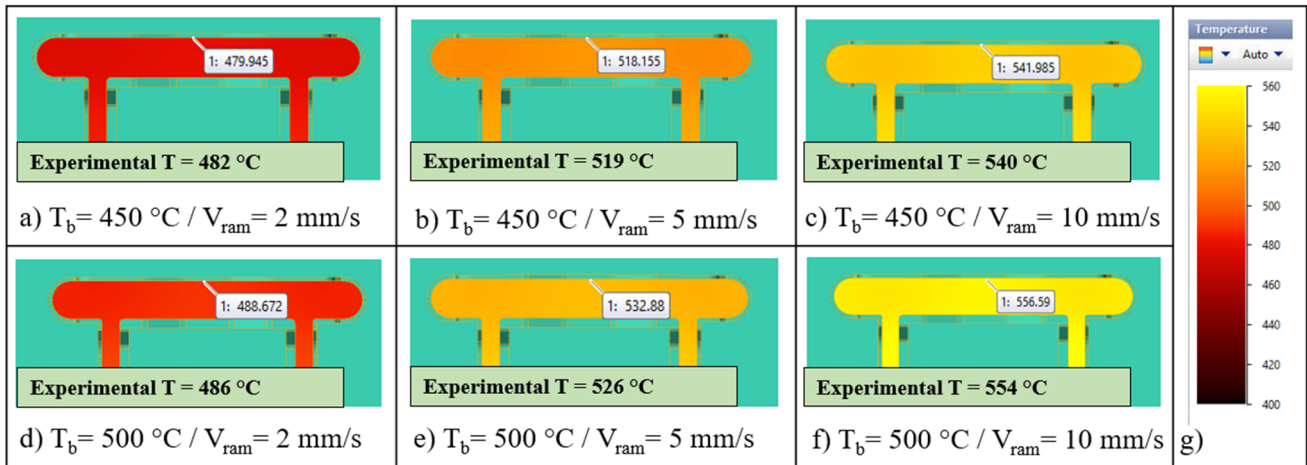


Figure 6.35: Experimental vs numerical exit temperature on the extrusion of Profile *a*.

A similar accuracy in the average error for the extrusion load and exit temperature prediction for profile b.

6.2.4 Comparison Between Numerical and Experimental Results

In order to predict the extension of the PCG zones, simulations of the extrusion processes were carried out and the values of temperature, strain and strain rate were collected. The recrystallization model was developed and implemented within the Qform UK® environment with the aim of calculating the required parameters for the prediction of the defect.

In Fig. 6.36, the results of the DRX simulations for the Profile *a* extruded with $T_b=500\text{°C}$ are reported. The areas with X_{DRX} value of 0 represent the zones of the profile in which the strain value is below the critical strain $\varepsilon_c=3$. The areas with X_{DRX} value of 1 represent the zones of the profile in which the strain value is higher than the saturated strain $\varepsilon_s=16$. The values of ε_c and ε_s were obtained by comparing the numerical and experimental results for the Profile *a* extrusions. As clearly visible from Fig. 6.36, there is no significant difference between the three cases in terms of DRX, as the strain values can be considered stable with the variation of the extrusion speed. DRX zones with X_{DRX} values of 1 match the PCG zones when the profile is extruded at high ram speed. This consideration, combined with the fact that high DRX areas do not always correspond to PCG, leads to the conclusion that high DRX is a condition but not the only one that leads to the formation of the defect.

In Fig. 6.37 and Fig. 6.38, the predictions of the Stored Energy P_d and the maximum value of strain rate reached during the deformation path are reported for Profile *a* extruded with $T_b=500\text{°C}$. Two different trends can be noticed by analyzing the results of Fig. 6.37. First of all, as previously discussed in the PCG Modeling section, the values of P_d increase from the inner part to the edge of the profile. Moreover, the values of the Stored Energy decrease with the increase in the ram speed.

This is explainable because, as the ram speed increase, the temperature increase leading to lower P_d values [9]. About the maximum value of strain rate reached during the deformation path, as expectable, Fig. 6.38 shows that higher ram speeds led to higher values of maximum strain rate.

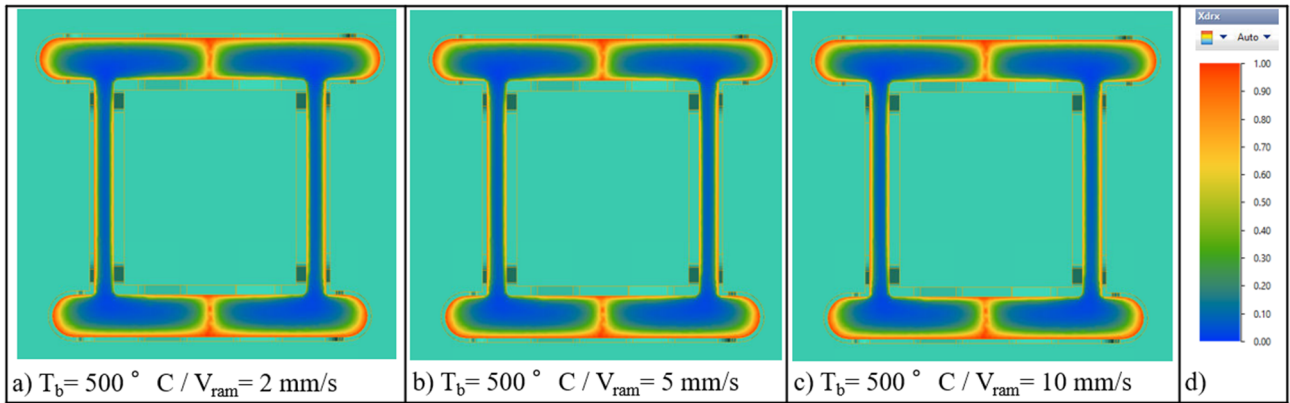


Figure 6.36: DRX simulation results.

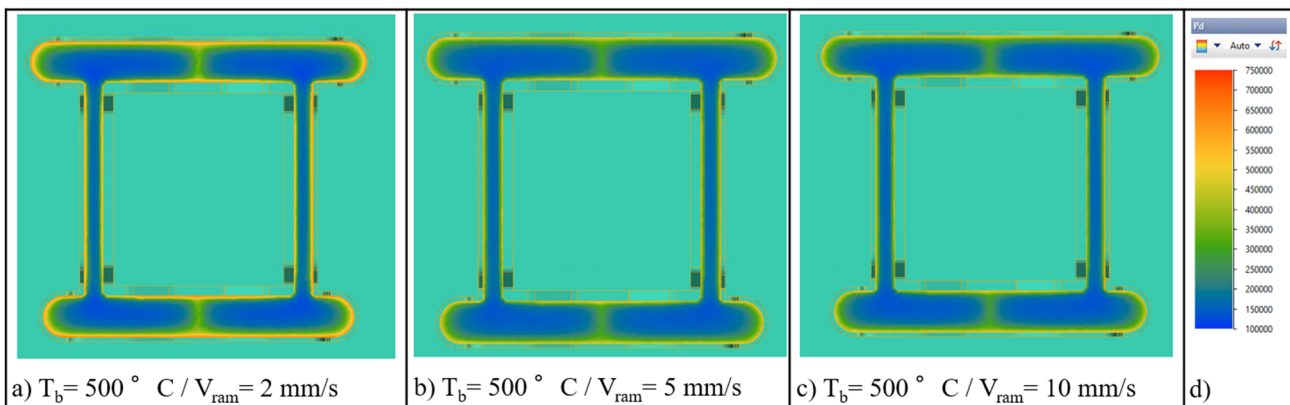


Figure 6.37: Stored Energy P_d simulation results.

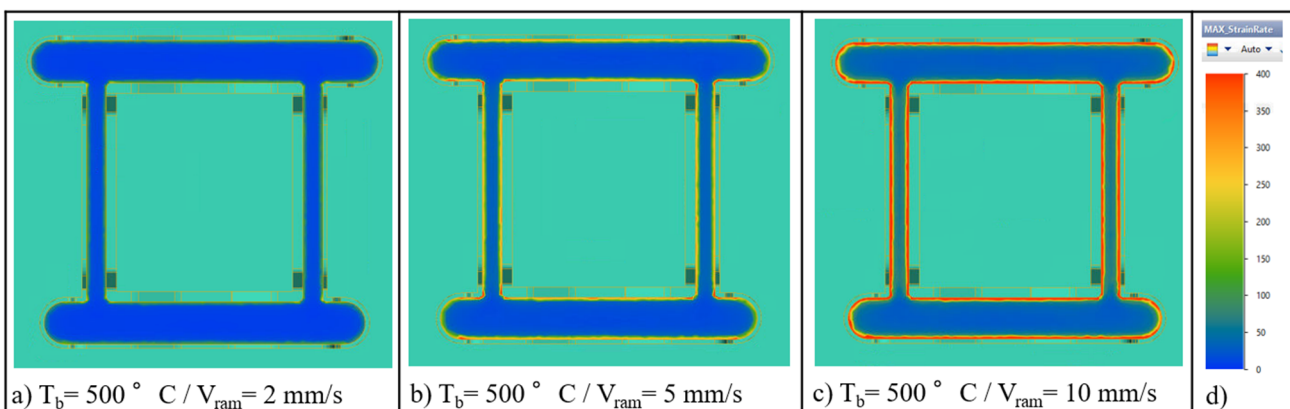


Figure 6.38: Maximum strain rate simulation results.

After the simulations of the parameters that lead to the PCG formation, the defect prediction was carried out according to the proposed modeling (Fig. 6.32). All the values of Profile *a* were used for

the calibration of the model, while the data of Profile *b* were used for the validation. During the calibration phase, the limit values of the three conditions leading to the formation of PCG were found. Regarding the dynamic recrystallization condition, the limit value of X_{DRX} was set to 0.60. About the strain rate condition, the C_{sr} variable, which depends on the maximum strain rate reached during the deformation path, it has been calculated as in Fig. 6.39. The reported trend of C_{sr} needs to be investigated and validated by further experimental and numerical campaigns. Regarding the temperature condition, Agustianingrum M.P. et al. [15] observed that the recrystallization temperature in an aluminum alloy containing Cr did not occurred in samples annealed at 400°C but occurred in samples annealed at 500°C. In this work, the recrystallization limit temperature has been set to 460 °C.

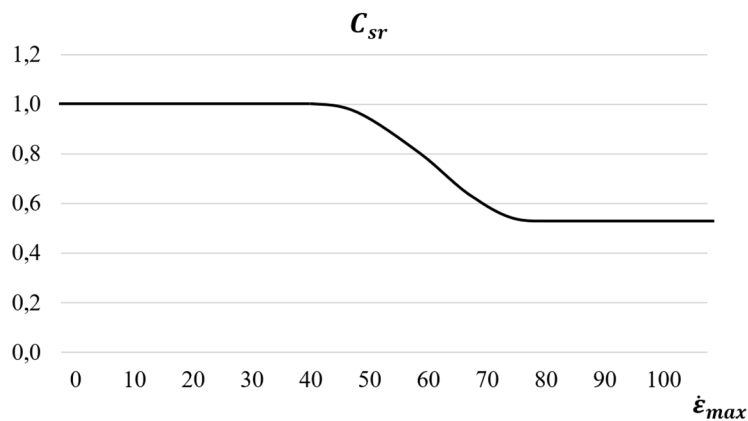


Figure 6.39: C_{sr} behaviour.

In Fig. 6.40 and Fig. 6.41, the results of the PCG simulation of Profile *a* are reported. The areas in red are the PCG areas while the ones in blue are the areas without PCG formation, where the grains are fibrous. As clearly visible from the comparisons reported in Fig. 6.40 and Fig. 6.41, the matching between the experimental (Fig. 6.40d,e,f and Fig. 6.41d,e,f) and numerical (Fig. 6.40a,b,c and Fig. 6.41a,b,c) PCG formation is good both for the extrusions made with billet temperature of 450 °C and 500 °C. Moreover, the same recrystallization model was applied in the extrusion of Profile *b*, showing the same level of reliability (Fig. 6.42). In this case, the model was tested in a wider range of ram speeds without losing the accuracy shown for the prediction of the defect behaviour in Profile *a*.

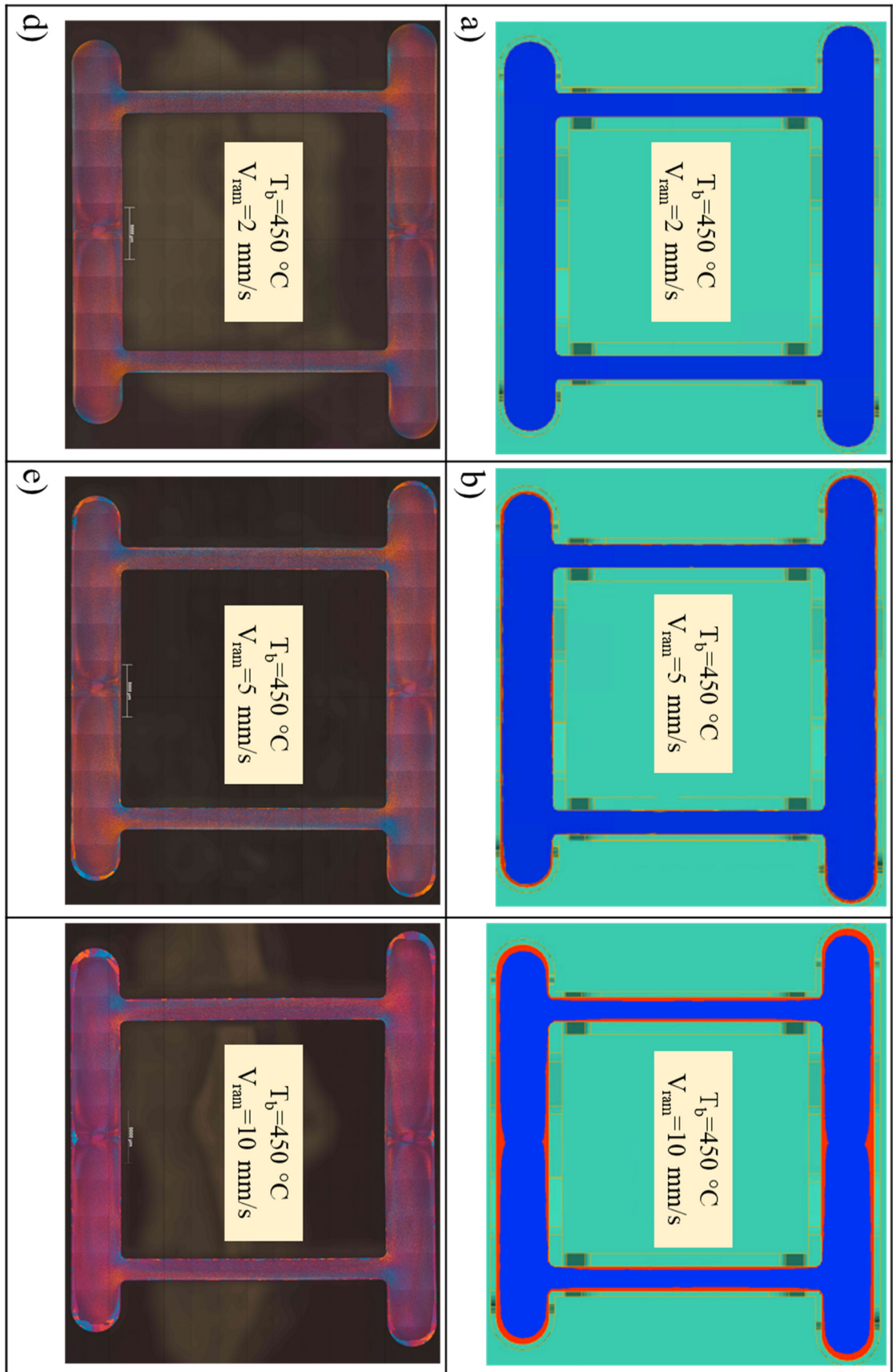


Figure 6.40: Comparison between predicted and experimental PCG formation in the extrusion of Profile *a* with $T_b = 450\text{ °C}$.

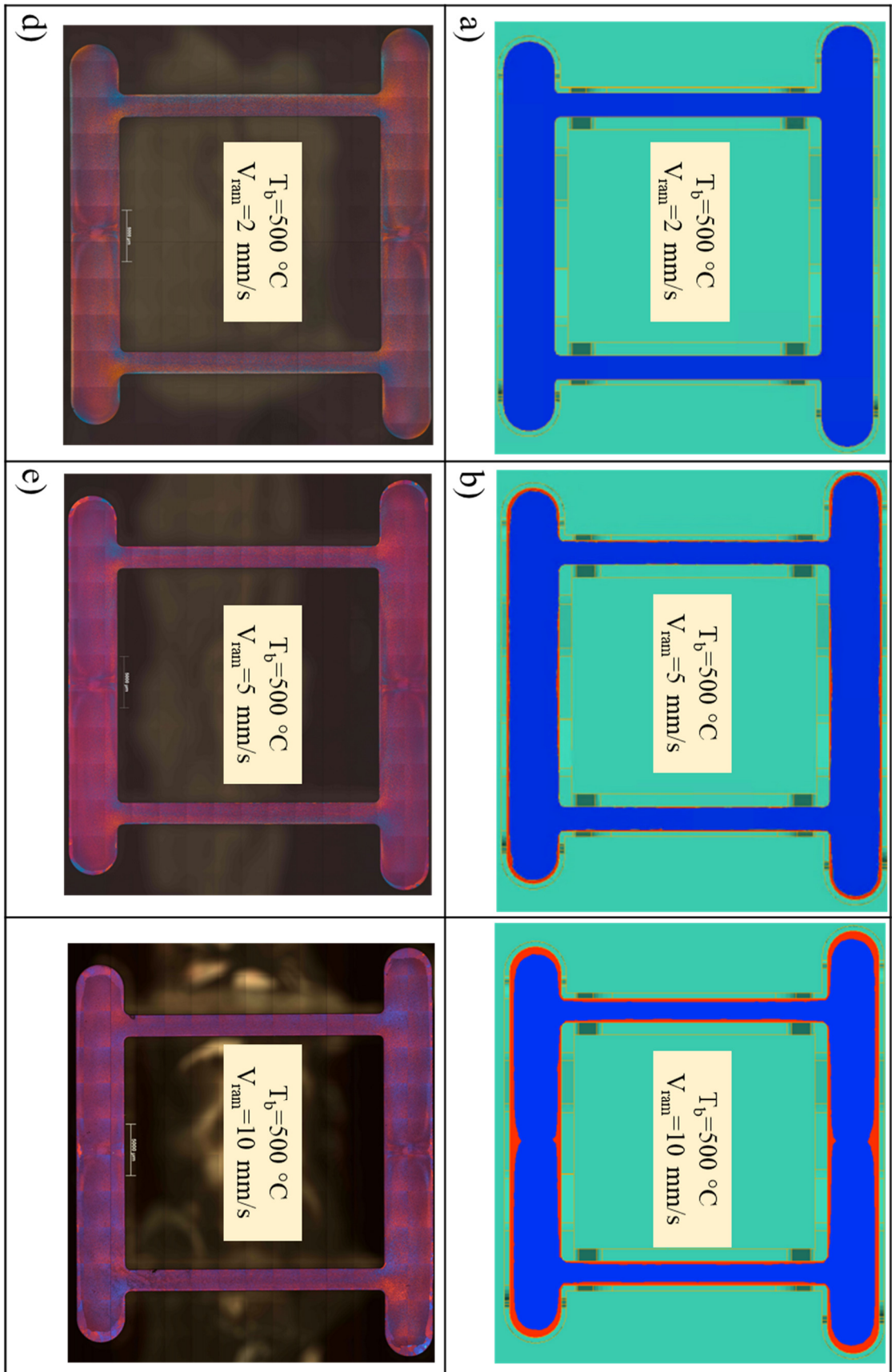


Figure 6.41: Comparison between predicted and experimental PCG formation in the extrusion of Profile *a* with $T_b = 500\text{ °C}$.

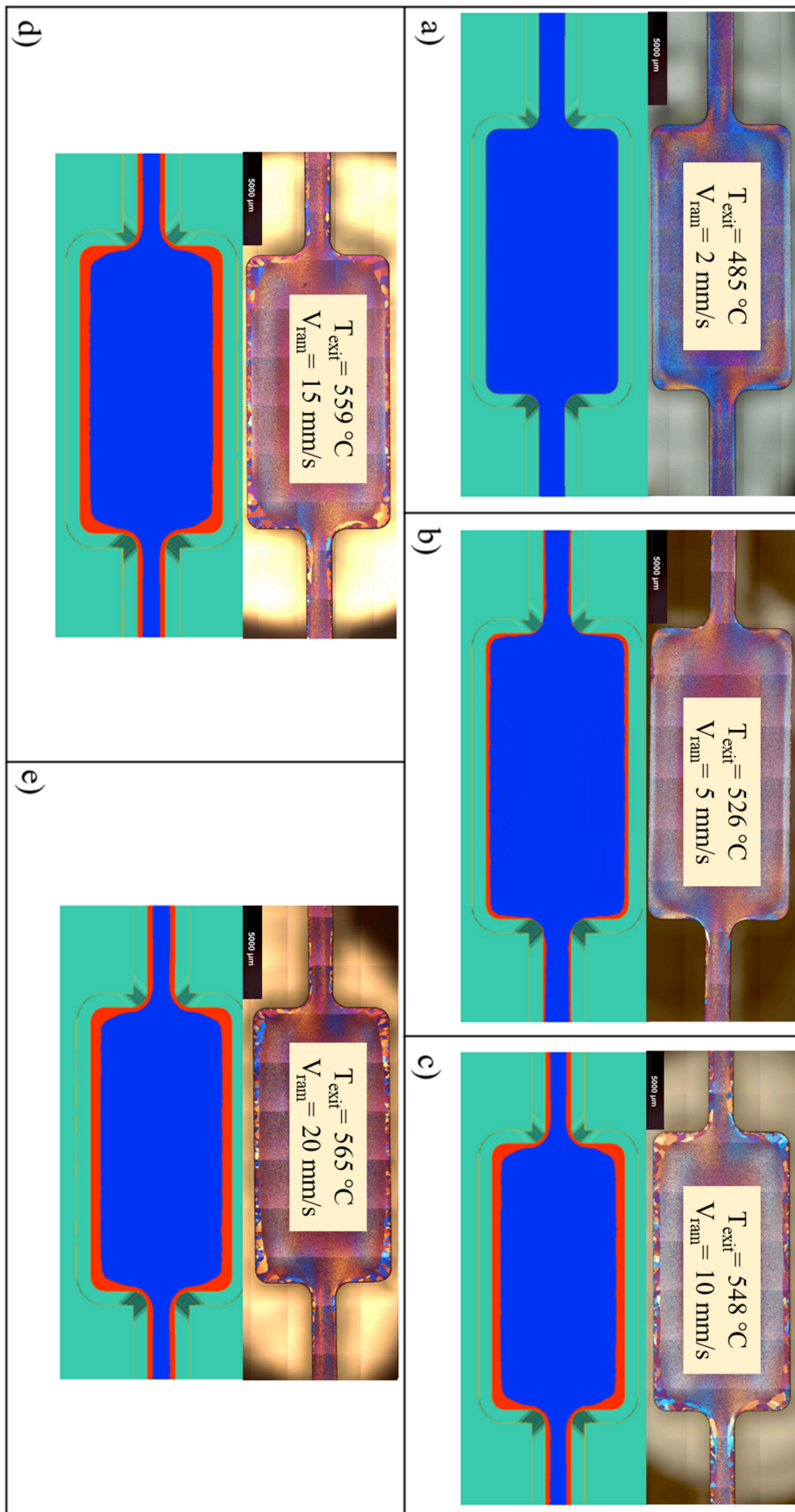


Figure 6.42: Comparison between predicted and experimental PCG formation in the extrusion of Profile b.

6.2.5 Remarks

In the present work, the development of the recrystallization model for the AA6082 aluminum alloy was carried out together with the FEM simulation of two different extrusion profiles using Qform Extrusion® FEM code. The microstructural analysis of the two profiles were performed and the collected data were used for the calibration and validation of the proposed model. The main outcomes of this work can be summarized as following:

- The results of the extensive experimental analysis on the recrystallization of a AA6082 alloy were collected and discussed by comparing the microstructures of the extruded profiles with the research activities already reported in literature. As a result, the main parameters that lead to the PCG formation were identified: high DRX zones, high temperature and high maximum strain rate reached during the deformation of the material.
- From the SEM analysis of the extruded profiles it can be noticed that the distribution of dispersoids is not constant from the billet to the extruded profile. This distribution varies according to the temperatures reached during the extrusion process. In fact, in case of extrusion at high speeds and therefore high exit temperature of the profile, an increase in the number of small-sized dispersoids (0-50 nm) was found.
- An innovative modeling for the evaluation of the PCG formation in the extrusion of AA6082 aluminum alloys was proposed and tested. The results show a good correlation between numerical predictions and experimental data in the PCG thickness both for the hollow and the solid profiles in all the different process conditions.

References

- [1] N. Parson, A. Maltais, C. Jowett, (2012) The Influence of Die Bearing Geometry on Surface Recrystallisation of 6xxx Extrusions, Proceedings of the Tenth International Aluminum Extrusion Technology Seminar ET2012 1: 19-32.
- [2] P. Rios, F. Siciliano, H. Sandim, R. Lesley, A. Padilha (2005) Nucleation and growth during recrystallization, *Materials Research* 8(3): 225-238.
- [3] C.M. Sellars, Q. Zhu (2000) Microstructural modelling of aluminium alloys during thermomechanical processing, *Materials Science and Engineering: A* 280: 1-7.
- [4] Q. Zhu, M.F. Abbod, J. Talamantes-Silva, C.M. Sellars, D.A. Linkens, J.H. Beynon (2003) Hybrid modeling of aluminium-magnesium alloys during thermomechanical processing in terms of physically-based, neuro-fuzzy and finite elements models, *Acta Materialia* 51, 5051-5062.
- [5] L. Donati, A. Segatori, M. El Mehtedi, L. Tomesani (2013) Grain evolution analysis and experimental validation in the extrusion of 6XXX alloys by use of a lagrangian FE code, *International Journal of Plasticity* 46: 70-81.
- [6] I. Schindler, P. Kawulok, V. Ocenasek, P. Opěla, R. Kawulok, S. Ruzs (2019) Flow Stress and Hot Deformation Activation Energy of 6082 Aluminium Alloy Influenced by Initial Structural State, *Metals* 9: 1248-1263.
- [7] F.J. Humphreys, M. Hatherly (2004) Recrystallization and related annealing phenomena, Second edition, Elsevier, Oxford, UK.
- [8] A. Hensel, T. Spittel (1978) Kraft und Arbeitsbedarf bildsamer Formgebungsverfahren, 1. Auflage, Leipzig: VEB Deutscher Verlag für Grundstoffindustrie.
- [9] M. Negozio, R. Pelaccia, L. Donati, B. Reggiani, T. Pinter, L. Tomesani (2021) Finite Element Model Prediction of Charge Weld Behaviour in AA6082 and AA6063 Extruded Profiles, *Journal of Materials Engineering and Performance* 30: 4691–4699.
- [10] L. De Pari, W.Z. Misiolek (2008) Theoretical predictions and experimental verification of surface grain structure evolution for AA6061 during hot rolling, *Acta Materialia* 56: 6174–6185.
- [11] A. R. Eivani, J. Zhou, J. Duszczuk (2016) Mechanism of the formation of peripheral coarse grain structure in hot extrusion of Al-4.5Zn-1Mg, *Philosophical Magazine* 96(12): 1188-1196.
- [12] L. De Peri Jr., W.J. Misiolek (2008) Theoretical prediction and experimental verification of surface grain structure evolution for AA6061 during hot rolling, *Acta Materialia*, 56: 6174-6185.
- [13] W. Misiolek, W.H. Van Geertruyden (2009) Combined Numerical Simulation and Microstructure Characterization for Prediction of Physical Properties in Extruded Aluminum Alloys. *Key Engineering Materials* 424: 1-8.

- [14] C. Zhang, C. Wang, R. Guo, G. Zhao, L. Chen, W. Sun, X. Wang (2019) Investigation of dynamic recrystallization and modeling of microstructure evolution of an Al-Mg-Si aluminum alloy during high-temperature deformation, *Journal of Alloys and Compounds* 773: 59-70.
- [15] M.A. Agustianingrum, N.A. Arandana, R. Wijanarko, B.T. Sofyan (2018). Effect of deformation and annealing temperature on the mechanical properties and microstructure of Al-4.5Zn-1.5Mg-0.9Cr (wt. %) alloy fabricated by squeeze casting, *MATEC Web of Conferences*. 153: 01001.

7. Summary, Conclusions and Future Work

This PhD thesis was focused on the experimental and numerical analysis of the microstructure evolution during the hot extrusion of 6XXX aluminum alloys. In this context, an extensive literature review revealed how chemical composition, grain size and texture affect the mechanical, corrosion, aesthetic, crash and fatigue properties of the material. Once the importance of the microstructure for extruded profiles had been determined, an in-depth research activity was carried out for the investigation of the recrystallization kinetics that occurs during the extrusion process.

With the aim of developing models for the microstructure prediction during manufacturing processes through the use of finite element codes, potentialities and limits of the recrystallization models already present in literature were analyzed. Qform Extrusion UK software was selected as FEM code since previous studies demonstrated the capabilities of the software in accurately predicting the extrusion process global behaviour and the local forming conditions, thus allowing the simulation parameters optimization. The chosen software is a commercial FEM code which allows the simulation of the extrusion process through an ALE approach and the creation of user-customized subroutines for the post-processing calculation of the microstructure of the extruded profile.

From an experimental point of view, campaigns have been conducted with the dual purpose of providing a deeper understanding of the influence of process parameters on the recrystallization of 6XXX alloys but also for the development and validation of new recrystallization models. The reported extruded profiles are industrial-scale profiles with different characteristics in terms of temperatures, profile shapes, dimensions and extrusion ratios, thus producing a reliable amount of data for the numerical model validation. With a particular focus on the mechanisms of PCG formation during the extrusion of AA6082 aluminum alloys, which is fundamental for the development of crash components for automotive applications, the lack of knowledge on the identification of the main parameters responsible for the PCG formation has been filled with the results of the reported analysis: the die design (choke angle, bearings length and geometry) influence on the microstructure of the final component and, consequently, the properties of the material has been examined. It has been proven that the main parameters that lead to the PCG formation are high DRX zones, high temperature and high maximum strain rate reached during the deformation of the material. In more detail, a direct proportionality between the ram speed and PCG thickness was found. On the other hand, the temperature must be higher than a critical value to trigger the conditions necessary for recrystallization but it has less influence on the PCG formation if compared to the ram speed and, consequently, to the achieved strain rate. Moreover, from the SEM analysis of the extruded profiles

it can be noticed that the distribution of dispersoids is not constant from the billet to the extruded profile. This distribution varies according to the temperatures reached during the extrusion process. In fact, in case of extrusion at high speeds and therefore high exit temperature of the profile, an increase in the number of small-sized dispersoids (0-50 nm) was found.

Starting from the recrystallization models available in the literature, evolutive ones have been proposed and validated. As examples, a regression approach was innovatively proposed for the identification of material constants in the models in order to overcome the limits, uncertainties and consequently errors generated by literature assumptions. An innovative equation for the prediction of the grain boundary area per volume at a given strain was proposed and validated. Finally, a more accurate estimation of the final Zener-Hollomon parameter was realized by the implementation of a new user-subroutine in the Qform code that calculates, in each point of the profile cross-section, the maximum strain rate reached in the deformation path during the material flow. That was necessary because the FEM results of the strain rate values calculated in the profile cross-section (immediately after the bearing zone) are always nearby zero. The experimentally acquired data on grain size of AA6063, AA6060 and AA6082 aluminum alloys were used to optimize these models for the prediction of the thickness of the recrystallized layer and the final grain size of the extruded profile after dynamic and static recrystallization. Moreover, it was also developed a new PCG model for the prediction of the defect behaviour. By a methodological point of view, some experiments were used in order to regress material constants while different experimental set-up on the same alloy were used to validate the models predictions. In the grain size prediction, a good experimental-numerical agreement was found which shows, in the prediction of both dynamic and static recrystallized grains, an error always below 25%. Since the high number of both process and metallurgical factors affecting the final grain size, the industrial complexity of the analysed extruded geometries and the approximations deriving from the selected measurement methodology for the experimental analysis of the grain dimension, the range of $\pm 25\%$ of error was considered as a range of excellent prediction accuracy. However, the grain size prediction in the simulation of AGG/PCG grains needs to be further improved to increase the accuracy and the reliability of the models. In the PCG layer thickness prediction, an almost perfect experimental-numerical agreement was found for both the analysed profiles, which proved the reliability of the developed model and allows its application in the industrial field for mechanical and crash properties optimization at a die design stage, without performing time consuming and expensive experimental analyses.

Future developments of this work include the validation of the proposed models in the extrusion of additional AA6063, AA6060 and AA6082 aluminum alloy profiles, the development of

recrystallization models for other 6XXX alloys and the improvement of the AGG/PCG grain size prediction. In addition, another future development of the work carried out during my PhD period will be the study, through a multi-objective approach that combines the setting of process parameters and numerical simulation, of the die design optimization for the production of profiles for crash applications.